Novel Wide Bandgap Polymer Donors Containing Benzodithiophene and Substituted-Thiophene as Donating and Accepting Units for High Performance Non-Fullerene Acceptor Based Organic Solar Cells

by

Yi Yuan

A thesis

presented to the University of Waterloo

in fulfillment of the

thesis requirement for the degree of

Doctor of Philosophy

in

Chemical Engineering

Waterloo, Ontario, Canada, 2024

© Yi Yuan 2024

Examining Committee Membership

The following served on the Examining Committee for this thesis. The decision of the Examining Committee is by majority vote.

External Examiner	Prof. Timothy P. Bender (University of Toronto)
Supervisor	Prof. Yuning Li (University of Waterloo)
Internal Members	Prof. Leonardo Simon (University of Waterloo) Prof. Xianshe Feng (University of Waterloo)
Internal-External Member	Prof. Jean Duhamel (University of Waterloo)

Author's Declaration

This thesis consists of material all of which I authored or co-authored: See Statement of Contributions included in the thesis. This is a true copy of the thesis, including any required final revisions, as accepted by my examiners. I understand that my thesis may be made electronically available to the public.

Statement of Contribution

This thesis consists of materials from several published papers, whereby I, Yi Yuan, was listed as the principal author or co-author. The following publications could not be accomplished without the contribution from my colleagues.

The part of contents in Chapter 1 has been published in

- K. He, P. Kumar, Y. Yuan, Y. Li, *Mater. Adv.*, **2021**, 2, 115.
- Y. Yuan, S. Cui, X. Li, H. Liu, J. Wang, Y. Li, *Macromolecules*, **2024**, 57, 10, 4757–4768.

The contents in Chapter 2 have been published in

- Y. Yuan, P. Kumar, J. Ngai, X. Gao, X. Li, H. Liu, J. Wang, Y. Li, *Macromol. Rapid Commun.* **2022**, 2200325.

The contents in Chapter 3 have been published in

- Y. Yuan, S. Cui, X. Li, H. Liu, J. Wang, Y. Li, *Macromolecules*, **2024**, 57, 10, 4757–4768.

The contents in Chapter 4 have been published in

- Y. Yuan, S. Flynn, X. Li, H. Liu, J. Wang, Y. Li, *Macromol. Rapid Commun.* **2024**, 2400275.

Abstract

Organic solar cells (OSCs), or organic photovoltaics (OPVs), have attracted widespread attention as a promising technology for converting solar energy to electricity owing to their advantages of good mechanical flexibility, lightweight, low-cost and large-area fabrication durability. Over the decades, OSCs have improved rapidly since Heeger's group reported the first bulk heterojunction (BHJ) OSC which is composed of a blend active layer containing a p-type conjugated polymer as a donor and an n-type small molecule organic semiconductor as an acceptor. Recently, significant progress has been achieved with the highest power conversion efficiency (PCE) over 19%, ascribed to the rational design and matching of the conjugated polymer donors with the novel non-fullerene acceptors (NFAs). By reviewing the remarkable progress achieved for OSCs in the past three decades, it is noteworthy that the benzodithiophene (BDT) and thiophene units showed much potential for constructing polymer donors which showed great photovoltaic performance. However, several challenges remained with further development of OSCs including cost-efficiency. It is important to develop new wide bandgap (WBG) conjugated polymer donor materials to balance material cost and device efficiency for high performance NFA-based solar cell towards commercialization.

In this thesis, three series of WBG conjugated polymer donors using BDT as donating units and substituted thiophene as accepting units were designed and synthesized for achieving high photovoltaic performance in the solar cell devices. The first polymer used methyl thiophene-3-acrylate (TA) as an electron-accepting building block to copolymerize with a BDT monomer. The polymer PBDT-TA together with a reference polymer namely PBDT-TC were also synthesized, while PBDT-TA showed an increased polarity compared to that of PBDT-TC due to the simple introduction of the vinyl bridge between the thiophene and ester groups, leading to an increased dielectric constant and reduced exciton binding energy. The organic solar cell device based on the blend of PBDT-TA:ITIC (a commonly used NFA) achieved a higher PCE of 10.47% than that of the PBDT-TC:ITIC-based device (9.68%). The second series of polymers, namely PBDT-TDF and PBDT-TDCl, were designed and synthesized with *gem*-dihalovinyl thiophene as electron-accepting building blocks and BDT as electron-donating building blocks. Both polymers exhibit appropriate energy levels matched with narrow bandgap acceptor Y6. The PBDT-TDF:Y6-based OSC device has achieved a PCE of 8.83%, while the PBDT-TDCl:Y6-based device has a higher PCE of 11.02% due to enhanced short-circuit current density (J_{sc}). The conformational locking effect was discovered in PBDT-TDCl, which allows it to become more

coplanar on the backbone than PBDT-TDF, resulting in higher space-charge-limited current (SCLC) hole mobility which is attributed to the enhanced J_{sc}. At last, the succinimide-substituted thiophene weak electron-accepting building blocks were developed and copolymerized with BDT and its derivatives. Three novel polymers, namely PBDT-TS-C5, PBDT-TSBT-C12 and PBDTF-TSBT-C16 were designed and synthesized. The PBDT-TS-C5:Y6-based OSC device showed a PCE of 8.51%, with a J_{sc} of 19.36 mA/cm^2, an open-circuit voltage (V_{oc}) of 0.89 V and a fill factor (FF) of 0.50. Since the FF is limiting the OPV performance of polymer PBDT-TS-C5, thiophene was introduced as the π-spacer between the donor and acceptor units to improve the planarity of the polymer backbone, hence improve the mobility. The PBDT-TSBT-C12:Y6-based OSC device showed a higher PCE of 10.47%, attributed to enhanced current density and improved FF. To further improve the overall OPV performance of this series of polymers, the fluorine atoms were introduced to BDT units, aiming to lower the highest occupied molecular orbital (HOMO) energy level of the polymer donor and obtain a higher V_{oc} in the devices. The OSC devices based on the blend of PBDTF-TSBT-C16:Y6 demonstrated the highest PCE of 13.21%, with a J_{sc} of 26.83 mA/cm^2, a V_{oc} of 0.80 V and an FF of 0.62. This thesis demonstrates the great design strategies of conjugated polymers containing BDT and substituted thiophene for developing cost-effective high-performance solar cells and other organic electronic applications.

Acknowledgements

I would like to sincerely thank my supervisor, Dr. Yuning Li, for giving me the opportunity to pursue my graduate study at the University of Waterloo. His guidance, advice, patience and encouragement helped me to develop my research skills and resolve research problems during the program. His knowledge and experience provided strong support to me throughout my degree.

I would like to thank my colleague, Dr. Arthur D. Hendsbee, who provided me with the initial training in Printed Electronic Materials Lab (PEML) which helped me to develop my skills in organic synthesis and characterizations including CV, UV measurements and OTFT performance test.

I would like to thank my colleague, Pankaj Kumar, for giving me the training and help on solar cell device fabrication and performance test. I also want to thank Pankaj for his assistance with the material characterizations including PL quenching measurement and AFM measurement.

I would like to thank all my committee members, Dr. Timothy P. Bender, Dr. Leonardo Simon, Dr. Xianshe Feng and Dr. Jean Duhamel, for taking time to review my work.

I would like to thank my colleagues, Jenner H. L. Ngai, who provided me the training with the XRD measurement and Xiguang Gao, who gave me the help with TGA and DSC measurements. I would like to thank all other colleagues including Guanlin Wang, Chenyang Guo, Wuqi Li, Haitao Liu, Xu Li, Zhifang Zhang, Marwa Abd-Ellah, Keqiang He, Guan Xi, Zhong Ma, Belle Jiang, Zhaoyi Yin, John Polena, Zhe Huang, Yonglin Wang, Naixin Zhao, Venkateswarlu Samala, Ravinder Singh, Sung jae Jeon, Daniel Afzal, Merlan Nurzhanov, Haoyu Fu, Scott Flynn, Yvonne Zhong, Andrew Stella, Yas Fazaeli, and Songbo Cui for the assistance my research as well as friendship through my time at the University of Waterloo.

Finally, I would like to acknowledge the unequivocal support from my family, especially my parents, Huiling Li and Pengyun Yuan. I would also like to thank my friends for their constant support.

Table of Contents

Examining Committee Membership ..... **ii**

Author's Declaration ..... **iii**

Statement of Contribution ..... **iv**

Abstract ..... **v**

Acknowledgements ..... **vii**

Table of Contents ..... **viii**

List of Figures ..... **xi**

List of Tables ..... **xvi**

List of Schemes ..... **xviii**

List of Symbols ..... **xix**

List of Abbreviations ..... **xx**

Chapter 1 Introduction **1**

1.1 Overview of Organic Solar Cell 1

1.2 The Working Mechanism of Bulk Heterojunction Organic Solar Cell 5

1.3 High-Performance Wide Bandgap Polymer Donors for NFAs 9

1.4 Techniques for Characterization of Key Properties of Polymers and OSC Device 10

1.5 Objective and the Structure of This Thesis 13

Chapter 2 Synthesis and Characterization of Methyl Thiophene-3-acrylate-based Polymers **15**

2.1 Introduction 15

2.2 Theoretical Study of PBDT-TA 17

2.3 Synthesis of PBDT-TA 19

2.4 Characterization of PBDT-TA 20
2.4.1 Thermal properties 20
2.4.2 Optical and electrochemical properties 21
2.4.3 Dielectric constant and exciton binding energy 22
2.4.4 I-V Characterization 24
2.4.5 Photovoltaic performance 28
2.4.6 Film morphology and microstructure 32
2.5 Conclusion 35
2.6 Experimental Section 35
2.6.1 General Methods. 35
2.6.2 Synthetic Procedures 36
2.6.3 Measurement of dielectric constant 40
2.6.4 OSC device fabrication 41
2.6.5 Appendix 42
Chapter 3 Synthesis and Characterization of Dihalovinyl Thiophene-based Polymers 50
3.1 Introduction 50
3.2 Theoretical Study of PBDT-TDX 51
3.3 Synthesis of PBDT-TDX 53
3.4 Characterization of PBDT-TDX 55
3.4.1 Thermal properties 55
3.4.2 Optical and electrochemical properties 56
3.4.3 I-V Characterization 61
3.4.4 Photovoltaic performance 65
3.4.5 Film morphology and microstructure 71
3.5 Conclusion 75
3.6 Experimental Section 76
3.6.1 General Methods. 76
3.6.2 Synthetic Procedures 77
3.6.3 OSC device fabrication 80
3.6.4 Appendix 81

Chapter 4 Synthesis and Characterization of Succinimide-substituted Thiophene-based Polymers 88

4.1 Introduction 88

4.2 Theoretical Study of Succinimide Based Polymers 89

4.3 Synthesis of Succinimide Based Polymers 91

4.4 Characterization of Succinimide Based Polymers 93

4.4.1 Thermal properties 93

4.4.2 Optical and electrochemical properties 94

4.4.3 I-V Characterization 96

4.4.4 Photovoltaic performance 102

4.4.5 Film morphology and microstructure 108

4.5 Conclusion 111

4.6 Experimental Section 112

4.6.1 General Methods. 112

4.6.2 Synthetic Procedures 113

4.6.3 OSC device fabrication 123

4.6.4 Appendix 124

Chapter 5 Conclusion and Future Direction 153

References 156

List of Figures

Figure 1-1. The best research-cell efficiencies over time (1975-2024).[21] 2
Figure 1-2. The chemical structures of PffBT4T-C9C13, $PC_{61}BM$, ITIC, IT-4F and Y6. 3
Figure 1-3. The chemical structures of D18 and PM6. 5
Figure 1-4. The structure of bulk heterojunction organic solar cell. Reprinted with permission from ref. 61, Copyright 2020, Springer Nature.[61] 6
Figure 1-5. Photovoltaic processes in a bulk heterojunction organic solar cell. Reprinted with permission from ref. 66, Copyright 2019, John Wiley and Sons.[66] 7
Figure 1-6. The J-V curve of a solar cell with all the relevant parameters.[67] 8
Figure 1-7. The structure of D-A polymer donors and the representative D and A building blocks. 10
Figure 2-1. The chemical structures of PBDT-TC (or 3MT-Th) and PBDT-TA. 17
Figure 2-2. DFT simulation results of model compounds di-BDT-TA (a dimer of PBDT-TA) and di-BDT-TC (a dimer of PBDT-TC): Molecular geometries (a, b, e, f), LUMOs (c, g), and HOMOs (d, h). Dipole moment (μ) values of the two compounds are shown in (b) and (f). 18
Figure 2-3. DSC curves of (a) PBDT-TA and (b) PBDT-TC. 20
Figure 2-4. TGA curves of (a) PBDT-TA and (b) PBDT-TC. 20
Figure 2-5. (a) UV-Vis spectra of PBDT-TA and PBDT-TC in solution (chloroform) and thin film states and (b) Cyclic voltammograms of PBDT-TA and PBDT-TC films. 22
Figure 2-6. Dielectric constant of PBDT-TA and PBDT-TC polymers. 23
Figure 2-7. EQE spectra of neat polymer films showing primary and secondary onsets, corresponding to the optical band gap and transport gap. 24
Figure 2-8. (a) Output and (b) transfer (V_{DS} = -100 V) characteristics of a typical OTFT device of PBDT-TA with the annealing temperature of 100 °C. 25
Figure 2-9. (a) Output and (b) transfer (V_{DS} = -100 V) characteristics of a typical OTFT device of PBDT-TC with the annealing temperature of 150 °C. 27
Figure 2-10. (a) OSC device structure; (b) Energy diagram of the materials used in OSCs, where the energy levels of ITO, ZnO, MoO_3, and Ag are taken from the literature; (c) J-V curves of OSC devices; (d) EQE curves of OSC devices; (e) The chemical structure of ITIC. 29
Figure 2-11. PL quenching data for (a) PBDT-TA and (b) PBDT-TC polymers for neat and blend films on glass. The excitation wavelength was 500 nm for donor and 690 nm for acceptor excitation. 31
Figure 2-12. AFM height images of blend films based on (a) PBDT-TA:ITIC and (b) PBDT-TC:ITIC. 33
Figure 2-13. In-plane (IP) and out-of-plane (OOP) 2D-GIXD patterns of PBDT-TA (a, b), PBDT-TA:ITIC (c), PBDT-TC (d ,e) and PBDT-TC:ITIC. 34
Figure 2-14. HT-GPC data of polymer PBDT-TA. 42

Figure 2-15. HT-GPC data of polymer PBDT-TC. 42
Figure 2-16. ^{1}H NMR (300MHz, DMSO) spectra of (E)-3-(2,5-dibromothiophen-3-yl) acrylic acid (2). 45
Figure 2-17. ^{13}C NMR (300MHz, DMSO) spectra of (E)-3-(2,5-dibromothiophen-3-yl) acrylic acid (2). 46
Figure 2-18. ^{1}H NMR (300MHz, $CDCl_3$) spectra of methyl (E)-3-(2,5-dibromothiophen-3-yl) acrylate (3). 47
Figure 2-19. ^{13}C NMR (300MHz, $CDCl_3$) spectra of methyl (E)-3-(2,5-dibromothiophen-3-yl) acrylate (3). 48
Figure 2-20. ^{1}H NMR (300MHz, $CDCl_3$) spectra of methyl 2,5-dibromothiophene-3-carboxylate (5). 49
Figure 3-1. The chemical structures of PM6, PM7, D18, D18-Cl, PBDT-TDF and PBDT-TDCl. 51
Figure 3-2. Simulation data from DFT analysis of di-BDT-TDF (a dimer of PBDT-TDF) and di-BDT-TDCl (a dimer of PBDT-TDCl): Molecular geometries (a, b, e, f), LUMOs (c, g), and HOMOs (d, h). 53
Figure 3-3. DSC curves of (a) PBDT-TDF and (b) PBDT-TDCl. 55
Figure 3-4. TGA curves of (a) PBDT-TDF and (b) PBDT-TDCl. 56
Figure 3-5. (a) Ultraviolet-visible absorption spectra of PBDT-TDF, PBDT-TDCl, Y6 in thin film states and in solution (chloroform), (b) UV-Vis spectra of blend PBDT-TDF:Y6 (w/w = 1:1), PBDT-TDCl:Y6 (w/w = 1:1) in thin film states and in solution (chloroform), (c) Cyclic voltammograms of PBDT-TDF and PBDT-TDCl films, and (d) illustrative conformational structures of PBDT-TDF and PBDT-TDCl, revealing that PBDT-TDF has relatively coplanar TDF units but a more twisted backbone, while PBDT-TDCl has more twisted TDCl units but a more coplanar backbone. 59
Figure 3-6. (a) Output and (b) transfer (V_{DS} = -100 V) characteristics of a representative OTFT device using PBDT-TDF without annealing (room temperature). 62
Figure 3-7. (a) Output and (b) transfer (V_{DS} = -100 V) characteristics of a representative OTFT device using PBDT-TDCl with an annealing temperature of 200 °C. 64
Figure 3-8. (a) The inverted architecture of an OSC device, energy diagram of key materials, and chemical structure of Y6, (b) J-V curves, and (c) EQE curves of PBDT-TDF and PBDT-TDCl-based devices. 66
Figure 3-9. Photoluminescence (PL) quenching data for neat and blend films of PBDT-TDF (a, c) and PBDT-TDCl (b, d) on glass substrates. The excitation wavelength was set at 550 nm for the donor and 800 nm for the acceptor. 69
Figure 3-10. $J^{1/2}$-V curves of hole-only (a and b) and electron-only (c and d) devices of PBDT-TDF:Y6 and PBDT-TDCl:Y6 by fitting the modified Mott-Gurney equation: $J = 9\varepsilon_0\varepsilon_r\mu V^2/8L^3$, where ε_0 is the permittivity of the free space (8.8542×10^{-12} $CV^{-1}m^{-1}$), ε_r is the active layer electric constant, μ is the carrier mobility and L is active layer thickness. 70
Figure 3-11. AFM height and phase images of blend films based on PBDT-TDF:Y6 (a, b) and PBDT-TDCl:Y6 (c, d). 72
Figure 3-12. Out-of-plane (OOP) and in-plane (IP) 2D-GIXD patterns of neat film PBDT-TDF (a, b), neat film PBDT-TDCl (e, f), blend film PBDT-TDF:Y6 (c, d) and blend film PBDT-TDCl:Y6 (g, h) without annealing (RT) and annealed at different temperatures. 73

Figure 3-13. 2D XRD images for thin films of (a) PBDT-TDF annealed at 200 °C, (b) PBDT-TDF:Y6 annealed at 50 °C, (c) PBDT-TDCl annealed at 200 °C and (d) PBDT-TDCl:Y6 annealed at 200 °C. 74
Figure 3-14. HT-GPC data of PBDT-TDF. 81
Figure 3-15. HT-GPC data of PBDT-TDCl. 81
Figure 3-16. ^{1}H NMR (300 MHz, $CDCl_3$) spectrum of 2,5-dibromo-3-(2,2-difluorovinyl)thiophene (7). 84
Figure 3-17. ^{13}C NMR (75 MHz, $CDCl_3$) spectrum of 2,5-dibromo-3-(2,2-difluorovinyl)thiophene (7). 85
Figure 3-18. ^{1}H NMR (300 MHz, $CDCl_3$) spectrum of 2,5-dibromo-3-(2,2-dichlorovinyl)thiophene (8). 86
Figure 3-19. ^{13}C NMR (75 MHz, $CDCl_3$) spectrum of 2,5-dibromo-3-(2,2-dichlorovinyl)thiophene (8). 87
Figure 4-1. General structure of polymer donors comprising BDT and thiophene building blocks, and representative substituted thiophene (TX) acceptor building blocks, including the succinimide-substituted thiophene reported in this work. 89
Figure 4-2. DFT simulation results of model compounds di-BDT-TS (a dimer of PBDT-TS-C5), di-BDT-TSBT (a dimer of PBDT-TSBT-C12) and di-BDTF-TSBT (a dimer of PBDTF-TSBT-C16): Molecular geometries (a, b, e, f, i, j), LUMOs (c, g, k), and HOMOs (d, h, l). 91
Figure 4-3. DSC measurement of (a) PBDT-TS-C5, (b) PBDT-TSBT-C12 and (c) PBDTF-TSBT-C16. 93
Figure 4-4. TGA measurement of (a) PBDT-TS-C5, (b) PBDT-TSBT-C12 and (c) PBDTF-TSBT-C16. 94
Figure 4-5. (a) UV-Vis spectra of PBDT-TS-C5, PBDT-TSBT-C12 and PBDTF-TSBT-C16 in solution (chloroform) and thin film states and (b) Cyclic voltammograms of PBDT-TS-C5, PBDT-TSBT-C12 and PBDTF-TSBT-C16 films. 95
Figure 4-6. (a) Output and (b) transfer (V_{DS} = -100 V) characteristics of a representative OTFT device using PBDT-TS-C5 with an annealing temperature of 150 °C. 97
Figure 4-7. (a) Output and (b) transfer (V_{DS} = -100 V) characteristics of a representative OTFT device using PBDT-TSBT-C12 with an annealing temperature of 200 °C. 99
Figure 4-8. (a) Output and (b) transfer (V_{DS} = -100 V) characteristics of a representative OTFT device using PBDTF-TSBT-C16 with an annealing temperature of 100 °C. 101
Figure 4-9. (a) The energy diagrams of PBDT-TS-C5, PBDT-TSBT-C12, PBDTF-TBST-C16 and Y6, (b) J-V curves, (c) EQE curves of PBDT-TS-C5, PBDT-TSBTC-C12 and PBDTF-TSBT-C16 based devices, and (d) the chemical structure of Y6 103
Figure 4-10. PL quenching data for PBDT-TS-C5 (a, d), PBDT-TSBT-C12 (b, e) and PBDTF-TSBT-C16 (c, f) and their blend films with Y6 (with a 1:1 ratio) on glass. The excitation wavelengths were 550 nm (PBDT-TS-C5), 570 nm (PBDT-TSBT-C12). and 550 nm (PBDTF-TSBT-C16) for donors respectively and 800 nm for the acceptor (Y6). 106
Figure 4-11. AFM height and phase images of blend films based on PBDT-TS-C5:Y6 (a, d), PBDT-TSBT-C12:Y6 (b, e) and PBDTF-TSBT-C16:Y6 (c, f). 109

Figure 4-12. Out-of-plane (OOP) and in-plane (IP) 2D-GIXD patterns of neat film PBDT-TS-C5 (a, b), neat film PBDT-TSBT-C12 (e, f), neat film PBDTF-TSBT-C16 (i, j), blend film PBDT-TS-C5:Y6 (c, d), blend film PBDT-TSBT-C12:Y6 (g, h), and blend film PBDTF-TSBT-C16:Y6 (k, l) without annealing (RT) and annealed at different temperatures. 111
Figure 4-13. HT-GPC data of polymer PBDT-TS-C5. 124
Figure 4-14. HT-GPC data of polymer PBDT-TSBT-C12. 125
Figure 4-15. HT-GPC data of polymer PBDTF-TSBT-C16. 126
Figure 4-16. ^{1}H NMR (300MHz, $CDCl_3$) spectra of 1-(pentan-3-yl)-1H-pyrrole-2,5-dione (S-C5). 132
Figure 4-17. ^{1}H NMR (300MHz, $CDCl_3$) spectra of 3-((2,5-dibromothiophen-3-yl)methylene)-1-(pentan-3-yl)pyrrolidine-2,5-dione (TS-C5-Br). 133
Figure 4-18. ^{13}C NMR (75MHz, $CDCl_3$) spectra of 3-((2,5-dibromothiophen-3-yl)methylene)-1-(pentan-3-yl)pyrrolidine-2,5-dione (TS-C5-Br). 134
Figure 4-19. ^{1}H NMR (300MHz, $CDCl_3$) spectra of 1-(2-butyloctyl)-1H-pyrrole-2,5-dione (S-C12). 135
Figure 4-20. ^{1}H NMR (300MHz, $CDCl_3$) spectra of 1-(2-butyloctyl)-3-((2,5-dibromothiophen-3-yl)methylene)pyrrolidine-2,5-dione (TS-C12-Br). 136
Figure 4-21. ^{1}H NMR (300MHz, CDCl3) spectra of 3-([2,2':5',2''-terthiophen]-3'-ylmethylene)-1-(2-butyloctyl)pyrrolidine-2,5-dione (TSBT-C12). 137
Figure 4-22. ^{13}C NMR (75MHz, $CDCl_3$) spectra of 3-([2,2':5',2''-terthiophen]-3'-ylmethylene)-1-(2-butyloctyl)pyrrolidine-2,5-dione (TSBT-C12). 138
Figure 4-23. ^{1}H NMR (300MHz, $CDCl_3$) spectra of 1-(2-butyloctyl)-3-((5,5''-dibromo-[2,2':5',2''-terthiophen]-3'-yl)methylene)pyrrolidine-2,5-dione (TSBT-C12-Br). 139
Figure 4-24. ^{13}C NMR (300MHz, $CDCl_3$) spectra of 1-(2-butyloctyl)-3-((5,5''-dibromo-[2,2':5',2''-terthiophen]-3'-yl)methylene)pyrrolidine-2,5-dione (TSBT-C12-Br). 140
Figure 4-25. ^{1}H NMR (300MHz, $CDCl_3$) spectra of 1-(2-hexyldecyl)-1H-pyrrole-2,5-dione (S-C16). 141
Figure 4-26. ^{13}C NMR (75MHz, $CDCl_3$) spectra of 1-(2-hexyldecyl)-1H-pyrrole-2,5-dione (S-C16). 142
Figure 4-27. ^{1}H NMR (300MHz, $CDCl_3$) spectra of 3-((2,5-dibromothiophen-3-yl)methylene)-1-(2-hexyldecyl)pyrrolidine-2,5-dione (TS-C16-Br). 143
Figure 4-28. ^{1}H NMR (300MHz, $CDCl_3$) spectra of 3-([2,2':5',2''-terthiophen]-3'-ylmethylene)-1-(2-hexyldecyl)pyrrolidine-2,5-dione (TSBT-C16). 144
Figure 4-29. ^{1}H NMR (300MHz, $CDCl_3$) spectra of 3-((5,5''-dibromo-[2,2':5',2''-terthiophen]-3'-yl)methylene)-1-(2-hexyldecyl)pyrrolidine-2,5-dione (TSBT-C16-Br). 145
Figure 4-30. ^{13}C NMR (75MHz, $CDCl_3$) spectra of 3-((5,5''-dibromo-[2,2':5',2''-terthiophen]-3'-yl)methylene)-1-(2-hexyldecyl)pyrrolidine-2,5-dione (TSBT-C16-Br). 146
Figure 4-31. ^{1}H NMR (300MHz, $CDCl_3$) spectra of PBDT-TS-C5. 147
Figure 4-32. ^{1}H NMR (300MHz, $CDCl_3$) spectra of PBDT-TSBT-C12. 148

Figure 4-33. ^{1}H NMR (300MHz, $CDCl_3$) spectra of PBDTF-TSBT-C16. 149
Figure 4-34. MALDI MS spectrum of 3-((2,5-dibromothiophen-3-yl)methylene)-1-(pentan-3-yl)pyrrolidine-2,5-dione (TS-C5-Br). 150
Figure 4-35. MALDI MS spectrum of 1-(2-butyloctyl)-3-((5,5''-dibromo-[2,2':5',2''-terthiophen]-3'-yl)methylene)pyrrolidine-2,5-dione (TSBT-C12-Br). 151
Figure 4-36. MALDI MS spectrum of 3-((5,5''-dibromo-[2,2':5',2''-terthiophen]-3'-yl)methylene)-1-(2-hexyldecyl)pyrrolidine-2,5-dione (TSBT-C16-Br). 152

List of Tables

Table 2-1. UV-vis and CV data of PBDT-TA and PBDT-TC. 22
Table 2-2. Dielectric constant and exciton binding energy of PBDT-TA and PBDT-TC. 24
Table 2-3. OTFT properties of PBDT-TA. 26
Table 2-4. OTFT properties of PBDT-TC. 28
Table 2-5. Photovoltaic parameters of PBDT-TA:ITIC and PBDT-TA:ITIC. 30
Table 2-6. SCLC data of PBDT-TA and PBDT-TC based devices. 32
Table 2-7. Summary of the photovoltaic properties of the PBDT-TA:ITIC devices processed at different RPMs at annealing temperature of 130 °C. 43
Table 2-8. Summary of the photovoltaic properties of the PBDT-TA:ITIC devices processed with different annealing temperatures and solvents for 10 min and 600 RPM. 43
Table 2-9. Summary of the photovoltaic properties of the PBDT-TA:ITIC devices processed with different solvents at annealing temperature of 130 °C and 600 RPM. 44
Table 2-10. Summary of the photovoltaic properties of the devices processed with various additives at annealing temperature of 130 °C and 600 RPM. 44
Table 3-1. GPC, UV-vis and CV data of PBDT-TDF and PBDT-TDCl. 55
Table 3-2. Summary of UV-Vis spectroscopic data of PBDT-TDF, PBDT-TDCl, Y6, and PBDT-TDF:Y6, and PBDT-TDCl. 60
Table 3-3. OTFT properties of PBDT-TDF. 63
Table 3-4. OTFT properties of PBDT-TDCl. 65
Table 3-5. Photovoltaic performance of PBDT-TDF:Y6 and PBDT-TDCl:Y6 based devices. 66
Table 3-6. SCLC mobility data of PBDT-TDF and PBDT-TDCl. 71
Table 3-7. Summary of photovoltaic properties of PBDT-TDF:Y6-based devices processed at different spin coating rates (in rotations per minute, RPM) and different annealing temperatures. Active layer thickness: ~120 nm for films spin-coated at 1500 RPM, ~100 nm for films spin-coated at 2500 RPM. 82
Table 3-8. Summary of photovoltaic properties of PBDT-TDF:Y6-based devices processed with different donor: acceptor mass ratios, spin-coated at 2500 RPM, and annealed at 100 °C. 82
Table 3-9. Summary of photovoltaic properties of PBDT-TDF:Y6-based devices processed using chloroform with different solvent additives, spin-coated at 2500 RPM, and annealed at 100 °C. 83
Table 3-10. Summary of photovoltaic properties of PBDT-TDCl:Y6-based devices processed at different spin-coating rates and annealed at 100 °C. Active layer thickness: Active layer thickness: ~140 nm for films spin-coated at 500 RPM, ~130 nm for films spin-coated at 1000 RPM, and ~120 nm for films spin-coated at 1500 RPM. 83

Table 3-11. Summary of photovoltaic properties of devices based on PBDT-TDCl:Y6 films spin-coated at 500 RPM and annealed at different temperatures. 84
Table 4-1. GPC, UV-vis and CV data of PBDT-TS-C5, PBDT-TSBT-C12 and PBDTF-TSBT-C16. 93
Table 4-2. OTFT properties of PBDT-TS-C5. 98
Table 4-3. OTFT properties of PBDT-TSBT-C12. 100
Table 4-4. OTFT properties of PBDTF-TSBT-C16. 102
Table 4-5. Photovoltaic parameters of OSCs fabricated using PBDT-TS-C5:Y6, PBDT-TSBT-C12:Y6 and PBDTF-TSBT-C16:Y6 under optimized conditions.[a] 103
Table 4-6. SCLC data of PBDT-TS-C5, PBDT-TSBT-C12 and PBDTF-TSBT-C16. 108
Table 4-7. Summary of the photovoltaic properties of the PBDT-TS-C5:Y6 devices processed with chloroform at different RPMs at room temperature. 126
Table 4-8. Summary of the photovoltaic properties of the PBDT-TS-C5:Y6 devices processed with chloroform at different annealing temperatures with 2500 RPM. 127
Table 4-9. Summary of the photovoltaic properties of the PBDT-TS-C5:Y6 devices processed with chloroform with different solvent additives annealed at 150°C with 2500 RPM. 127
Table 4-10. Summary of the photovoltaic properties of the PBDT-TS-C5:Y6 devices processed with chloroform with different weight ratio of donor and acceptor annealed at 150°C with 2500 RPM. 127
Table 4-11. Summary of the photovoltaic properties of the PBDT-TSBT-C12:Y6 devices processed with chloroform at different RPMs at room temperature. 128
Table 4-12. Summary of the photovoltaic properties of the PBDT-TSBT-C12:Y6 devices processed with chloroform at different annealing temperatures with 1500 RPM. 128
Table 4-13. Summary of the photovoltaic properties of the PBDT-TSBT-C12:Y6 devices processed with chloroform with different solvent additives annealed at 100°C with 1500 RPM. 129
Table 4-14. Summary of the photovoltaic properties of the PBDT-TSBT-C12:Y6 devices processed with chloroform with different weight ratio of donor and acceptor annealed at 100°C with 1500 RPM. 129
Table 4-15. Summary of the photovoltaic properties of the PBDTF-TSBT-C16:Y6 devices processed with chloroform at different RPMs at room temperature. 130
Table 4-16. Summary of the photovoltaic properties of the PBDTF-TSBT-C16:Y6 devices processed with chloroform at different annealing temperatures with 2500 RPM. 130
Table 4-17. Summary of the photovoltaic properties of the PBDTF-TSBT-C16:Y6 devices processed with chloroform with different solvent additives annealed at 150°C with 2500 RPM. 131
Table 4-18. Summary of the photovoltaic properties of the PBDTF-TSBT-C16:Y6 devices processed with chloroform and 0.5%CN with different weight ratio of donor and acceptor annealed at 150°C with 2500 RPM. 131

List of Schemes

Scheme 2-1. Synthesis of PBDT-TA and PBDT-TC: i) malonic acid/piperidine/pyridine, reflux/18 h; ii) a) oxalyl chloride/DMF/$CHCl_3$, 0 °C-r.t./4 h; b) MeOH, 0 °C-r.t./24 h; iii) $Pd_2(dba)_3$/P(o-tolyl)$_3$/chlorobenzene, 90 °C/24 h. 19

Scheme 3-1. Synthesis of PBDT-TDF and PBDT-TDCl: i) 2-chloro-2,2-difluoroacetate/PPh_3/DMF, 110 °C/2 h, 70% yield; ii) hydrazine/NH_4OH/Cu_2Cl_2/CCl_4/DMSO, r.t./7 h, 61% yield; iii) $Pd_2(dba)_3$/P(o-tolyl)$_3$/chlorobenzene, 90 °C/24 h, 99% (PBDT-TDF) and 99% (PBDT-TDCl) yields..... 54

Scheme 4-1. Synthesis of PBDT-TS-C5, PBDT-TSBT-C12 and PBDTF-TSBT-C16: i) alkylamine/acetic acid, reflux/8 h; ii) 2,5-dibromothiophene-3-carboxaldehyde/PPh_3/DCM, r.t./24 h; iii) 2-(tributylstannyl)thiophene/$Pd(PPh_3)_4$/DMF, 100 ˚C/24 h; iv) NBS/DMF, r.t./24 h; v) $Pd_2(dba)_3$/P(o-tolyl)$_3$/chlorobenzene, 90 ˚C/24 h. 92

List of Symbols

e: elementary charge, 1.60218×10^{-19} C

h: Planck's constant, 6.6207×10^{-34} m^2 kg s^{-1}

ε: dielectric constant

E_g: optical bandgap

V_{oc}: open-circuit voltage

J_{sc}: short-circuit current density

E_{HOMO}: energy of the highest occupied molecular orbital

E_{LUMO}: energy of the lowest unoccupied molecular orbital

λ_{max}: maximum absorption wavelength

M_n: number average molecular weight

M_w: mass average molecular weight

$Đ$: dispersity

V_{DS}: drain-source voltage

V_G: gate voltage

V_{th}: threshold voltage

I_{DS}: drain-source current

I_{on}/I_{off}: current ON/OFF ratio

μ_h: hole mobility

μ_e: electron mobility

R_s: series resistance

R_{sh}: shunt resistance

List of Abbreviations

AFM: atomic force microscopy

BGBC: bottom gate bottom contact

BHJ: bulk heterojunction

CV: cyclic voltammetry

DFT: density functional theory

DSC: differential scanning calorimetry

EQE: external quenching efficiency

ETL: electron transport layer

FF: fill factor

FMO: frontier molecular orbital

GPC: gel permeation chromatography

HOMO: highest occupied molecular orbital

HTL: hole transport layer

LUMO: lowest unoccupied molecular orbital

NFA: non-fullerene acceptor

NMR: nuclear magnetic resonance

OFET: organic field effect transistor

OPV: organic photovoltaic

OTFT: organic thin film transistor

OSC: organic solar cell

PCE: power conversion efficiency

PL: photoluminescence

RMS: root-mean square

SCLC: space-charge-limited current

SMA: small molecular acceptor

TGA: thermogravimetric analysis

UV-vis-NIR: ultraviolet-visible-near-infrared

WBG: wide bandgap

XRD: X-ray diffraction

Chapter 1
Introduction

This chapter is based on the following publications:

K. He, P. Kumar, Y. Yuan, Y. Li, *Mater. Adv.*, **2021**, 2, 115.

Y. Yuan, S. Cui, X. Li, H. Liu, J. Wang, Y. Li, *Macromolecules*, **2024**, 57, 10, 4757–4768.

1.1 Overview of Organic Solar Cell

With the increasing demand for sustainable energy, solar photovoltaic technology has attracted significant attention in the past three decades. Silicon-based solar cells have been well developed and become dominant in the solar cell market, achieving power conversion efficiency (PCE) of up to 26.1% (see **Figure 1-1**).[1] However, their drawbacks also emerged including cost, pollution concerns, and rigidity, which limit the further development of silicon-based solar cells. Organic solar cells (OSCs), which act as the potential alternative candidate for silicon solar cells, are emerging as a promising solar technology to convert solar energy to electricity for the future owing to their low-cost, lightweight, flexibility, and feasibility for large-area manufacturing.[2–13] In 1995, Heeger and his coworkers reported the first bulk heterojunction (BHJ) OSC with a blend active layer of a p-type conjugated polymer donor and an n-type fullerene-based small molecule acceptor (SMA).[14] Over the decades, significant improvements have been achieved in the study of BHJ organic solar cells. The PCE of organic solar cells has reached over 19%, primarily due to the tremendous efforts made in the development of donor and acceptor materials.[15–20]

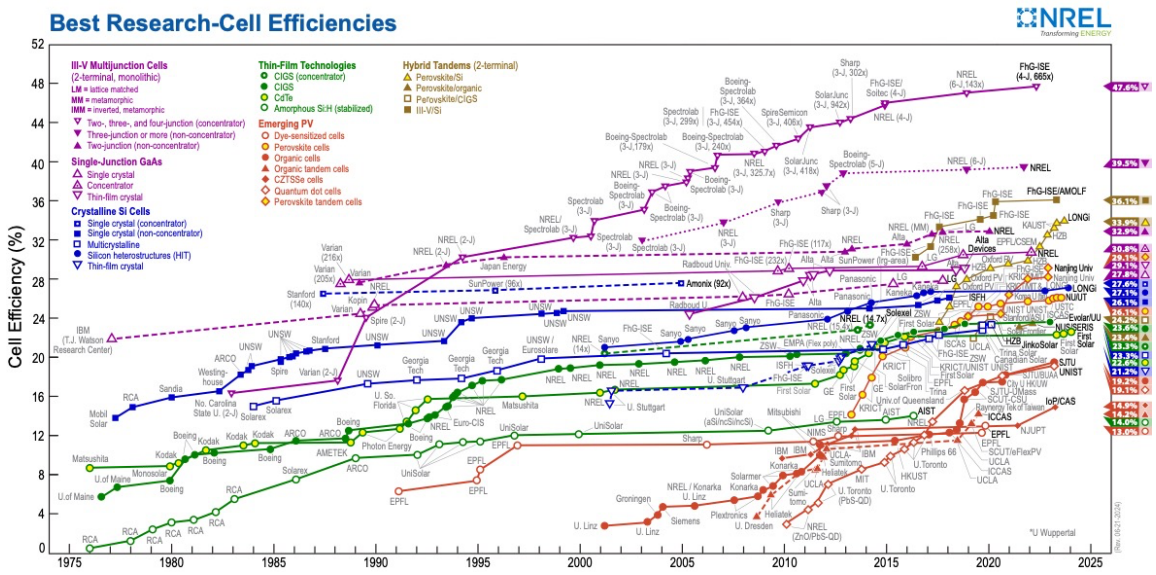


Figure 1-1. The best research-cell efficiencies over time (1975-2024).[21]

The acceptor materials used in the early-stage BHJ OSCs were primarily fullerene-based acceptors (FAs), which contain fullerene derivatives such as phenyl-C_{61} (or C_{71})-butyric acid methyl ester ($PC_{61}BM$ or $PC_{71}BM$) developed by Wudl's group (see **Figure 1-2**).[22] Due to their good solubility in common organic solvents and high electron mobility, FAs became the primary focus, leading to the development of various polymer donors to match these acceptors. Among these polymer donors, Zhao et al. developed a polymer donor named PffBT4T-C9C13 (**Figure 1-2**), achieving a remarkable PCE of 11.7% for BHJ fullerene-based OSCs.[23] However, FAs have some limitations, such as weak absorption in the visible spectral region, and limited energy level tunability, resulting in the photovoltaic performance remaining ~12% for fullerene-based OSCs.[24]

To overcome these limitations, numerous narrow bandgap non-fullerene acceptors (NFAs) have been developed. Compared to fullerene acceptors, NFAs exhibit strong light absorption in the visible spectral region, tunable energy levels, and superior morphological stability. In 2015, Lin et al. developed ITIC, which has become a widely used NFA in solar cell devices.[24–27] ITIC features a rigid indacenodithienothiophene (IDTT) central unit and a narrow bandgap of 1.59 eV. Since the light absorption of ITIC is red-shifted compared to that of the fullerene-based acceptors, a wide bandgap polymer donor (E_g = 1.8-2.0 eV) is required to match ITIC to obtain complementary absorption. In 2019, Li et al. developed the polymer donor PBTA-PSF, which exhibited a bandgap of 1.98 eV, matching well with ITIC to form complementary absorption. The OSC device based on the blend of

PBTA-PSF:ITIC achieved a PCE of 13.91%, which is the highest PCE among ITIC-based OSCs.[28] The introduction of electron-donating and electron-withdrawing groups to ITIC can tune the energy levels, leading to the development of ITIC derivatives such as IT-M, IT-DM, and IT-4F, which further improve the PCE of OSCs.[29–39] In 2019, Yuan et al. developed a new NFA named Y6, which has a dithienthiophen[3.2-b]-pyrrolobenzothiadiazole core with an even narrower bandgap of 1.33 eV compared to ITIC.[40] Due to the better absorption in the long wavelength region, the Y6-based OSC devices have achieved higher PCEs when matching with appropriate polymer donors.[16,25,41–45] Since then, remarkable progress has been made in achieving high PCE, and several systems achieved PCEs over 19%.[15–20] Owing to the rapid development of acceptor materials, the photovoltaic performance of solar cells has been significantly improved, and NFA materials like ITIC, IT-4F, and Y6 are widely used as acceptors for OSC devices currently (see **Figure 1-2**). To further improve the performance of the organic solar cell, it is essential to rationally design the conjugated polymer donors to match with these narrow bandgap NFAs.

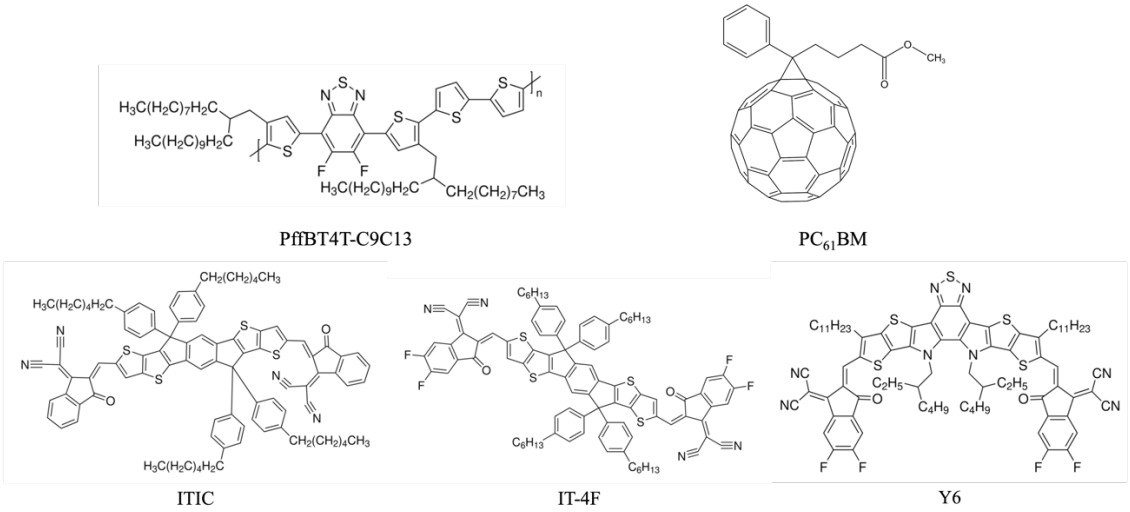


Figure 1-2. The chemical structures of PffBT4T-C9C13, $PC_{61}BM$, ITIC, IT-4F and Y6.

The state-of-the-art OSC device features a BHJ structured active layer which contains a bi-continuous nanophase separation. The desired BHJ structure is typically obtained through the self-assembly of a polymer electron donor and a small molecule electron acceptor blend during the processing stage, followed by optional post-deposition treatments like thermal annealing. To achieve a high-performance OSC, it is crucial to consider the following design aspects for an appropriate polymer donor material: (1) optimizing the highest occupied molecular orbital energy level (E_{HOMO}) to achieve

a high open circuit voltage (V_{oc}), (2) ensuring a complementary absorption spectrum when combined with an appropriate acceptor material to enhance the short-circuit current density (J_{sc}), and (3) achieving a high hole mobility ($\mu_h > 10^{-4}$ cm^2 V^{-1} s^{-1}) while maintaining a suitable balance with the electron mobility (μ_e) of the acceptor in order to increase the fill factor (FF).[46–48] Another important factor, the synthesis cost of the polymer donors, should also be considered for the OSCs towards commercialization, since the current high-performance polymer donors have complicated structures and tedious synthesis routes, which challenge the commercial viability of OSCs.[49–53]

Benzodithiophene (BDT) and its derivatives have emerged as pivotal materials in OSCs due to their unique electronic and physicochemical properties. Their rigid and extended π-conjugation structures allow them to maintain backbone coplanarity and facilitate efficient charge transport.[25,54–57] In addition, thiophene is also widely used as a building block owing to its simple and electron-rich structure. The most common high-performance wide bandgap polymer donors, such as PM6 and D18 (see **Figure 1-3**), are composed of a repeat unit that combines a BDT donor unit with a weakly electron-accepting unit, along with thiophene spacers.[40,58] The BDT unit plays a crucial role in providing high carrier mobility and promoting a desirable face-on orientation. Meanwhile, the incorporation of a weakly electron-withdrawing unit effectively reduces the E_{HOMO}, contributing to the attainment of a high V_{oc}. The inclusion of spacer units helps mitigate steric effects between donor and acceptor units, thereby enhancing carrier mobility.[59,60] By rationally designing the chemical structures of polymer donors as well as considering their synthesis complexity, it is possible to achieve the commercialization of organic solar cells in the future.

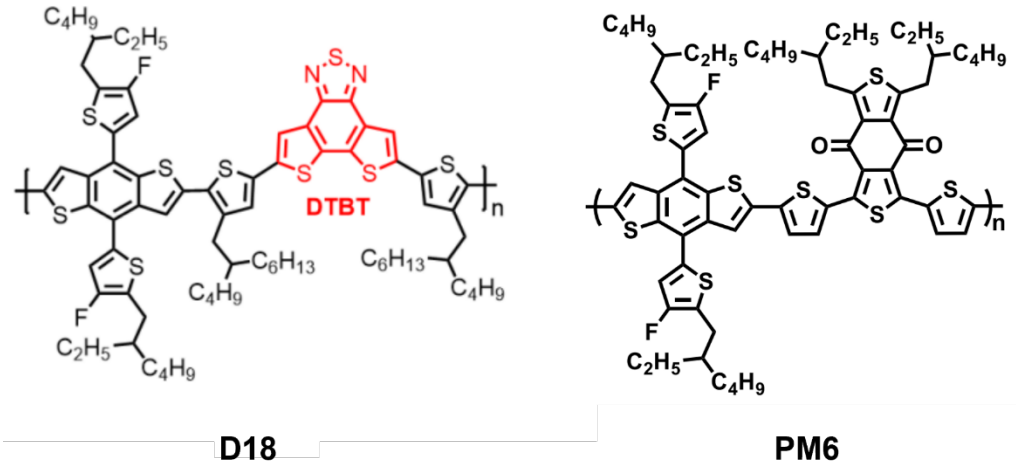


Figure 1-3. The chemical structures of D18 and PM6.

1.2 The Working Mechanism of Bulk Heterojunction Organic Solar Cell

The classic organic solar cell usually consists of a polymer donor and a small molecule acceptor to form a BHJ active layer with nanoscale interpenetrating donor and acceptor phases (see **Figure 1-4**).[14] This active layer is sandwiched by hole/electron transport layers and then an anode or a cathode, respectively. The two electrodes will collect the free electrons and holes generated in the active layer, and a hole transport layer (HTL) such as MoO_3 or PEDOT:PSS is used between the active layer and the anode to facilitate the collection of holes and blocking of electrons, while an electron transport layer (ETL) such as ZnO or LiF is used between the active layer and the cathode to improve the collection of electrons and blocking of holes. In general, at least one of the electrodes should be transparent, so that the sunlight can go through the transparent electrode and be absorbed by the active layer. Indium-doped tin oxide (ITO) is well studied and commonly used as one of the electrodes in the OSC device owing to its superior conductivity and high transmission of light.

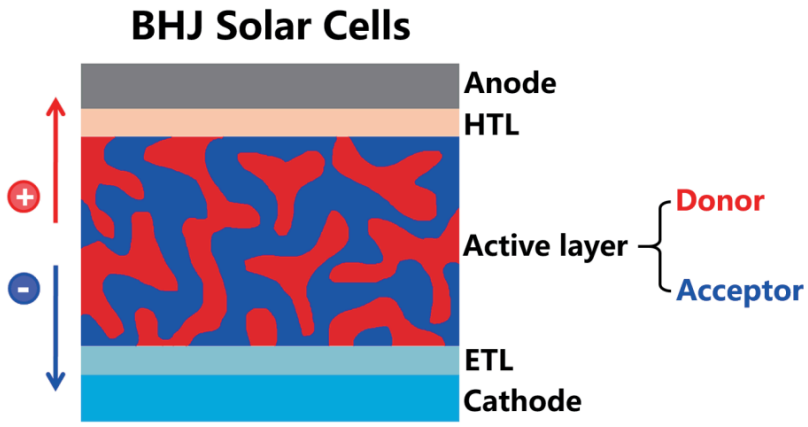


Figure 1-4. The structure of bulk heterojunction organic solar cell. Reprinted with permission from ref. 61, Copyright 2020, Springer Nature.[61]

The BHJ active layer is the most important part in the OSC devices because it dominates the overall photovoltaic performance of the system. The donor material in the active layer acts as a p-type semiconductor which has a relatively high-lying highest occupied molecular orbital energy level (E_{HOMO}) and lowest unoccupied molecular orbital energy level (E_{LUMO}), while the acceptor material acts as an n-type semiconductor which has a relatively low-lying E_{HOMO} and E_{LUMO} that match with those of donor materials. Usually, the HOMO energy offset (ΔE_{HOMO}) should be greater than 0.3 eV for efficient exciton dissociation.[62,63] The photogenerated free holes and electrons can be stabilized and transported by the donor and acceptor, respectively. The photovoltaic process in an OSC device can be described as four steps: (1) Exciton (hole-electron pair) generation due to the absorption of photon; (2) The diffusion of photogenerated exciton to the donor-acceptor interface; (3) The dissociation of exciton at the interface and the generation of free charge carriers; (4) The transport and collection of free charge carriers (**Figure 1-5**).[56,64,65]

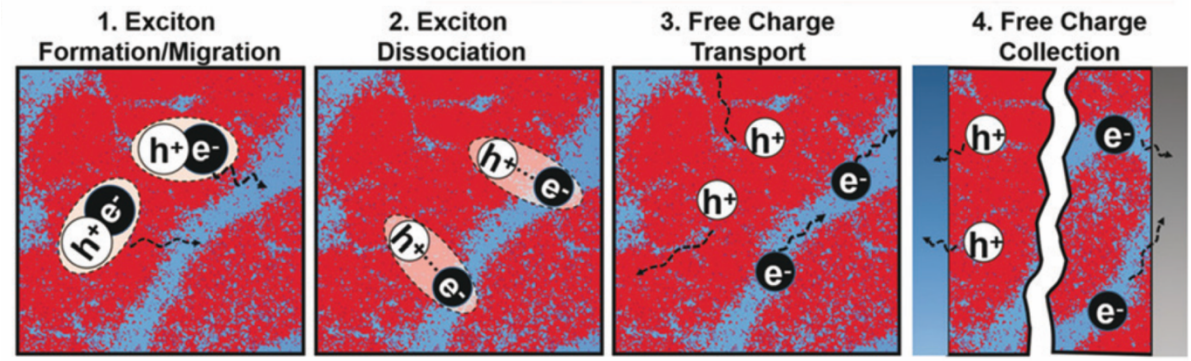


Figure 1-5. Photovoltaic processes in a bulk heterojunction organic solar cell. Reprinted with permission from ref. 66, Copyright 2019, John Wiley and Sons.[66]

To evaluate the photovoltaic performance of an OSC device, the current density-voltage (*J*-*V*) curve is introduced where power conversion efficiency (PCE) can be used as the ultimate photovoltaic performance parameter (refer to **Figure 1-6**). PCE is the percentage of generated electric energy by an OSC over the total incident energy onto the device under the standardized AM 1.5G solar spectrum with an intensity of 100 mW/cm^2, which is determined by the following three factors: open-circuit voltage (V_{oc}, V), short-circuit current density (J_{sc}, mA/cm^2) and fill factor (FF). V_{oc} is the voltage when the external circuit is open under the light, which is the maximum output voltage of a solar cell. J_{sc} is the current density when the external circuit is short-circuited under the light, which is the maximum output current of a solar cell. FF is defined as the ratio of the maximum power of a solar cell to the product of V_{oc} and J_{sc}. PCE can be expressed as **Eq. 1.1**:

$$PCE = \frac{J_{sc} \times V_{oc} \times FF}{P_{in}} \quad \text{(Eq. 1.1)}$$

where P_{in} is the input power density of the light source under the standardized AM 1.5G solar spectrum.

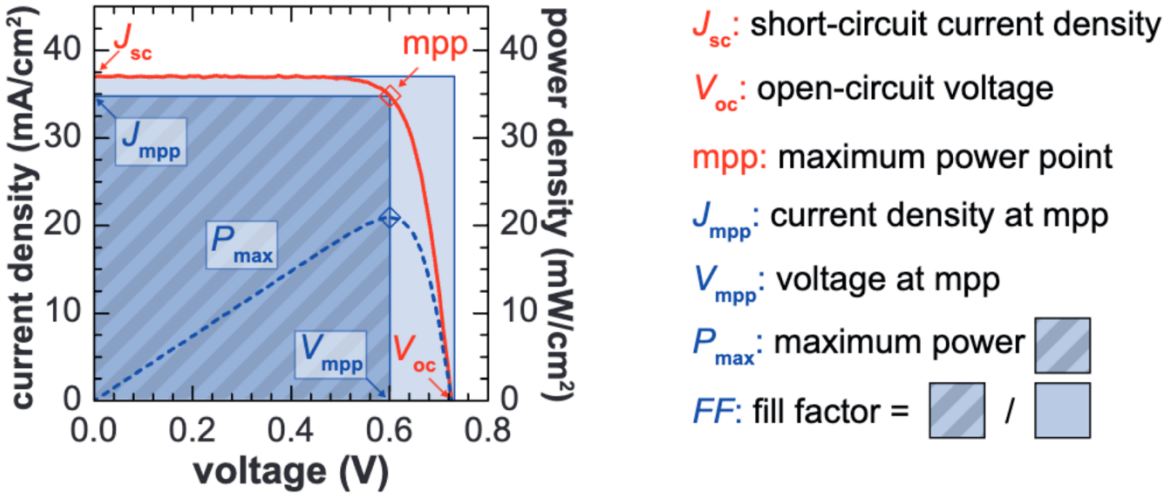


Figure 1-6. The *J*-*V* curve of a solar cell with all the relevant parameters.[67]

In order to obtain high photovoltaic performance in organic solar cells, it is desirable to achieve high V_{oc}, J_{sc} and FF in the device which contribute to PCE. Specifically, V_{oc} is mainly determined by the difference between E_{HOMO} of the donor and E_{LUMO} of the acceptor. Therefore, when designing the polymer donor, a lower E_{HOMO} of the polymer donor is favorable for achieving high V_{oc}. However, the offset between E_{HOMO} of donor and acceptor should be large enough to dissociate excitons as well. Typically, organic donors necessitate an E_{HOMO} higher than approximately -5.6 eV, while stable electron transport in organic acceptors requires an E_{LUMO} of about -4.0 eV or lower.[68–70] J_{sc} is influenced throughout the whole photovoltaic process, including exciton generation, exciton diffusion, exciton dissociation, charge transport and charge collection. Firstly, J_{sc} is related to the number of generated excitons which depends on the absorption coefficient (α) and the bandgap (E_g) of the polymer donor in order to achieve a complementary absorption spectrum with the acceptor. Then, during exciton diffusion, an appropriate phase size is needed to reduce the probability of exciton recombination. If the phase is too large, generated excitons will recombine because the distance between the region that generated excitons and the interface between donor and acceptor is larger than the exciton diffusion length. Exciton dissociation is influenced by the dielectric constant and the HOMO and LUMO energy offsets, i.e. ΔE_{HOMO} and ΔE_{LUMO}, between the donor and the acceptor. A large dielectric constant can reduce the exciton binding energy and subtract exciton recombination.[71] Charge transport and collection processes are determined by the hole mobility (μ_h) of the donor and its balance with the electron mobility (μ_e) of the acceptor. High and balanced hole mobility can result in efficient charge transport

and collection. FF is mainly influenced by the hole mobility of donor and its balance with the electron mobility of the acceptor. High and balanced hole and electron mobilities of donor and acceptor are favorable for achieving high FF, where $\mu_h > 10^{-4}$ cm^2 V^{-1} s^{-1} is required for high-performance polymer donors.[46,47] In order to obtain high hole mobility of the donor, several factors should be considered including building block, side chain, molecular weight and defects which result in the crystallinity and morphology of the nano-/microstructure. A face-on lamellar packing of polymer donor in an OSC device is favorable because the charge transport is promoted through the vertically π-π stacking of polymer donor.

1.3 High-Performance Wide Bandgap Polymer Donors for NFAs

Based on the optical bandgap, polymer donors can be classified as low bandgap (LBG, $E_g < 1.6$ eV), medium bandgap (MBG, 1.6 eV < E_g < 1.8 eV) and wide bandgap (WBG, $E_g > 1.8$ eV) polymers.[72] To form complementary absorption with narrow bandgap NFAs, polymer donors with wide bandgap are desired. In addition, donor-acceptor (D-A) polymers composed of an alternating D and A building blocks on the polymer backbone have been developed (see **Figure 1-7**), and the strategy is commonly used for the WBG polymer donors because the incorporation of different D and A units can easily tune the optical bandgap and frontier molecular orbitals (FMOs) energy levels of the polymer donor, allowing polymer donors being designed with desired absorption range and energy levels that can match well with particular NFA.

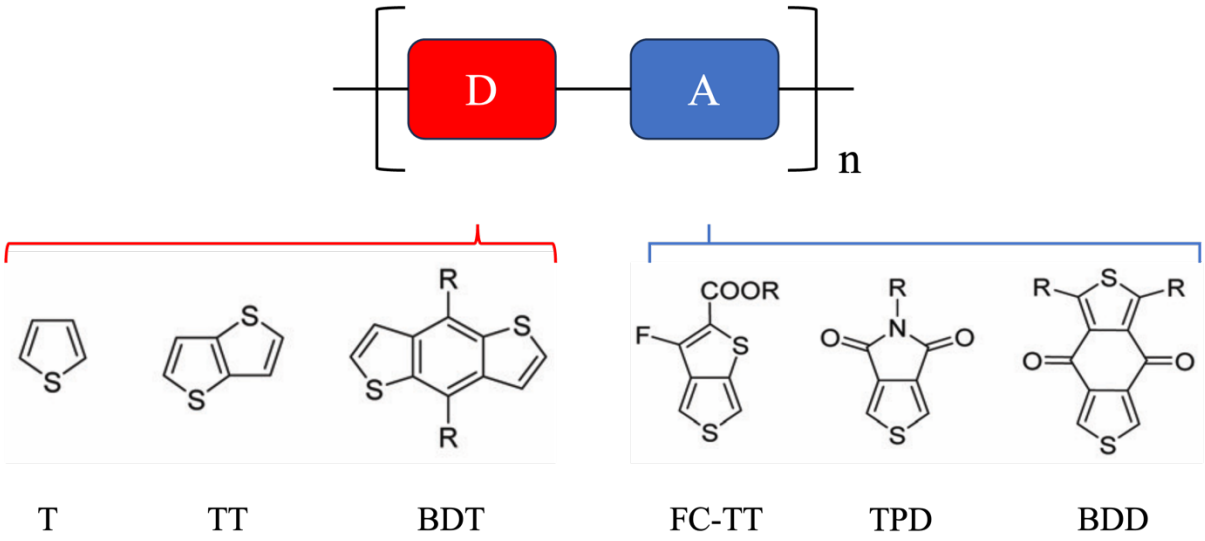


Figure 1-7. The structure of D-A polymer donors and the representative D and A building blocks.

The D building blocks commonly used in the D-A polymer design have a thiophene based structure such as thiophene (T), 2,2'-bithiophene (BT), thieno[3,2-b]thiophene (TT) and benzo[1,2-b:4,5-b']dithiophene (BDT), due to their appropriate electron donating abilities and low steric effect. While the A building blocks usually used in D-A polymer design contain thiophene, benzene or fused ring with electron withdrawing groups such as ester, imide, diketone etc. The representative A units are 3-fluorothieno[3,4-b]thiophene-2-carboxylate (FC-TT),[73] thieno[3,4-c]pyrrole-4,6-dione (TPD)[74] and benzo[1,2-c:4,5-c']dithiophene-4,8-dione (BDD),[75] which are all thiophene containing building blocks. Different incorporation of D and A building blocks can result in a significant difference in the device performance, so the appropriate design and selection of D and A building blocks are important for the study of organic solar cells. Although many superior D-A polymers are developed as the donors in BHJ OSC devices and excellent OPV performances are achieved, the cost-efficiency of the materials should also be considered in order to commercialize them in the future.

1.4 Techniques for Characterization of Key Properties of Polymers and OSC Device

Characterization of the structure and properties of polymer donor materials are essential for the study of organic solar cells. The commonly used methods for characterization of their key properties are described below.

Nuclear magnetic resonance (NMR). NMR spectroscopy is the most widely used technique to characterize the purity of the products and confirm the chemical structures. For organic compounds, proton and carbon NMR (^{1}H NMR and ^{13}C NMR) are usually used and chemical shifts are reported for each synthesized product relative to an internal tetramethylsilane standard (TMS, 0 ppm).

UV-vis-NIR spectroscopy. UV-vis-NIR spectroscopy is commonly used to determine the optical properties of polymers. By determining the absorption spectra of polymers, the optical bandgap (E_g) of donor and acceptor materials can be accessed by using the absorption onset wavelength. The E_g can be calculated by using the equation (**Eq. 1.2**) below:

$$E_g = hv = h\frac{c}{\lambda_{onset}} = \frac{1240}{\lambda_{onset}} \quad \text{(Eq. 1.2)}$$

where h is the Planck constant, v is the photon frequency, c is the speed of light in vacuum, λ_{onset} is the onset wavelength of the photon.

Cyclic voltammetry (CV). CV is a technique to determine the electrochemical properties of donor and acceptor materials. The FMO energy levels (i.e. E_{HOMO} and E_{LUMO}) can be estimated by using the onset oxidation and reduction potentials of CV curves with a reference electrode that has a known energy level. However, most donor and acceptor materials only show their oxidation or reduction during CV measurement due to their strong electron rich or electron deficient properties, respectively. In these cases, the optical bandgap obtained from a UV spectrum is considered as the difference between E_{HOMO} and E_{LUMO} of the material. It was used together with E_{HOMO} of donor or E_{LUMO} of acceptor to calculate E_{LUMO} of donor or E_{HOMO} of acceptor, respectively. Although the energy levels determined by CV measurement usually vary under different experimental conditions, the E_{HOMO} and E_{LUMO} of donor and acceptor materials obtained under similar conditions are still very useful for calculating the energy offsets.[76,77] Alternatively, ultraviolet photoelectron spectroscopy (UPS) and inverse photoemission spectroscopy (IPES) are more accurate for measuring E_{HOMO} and E_{LUMO} of materials. However, they are more expensive and complicated for operation compared with the CV measurement.

Photoluminescence quenching measurement. Photoluminescence (PL) quenching is a very useful method to evaluate the efficiency of exciton diffusion and dissociation. The quenching efficiency at the donor phase and the acceptor can be calculated from the PL quenching curve, and it is desired to obtain

over 90% of quenching efficiency at both phases to achieve high photovoltaic performance in the OSC device.

Differential scanning calorimetry (DSC) measurement and thermogravimetric analysis (TGA). DSC and TGA are the methods to evaluate thermal properties of polymer materials. DSC can be used to study the thermal phase transition of polymer materials and TGA is used to investigate the thermal stability of polymers. Good thermal stability of polymer materials is needed because various thermal treatments would be applied to the polymers during the material characterization and device fabrication.

External quenching efficiency (EQE) and exciton binding energy measurement (E_b). EQE is a method to evaluate the conversion efficiency of incident light to electricity of the OSC device at different wavelengths. A high EQE spectrum is desired for a BHJ system because it would contribute to high J_{sc} of the devices. Additionally, EQE is also used to investigate the E_b of different materials. The exciton binding energy can be evaluated by using **Eq. 1.3**,

$$E_b = E_g^t - E_g^{opt} \quad \text{(Eq. 1.3)}$$

where E_g^t is transport gap and E_g^{opt} is optical bandgap, determined by the secondary onset energy and primary onset energy, respectively.[63,78]

A low exciton binding energy can help exciton diffusion and dissociation to prevent charge recombination, allowing small HOMO and LUMO energy offsets between donor and acceptor materials.

Space charge-limited current (SCLC) mobility measurement. SCLC mobility was estimated by fitting dark *J-V* curves of single carrier (hole/electron) devices using the Mott-Gurney equation (**Eq. 1.4**),

$$J_{sclc} = \frac{9}{8}\mu\varepsilon\frac{V_{appl}^2}{d^3} \quad \text{(Eq. 1.4)}$$

where $\varepsilon = \varepsilon_0\varepsilon_r$, ε_0 is the permittivity of free space, ε_r is the relative permittivity of the material, μ is the hole mobility, $V_{appl} = V - V_{bi}$ is the applied voltage corrected for built in potential V_{bi}, and d is the thickness of the film.

The SCLC mobility plays an important role in photovoltaic solar cell performance of devices as this mobility along the vertical direction can influence FF dramatically. High and balanced SCLC hole (μ_h) and electron (μ_e) mobilities are required for achieving high-performance solar cells.[79,80]

Atomic force microscopy (AFM) and X-ray diffraction (XRD) measurements. As for the film morphology and microstructure, AFM is carried out to obtain the morphological features of the samples, such as root-mean roughness (RMS) and donor-acceptor phase separation, which can influence photovoltaic process significantly. XRD is commonly used to study the crystal structure of the material, and 2D grazing incidence wide angle X-ray scattering (GIWAXS) is employed to get the information about the molecular packing and orientation of mixed BHJ film in the in-plane (IP) and out-of-plane (OPP) directions. An OSC device with face-on orientation of the blended active layer is preferred as the SCLC mobility can be notably improved which is beneficial for the FF.

1.5 Objective and the Structure of This Thesis

Despite the rapid development of organic solar cells over the decades, OSCs still lag behind commercialized silicon solar cells and emerging perovskite solar cells regarding efficiency. Hence, the ongoing efforts are focused on designing new conjugated WBG polymers that can balance cost-efficiency towards commercialization. Due to the limited electron withdrawing building blocks for polymer donors in OSC currently, it is still a big challenge to develop new WBG polymer donors that can achieve high photovoltaic performance in OSC devices while maintaining low-cost. Therefore, the objective of this thesis is to develop new WBG polymer donors with three novel substituted thiophenes as electron-accepting building blocks for high-performance NFA-based organic solar cells. Specifically, the goal is to develop polymer donor materials with simple synthesis routes to reduce cost. These donor materials should have desirable bandgaps in the range of 1.8 eV - 2.0 eV to form complementary absorption spectra with popular NFAs such as ITIC and Y6. They should also have compatible energy levels with NFAs, characterized by small HOMO offsets (< 0.3 eV), and high hole mobilities greater than 10^{-4} cm^2 V^{-1} s^{-1}, matching the electron mobilities of popular NFAs. The thesis is organized as follows.

In Chapter 1, the background of the organic solar cells was briefly introduced, highlighting the key properties that guide the development of new polymer donor materials for high-performance NFA-based organic solar cells.

In Chapter 2, the vinyl bridge was introduced on the side chain of thiophene, aiming to enhance the dielectric constant and reduce exciton binding energy. Two polymers, namely PBDT-TA and PBDT-TC (reference polymer) were synthesized. Prior to the synthesis of the new polymer PBDT-TA, density

functional theory simulation (DFT) was carried out to study the influence of inserting a vinyl bridge. After two polymers were synthesized via straightforward routes, they were characterized by several techniques, such as DSC, TGA, UV-vis-NIR and CV, to study the thermal, optical, electrochemical properties. The OSC devices in an inverted structure were fabricated using the PBDT-TA:ITIC and PBDT-TC:ITIC blend film as active layer to investigate their photovoltaic performance. Additional experiments, such as PL quenching, EQE, dielectric constant, SCLC, AFM and XRD measurements, were carried out to further understand material properties, giving directions to optimize the devices.

In Chapter 3, two novel WBG polymer donors, namely PBDT-TDF and PBDT-TDCl, were synthesized with *gem*-dihalovinyl substituted building blocks, namely 3-(2,2-difluorovinyl)thiophene (TDF) and 3-(2,2-dichlorovinyl)thiophene (TDCl), in these polymers which possess a weak electron-withdrawing character. DFT simulation was employed to study the effect of geometry and FMOs using these two building blocks. Then, the polymers were synthesized in simple synthetic routes. UV and CV were used to study the optical and electrochemical properties of the two new polymers. Based on the energy levels and bandgaps obtained, NFA Y6 was chosen to match them for the OSC fabrication. The PBDT-TDF:Y6 and PBDT-TDCl:Y6 based inverted devices were made and their photovoltaic performances were tested. Finally, PL quenching, EQE, SCLC mobility, AFM and XRD were used to study the structure-property relationships of these devices.

In Chapter 4, three succinimide based polymers were synthesized, namely PBDT-TS-C5, PBDT-TSBT-C12 and PBDTF-TSBT-C16. Before the synthesis of polymers, DFT simulation was conducted to study the molecular geometry and FMOs of the three polymers. The polymers were synthesized and tested by UV and CV to get the information about the absorption profiles and FMOs. Y6 was chosen as the acceptor and photovoltaic performance was investigated for three polymers matching with Y6 in the inverted structure. Techniques like EQE, PL quenching, SCLC mobility, AFM and XRD were applied for the three polymers to further understand the material properties, revealing the reasons for their different photovoltaic performance.

In Chapter 5, the work of this thesis is concluded, and future directions are given to further study the topic.

Chapter 2
Synthesis and Characterization of Methyl Thiophene-3-acrylate-based Polymers

This chapter is based on the following publication:

Y. Yuan, P. Kumar, J. Ngai, X. Gao, X. Li, H. Liu, J. Wang, Y. Li, *Macromol. Rapid Commun.* **2022**, 2200325.

2.1 Introduction

The dielectric constant or relative permittivity (ε_r) of the semiconductor in the active layer has an overwhelming impact on the solar cell performance.[71] Due to the non-polar nature, the ε_r of organic semiconductors including polymer semiconductors is typically ~3 – 4, which is much lower than that of inorganic semiconductors such as silicon (ε_r = 11.7)[81] and the organic-inorganic hybrid perovskites (ε_r = ~11-17).[82] A low ε_r leads to a high exciton binding energy (E_b), as shown in: $E_b = e^2/(4\pi\varepsilon_r\varepsilon_0 r)$, where e is the elementary charge, ε_0 is the permittivity of vacuum, and r is the separation distance between electron and hole in the exciton.[83] Consequently, organic semiconductors have much higher E_b values (~0.3 – 1 eV) than those of inorganic and hybrid semiconductors, such as Si (E_b = 10 meV)[84] and perovskites (E_b = 5-16 meV).[82,85,86] The very high E_b of organic semiconductors results in short exciton lifetime. Therefore, formation of a BHJ structure with finely tuned donor/acceptor phase separation with a few nanometers in size is mandatary to prevent exciton recombination. However, it is very challenging to match the donor and acceptor to form a BHJ structure that satisfies both exciton diffusion and charge transport. More importantly, a high E_b requires a higher amount of energy to dissociate excitons into free electrons and holes and causes charge transfer state emission, leading to significantly reduced PCE.[71] Therefore, much effort has been made to develop high dielectric organic semiconductors in order to extend the PCE limit of OSCs.[83,87–90]

Alkyl thiophene-3-carboxylate (TC), which can be easily prepared from thiophene-3-carboxylic acid by esterification, is a weak electron acceptor building block used for some high-performance polymer donors.[91–95] For example, Hou et al. developed a polythiophene consisting of a dimer of 2-butyloctyl-thiophene-3-carboxylate, PDCBT, which achieved a high PCE of 10.16% when paired with ITIC.[92]

Choi's group used methyl thiophene-3-carboxylate (3MT) as the acceptor unit and a benzo[1,2-b:4,5-b']dithiophene) (BDT) as the donor unit to make a simple wide bandgap polymer 3MT-Th (**Figure 2-1**).[94] OSC devices using 3MT-Th as the donor and ITIC as the acceptor achieved a high PCE of 9.73%. A regiorandom polymer (ran-PThE) of ethyl thiophene-3-carboxylate (3ET) and BDT showed a PCE of 8.61% when paired with ITIC, while the regioregular polymer (reg-PThE) achieved a much higher PCE of 10.57%.[95] By using another acceptor FTIC to pair reg-PThE, a PCE of 12.07% was reached. Hou et al. synthesized a polymer PTO2 using the fluorinated BDT as the donor monomer and 3ET as the acceptor monomer.[93] When IT-4F (another name for 4F-ITIC) was used as the acceptor, the PTO2:IT-4F OSC achieved a high PCE of 14.7%.

Previously we found that introduction of an electron accepting side chain with an extended π-conjugation can effectively polarize the polymer, leading to a significant increase in the dielectric constant of the resulting polymer.[87] In this study, we insert a π-conjugated bridge, vinylene, between methyl carboxylate and thiophene, to obtain a new weak electron acceptor building block, methyl thiophene-3-acrylate (TA). The addition of vinyl group allows for better orbital overlap between methyl carboxylate and thiophene in TA unit compared to that of direct single bond between carbonyl and thiophene in TC unit. This more distantly positioned electron-withdrawing carboxylate group from the electron-rich backbone is expected to effectively polarize the polymer and thus increase the dielectric constant, resulting in a lower exciton binding energy. As a proof of concept, a polymer PBDT-TA was synthesized using TA as the acceptor unit and BDT as the donor unit (**Figure 2-1**). In comparison, we also synthesized its methyl thiophene-3-carboxylate (3MT) counterpart polymer 3MT-Th (denoted as PBDT-TC).

PBDT-TA has a wide bandgap of 2.02 eV, which is similar to that (2.00 eV) of PBDT-TC. The highest occupied molecular orbital (HOMO) and lowest unoccupied molecular orbital (LUMO) energy levels, E_{HOMO} and E_{LUMO}, of PBDT-TA are -5.46 and -3.44 eV, respectively, which are slightly higher than those (-5.49 eV / -3.49 eV) of PBDT-TC. In good agreement to the computer simulation results, PBDT-TA showed a higher dielectric constant (ε_r = 3.78) and lower exciton binding energy (E_b = 0.415 eV) than those of PBDT-TC (ε_r = 3.55; E_b = 0.430 eV). The OSC device based on the blend of PBDT-TA:ITIC showed a V_{oc} of 0.96 V, a J_{sc} of 19.43 mA cm^{-2}, an FF of 0.56, and a PCE of 10.47%, which has improved compared to the OSC device based on the blend of PBDT-TC:ITIC (V_{oc} = 0.96 V, J_{sc} = 18.23 mA cm^{-2}, FF = 0.55, and PCE = 9.68%). Higher SCLC hole and electron mobilities of 2.00×10^{-4} cm^2 V^{-1} s^{-1} and 8.68×10^{-5} cm^2 V^{-1} s^{-1}, respectively, were obtained for the blend film of PBDT-TA:ITIC,

which contribute to the enhanced J_{sc} of OSC devices. This work shows that TA is a promising simple electron acceptor building block for constructing polymer donors for high performance OSCs and also demonstrates the effectiveness of using acrylate side chains to increase the dielectric constant, reduce the exciton binding energy, and enhance the solar cell efficiency of polymer semiconductors.

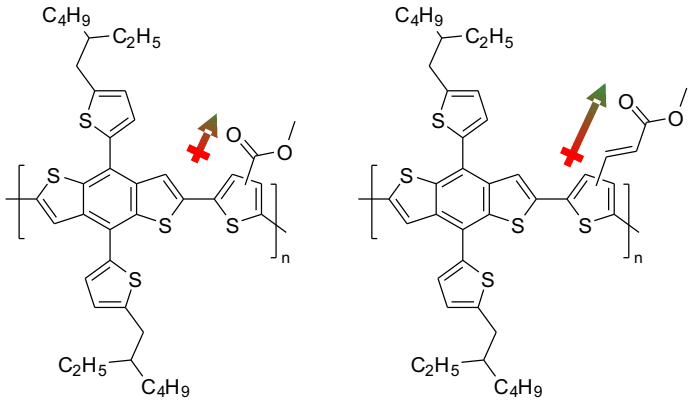


Figure 2-1. The chemical structures of PBDT-TC (or 3MT-Th) and PBDT-TA.

2.2 Theoretical Study of PBDT-TA

Prior to polymer synthesis, density functional theory (DFT) simulations were performed on a dimer unit of PBDT-TA, di-BDT-TA at the B3LYP/6-31G (d,p) level, to gain insight into the geometry and frontier molecular orbitals (FMOs) and the polarity (dipole moment) of PBDT-TA. Methyl groups were used to replace 2-ethylhexyl side chains on BDT units to save computing time. For comparison, a dimer of PBDT-TC, di-BDT-TC, was also simulated.

As shown in **Figure 2-2**, the dihedral angle between the first BDT and the first TA from the left in di-BDT-TA is 33.9°, which is much greater than that of the dihedral angle (11.9°) between the first TA and the second BDT, indicating that the methyl acrylate side chain has a large steric interaction with the adjacent first BDT. For di-BDT-TC, the respective dihedral angles are smaller at 24.8° and 8.5°, respectively. The results indicate that the TA unit with an additional C=C double bond increases the steric effect on the adjacent BDT unit, which may lead to a more twisted polymer backbone of PBDT-TA than PBDT-TC. The calculated E_{HOMO}/E_{LUMO} are -5.05/-2.29 eV for BDT-TA and -4.99/-2.22 eV for BDT-TC, which indicates that the TA unit has a slightly stronger electron-withdrawing effect than

the TC unit. In **Figure 2-2c** and **2-2g**, more electron density resides on the LUMO of di-BDT-TA than di-BDT-TC, which indicates a better orbital overlap in di-BDT-TA.

DFT simulations also provided crucial information about polymer polarity. As shown in **Figure 2-2b** and **2-2f**, the dipole moment (μ) of di-BDT-TA is 4.82 D, which has notably increased compared to di-BDT-TC that has a dipole moment of 4.31 D. As expected, the introduction of the vinylene bridge between the electron-withdrawing carboxylate group and the electron-donating thiophene in TA can increase the polarity of the polymer, which is beneficial for lowering the exciton binding energy.

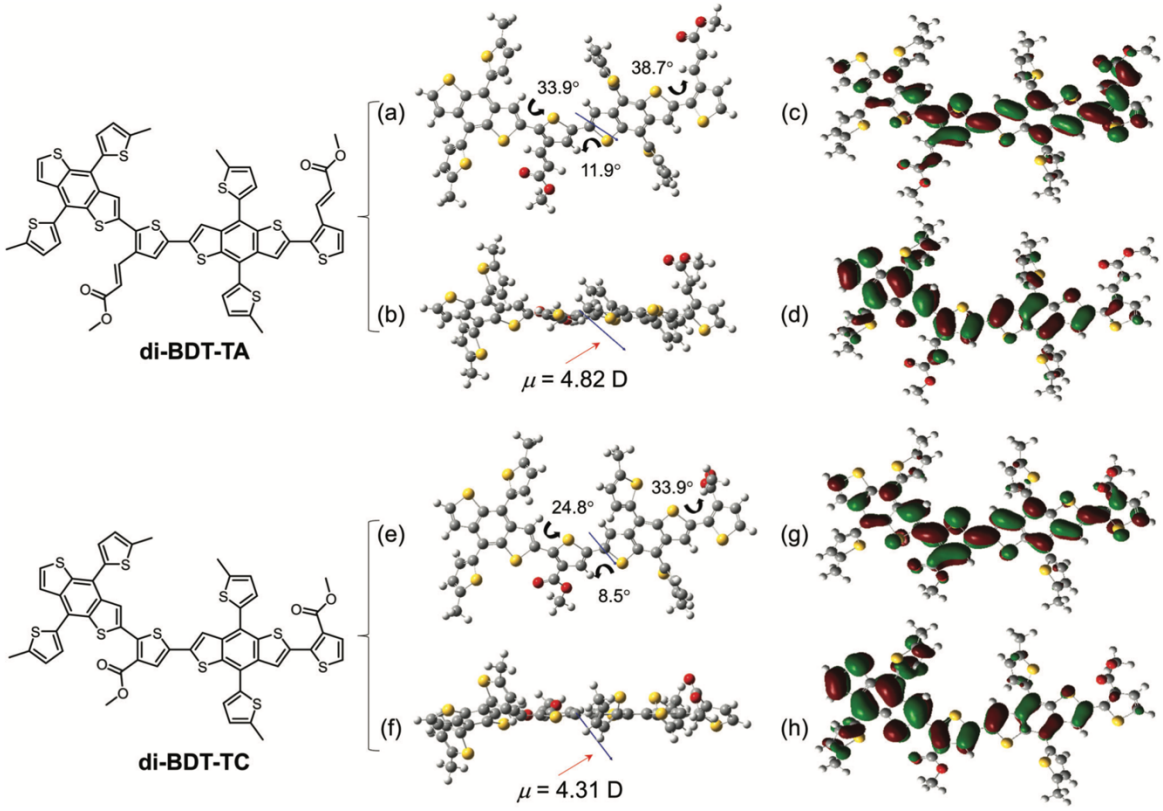
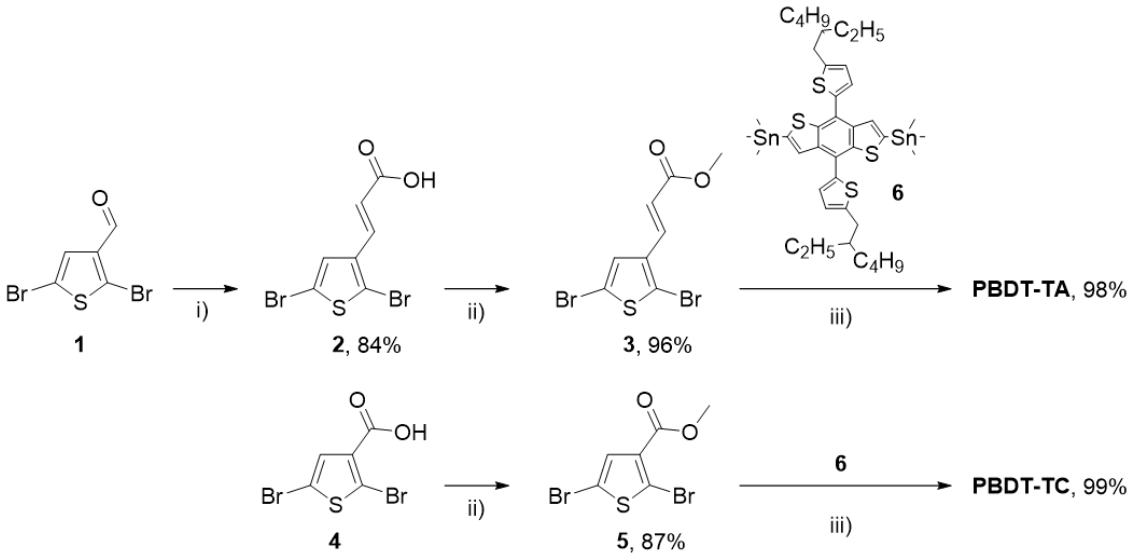


Figure 2-2. DFT simulation results of model compounds di-BDT-TA (a dimer of PBDT-TA) and di-BDT-TC (a dimer of PBDT-TC): Molecular geometries (a, b, e, f), LUMOs (c, g), and HOMOs (d, h). Dipole moment (μ) values of the two compounds are shown in (b) and (f).

2.3 Synthesis of PBDT-TA

PBDT-TA was synthesized following the route illustrated in **Scheme 2-1**. (E)-3-(2,5-Dibromothiophen-3-yl) acrylic acid (**2**) was conveniently synthesized in a good yield of 84% by refluxing 2,5-dibromothiophene-3-carbaldehyde (**1**) in pyridine in the presence of a small amount of piperidine as a catalyst. Esterification of **2** was carried out by reaction with oxalyl chloride and then methanol in one-pot to afford the monomer methyl (E)-3-(2,5-dibromothiophen-3-yl) acrylate (**3**) in 96% yield. Finally, polymerization between **3** and 2,6-bis(trimethytin)-4,8-bis(5-(2-ethylhexyl)thiophen-2-yl)benzo[1,2-b:4,5-b']dithiophene (**6**) under conventional Stille coupling conditions gave PBDT-TA in 98% after purification. The number average molecular weight (M_n = 27.4 kg mol^{-1}), weight average molecular weight (M_w = 47.6 kg mol^{-1}), and dispersity ($Đ$ = 1.74) of PBDT-TA were determined by high-temperature gel-permeation chromatography (HT-GPC) using 1,2,4-trichlorobenzene as the eluent at 110 °C. The reference polymer PBDT-TC was similarly synthesized, which has an M_n of 66.1 kg mol^{-1}, an M_w of 172.1 kg mol^{-1} and a $Đ$ of 2.60.



Scheme 2-1. Synthesis of PBDT-TA and PBDT-TC: i) malonic acid/piperidine/pyridine, reflux/18 h; ii) a) oxalyl chloride/DMF/$CHCl_3$, 0 °C-r.t./4 h; b) MeOH, 0 °C-r.t./24 h; iii) $Pd_2(dba)_3$/P(o-tolyl)$_3$/chlorobenzene, 90 °C/24 h.

2.4 Characterization of PBDT-TA

2.4.1 Thermal properties

Differential scanning calorimetry (DSC) measurements and thermogravimetric analysis (TGA) were conducted to characterize the thermal properties of PBDT-TA and PBDT-TC. DSC thermograms of the two polymers show no apparent thermal transition (**Figure 2-3**), indicating their rather disordered nature, which was further verified by XRD measurements. As shown in **Figure 2-4**, the 5% weight loss temperatures of PBDT-TA and PBDT-TC are 376 and 419 °C, respectively, indicating both polymers have good thermal stability.

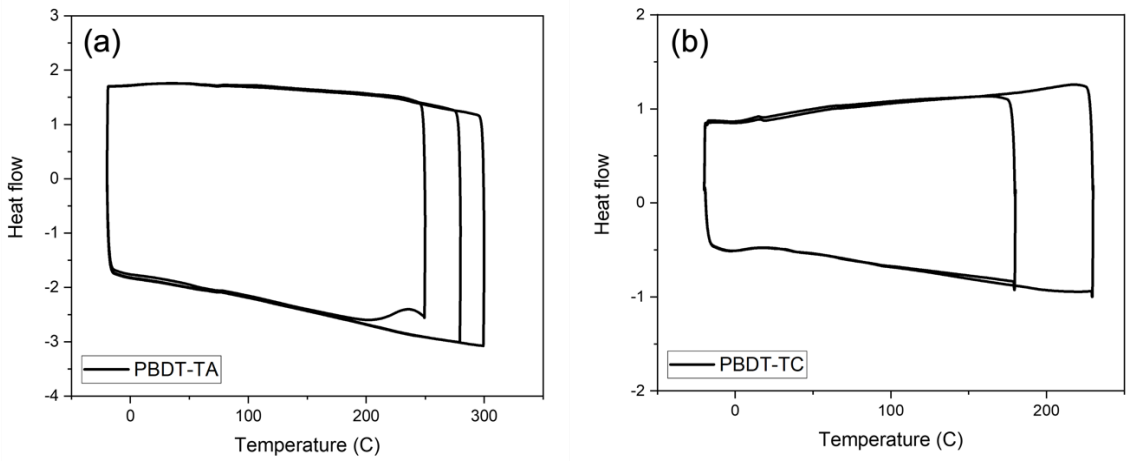


Figure 2-3. DSC curves of (a) PBDT-TA and (b) PBDT-TC.

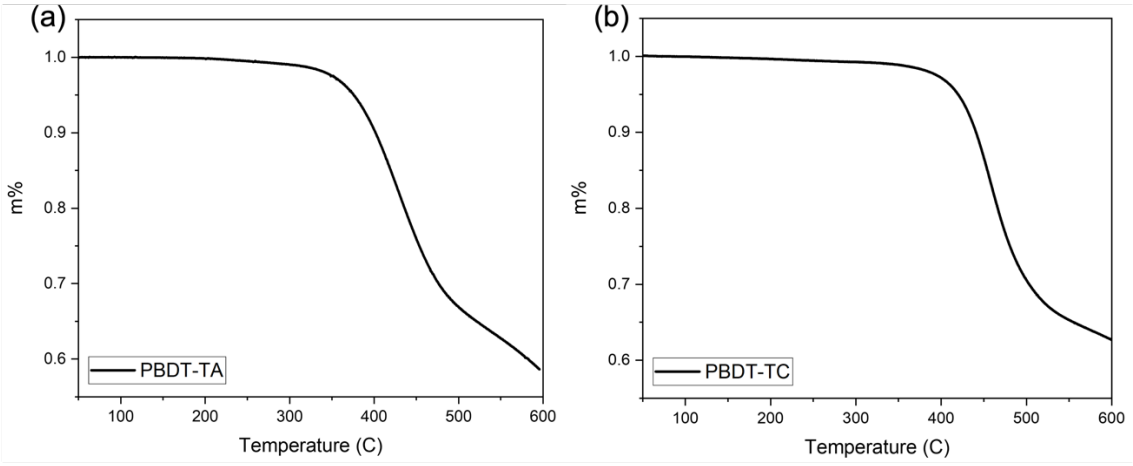


Figure 2-4. TGA curves of (a) PBDT-TA and (b) PBDT-TC.

2.4.2 Optical and electrochemical properties

The optical properties of PBDT-TA and PBDT-TC were characterized by ultraviolet-visible (UV-Vis) spectroscopy. As shown in **Figure 2-5a** and **Table 2-1**, the solution of PBDT-TA in chloroform exhibits a high energy absorption peak at 350 nm and a low energy absorption peak at 517 nm, which result from the thienyl side chains of the BDT units and the π-π* transition of the polymer backbone, respectively.[96–98] A shoulder peak at 540 nm is observed due to some degree of chain aggregation of this polymer in solution.[99,100] As for the PBDT-TC solution, the corresponding high and low energy peaks appeared at 347 nm and 510 nm, respectively. They are slightly blue-shifted compared to those of PBDT-TA. The molar coefficients of PBDT-TA and PBDT-TC are similar at 2.24×10^4 M^{-1} cm^{-1} and 2.34×10^4 M^{-1} cm^{-1}, respectively.

Compared with their solution spectra, their film spectra show a 24 nm red shift in the low-energy peak, reflecting the more extended conjugation of their polymer backbones in the solid state. The optical bandgaps calculated from the onset of the UV absorption for PBDT-TA and PBDT-TC are 2.02 eV and 2.00 eV, respectively. The UV-vis profile and wide bandgap of PBDT-TA are desirable for obtaining a complementary absorption spectrum with a narrow bandgap NFA.

Cyclic voltammetry (CV) was used to determine the FMO energy levels of PBDT-TA and PBDT-TC. As shown in **Figure 2-5b**, the oxidation onset potential of PBDT-TA relative to the ferrocene/ferrocenium (Fc/Fc^+) couple is 0.66 V, which corresponds to a HOMO energy level (E_{HOMO}) of -5.46 eV. No reduction peak was observed, so the LUMO energy level (E_{LUMO}) of PBDT-TA is calculated by adding the optical bandgap to the E_{HOMO} to be -3.44 eV. The E_{HOMO} and E_{LUMO} of the reference polymer PBDT-TC were determined similarly to be -5.49 eV and -3.49 eV, respectively. These results are unexpected since the DFT simulations showed that the FMO energy levels of PBDT-TA are lower than those of PBDT-TC. The discrepancies could be caused by the more twisted vinyl bridge in the acrylate of TA in the solid state, making the acrylate less electron-withdrawing.

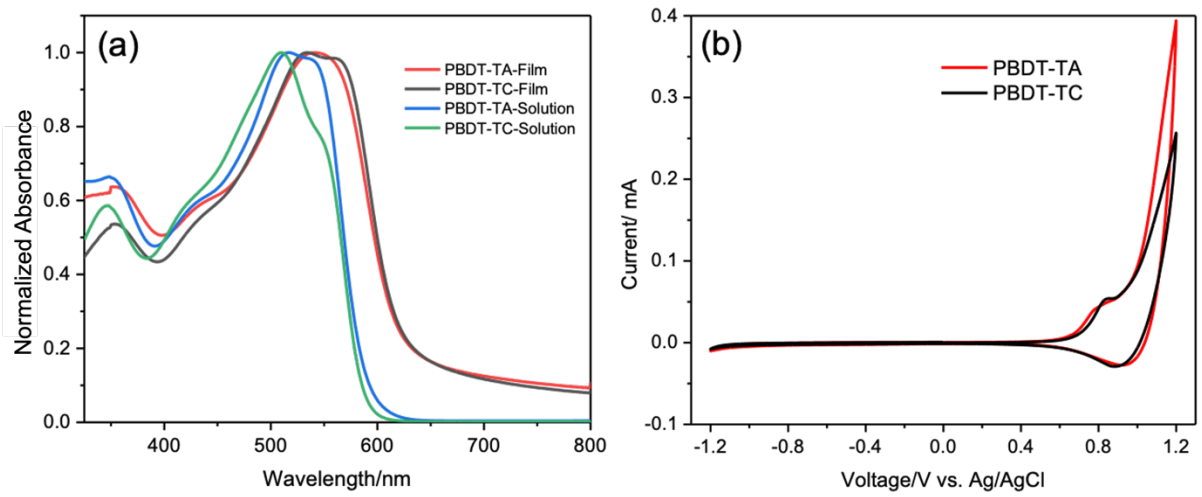


Figure 2-5. (a) UV-Vis spectra of PBDT-TA and PBDT-TC in solution (chloroform) and thin film states and (b) Cyclic voltammograms of PBDT-TA and PBDT-TC films.

Table 2-1. UV-vis and CV data of PBDT-TA and PBDT-TC.

Polymer	λ_{max}	λ_{max}	E_g^{opt}	E_{HOMO}	E_{LUMO}[a]
	nm (sol)	nm (film)	eV	eV	eV
PBDT-TA	517	541	2.02	-5.46	-3.44
PBDT-TC	510	534; 563 (sh)	2.00	-5.49	-3.49

[a] $E_{LUMO} = E_{HOMO} + E_g^{opt}$

2.4.3 Dielectric constant and exciton binding energy

The dielectric constants of the two polymers were measured by using impedance spectroscopy to be 3.78 for PBDT-TA and 3.55 for PBDT-TC (**Figure 2-6**). The higher dielectric constant of PBDT-TA reflects its larger polarity, which agrees well with the DFT simulation results. The increase in the dielectric constant of PBDT-TA is expected to decrease the exciton binding energy (E_b). To confirm this, the exciton binding energies of the two polymers were measured using an established method[63] by measuring EQE as a function of photon excitation energy (wavelength) (**Figure 2-7**). Indeed, the exciton binding energy of PBDT-TA (0.415 eV) is smaller than that of PBDT-TC (0.430 eV). Since

PBDT-TA has a lower binding energy, in principle, it would require smaller ΔE_{HOMO} and ΔE_{LUMO} for exciton dissociation to prevent the charge recombination,[71] which would help reduce energy loss. Furthermore, smaller exciton binding energy can extend the exciton diffusion distance, which can alleviate the stringent nanophase separation requirement of BHJ OSCs and even enable bilayer OSCs.

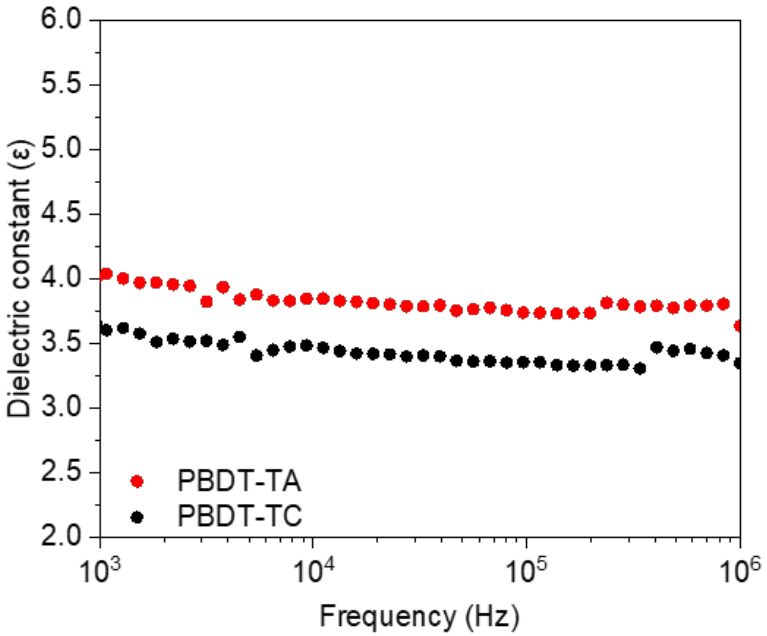


Figure 2-6. Dielectric constant of PBDT-TA and PBDT-TC polymers.

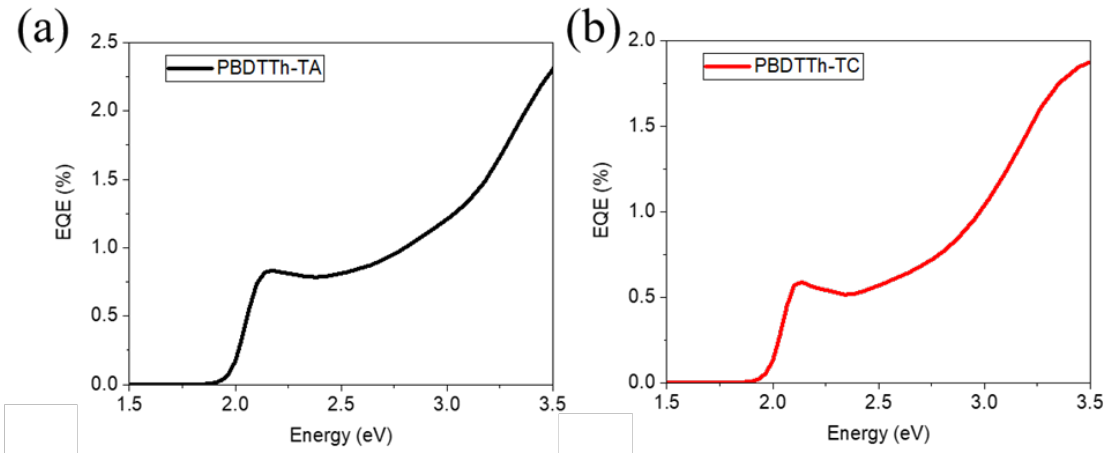


Figure 2-7. EQE spectra of neat polymer films showing primary and secondary onsets, corresponding to the optical band gap and transport gap.

Table 2-2. Dielectric constant and exciton binding energy of PBDT-TA and PBDT-TC.

Polymer	Dielectric constant, ε_r	Exciton binding energy, E_b (eV)
PBDT-TA	3.78 ± 0.06	0.415 ± 0.057
PBDT-TC	3.55 ± 0.21	0.430 ± 0.036

2.4.4 I-V Characterization

PBDT-TA and PBDT-TC were evaluated as a channel semiconductor in bottom gate bottom contact (BGBC) configuration for OTFT devices. A solution of PBDT-TA (PBDT-TC) in chloroform was spin-coated on a dodecyltrichlorosilane (DDTS) modified SiO_2/Si wafer substrate with prepatterned Au source and drain pairs, and then they were annealed at different temperatures for 15 min in the glove box filled with nitrogen. All OTFT devices showed typical p-type dominant field effect transistor performance (**Figure 2-8** and **Figure 2-9**, **Table 2-3** and **Table 2-4**). The best hole mobility of 3.01 × 10^{-3} $cm^2V^{-1}s^{-1}$ was obtained for a PBDT-TA coated device with the annealing temperature of 100 °C, while the best hole mobility of 2.83 × 10^{-3} $cm^2V^{-1}s^{-1}$ was achieved for a PBDT-TC based device annealed at 150 °C.

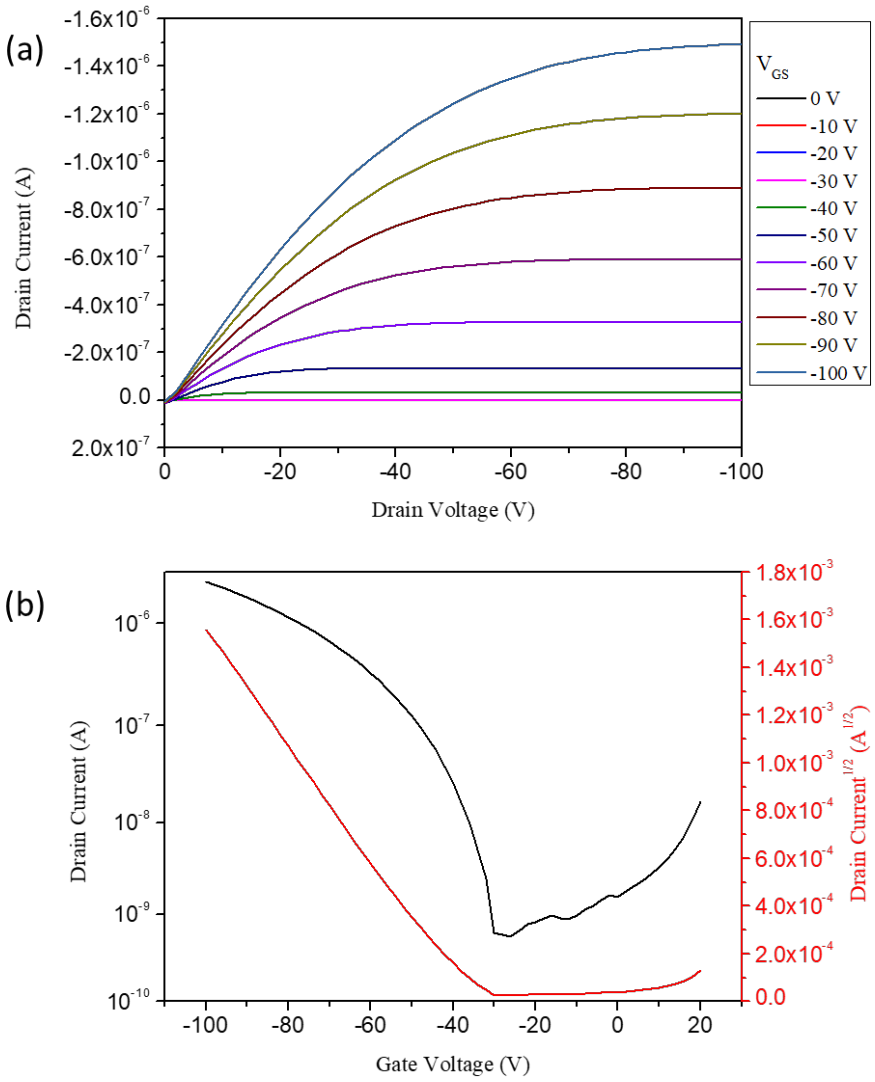


Figure 2-8. (a) Output and (b) transfer (V_{DS} = -100 V) characteristics of a typical OTFT device of PBDT-TA with the annealing temperature of 100 °C.

Table 2-3. OTFT properties of PBDT-TA.

Temperature (°C)	**Best mobility ($cm^2V^{-1}s^{-1}$)**	**Avg mobility ($cm^2V^{-1}s^{-1}$)**	**Avg I_{on}/I_{off}**	**Avg V_{th} (V)**
RT	2.06×10^{-3}	$1.87\times10^{-3}\pm1.42\times10^{-4}$	2800	-25.79±1.43
50	2.71×10^{-3}	$2.22\times10^{-3}\pm2.98\times10^{-4}$	4600	-31.45±4.38
100	3.01×10^{-3}	$2.67\times10^{-3}\pm2.35\times10^{-4}$	8200	-31.29±4.35
150	2.73×10^{-3}	$2.61\times10^{-3}\pm1.07\times10^{-4}$	6400	-24.47±3.10
200	2.49×10^{-3}	$2.32\times10^{-3}\pm1.05\times10^{-4}$	6400	-27.51±3.94

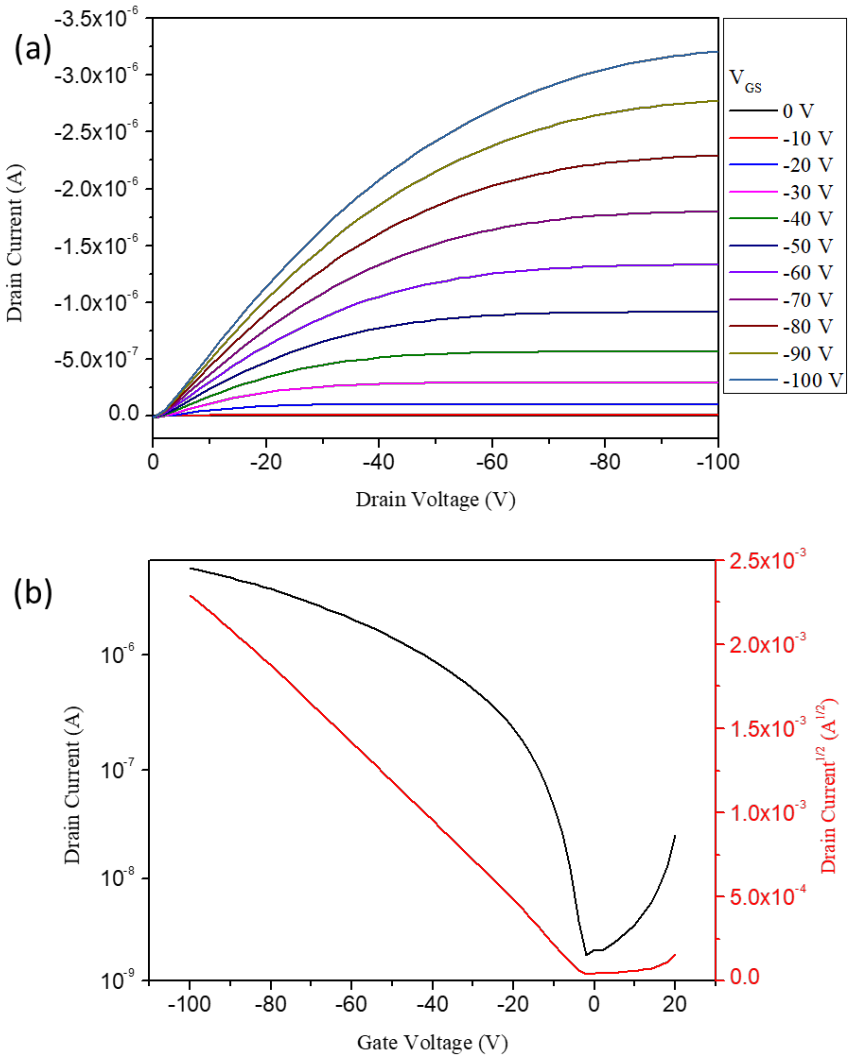


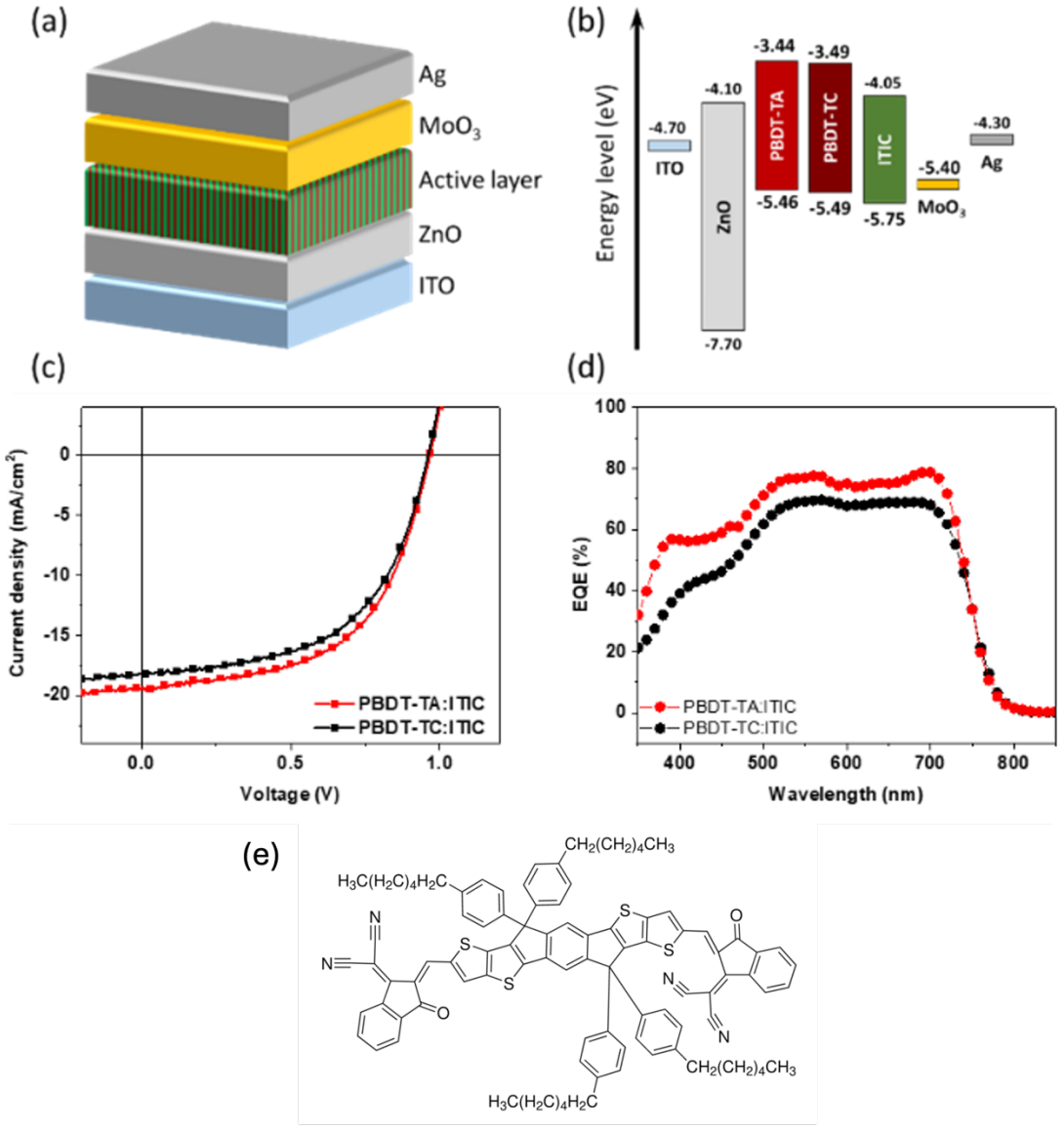
Figure 2-9. (a) Output and (b) transfer (V_{DS} = -100 V) characteristics of a typical OTFT device of PBDT-TC with the annealing temperature of 150 °C.

Table 2-4. OTFT properties of PBDT-TC.

Temperature (°C)	Best mobility ($cm^2V^{-1}s^{-1}$)	Avg mobility ($cm^2V^{-1}s^{-1}$)	Avg I_{on}/I_{off}	Avg V_{th} (V)
RT	2.41×10^{-3}	$2.30\times10^{-3}\pm1.10\times10^{-4}$	2800	1.89±1.24
50	2.34×10^{-3}	$2.27\times10^{-3}\pm0.93\times10^{-4}$	2800	-3.60±4.18
100	2.78×10^{-3}	$2.26\times10^{-3}\pm0.54\times10^{-4}$	2800	-13.38±10.29
150	2.83×10^{-3}	$2.62\times10^{-3}\pm2.32\times10^{-4}$	3250	-1.95±3.08
200	2.64×10^{-3}	$2.44\times10^{-3}\pm0.28\times10^{-4}$	5500	-9.57±3.12

2.4.5 Photovoltaic performance

The photovoltaic properties of PBDT-TA were investigated in devices with an inverted structure: ITO/ZnO (35 nm)/active layer/MoO_3 (10 nm)/Ag (100 nm) (**Figure 2-10a**). The active layer was composed of polymer donor PBDT-TA (or the reference PBDT-TC) and a non-fullerene acceptor ITIC. The energy levels of the materials used in the devices are shown in **Figure 2-10b**. The donor-acceptor blend concentration, spin-coating rate, thermal annealing, and additives were systematically screened, and the obtained photovoltaic parameters are presented in **Table 2-7** to **Table 2-10**. The optimized active-layer thickness of ~120 nm (prepared by spin coating a solution in o-DCB at 600 rpm) and optimum annealing temperature of 130 °C resulted in the highest PCE of 10.47% with an open-circuit voltage (V_{oc}) of 0.96 V, a short-circuit current density (J_{sc}) of 19.43 mA cm^{-2}, and a fill factor (FF) of 0.56. OSC devices using the reference polymer PBDT-TC achieved the highest PCE of 9.68% (V_{oc} = 0.96 V, J_{sc} = 18.23 mA cm^{-2}, and FF = 0.55), which is very close to the value of 9.73% reported by Park et al. for this polymer.[94] The current density-voltage (*J-V*) and external quantum efficiency (EQE) curves of the devices are displayed in **Figure 2-10c**, **d**.



ITIC

Figure 2-10. (a) OSC device structure; (b) Energy diagram of the materials used in OSCs, where the energy levels of ITO, ZnO, MoO_3, and Ag are taken from the literature; (c) *J-V* curves of OSC devices; (d) EQE curves of OSC devices; (e) The chemical structure of ITIC.

Table 2-5. Photovoltaic parameters of PBDT-TA:ITIC and PBDT-TA:ITIC.

Active layer	Solvent	J_{sc} (mA cm^{-2})	V_{oc} (V)	FF	PCE (%)
PBDT-TA:ITIC	DCB	19.43	0.96	0.56	10.47
PBDT-TA:ITIC	Xylene	19.63	0.98	0.51	9.76
PBDT-TC:ITIC	DCB	18.23	0.96	0.55	9.68

Since both PBDT-TA:ITIC and PBDT-TC:ITIC based devices have achieved the same V_{oc} = 0.96 V, they have the same energy loss (E_{loss}) of 0.66 eV, which was calculated using $E_{loss} = E_{gap}/q - V_{oc}$, where E_{gap} is the lowest optical bandgap among the donor and acceptor components and q is the elementary charge.[99,101,102] The FF of the PBDT-TA:ITIC device (0.56) is only slightly better than that of the PBDT-TC:ITIC device (0.55). Therefore, the improved performance of the PBDT-TA:ITIC based OSCs is mainly due to the increased J_{sc}. From the EQE curve of the PBDT-TA:ITIC device (**Figure 2-10d**), it can be seen that the EQE in the wavelength range of ~350-600 nm is quite high (> 60% in average), which is better than the PBDT-TC:ITIC device. The achieved J_{sc} of 19.43 mA cm^{-2} is higher than previously reported high performance OSCs with ITIC as acceptor.

To further investigate the reason for the enhanced J_{sc} of the PBDT-TA:ITIC devices, photoluminescence (PL) quenching experiments were carried out to characterize the effectiveness of exciton diffusion and charge transfer of the BHJ active layer. As shown in **Figure 2-11**, the PBDT-TA and ITIC neat films show photoluminescence emission in the regions of 600-750 and 750-850 nm, respectively. For the PBDT-TA:ITIC blend film, a high PL quenching efficiency of 99.5% for the PBDT-TA phase was observed, suggesting that the exciton diffusion from the donor phase to the donor-acceptor interface and the subsequent charge transfer from donor to acceptor (the contribution of the channel I photocurrent by transfer of electrons from the donor to the acceptor) are highly efficient.[103] The acceptor PL quenching is also quite high (95.5%), indicating that transfer of holes from the acceptor to the donor (the channel II photocurrent) is also very efficient. For the PBDT-TC:ITIC blend film, quenching efficiencies of the donor (99.1%) and acceptor (92.0%) phases are also quite high, but both are slightly lower than those for the PBDT-TA blend film. The better PL quenching of the PBDT-TA:ITIC blend might be due to the lower exciton binding energy of PBDT-TA, which would facilitate the exciton diffusion and dissociation, which contribute to the improved J_{sc}.

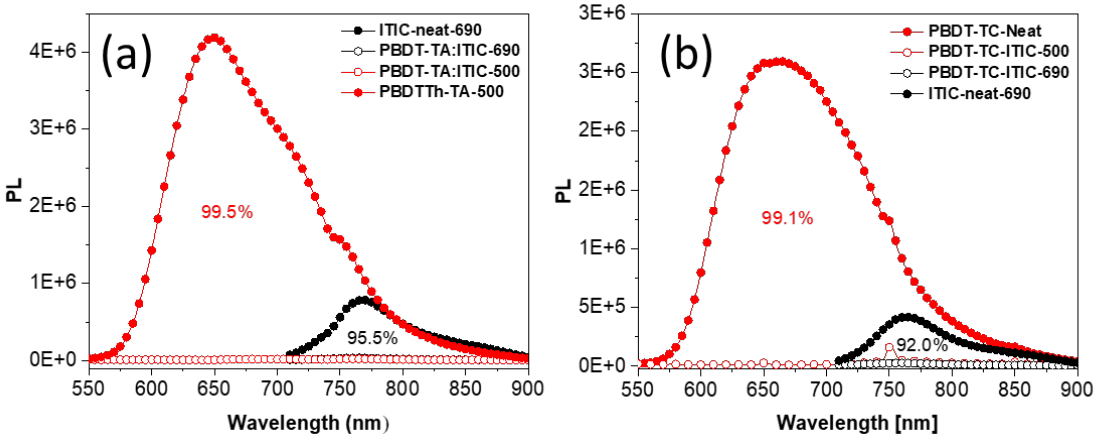


Figure 2-11. PL quenching data for (a) PBDT-TA and (b) PBDT-TC polymers for neat and blend films on glass. The excitation wavelength was 500 nm for donor and 690 nm for acceptor excitation.

The J_{sc} is also affected by the transport of free holes and electrons, which are generated by the dissociation of excitons at the donor/acceptor interface, through the donor phase and acceptor phase to the anode and cathode, respectively. Achieving high and balanced hole and electron mobilities (> 10^4 cm^2 V^{-1} s^{-1}) of the active layer is also crucial to obtain a high FF.[104] The hole (μ_h) and electron (μ_e) mobilities of the blend film were measured by the space charge limited current (SCLC) method using the device structures of ITO/PEDOT:PSS (30 nm)/active layer/MoO_x (10 nm)/Ag (100 nm) and ITO/ZnO (35 nm)/active layer/LiF (1 nm)/Al (100 nm), respectively. As shown in **Table 2-6**, the electron and hole mobilities of PBDT-TA:ITIC devices are up to 1.11×10^{-4} cm^2 V^{-1} s^{-1} (8.68×10^{-5} on average) and 2.17×10^{-4} cm^2 V^{-1} s^{-1} (2.00×10^{-4} on average), respectively, with an average μ_h/μ_e ratio of 2.30. In comparison, the average electron and hole mobilities of PBDT-TC:ITIC based devices are 4.39×10^{-5} cm^2 V^{-1} s^{-1} and 7.59×10^{-5} cm^2 V^{-1} s^{-1} (with an average μ_h/μ_e ratio of 1.73), respectively, which are lower than those of the PBDT-TA:ITIC film. Therefore, the higher hole and electron mobilities of the PBDT-TA:ITIC blend could also help increase the J_{sc} of OSC devices. However, higher mobilities of 4×10^{-4} - 8×10^{-4} cm^2 V^{-1} s^{-1} are required to achieve a very high FF. Compared to the FF of the state-of-the art NFA-based OSCs (> 0.70), the relatively low FF (0.56) of the PBDT-TA:ITIC based OSCs may be attributed to the insufficient hole and electron mobilities of the active layer. The lower SCLC hole mobility of PBDT-TC:ITIC than that of PBDT-TA:ITIC is considered due

to the undesirable edge-on chain orientation of PBDT-TC in the blend since the hole mobility values of PBDT-TC in organic thin field transistors (OTFTs) are similar to those of PBDT-TA.

Table 2-6. SCLC data of PBDT-TA and PBDT-TC based devices.

	Electron mobility [$cm^2 V^{-1} s^{-1}$]		**Hole mobility [$cm^2 V^{-1} s^{-1}$]**	
	Maximum	**Average [SD]**	**Maximum**	**Average [SD]**
PBDT-TA:ITIC	1.11×10^{-4}	8.68×10^{-5} [1.51×10^{-5}]	2.17×10^{-4}	2.00×10^{-4} [1.90×10^{-5}]
PBDT-TC:ITIC	7.72×10^{-5}	4.39×10^{-5} [1.84×10^{-5}]	9.37×10^{-5}	7.59×10^{-5} [1.53×10^{-5}]
Neat PBDT-TA	-	-	8.12×10^{-4}	6.13×10^{-4} [1.57×10^{-5}]
Neat PBDT-TC	-	-	7.76×10^{-4}	5.65×10^{-4} [1.37×10^{-4}]
PBDT-TC:ITIC[a]	-	5.98×10^{-5}	-	4.21×10^{-5}

[a] From reference; SD: standard deviation from min 4 devices

Halogenated solvents commonly used for fabricating OSCs, such as chloroform, chlorobenzene, and o-dichlorobenzene (DCB), are pollutants that are incompatible with the eco-friendly large-scale production of OSCs. PBDT-TA is soluble in a non-halogenated solvent, xylene. As shown in **Table 2-5**, J_{sc} and V_{oc} of the OSC devices process with xylene are even higher than those of the devices fabricated with o-DCB. Despite a large drop in FF (0.51), a high PCE of 9.76% was achieved.

2.4.6 Film morphology and microstructure

The morphology of the blend films of PBDT-TA:ITIC and PBDT-TC:ITIC processed with DCB was investigated by atomic force microscopy (AFM). As shown in **Figure 2-12**, the PBDT-TA:ITIC film shows a smooth surface morphology with a small root-mean roughness (RMS) of 0.98 nm. The film is composed of worm-shaped aggregates with smaller, tightly connected grains, which can be beneficial for charge transport. The PBDT-TC:ITIC blend film is also quite smooth with a slightly larger RMS of 1.14 nm. However, larger and more isolated grains are observed in this sample. The more desirable morphology may also contribute to the higher J_{sc} and FF of the PBDT-TA:ITIC based OSCs.[105]

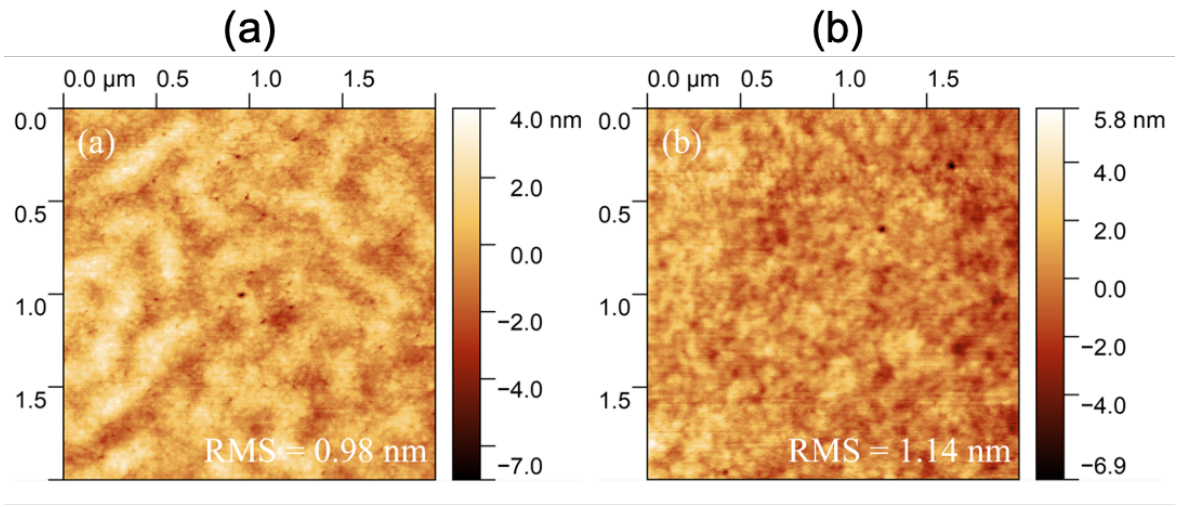


Figure 2-12. AFM height images of blend films based on (a) PBDT-TA:ITIC and (b) PBDT-TC:ITIC.

Two-dimensional grazing incidence X-ray diffraction (2D-GIXD) patterns were obtained to study the microstructure of the neat and blend polymer films. **Figures 2-13a** and **b** show the in-plane (IP) and out-of-plane (OOP) X-ray diffraction patterns of the neat PBDT-TA thin film sample. No obvious diffraction peaks or very broad peaks (at 2θ = ~21° for the samples annealed at 100 °C and 200 °C) in the in-plane direction were observed, indicating that the polymer is quite disordered in this direction. In the out-of-plane direction, the as-spun neat polymer film showed a peak at $2\theta = 3.63°$, corresponding to a d-spacing of 2.45 nm. This can be assigned to the distance between the (100) planes of lamellar packing in the thin film. When the film was annealed, the (100) peak position shifted to a larger diffraction angle. For the film annealed at 200 °C, the (100) peak position shifted to 3.79°, corresponding to a d-spacing of 2.33 nm, which indicates that a tighter lamellar packing was formed in the out-of-plane direction. As shown in **Figure 2-13d**, the in-plane XRD patterns of the neat PBDT-TC film also showed no peaks or very broad peaks at ~21°, which originate from the amorphous state and some low-order π-π stacking. In the out-of-plane direction (**Figure 2-13e**), the as-spun neat PBDT-TC film showed a peak at $2\theta = 3.86°$ (d-spacing = 2.29 nm), which represents the (100) lamellar planes. This interlamellar distance is shorter than that (2.45 nm) of PBDT-TA due to the shorter methyl carboxylate group in TC than the methyl acrylate group in TA. Interestingly, when the film was annealed the (100) peak shifted towards low diffraction angles of 3.67° (d = 2.41 nm) at 50 °C, 3.59° (d = 2.46 nm) at 100 °C, 3.18° (d = 2.78 nm) at 150 °C, and 3.53° (d = 2.50 nm) at 200 °C. The increase in the interlamellar distance with annealing temperature observed for PBDT-TC may be due to the

thermal relaxation of the side chains, while the opposite trend observed for PBDT-TA may be caused by the increased degree of backbone twisting due to the sterically more demanding methyl acrylate groups.

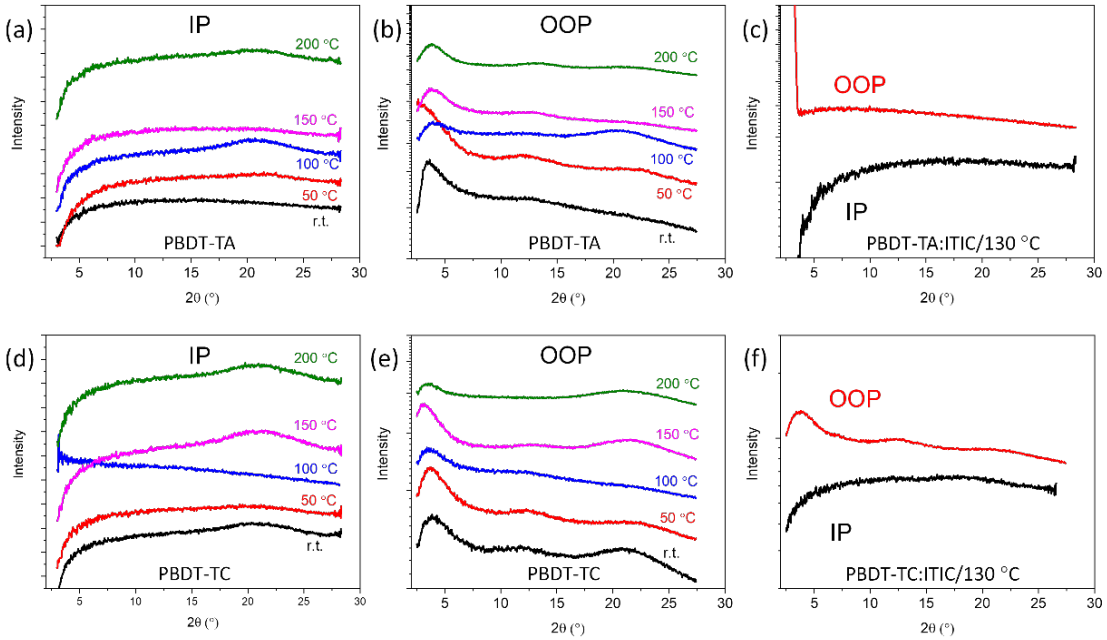


Figure 2-13. In-plane (IP) and out-of-plane (OOP) 2D-GIXD patterns of PBDT-TA (a, b), PBDT-TA:ITIC (c), PBDT-TC (d ,e) and PBDT-TC:ITIC (f).

As shown in **Figure 2-13c**, the PBDT-TA:ITIC blend film showed no obvious peaks in either in-plane or out-of-plane direction, indicating that the polymer chains in the blend film are quite disordered. While the PBDT-TC:ITIC based blend film showed no obvious peaks in the in-plane direction, an intense peak at 2θ = 3.80° (d-spacing = 2.33 nm) was observed (**Figure 2-13f**), indicating the presence of ordered lamellar packing in the out-of-plane direction. Thus, the PBDT-TC polymer chains in the PBDT-TC:ITIC blend film favored the edge-on orientation, which is undesirable for the charge transport along the direction perpendicular to the active layer in the OSC devices. The higher crystallinity of PBDT-TC also agrees with the more defined grains observed in the AFM image of the PBDT-TC:ITIC blend film (**Figure 2-12b**).[106] Nonetheless, to further improve the solar cell performance, it is necessary to improve the crystallinity of PBDT-TA, which may be achieved by rigorous optimization of the film processing conditions. Incorporation of fluorine atoms on the donor

BDT unit may improve the chain packing and thus the hole mobility.[93] Alternatively, by synthesizing a regioregular PBDT-TA, the crystallinity and thus the hole mobility are also expected to be improved.[95]

2.5 Conclusion

In summary, a novel weakly electron-withdrawing building block, methyl thiophene-3-acrylate (TA) was developed, aiming to increase the dielectric constant and reduce the exciton binding energy of polymer semiconductors. The polymer PBDT-TA was synthesized using TA as the acceptor unit and benzodithiophene (BDT) as the donor unit. PBDT-TA showed an increased dielectric constant (ε_r = 3.78) and reduced exciton binding energy (E_b = 0.415 eV) compared to those (ε_r = 3.55; E_b = 0.430 eV) of the analogous polymer PBDT-TC, which is composed of BDT and a less polar methyl thiophene-3-carboxylate (TC) building block. The π-conjugated vinyl bridge between thiophene and the carboxylate group in TA increases the polarization of PBDT-TA compared to the TC building block in PBDT-TC, which has been confirmed by the DFT simulations. PBDT-TA has a wide bandgap of 2.02 eV, E_{HOMO} of -5.46 eV, and E_{LUMO} of -3.44 eV, which match well with a non-fullerene acceptor ITIC. The organic solar cell based on the blend layer of PBDT-TA:ITIC exhibited a higher PCE of 10.47% than that (9.68%) of the PBDT-TC:ITIC based solar cell. In addition to the reduced E_b, the improved charge transport and morphology of the active layer also contribute to the enhanced solar cell performance of the PBDT-TA:ITIC based solar cell. This work shows that the introduction of simple acrylate side chains can effectively increase the dielectric constant, reduce the exciton binding energy, and improve the solar cell efficiency of polymer semiconductors.

2.6 Experimental Section

2.6.1 General Methods.

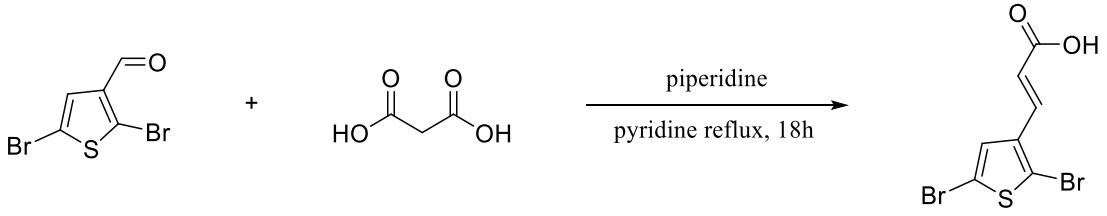
^{1}H NMR and ^{13}C NMR spectra were recorded on Bruker DPX 300-MHz or 500-MHz spectrometer in $CDCl_3$. Chemical shifts were reported relative to tetramethylsilane used as an internal standard (TMS, 0 ppm). High temperature gel permeation chromatography (GPC) measurements were performed on an Aligent PL-GPC220 system using 1, 2, 4-trichlorobenzene as an eluent at 110 °C with a sample concentration of 10 mg mL^{-1}. Specifically, the GPC column is a highly cross-linked, porous

polystyrene/divinylbenzene column of the type PLgel MIXED-B, and the detector employed is a differential refractive index (RI) detector. Density functional theory (DFT) calculations were conducted using GaussView 9.0 at the B3LYP/6-31G (d,p) level. The UV-Vis absorption spectra of polymers were recorded on a Cary 7000 Universal Measurement Spectrophotometer (UMS). Cyclic voltammetry (CV) data were obtained on a CHI600E electrochemical analyzer using an Ag/AgCl reference electrode and two Pt disk electrodes as the working and counter electrodes, respectively, in 0.1 M tetrabutylammonium hexafluorophosphate solution in dry acetonitrile at a scan rate of 100 mV s^{-1}. Ferrocene was used as the reference, which has a HOMO energy level of -4.8 eV. Atomic force microscopy (AFM) images of polymer films were taken using a Dimension 3100 scanning probe microscope. PL quenching measurements were conducted on thin films spin-coated on glass substrates using a Horiba PTI QuantaMaster™ 8000 Series Fluorimeter. X-ray diffraction (XRD) patterns were collected using a Bruker D8 Discover powder diffractometer with standard Bragg-Brentano geometry and Cu Kα radiation (λ = 1.5418 Å).

2.6.2 Synthetic Procedures

2,5-Dibromothiophene-3-carbaldehyde (**1**)[87] and 2,5-dibromothiophene-3-carboxylic acid (**4**)[93] were prepared according to literature procedures. 2,6-Bis(trimethytin)-4,8-bis(5-(2-ethylhexyl)thiophen-2-yl)benzo[1,2-b:4,5-b']dithiophene (**6**) was purchased from 1-Material.

Synthesis of (E)-3-(2,5-dibromothiophen-3-yl) acrylic acid (2).

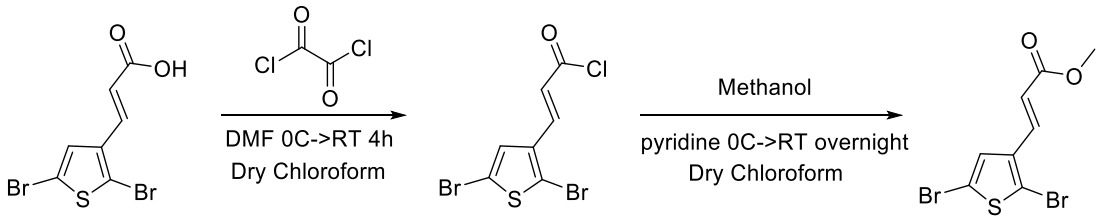


1 **2**

2,5-Dibromothiophene-3-carbaldehyde (**1**) (1.74 g, 6.41 mmol), malonic acid (0.86 g, 8.33 mmol) were dissolved in pyridine (6 mL) and piperidine (0.1 mL) was added. Then, the mixture was refluxed for 18 h. After cooling to room temperature, the reaction mixture was poured into a mixture of ice and

water and acidified with dilute HCl (aq.). Then, the mixture was filtered and the solid was washed with chloroform to afford (E)-3-(2,5-dibromothiophen-3-yl) acrylic acid (**2**) as a white solid. Yield: 1.67 g (84%). ^{1}H NMR (300 MHz, DMSO-d6): δ 12.62 (s, 1H), 7.77 (s, 1H), 7.31-7.37 (d, J = 15 Hz, 1H), 6.50-6.55 (d, J = 15 Hz, 1H). ^{13}C NMR (75 MHz, DMSO-d6): δ 167.80, 137.53, 133.96, 129.57, 122.82, 116.03, 112.79.

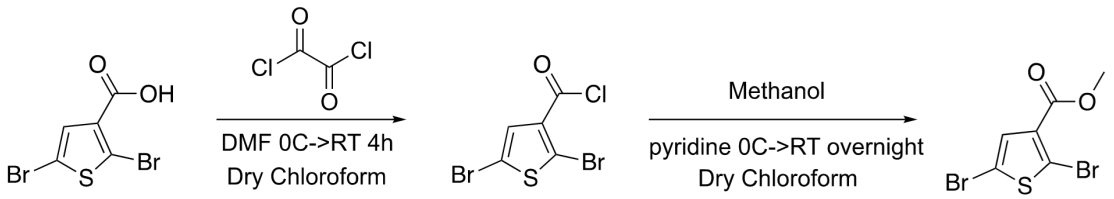
Synthesis of methyl (E)-3-(2,5-dibromothiophen-3-yl) acrylate (3)



2 **3**

A solution of (E)-3-(2,5-dibromothiophen-3-yl) acrylic acid (**2**) (0.40 g, 1.28 mmol) in anhydrous chloroform (2.50 mL) was added into a dry 3-neck round bottom flask under nitrogen and cooled to 0 °C with an ice-water bath. Oxalyl chloride (0.12 mL, 1.41 mmol) was added dropwise using a dropping funnel, followed by N, N-dimethylformamide (0.10 mL) as a catalyst. Then, the reaction mixture was allowed to warm to room temperature and stirred for 4 h. Unreacted oxalyl chloride was removed under reduced pressure using a glass vacuum trap in a dry ice-acetone ice bath (-78 °C). Next, anhydrous chloroform (2.50 mL) was added, and the mixture was cooled to 0 °C with an ice-water bath. Methanol (0.05 mL, 1.28 mmol) was added slowly, followed by pyridine (0.10 mL, 1.28 mmol). The reaction mixture was allowed to warm to room temperature and stirred for 24 h. Then, water was added to stop the reaction and the mixture was extracted with ethyl acetate. The organic phase was dried and the solvent was removed by rotary evaporation. The crude product was purified by column chromatography on silica gel using a mixture of hexane and dichloromethane (v:v = 1:1) as the eluent to obtain (E)-3-(2,5-dibromothiophen-3-yl) acrylate (**3**) as a yellow solid. Yield: 0.40 g (96%). ^{1}H NMR (300 MHz, $CDCl_3$): δ 7.53-7.58 (d, J = 15 Hz, 1H), 7.12 (s, 1H), 6.20-6.25 (d, J = 15 Hz, 1H), 3.81 (s, 3H). ^{13}C NMR (75 MHz, $CDCl_3$): δ 166.95, 136.83, 134.98, 127.60, 120.05, 116.24, 112.76, 51.89.

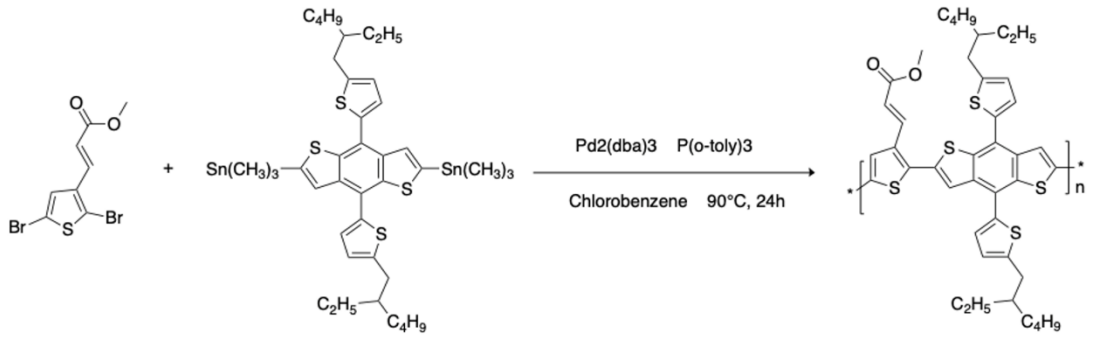
Synthesis of methyl 2,5-dibromothiophene-3-carboxylate (5)



4 **5**

A solution of 2,5-dibromothiophene-3-carboxylic acid (**4**) (0.572 g, 2.00 mmol) in anhydrous chloroform (4 mL) was put into a dry 3-neck round bottom flask under nitrogen, and then the solution was cooled to 0 °C by using an ice-water bath. Oxalyl chloride (0.19 mL, 2.20 mmol) was added dropwise using a dropping funnel, followed with N, N-dimethylformamide (0.1 mL) as a catalyst. After the addition of oxalyl chloride, the reaction mixture was allowed to warm to room temperature and stirred for 4 h. Unreacted oxalyl chloride was removed under reduced pressure with a glass vacuum trap in a dry ice-acetone bath (-78 °C) for 4 h. Then, anhydrous chloroform (4 mL) was added and the obtained solution was cooled to 0 °C with an ice-water bath. Methanol (0.08 mL, 2.00 mmol) was added slowly, followed by pyridine (0.16 mL, 2.00 mmol). The reaction mixture was allowed to warm to room temperature and stirred for 24 hours. Then, water was added and the reaction mixture was extracted with ethyl acetate. The organic solvent was removed, and the crude product was purified by column chromatography on silica gel using a mixture of hexane and dichloromethane mixture (v:v = 1:1) as the eluent to obtain methyl 2,5-dibromothiophene-3-carboxylate (**5**) as a white solid. Yield: 0.52 g (87%). ^{1}H NMR (300MHz, $CDCl_3$): δ 7.35 (s, 1H), 3.87 (s, 3H).

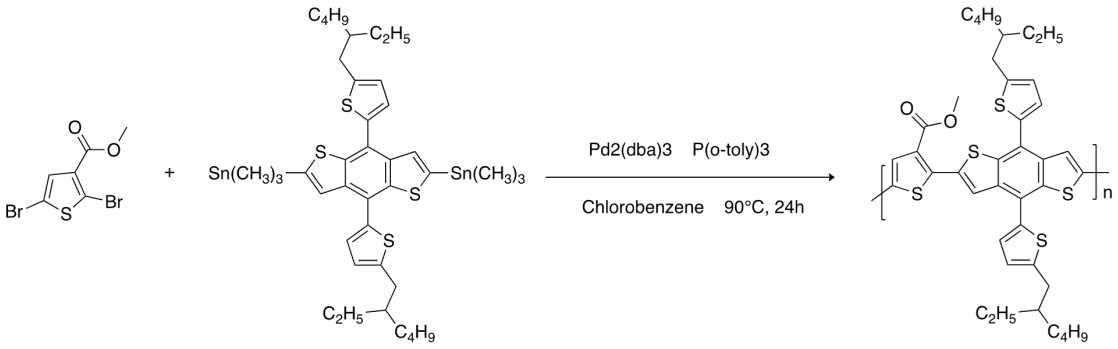
Synthesis of poly{(4,8-bis(5-(2-ethylhexyl)thiophen-3-yl)benzo[1,2-b:4,5-b']dithiophen-2,6-diyl)-co-[methyl (E)-thiophene-3-acrylate-2,5-diyl] (PBDT-TA)



3 **6** **PBDT-TA**

To a 25 mL two-neck round bottom flask, (E)-3-(2,5-dibromothiophen-3-yl) acrylate (**3**) (54.1 mg, 0.166 mmol), 2,6-Bis(trimethytin)-4,8-bis(5-(2-ethylhexyl)thiophen-2-yl)benzo[1,2-b:4,5-b']dithiophene (**6**) (150 mg, 0.166 mmol) and P(o-tolyl)$_3$ (4 mg, 0.0133 mmol) were added. After the reaction system was purged with argon and evacuated three times, anhydrous chlorobenzene (5 mL) was added to dissolve the mixture, and then $Pd_2(dba)_3$ (3 mg, 0.0033 mmol) was added. The reaction mixture was stirred under argon at 90 °C for 24 h before it was cooled to room temperature. The reaction mixture was poured into methanol (100 mL), stirred for 1 h, and filtered to obtain a dark red solid. The solid was extracted with acetone, hexane, and then chloroform in a Soxhlet extractor for 24 h each to give PBDT-TA as a red solid from the chloroform portion. Yield: 121 mg (98%). GPC: M_n = 27.4 kg mol^{-1}, M_w = 47.6 kg mol^{-1}, and $Đ$ = 1.74.

Synthesis of poly{(4,8-bis(5-(2-ethylhexyl)thiophen-3-yl)benzo[1,2-b:4,5-b']dithiophen-2,6-diyl)-co-[methyl thiophene-3-carboxylate-2,5-diyl] (PBDT-TC)



5 **6** **PBDT-TC**

To a 25 mL two-neck round bottom flask, methyl 2,5-dibromothiophene-3-carboxylate (**5**) (49.7 mg, 0.166 mmol), 2,6-Bis(trimethytin)-4,8-bis(5-(2-ethylhexyl)thiophen-2-yl)benzo[1,2-b:4,5-b']dithiophene (**6**) (150 mg, 0.166 mmol) and P(o-tolyl)$_3$ (4 mg, 0.0133 mmol) were added. After the reaction system was purged with argon and evacuated three times, anhydrous chlorobenzene (5 mL) was added to dissolve the mixture, followed by $Pd_2(dba)_3$ (3 mg, 0.0033 mmol). The reaction mixture was then stirred under argon at 90 °C for 24 h before it was cooled to room temperature. A similar purification procedure used for PBDT-TA afforded PBDT-TC as a red solid from the chloroform extraction fraction. Yield: 118 mg (99%). GPC: M_n = 66.1 kg mol^{-1}, M_w = 172.1 kg mol^{-1}, and $Đ$ = 2.60.

2.6.3 Measurement of dielectric constant

Capacitor devices with a structure of Si/SiO_2 (300 nm)/PBDT-TA(PBDT-TC) (30 nm)/Au (100 nm) were fabricated to measure the dielectric constant (ε_r) of PBDT-TA and PBDT-TC with impedance spectroscopy. A BioLogic VSP Multichannel Multirole Electrochemical Station was used to obtain the effective capacitance (C_{eff}) of the device by sweeping at 20 mV A/C from -2 V to 2 V in the frequency range from 80,000 Hz to 4,000 Hz. The device is considered as a series of connected capacitors, where $1/C_{polymer} = 1/C_{eff} - 1/C_{SiO2}$. The dielectric constant of the polymer was calculated using the equation $C_{polymer} = \varepsilon_r S/4\pi kd$, where S is the area of the electrode, k is the Coulomb constant and d is the thickness of the dielectric (polymer film). The capacitance of SiO_2 was measured with a device configuration of Si/SiO_2 (300 nm))/Au (100 nm).

2.6.4 OSC device fabrication

Inverted polymer solar cells were fabricated with the configuration of ITO (150 nm)/ ZnO (35 nm)/ Active layer/ MoO_x (10 nm)/ Ag (100 nm). The conductive indium-doped tin oxide (ITO) glass substrate was cleaned with deionized water and acetone in an ultrasonic bath at 40 °C for 20 min each. The substrate was then removed and cleaned with a cotton swab moistened with acetone. The substrate was again sonicated in isopropanol (IPA) at 40 °C for 20 min. The substrate was dried with an N_2 stream and treated in an air plasma cleaner for 10 min. A thin layer of ZnO (~35 nm) was deposited by spin-coating a freshly prepared ZnO precursor solution at 3500 rpm which was subsequently annealed at 200 °C for 1 h in air. (The ZnO precursor solution was prepared by stirring a mixture of zinc acetate (197 mg), ethanolamine (54 µL), and 2-methoxyethanol (2 mL) at 50 °C overnight.) Then the substrates were transferred to a nitrogen filled glove box, where the donor (PBDT-TA or PBDT-TC) and acceptor (ITIC) mixture (at a 1:1 mass ratio) solution in an appropriate solvent (1,2-dichlorobenzene (o-DCB), chlorobenzene (CB), xylene, or chloroform (CF)) was spin-coated onto the ZnO layer at various speeds to obtain the blend layers with the desired thickness. The concentration of the donor/acceptor solution is 42 mg mL^{-1} in o-DCB, 36 mg mL^{-1} in CB or xylene, and 24 mg mL^{-1} in CF. After annealing for 10 min (except for the non-annealed devices), a thin MoO_x hole transport layer (10 nm) and an Ag electrode layer (100 nm) were sequentially thermally deposited onto the substrate at a pressure < 5.0×10^{-6} Pa. The active area of each OSC device is 0.0574 cm^2. The current density-voltage (*J-V*) characteristics of the solar cells were measured on an Agilent B2912A Semiconductor Analyzer and a ScienceTech SLB300-A Solar Simulator. A 450 W xenon lamp and an air mass (AM) 1.5 filter were used as the light source. External quantum efficiency (EQE) measurements were performed in air within 3 h after device fabrication using a QEX10 Solar Cell Quantum Efficiency Measurement System (PV measurements, Inc.).

2.6.5 Appendix

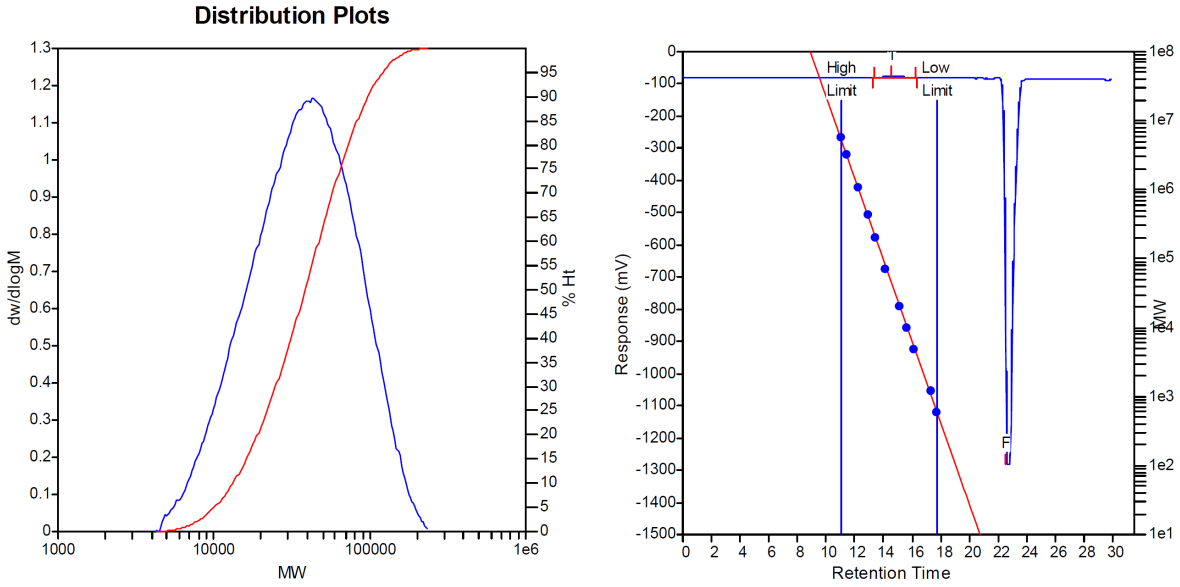


Figure 2-14. HT-GPC data of polymer PBDT-TA.

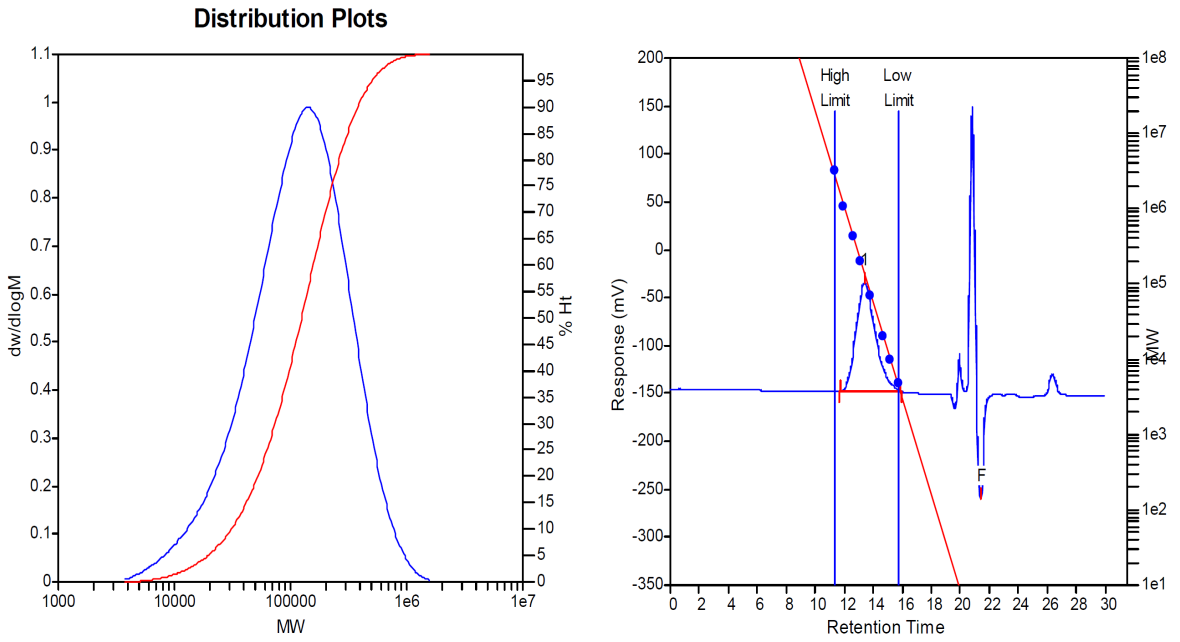


Figure 2-15. HT-GPC data of polymer PBDT-TC.

Table 2-7. Summary of the photovoltaic properties of the PBDT-TA:ITIC devices processed at different RPMs at annealing temperature of 130 °C.

RPM	Solvent	J_{sc} (mA/cm^2)	V_{oc} (V)	FF	PCE (%)
600	CB	-16.64	0.98	0.58	9.44
1000	CB	-13.56	0.98	0.55	7.38

Table 2-8. Summary of the photovoltaic properties of the PBDT-TA:ITIC devices processed with different annealing temperatures and solvents for 10 min and 600 RPM.

Annealing temperature	Solvent	J_{sc} (mA/cm^2)	V_{oc} (V)	FF	PCE (%)
RT	CB	-17.49	0.99	0.45	7.74
100	CB	-16.88	0.98	0.56	9.22
130	CB	-16.64	0.98	0.58	9.44
150	DCB	-19.01	0.99	0.52	9.72
130	DCB	-19.43	0.96	0.56	10.47

Table 2-9. Summary of the photovoltaic properties of the PBDT-TA:ITIC devices processed with different solvents at annealing temperature of 130 °C and 600 RPM.

Solvent	J_{sc} (mA/cm^2)	V_{oc} (V)	FF	PCE (%)
DCB	-19.43	0.96	0.56	10.47
CB	-20.34	0.97	0.52	10.19
Xylene	-19.63	0.98	0.51	9.76
CF	-18.89	1.00	0.47	8.90

Table 2-10. Summary of the photovoltaic properties of the devices processed with various additives at annealing temperature of 130 °C and 600 RPM.

Additives	Solvent	J_{sc} (mA/cm^2)	V_{oc} (V)	FF	PCE (%)
DIO [0.5% v/v]	DCB	-15.71	0.99	0.43	6.69
CN [0.5% v/v]	DCB	-17.39	0.98	0.55	9.39
DIO [0.25% v/v]	DCB	-16.29	0.99	0.57	9.22
CN [0.25% v/v]	DCB	-16.9	0.99	0.55	9.22

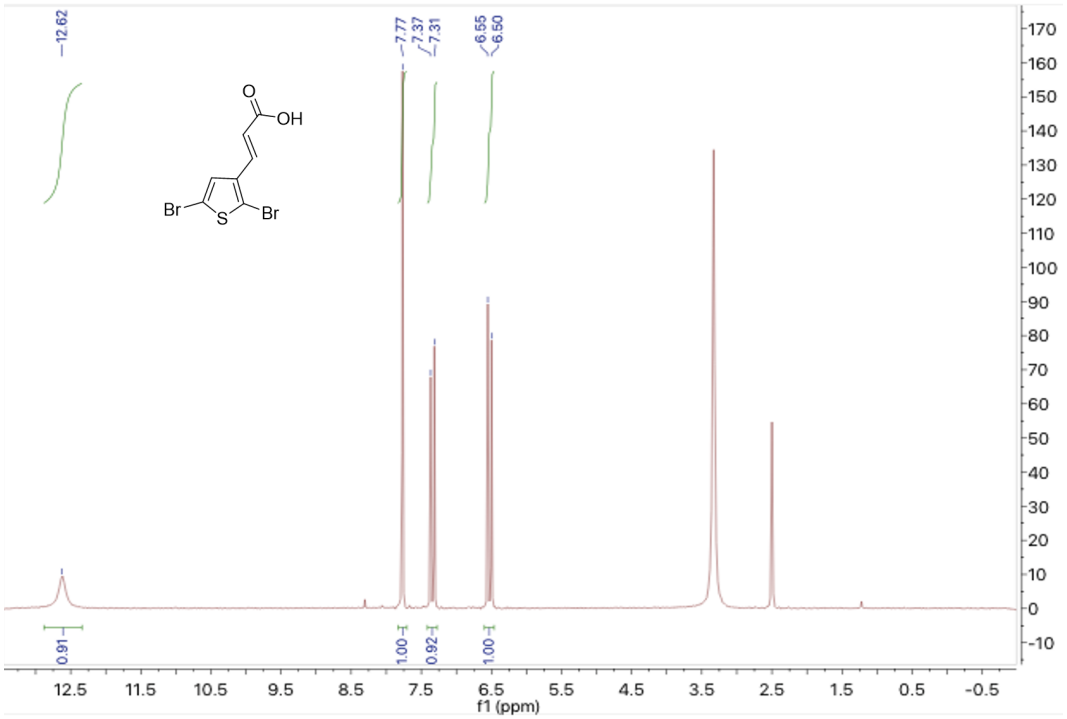


Figure 2-16. ^{1}H NMR (300MHz, DMSO) spectra of (E)-3-(2,5-dibromothiophen-3-yl) acrylic acid (2).

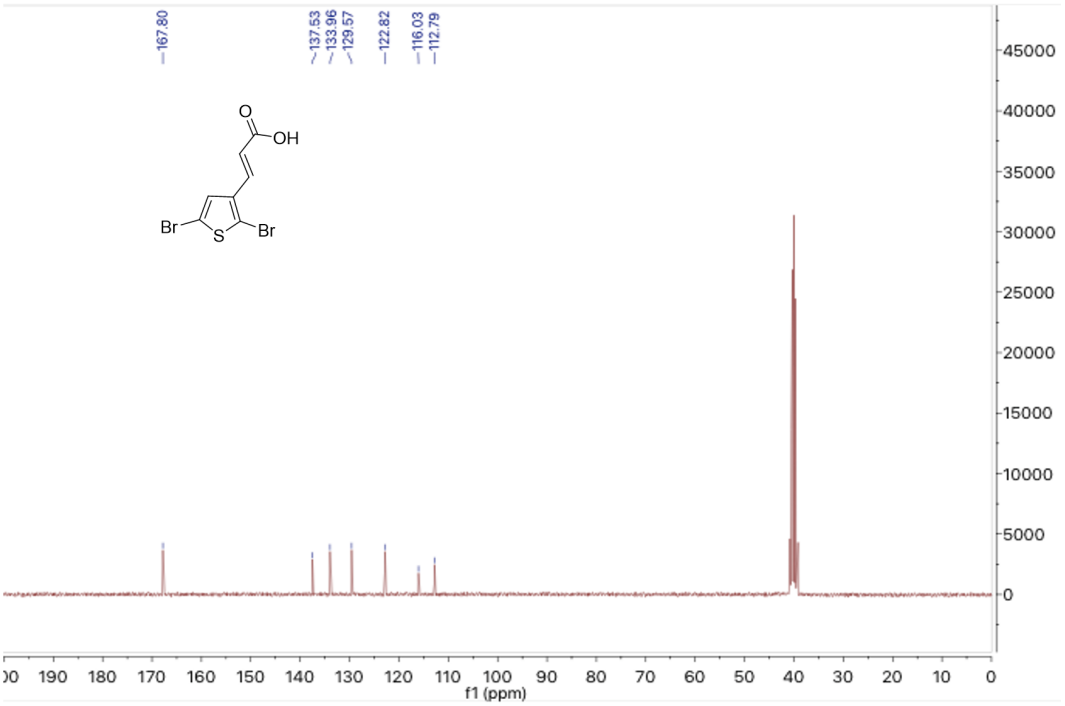


Figure 2-17. ^{13}C NMR (300MHz, DMSO) spectra of (E)-3-(2,5-dibromothiophen-3-yl) acrylic acid (2).

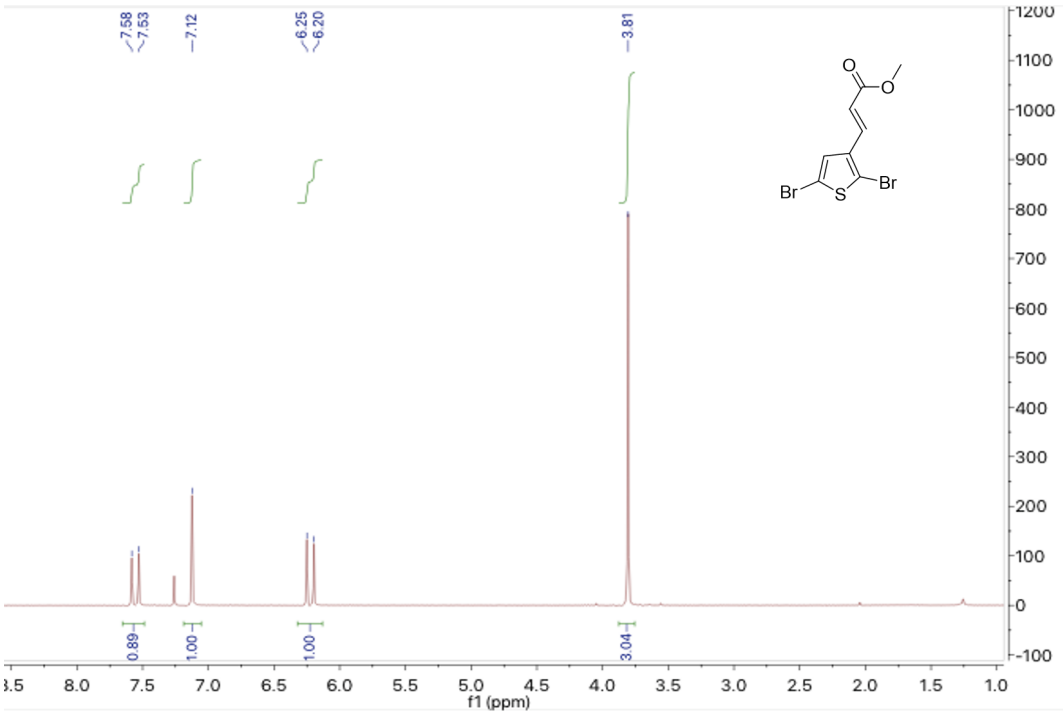


Figure 2-18. ^{1}H NMR (300MHz, $CDCl_3$) spectra of methyl (E)-3-(2,5-dibromothiophen-3-yl) acrylate (3).

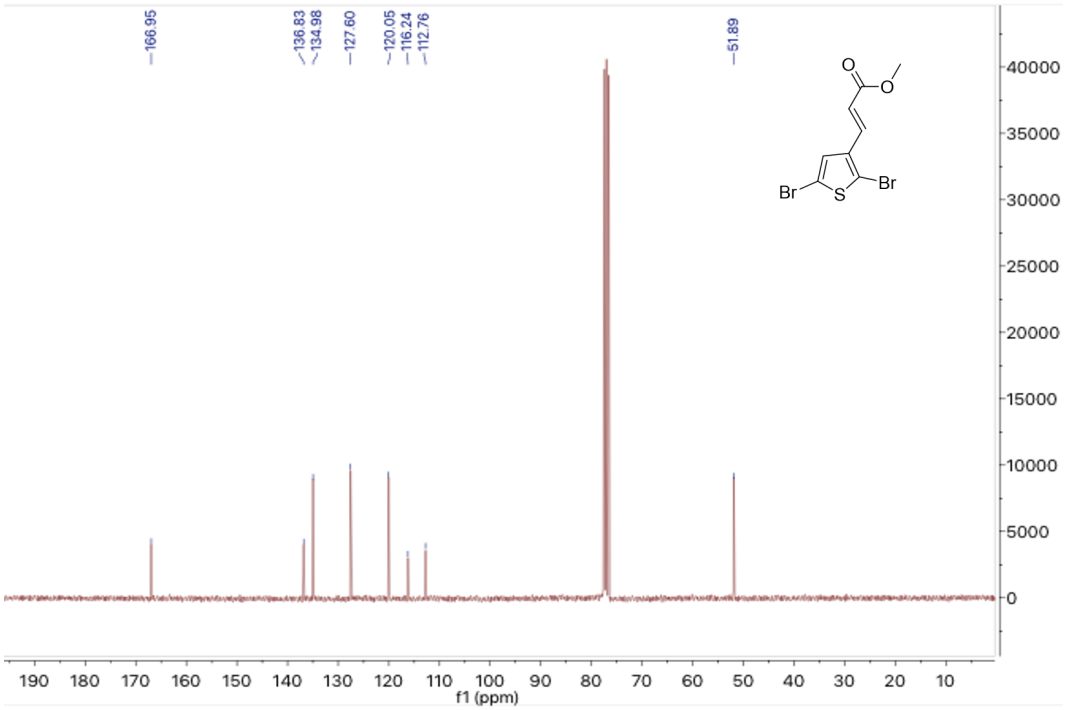


Figure 2-19. ^{13}C NMR (300MHz, $CDCl_3$) spectra of methyl (E)-3-(2,5-dibromothiophen-3-yl) acrylate (3).

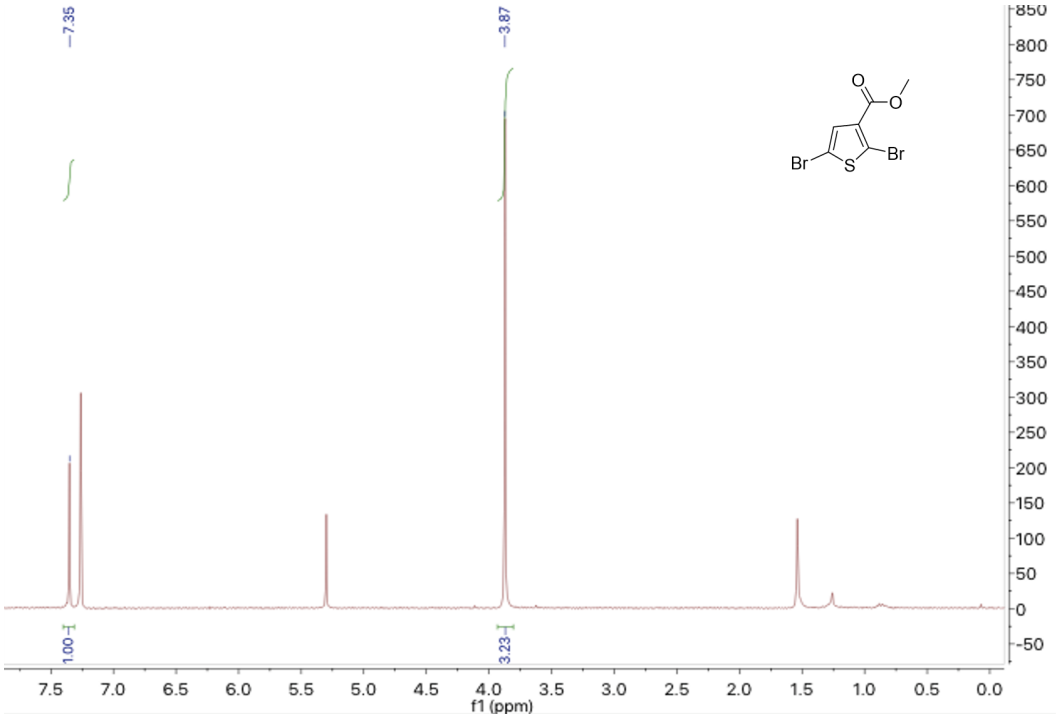


Figure 2-20. ^{1}H NMR (300MHz, $CDCl_3$) spectra of methyl 2,5-dibromothiophene-3-carboxylate (5).

Chapter 3

Synthesis and Characterization of Dihalovinyl Thiophene-based Polymers

This chapter is based on the following publication:

Y. Yuan, S. Cui, X. Li, H. Liu, J. Wang, Y. Li, *Macromolecules*, **2024**, 57, 10, 4757–4768.

3.1 Introduction

The most common high-performance wide bandgap polymer donors, such as PM6,[107,108] PM7,[109,110] D18[111] and D18-Cl[112] (**Figure 3-1**), are composed of a repeat unit that combines a benzodithiophene (BDT) donor unit with a weakly electron-accepting unit, along with thiophene spacers. The BDT unit plays a crucial role in providing high carrier mobility and promoting a desirable face-on orientation.[54–57,113] However, the synthesis of the acceptor unit and its connection with the spacers require multiple synthetic steps, contributing to the significant increase of the cost of these materials.[53] Furthermore, the inclusion of spacers reduces the E_{HOMO} of the polymer, resulting in a lower V_{oc}. To address this, fluorinated or chlorinated BDT units are introduced to reduce the E_{HOMO} of the polymer. However, the addition of fluorine or chlorine substituents to BDT further increases the cost of the polymer donor.[114]

Here, two new polymer donors, namely PBDT-TDF and PBDT-TDCl (**Figure 3-1**), were developed with novel *gem*-dihalovinyl thiophene-based building blocks. The *gem*-dihalovinyl substituted building blocks, namely 3-(2,2-difluorovinyl)thiophene (TDF) and 3-(2,2-dichlorovinyl)thiophene (TDCl), in these polymers possess a weak electron-withdrawing character. This is attributed to the highly electronegative difluoro or dichloro groups present, which effectively withdraw electrons from the connecting thiophene unit through the conjugated vinyl bridge. The monomers incorporating TDF and TDCl units were synthesized through straightforward synthetic routes. As for the comonomer, the commercially available BDT compound in its simplest form (without any fluorine or chlorine substitution) was used. PBDT-TDF and PBDT-TDCl are found to be wide bandgap polymers, exhibiting E_g of 2.02 eV and 1.99 eV, respectively. PBDT-TDF has E_{HOMO} and E_{LUMO} energy levels of -5.62 eV and -3.60 eV, respectively, while PBDT-TDCl has slightly higher levels of -5.48 eV and -3.49 eV, respectively. In light of the FMO alignment, Y6 was chosen as the NFA to assess the photovoltaic performance of these polymers in OSCs. The OSC device based on the PBDT-TDF:Y6 blend exhibited

a V_{oc} of 0.77 V, a J_{sc} of 20.54 mA cm^{-2}, a FF of 0.56, resulting in a PCE of 8.83%. On the other hand, the OSC device based on the PBDT-TDCl:Y6 blend showed a V_{oc} of 0.71 V, a J_{sc} of 25.95 mA cm^{-2}, a FF of 0.60, resulting in a higher PCE of 11.02%. The blend film of PBDT-TDCl:Y6 demonstrated higher average space-charge-limited current (SCLC) hole and electron mobilities of 4.46×10^{-4} cm^2 V^{-1} s^{-1} and 1.48×10^{-4} cm^2 V^{-1} s^{-1}, respectively, and stronger absorption characteristics, contributing to the very high J_{sc} in OSC devices. PBDT-TDF and PBDT-TDCl have also demonstrated excellent performance as p-type channel materials in organic thin film transistors (OTFTs), achieving hole mobility values of up to 2.60×10^{-3} cm^2 V^{-1} s^{-1} and 5.56×10^{-3} cm^2 V^{-1} s^{-1}, respectively. In comparison to the smaller difluorovinyl group, the larger dichlorovinyl group appears to induce a conformational locking effect, resulting in a polymer backbone that adopts a more coplanar arrangement. This effect plays a substantial role in the increased hole mobility observed in PBDT-TDCl when contrasted with PBDT-TDF. This work highlights the potential of both TDF and TDCl as simple electron acceptor building blocks for the development of high-performance and cost-effective polymer donors in OSCs and other organic electronic devices.

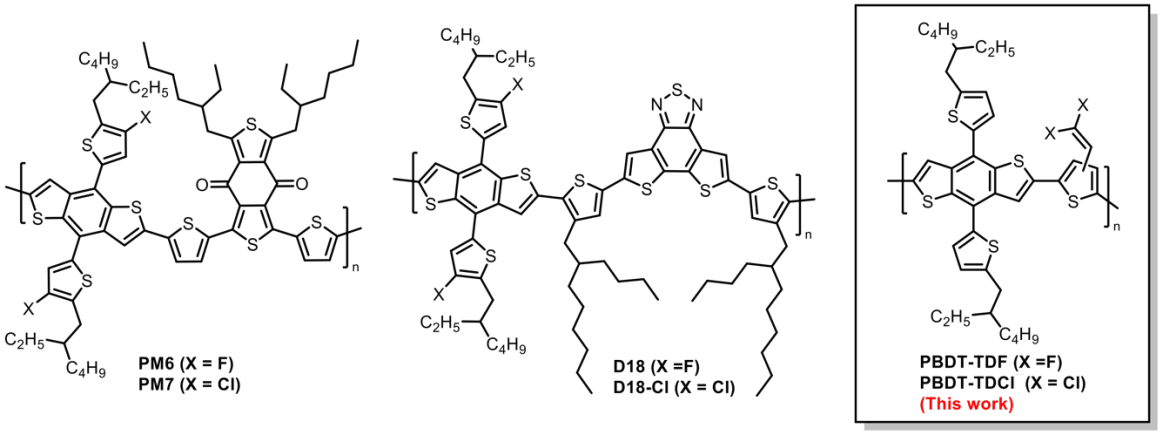


Figure 3-1. The chemical structures of PM6, PM7, D18, D18-Cl, PBDT-TDF and PBDT-TDCl.

3.2 Theoretical Study of PBDT-TDX

Computer simulations with density functional theory (DFT) were carried out on the dimer units of PBDT-TDF and PBDT-TDCl, namely di-BDT-TDF and di-BDT-TDCl, respectively, using the B3LYP/6-31G (d,p) level of the theory (**Figure 3-2**). These simulations aimed to provide valuable information regarding the geometry and FMOs of PBDT-TDF and PBDT-TDCl. To expedite the

computational process, methyl groups were employed as substitutes for the 2-ethylhexyl side chains on the BDT units.

As shown in **Figures 3-2a** and **b**, the dihedral angle between the first BDT and the first TDF from the left in di-BDT-TDF is 37.6°, notably larger than that of the dihedral angle (11.5°) between the first TDF and the second BDT. This observation indicates that the difluorovinyl side chain has a significant steric interaction with the neighboring BDT. The respective dihedral angles for di-BDT-TDCl are 35.0° and 12.9° (**Figures 3-2e** and **f**). The reduced dihedral angle between the dichlorovinyl side chain and the adjacent BDT unit indicates that the dichlorovinyl group causes less backbone twisting compared to the difluorovinyl group. In other words, the backbone of PBDT-TDCl is more coplanar compared to PBDT-TDF. The result is further demonstrated by the dihedral angle of the second BDT unit and the adjacent dihalovinyl group. The dihedral group of the second BDT and the second TDF in di-BDT-TDF is 36.3°, which is larger than that (34.5°) between the second BDT and the second TDCl unit.

As depicted in the enlarged insets within **Figures 3-2b** and **f**, the vinyl group (C1=C2 or C1'=C2') and its connecting double bond (C3=C4 or C3'=C4') of the TDF or TDCl units adopt a trans-isomer structure. In the case of the di-BDT-TDF construct, the dihedral angles of C1-C2-C3-C4 and C1'-C2'-C3'-C4' within the two TDF units are found to be 170.54° and 171.32°, respectively. Notably, the corresponding dihedral angles within the TDCl units in di-BDT-TDCl are smaller, at 155.72° and 157.02°, respectively. This observation highlights that the difluorovinyl substituent aligns in a more coplanar manner with the connecting thiophene unit compared to the dichlorovinyl unit. This phenomenon can be explained by considering the larger size of chlorine atoms, which induces a more pronounced steric effect when compared to the smaller fluorine atoms. Intriguingly, the data suggests that a greater deviation of the dichlorovinyl substituent from the plane of its connecting thiophene unit results in a reduced steric effect with the neighboring BDT unit, leading to a more coplanar backbone for di-BDT-TDCl. Although relatively uncommon, similar conformational locking effects have been noted for sterically demanding substituents such as o-tolyl[115] and 2,6-bis(hexyloxy)phenyl.[116] These bulky substituents can effectively restrict the rotation of the polymer backbone, favoring a more coplanar conformation.

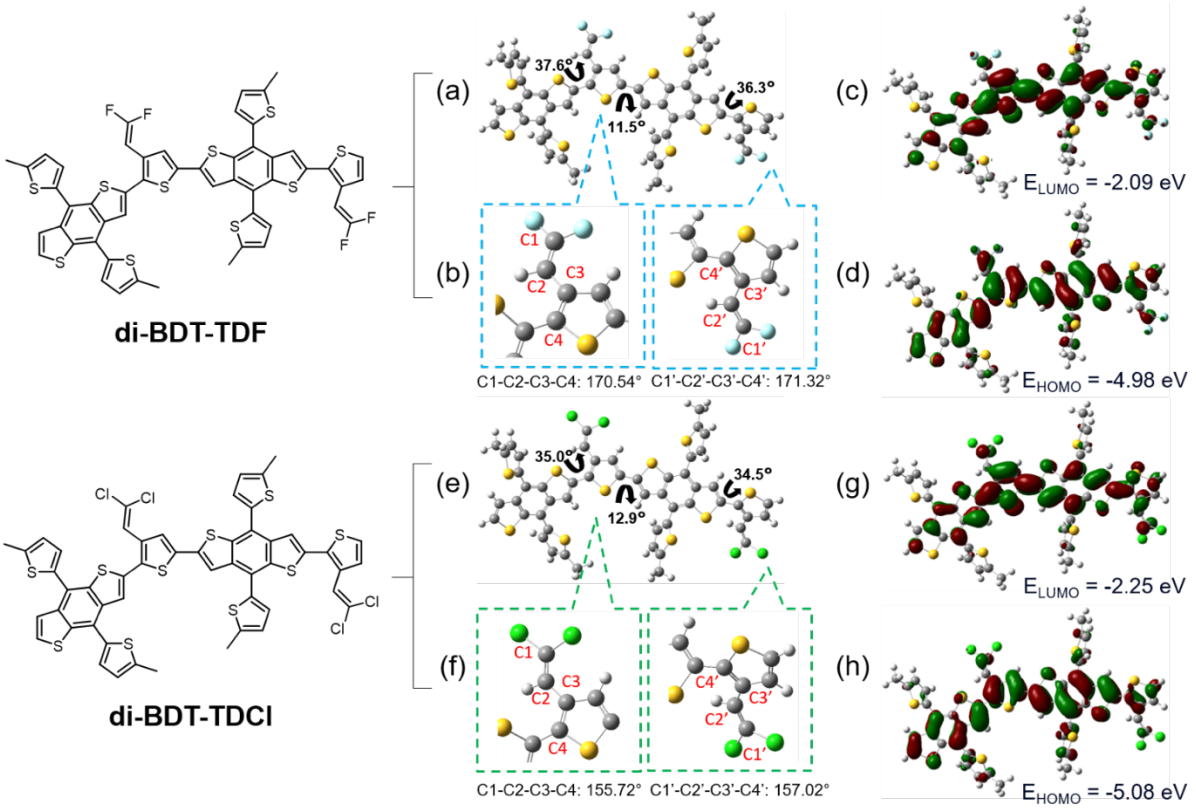


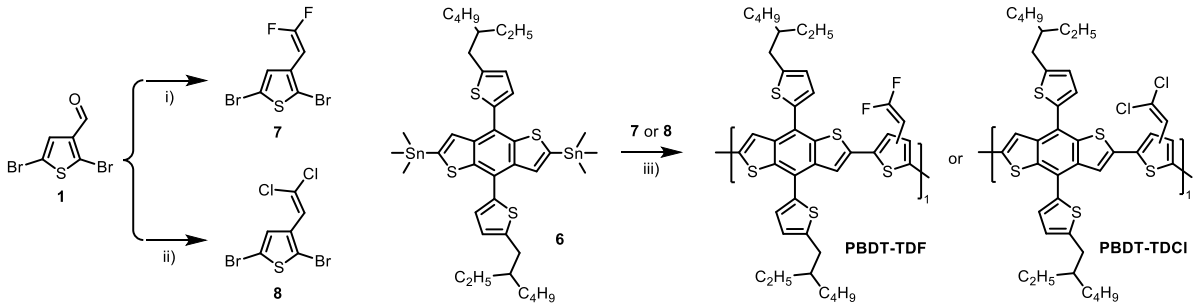
Figure 3-2. Simulation data from DFT analysis of di-BDT-TDF (a dimer of PBDT-TDF) and di-BDT-TDCl (a dimer of PBDT-TDCl): Molecular geometries (a, b, e, f), LUMOs (c, g), and HOMOs (d, h).

The calculated E_{HOMO}/E_{LUMO} values for di-BDT-TDF and di-BDT-TDCl are -4.98/-2.09 eV and -5.08/-2.25 eV, respectively, indicating that the dichlorovinyl group exhibits a stronger electron-withdrawing effect compared to the difluorovinyl group. The bandgap of di-BDT-TDF is 2.89 eV, which is larger than that of di-BDT-TDCl (2.83 eV), likely due to its more twisted backbone.

3.3 Synthesis of PBDT-TDX

PBDT-TDF and PBDT-TDCl were synthesized following the routes as illustrated in **Scheme 3-1**. While the syntheses of TDF-containing monomers, specifically 2,5-dibromo-3-(2,2-difluorovinyl)thiophene (**7**), and TDCl-containing monomer, 2,5-dibromo-3-(2,2-dichlorovinyl)thiophene (**8**), have not been documented, they can be readily prepared using well-established methods employed for synthesizing similar *gem*-dihalovinyl compounds.[117] Specifically,

compound **7** was conveniently synthesized using a classical Wittig approach.[118–120] Briefly, 2,5-dibromothiophene-3-carbaldehyde (**1**) was added dropwise to react with a fluorinated phosphonium ylide, which was generated *in situ* by reacting sodium 2-chloro-2,2-difluoroacetate with triphenylphosphine. The resulting crude product was purified using flash column chromatography on silica gel to afford the pure compound **7** in a good yield of 70%. Compound **8** was synthesized through a one-pot two-step process with a yield of 61%. The synthesis involved the reaction of compound **1** with hydrazine, forming a hydrazone intermediate. This intermediate was subsequently reacted with CCl_4 in the presence of a catalytic amount of Cu_2Cl_2.[121]



Scheme 3-1. Synthesis of PBDT-TDF and PBDT-TDCl: i) 2-chloro-2,2-difluoroacetate/PPh_3/DMF, 110 °C/2 h, 70% yield; ii) hydrazine/NH_4OH/Cu_2Cl_2/CCl_4/DMSO, r.t./7 h, 61% yield; iii) $Pd_2(dba)_3$/P(o-tolyl)$_3$/chlorobenzene, 90 °C/24 h, 99% (PBDT-TDF) and 99% (PBDT-TDCl) yields.

Polymerization between compound **7** or **8** and 2,6-bis(trimethytin)-4,8-bis(5-(2-ethylhexyl)thiophen-2-yl)benzo[1,2-b:4,5-b']dithiophene (**6**) using standard Stille coupling methods gave PBDT-TDF or PBDT-TDCl in quantitative yields (99%) after purification. The number average molecular weight (M_n), weight average molecular weight (M_w), and dispersity ($Đ$) of the polymers were measured by high-temperature gel-permeation chromatography (HT-GPC) using 1,2,4-trichlorobenzene as the eluent at 110 °C and the results are displayed in **Table 3-1**.

Table 3-1. GPC, UV-vis and CV data of PBDT-TDF and PBDT-TDCl.

Polymer	M_n, kDa	M_w, kDa	$Đ$	λ_{max}, nm (sol)	λ_{max}, nm (film)	E_g^{opt}, eV	E_{HOMO}, eV	E_{LUMO},[a] eV
PBDT-TDF	18.4	50.1	2.72	514	519	2.02	-5.62	-3.60
PBDT-TDCl	28.1	63.1	2.25	546	542	1.99	-5.48	-3.49

[a] $E_{LUMO} = E_{HOMO} + E_g^{opt}$

3.4 Characterization of PBDT-TDX

3.4.1 Thermal properties

To assess the thermal properties of PBDT-TDF and PBDT-TDCl, differential scanning calorimetry (DSC) measurements and thermogravimetric analysis (TGA) were carried out. The DSC thermograms of both polymers, as depicted in **Figure 3-3**, exhibit no discernible thermal transition, suggesting their amorphous nature. This observation was further confirmed through X-ray diffraction (XRD) measurements. The 5% weight loss temperatures of PBDT-TDF and PBDT-TDCl were determined to be 370 °C and 368 °C, respectively, from their TGA curves shown in **Figure 3-4**, indicating their good thermal stability.

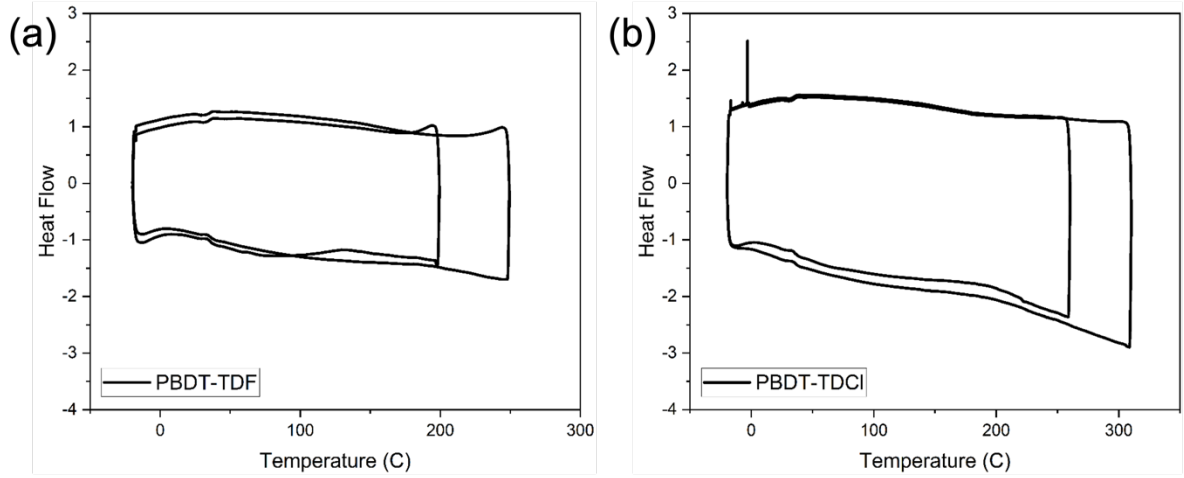


Figure 3-3. DSC curves of (a) PBDT-TDF and (b) PBDT-TDCl.

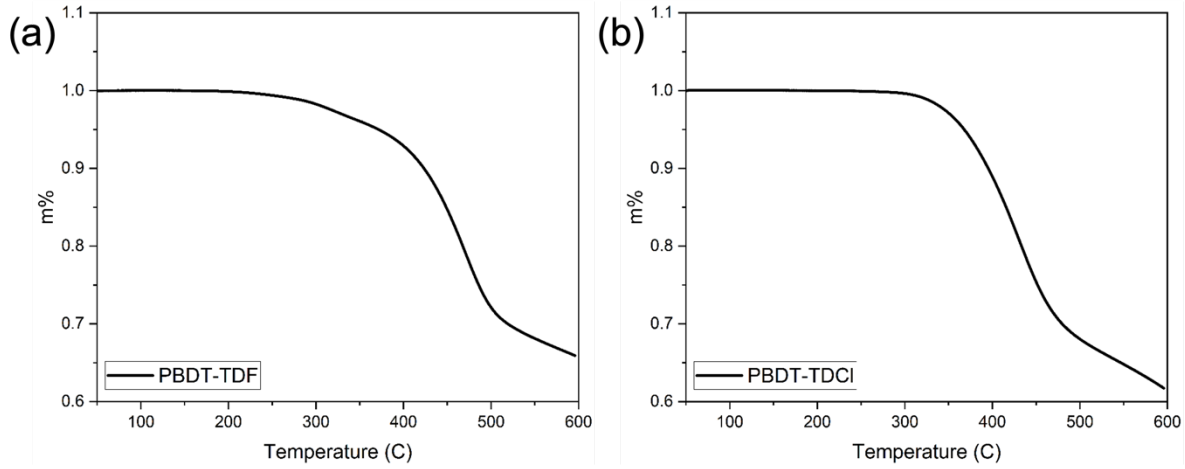


Figure 3-4. TGA curves of (a) PBDT-TDF and (b) PBDT-TDCl.

3.4.2 Optical and electrochemical properties

The light absorption characteristics of PBDT-TDF and PBDT-TDCl were determined by ultraviolet-visible (UV-Vis) spectroscopy (refer **Table 3-2** for detailed data). As depicted in **Figure 3-5a** and **Table 3-1**, the solution of PBDT-TDF in chloroform shows high and low absorption peaks at 352 nm and 514 nm, respectively, ascribed to the thienyl side chains of the BDT units and the π-π* transition of the polymer backbone, respectively.[57,96–98] A shoulder peak occurred at 546 nm beside the low energy absorption peak, attributed to the chain aggregation of PBDT-TDF in solution.[99,100] It was observed that PBDT-TDCl has very limited solubility in chloroform and other solvents. The dilute chloroform solution of PBDT-TDCl exhibits a high energy peak at 355 nm and a low energy peak at 546 nm, which occur at slightly longer wavelengths than those of PBDT-TDF. The molar absorption coefficient (ε) for the PBDT-TDF solution was found to be 0.35×10^5 M^{-1} cm^{-1} at λ_{max} = 514 nm, which is smaller than the value of 0.99×10^5 M^{-1} cm^{-1} at λ_{max} = 732 nm for the Y6 solution (**Table 3-2**). (The number of moles of the polymer was calculated using the molecular weight of the repeat unit.) Due to limited solubility, the PBDT-TDCl solution may contain significant chain aggregates, preventing the accurate determination of the molar absorption coefficient for PBDT-TDCl.

Compared with the solution, the PBDT-TDF film showed a 5 nm red shift in λ_{max} and an overall shift of the absorption spectrum towards longer wavelengths. The spectral red shift indicates more enhanced conjugation of the polymer backbone in the solid state for PBDT-TDF likely due to planarization of

the backbone and the presence of intermolecular interaction in the solid state. For the PBDT-TDCl film, while the long wavelength side of the spectrum slightly redshifted compared with the solution spectrum, a blue shift of 4 nm in λ_{max} was observed, which suggests that the polymer backbone was slightly more twisted or that H-aggregates formed in the solid state.[122–124] It is believed that this is related to the larger steric effect of the dichlorovinyl substituent in the TDCl unit. The optical bandgaps calculated from the absorption onset for PBDT-TDF and PBDT-TDCl films are 2.02 eV and 1.99 eV, respectively. The observed difference in bandgap between the two polymers, which amounts to 0.03 eV, is smaller than the value obtained from DFT simulations (0.06 eV). This disparity can primarily be attributed to the limited redshift observed in the film absorption spectrum of PBDT-TDCl, for reasons discussed above. The UV-vis profiles and wide bandgaps of PBDT-TDF and PBDT-TDCl are favorable to match with the narrow bandgap NFA such as Y6 to form a complementary absorption spectrum.

The absorption coefficients (α's) of PBDT-TDF and PBDT-TDCl thin films were determined to be 0.61×10^5 cm^{-1} at λ_{max} = 519 nm and 1.02×10^5 cm^{-1} at λ_{max} = 542 nm, respectively. Meanwhile, the absorption coefficient of the neat Y6 film was measured to be 1.06×10^5 cm^{-1} at λ_{max} = 820 nm. These findings indicate that PBDT-TDCl exhibits a stronger light-harvesting capability compared to PBDT-TDF and is close to that of Y6. The relatively modest absorption coefficient observed for PBDT-TDF is likely due to its more twisted backbone or shorter effective π-conjugation length.[125,126]

The UV-Vis absorption spectra of solutions and films for PBDT-TDF:Y6 and PBDT-TDCl:Y6 blends, with a D/A mass ratio of 1:1, are presented in **Figure 3-5b**. The PBDT-TDF:Y6 solution exhibits molar absorption coefficients of 0.43×10^5 M^{-1} cm^{-1} at λ_{max} = 513 nm (representing PBDT-TDF) and 1.25×10^5 M^{-1} cm^{-1} at λ_{max} = 733 nm (representing Y6). Compared to the pure PBDT-TDF solution ($\varepsilon = 0.35 \times 10^5$ M^{-1} cm^{-1}), the ε value at λ_{max} = 513 nm (representing PBDT-TDF) in the blend solution increased by 23%. This enhancement may stem from the contribution of Y6 absorption in this region. Interestingly, the molar absorption coefficient at λ_{max} = 733 nm (representing Y6) also significantly increased by 26% compared to the pure Y6 solution. Since there is no absorption by PBDT-TDF at this wavelength, the heightened light absorption of Y6 in the blend solution may result from interactions such as donor-acceptor interactions between Y6 and PBDT-TDCl. This interaction may also contribute to the increased molar absorption coefficient at λ_{max} = 513 nm.

As for the blend PBDT-TDCl:Y6 solution, the molar absorption coefficients are determined as 0.53 $\times 10^5$ M^{-1} cm^{-1} at λ_{max} = 550 nm (representing PBDT-TDCl) and 1.28×10^5 M^{-1} cm^{-1} at λ_{max} = 732 nm

(representing Y6). Although the absorption enhancement of PBDT-TDCl in the blend solution compared to the pure PBDT-TDCl solution cannot be assessed due to the unavailability of a fully dissolved PBDT-TDCl solution, a notable absorption enhancement (by 29%) of Y6 in the blend solution is observed. The pronounced promotion of PBDT-TDCl dissolution in the presence of Y6 indicates a robust interaction between Y6 and PBDT-TDCl, which leads to an augmentation in the light absorption of both Y6 and possibly PBDT-TDCl.

The PBDT-TDF:Y6 blend film exhibits absorption coefficients of 0.44×10^5 cm^{-1} at λ_{max} = 524 nm (representing PBDTT-TDF) and 0.63×10^5 cm^{-1} at λ_{max} = 811 nm (representing Y6). Considering that only 50% of the donor and acceptor are present in the blend films, their "actual" absorption coefficients of PBDT-TDF and Y6 in the blend films would be twice the above values, totaling 0.88×10^5 cm^{-1} and 1.26×10^5 cm^{-1}, respectively. These values increased by 44% and 19%, respectively, compared to their neat films. The PBDT-TDCl:Y6 blend film exhibits absorption coefficients at λ_{max} = 541 nm (representing PBDT-TDCl) and λ_{max} = 808 nm (representing Y6) are 0.60×10^5 cm^{-1} and 0.64×10^5 cm^{-1}, corresponding to the “actual” absorption coefficients of 1.20×10^5 cm^{-1} and 1.28×10^5 cm^{-1}, respectively. Similar to the PBDT-TDF:Y6 blend film, the absorption coefficients of PBDT-TDCl and Y6 in their blend film increased by 18% and 21%, respectively, compared to their neat films. Since PBDT-TDF and PBDT-TDCl films have weak absorption at the λ_{max} of the Y6 film, the absorption enhancement of Y6 in the blend films is also considered to be due to the interactions between Y6 and the donor polymer. Additionally, the Y6 phase could experience an augmentation in light absorption due to internal light scattering, further contributing to this phenomenon.[127] As for the increased absorption coefficients of PBDT-TDF and PBDT-TDCl in the blend films, besides the above two contributions, the absorption of Y6 in the donor absorption region is another contributor. Overall, PBDT-TDCl shows higher light harvesting ability than PBDT-TDF, which is beneficial for achieving high J_{sc} in OSC devices.

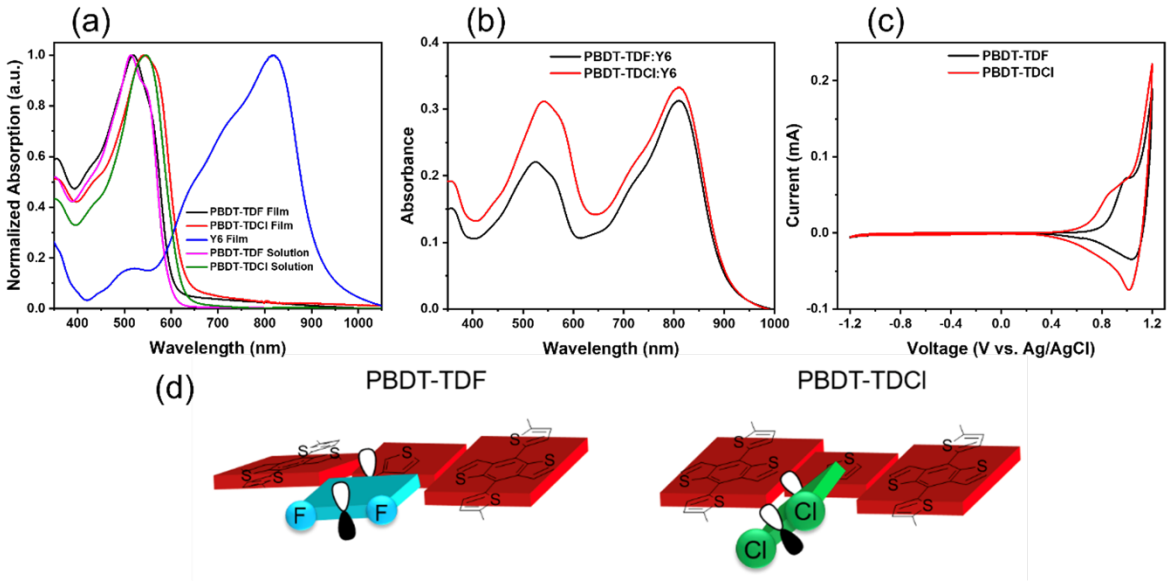


Figure 3-5. (a) Ultraviolet-visible absorption spectra of PBDT-TDF, PBDT-TDCl, Y6 in thin film states and in solution (chloroform), (b) UV-Vis spectra of blend PBDT-TDF:Y6 (w/w = 1:1), PBDT-TDCl:Y6 (w/w = 1:1) in thin film states and in solution (chloroform), (c) Cyclic voltammograms of PBDT-TDF and PBDT-TDCl films, and (d) illustrative conformational structures of PBDT-TDF and PBDT-TDCl, revealing that PBDT-TDF has relatively coplanar TDF units but a more twisted backbone, while PBDT-TDCl has more twisted TDCl units but a more coplanar backbone.

Table 3-2. Summary of UV-Vis spectroscopic data of PBDT-TDF, PBDT-TDCl, Y6, and PBDT-TDF:Y6, and PBDT-TDCl.

Material	**Solution (in chloroform)**		**Film**	
	$\lambda_{max,}$ ε (donor)	λ_{max} ε (acceptor)	λ_{max} α (donor)	λ_{max} α (acceptor)
PBDT-TDF	514nm 0.35×10^5 M^{-1} cm^{-1}		519nm 0.61×10^5 cm^{-1}	
PBDT-TDCl	546 nm n.d.		542nm 1.02×10^5 cm^{-1}	
Y6		732nm 0.99×10^5 $M^{-1}cm^{-1}$		820nm 1.06×10^5 cm^{-1}
PBDT-TDF:Y6 (1:1)	513nm 0.43×10^5 M^{-1} cm^{-1}	733nm 1.25×10^5 M^{-1} cm^{-1}	524nm 0.44×10^5 cm^{-1} (0.88×10^5 cm^{-1})	811nm 0.63×10^5 cm^{-1} (1.28×10^5 cm^{-1})
PBDT-TDF:Y6 (1:1)	550nm 0.53×10^5 M^{-1} cm^{-1}	732nm 1.28×10^5 M^{-1} cm^{-1}	541nm 0.60×10^5 cm^{-1} [a] (1.20×10^5 cm^{-1})[b]	808nm 0.64×10^5 cm^{-1} [a] (1.28×10^5 cm^{-1})[b]

[a] Calculated based on the blend film thickness.

[b] Calculated based on 50% of the blend film thickness, which is approximately the actual thickness of the donor or acceptor in the blend film.

Cyclic voltammetry (CV) measurements were carried out to determine the energy levels of PBDT-TDF and PBDT-TDCl. **Figure 3-5c** illustrates the CV results, showing that the oxidation onset potential of PBDT-TDF relative to the Ag/AgCl couple is 0.82 V, corresponding to an E_{HOMO} of -5.62 eV. No reduction peak was observed, so the E_{LUMO} of PBDT-TDF was calculated as the sum of the optical bandgap and the E_{HOMO}, which is -3.60 eV. Similarly, the E_{HOMO} and E_{LUMO} of PBDT-TDCl were calculated to be -5.48 eV and -3.49 eV, respectively.

However, these results diverge from the findings obtained through DFT simulations, initially suggesting that the FMO energy levels of PBDT-TDCl were lower compared to those of PBDT-TDF (as depicted in **Figure 3-2**). These substantial discrepancies can be attributed once again to the steric hindrance experienced by the dichlorovinyl group in PBDT-TDCl. Specifically, the presence of the sterically demanding dichlorovinyl substituent leads to increased torsion against the connecting thiophene unit. Conversely, the smaller difluorovinyl substituent exhibits a higher propensity to adopt a coplanar orientation with the connecting thiophene, as indicated by the DFT simulation results (**Figure 3-2**), and this tendency could be further enhanced in the solid state. This coplanar arrangement between the difluorovinyl group and the thiophene unit facilitates the efficient electron-withdrawing effect of the difluorovinyl group on the polymer backbone. In summary, PBDT-TDF features more coplanar TDF units but a more twisted backbone, while PBDT-TDCl possesses a more coplanar backbone but more twisted TDCl units as illustrated in **Figure 3-5d**. As a consequence, PBDT-TDF is characterized by greater electron deficiency and a less conjugated backbone, while PBDT-TDCl displays reduced electron deficiency and a more coplanar backbone.

3.4.3 I-V Characterization

Both *gem*-dihalovinyl thiophene based polymers were evaluated as channel semiconductors in BGBC devices. All OTFT devices with PBDT-TDF or PBDT-TDCl film showed typical p-type dominant field effect transistor performance (**Figure 3-6** and **Figure 3-7**, **Table 3-3** and **Table 3-4**). The J_{sc} is influenced by the charge transport of free carriers generated by the exciton dissociation of excitons at the donor/acceptor interface. Efficient transport of these hole and electron charge carriers traveled through the active layer phase to the electrodes, is crucial for achieving a high J_{sc}. The non-annealed PBDT-TDF film, utilized as the active layer in an OTFT device, exhibited a hole mobility of up to 2.60×10^{-3} cm^2 V^{-1} s^{-1} (**Table 3-3**). With increasing annealing temperature, the hole mobility gradually decreased. At an annealing temperature of 200 °C, the mobility dropped to 8.72×10^{-4} cm^2 V^{-1} s^{-1}. Conversely, the non-annealed PBDT-TDCl film displayed a hole mobility of 3.96×10^{-3} cm^2 V^{-1} s^{-1}, which increased with annealing temperature (**Table 3-4**). At an annealing temperature of 200°C, a high mobility of 5.56×10^{-3} cm^2 V^{-1} s^{-1} was achieved. At an annealing temperature of 100 °C, which is the same annealing temperature for fabricating the OSC active layer, PBDT-TDF and PBDT-TDCl exhibited hole mobilities of 1.63×10^{-3} cm^2 V^{-1} s^{-1} and 3.96×10^{-3} cm^2 V^{-1} s^{-1} in OTFTs, respectively.

These findings indicate that hole transport in PBDT-TDCl is considerably more efficient than in PBDT-TDF. As previously mentioned, the inclusion of the TDF unit induces greater twisting of the polymer backbone, impeding the intramolecular charge transport in PBDT-TDF.

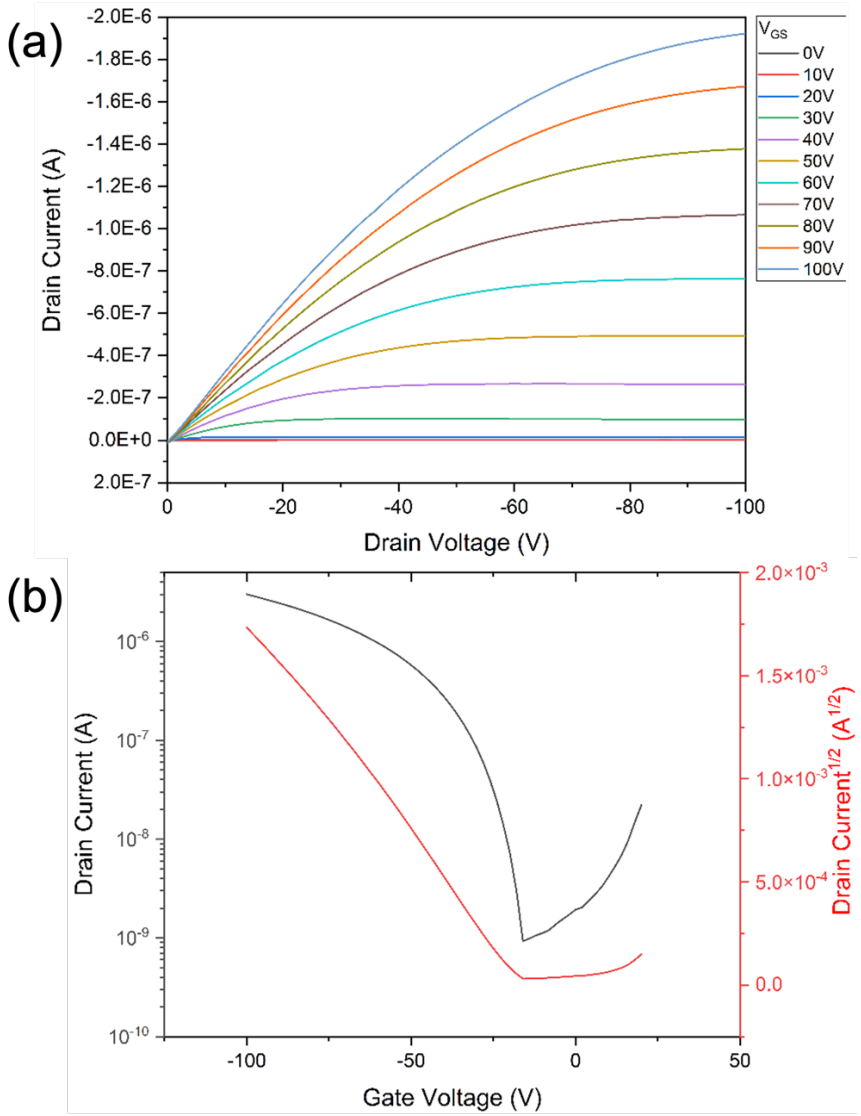


Figure 3-6. (a) Output and (b) transfer (V_{DS} = -100 V) characteristics of a representative OTFT device using PBDT-TDF without annealing (room temperature).

Table 3-3. OTFT properties of PBDT-TDF.

Temperature, °C	**Best mobility, $cm^2V^{-1}s^{-1}$**	**Avg. mobility, $cm^2V^{-1}s^{-1}$**	**Avg. I_{on}/I_{off}**	**Avg V_{th}, V**
RT	2.60×10^{-3}	$2.15\times10^{-3}\pm4.02\times10^{-4}$	2800	-17.04±2.50
50	2.41×10^{-3}	$1.93\times10^{-3}\pm3.26\times10^{-4}$	1000	-12.97±5.55
100	1.63×10^{-3}	$1.17\times10^{-3}\pm5.25\times10^{-4}$	1000	-4.86±6.53
150	1.61×10^{-3}	$9.22\times10^{-4}\pm5.44\times10^{-4}$	1000	-4.55±8.30
200	8.72×10^{-4}	$6.52\times10^{-4}\pm2.42\times10^{-4}$	1000	-12.97±5.55

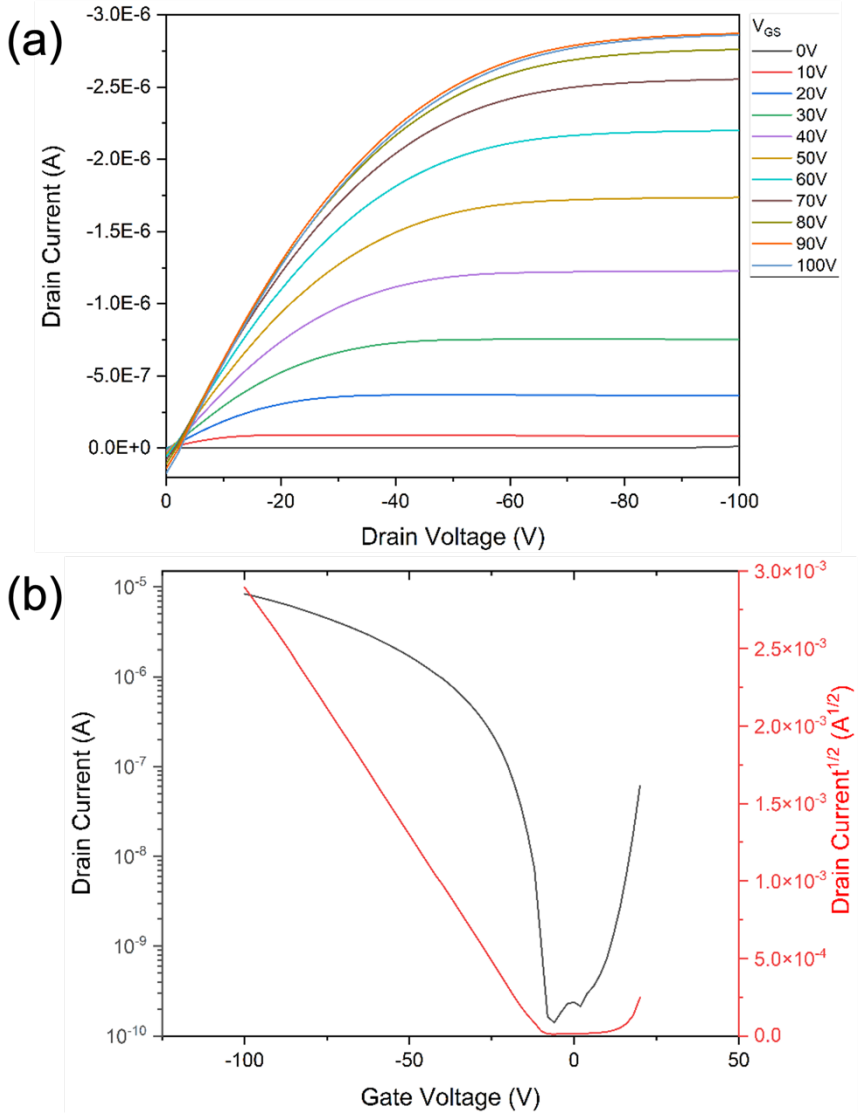


Figure 3-7. (a) Output and (b) transfer (V_{DS} = -100 V) characteristics of a representative OTFT device using PBDT-TDCl with an annealing temperature of 200 °C.

Table 3-4. OTFT properties of PBDT-TDCl.

Temperature, °C	Best mobility, $cm^2V^{-1}s^{-1}$	Avg. mobility, $cm^2V^{-1}s^{-1}$	Avg. I_{on}/I_{off}	Avg. V_{th}, V
RT	3.96×10^{-3}	$3.74\times10^{-3}\pm2.63\times10^{-4}$	10000	2.78±1.29
50	4.35×10^{-3}	$4.07\times10^{-3}\pm3.23\times10^{-4}$	10000	0.24±1.34
100	5.37×10^{-3}	$4.98\times10^{-3}\pm3.77\times10^{-4}$	40000	-3.71±2.56
150	5.48×10^{-3}	$5.16\times10^{-3}\pm3.96\times10^{-4}$	40000	-7.91±0.99
200	5.56×10^{-3}	$5.53\times10^{-3}\pm4.46\times10^{-5}$	70000	-9.98±0.54

3.4.4 Photovoltaic performance

The photovoltaic performance of PBDT-TDF and PBDT-TDCl was evaluated in inverted structural devices comprising ITO/ZnO (35 nm)/active layer/MoO_3 (10 nm)/Ag (100 nm) (**Figure 3-8a**). The active layer consisted of a blend of the polymer donor PBDT-TDF or PBDT-TDCl and the acceptor Y6. Several factors were examined, including the donor-acceptor ratio, spin-coating rate, active layer thickness, thermal annealing temperature, and solvent additives. The corresponding photovoltaic characteristics are detailed in **Tables 3-7** to **3-11**. It was found that devices fabricated with a donor-acceptor mass ratio of 1:1, an active-layer thickness of ~100 nm for PBDT-TDF:Y6, and ~140 nm for PBDT-TDCl:Y6, along with annealing conducted at 100 °C, demonstrated the highest PCE values. The OSC parameters of devices fabricated under optimized conditions are summarized in **Table 3-5** and the current density-voltage (*J-V*) curves of the best performing devices are shown in **Figure 3-8b**. The PBDT-TDF-based devices achieved a maximum PCE of 8.83%, characterized by a V_{oc} of 0.77 V, a J_{sc} of 20.54 mA cm^{-2}, and a FF of 0.56. On the other hand, the devices utilizing PBDT-TDCl demonstrated the highest PCE of 11.02% with V_{oc} = 0.71 V, J_{sc} = 25.95 mA cm^{-2}, and FF = 0.60. The J_{sc} of the PBDT-TDCl-based device is comparable to or even higher than that of OSCs utilizing Y6 with other wide bandgap polymers such as PM6.[107] However, the V_{oc} and FF of our devices fall considerably short in comparison.

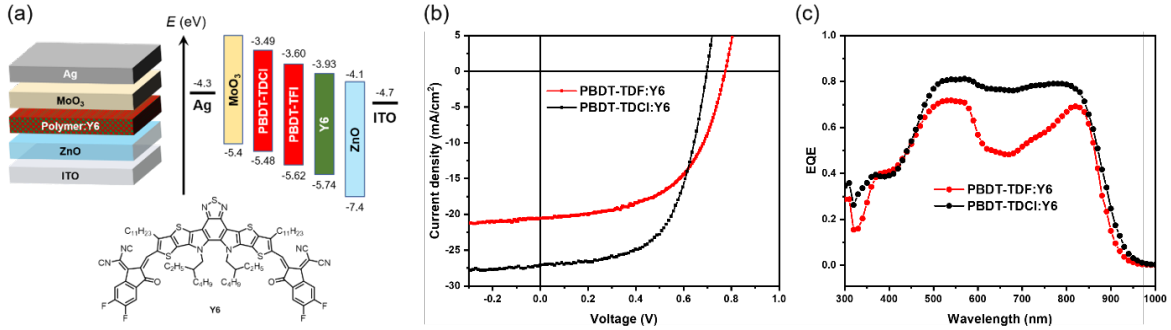


Figure 3-8. (a) The inverted architecture of an OSC device, energy diagram of key materials, and chemical structure of Y6, (b) *J-V* curves, and (c) EQE curves of PBDT-TDF and PBDT-TDCl-based devices.

Table 3-5. Photovoltaic performance of PBDT-TDF:Y6 and PBDT-TDCl:Y6 based devices.

Active layer	J_{sc},[a] mA cm^{-2}	V_{oc},[a] V	FF[a]	PCE,[a] %
PBDT-TDF:Y6	20.54[b] (20.46 ± 1.26)[b]	0.77 (0.77 ± 0.01)	0.56 (0.54 ± 0.04)	8.83 (8.42 ± 0.31)
PBDT-TDCl:Y6	25.95[c] (25.62 ± 0.53)[c]	0.71 (0.70 ± 0.01)	0.60 (0.59 ± 0.02)	11.02 (10.54 ± 0.41)

[a] Maximum value (average value ± standard deviation) from at least 5 devices.

[b] Integrated J_{sc} from the EQE spectrum in **Figure 3-8c**: 18.87 mA cm^{-2}.

[c] Integrated J_{sc} from the EQE spectrum in **Figure 3-8c**: 23.99 mA cm^{-2}.

The energy loss (E_{loss}) of the devices was calculated using $E_{loss} = E_{gap}/q - V_{oc}$, where E_{gap} is the lowest optical bandgap among the donor and acceptor components (the bandgap of Y6 is 1.33 eV) and q is the elementary charge.[99,101,102] The device based on PBDT-TDF:Y6 demonstrates a lower E_{loss} of 0.56 eV compared to the PBDT-TDCl:Y6-based device, which has an E_{loss} of 0.62 eV. The E_{loss} values of both solar cells are comparable to those of other high-performing NFA-based OSCs, which typically exhibit E_{loss} values of ca. 0.5-0.6 eV.[57,128–130] It is important to note that energy loss is contributed by both charge generation and radiative/non-radiative charge recombination.[130] For narrow bandgap NFA-based OSCs, the energy loss due to charge generation is the energy difference between the HOMO energy level and the charge transfer (CT) state energy level, which is approximately the HOMO energy difference between the donor and acceptor, $E_{HOMO}(D) - E_{HOMO}(A)$. After excluding their charge generation energy losses (0.12 eV for PBDT-TDF:Y6 and 0.26 eV for PBDT-TDCl:Y6), the

recombination energy losses are calculated to be 0.44 eV for PBDT-TDF:Y6 and 0.36 eV for PBDT-TDCl:Y6, respectively. In particular, the recombination energy loss for the PBDT-TDCl:Y6-based device is the same as that (0.35 eV) of the PM6:Y6 device (with a V_{oc} of 0.82 V).[107] The large energy loss of the former is mainly attributed to the charge generation loss, which is due to the unnecessarily higher HOMO energy level of PBDT-TDCl. Therefore, further decreasing the HOMO energy level of this polymer can potentially reduce the energy loss and increase the V_{oc}.

The external quantum efficiency (EQE) curves of the PBDT-TDF:Y6 and PBDT-TDCl:Y6 devices exhibit high efficiency in the wavelength range of ~500-850 nm (**Figure 3-8c**). The EQE curve of the PBDT-TDF-based device displays two prominent peaks (~70%) at 540 nm and 850 nm, corresponding to the absorption peaks of the PBDT-TDF donor and Y6 acceptor, respectively. A valley with lower efficiency (~50%) between these two peaks is observed. In contrast, the EQE of the PBDT-TDCl-based device maintains high (>70%) across the 500 nm to 850 nm range, with a maximum peak of 81.2% at 570 nm. The much higher EQE values explain the higher J_{sc} achieved by the PBDT-TDCl-based device compared to the PBDT-TDF-based device in the *J-V* curve. Consequently, the PCE of the PBDT-TDCl-based devices surpasses that of the PBDT-TDF-based devices. From the EQE curves of PBDT-TDF:Y6 based and PBDT-TDCl:Y6 based OSC devices, the integrated J_{sc} values were calculated to be 18.87 and 23.99 mA cm^{-2}, respectively, which are 8.5% and 7.8% lower compared to J_{sc} obtained from their *J-V* curves.

The significantly lower overall EQE of the PBDT-TDF:Y6-based solar cell, in comparison to the PBDT-TDCl:Y6-based cell, can largely be ascribed to the thinner active layer of PBDT-TDF:Y6 (approximately 100 nm) compared to PBDT-TDCl:Y6 (approximately 140 nm). Considering that the donor and acceptor have the same density and that light traverses through the active layer and is reflected by the Al cathode layer, the total light travel distance in the donor or acceptor phase would be the same as the active layer thickness. Using the absorption coefficients of the blend films determined earlier, the percent absorptivity values were computed at λ_{max}. In the PBDT-TDF:Y6 active layer, the percent absorptivity at λ_{max} is 86.9% for the PBDT-TDF phase (which includes some contribution from Y6) and 94.9% for the Y6 phase. For the PBDT-TDCl:Y6 active layer, the corresponding values were 97.9% for the PBDT-TDCl phase (with some contribution from Y6) and 98.6% for the Y6 phase. When comparing these values with the EQE_{max} values in the vicinity of the donor's λ_{max}, which are 71.8% for PBDT-TDF in the PBDT-TDF:Y6 active layer and 81.2% for PBDT-TDCl in the PBDT-TDCl:Y6 active layer, it appears that the lower EQE of PBDT-TDF is primarily due to its lower thickness

compared to PBDT-TDCl. However, it is noteworthy that the significant difference in EQE_{max} (9.8%) of the Y6 phase in the two active layers, 69.2% in PBDT-TDF:Y6 and 79.0% in PBDT-TDCl:Y6, cannot be attributed solely to the difference in their absorptivity values, which is only 3.7%.

To further investigate the factors contributing to the different J_{sc} values of the PBDT-TDCl:Y6 and PBDT-TDCl devices, photoluminescence (PL) quenching measurements were conducted to assess the effectiveness of exciton diffusion and dissociation within the BHJ active layer. The PL spectra of neat films of PBDT-TDF and Y6, as depicted in **Figures 3-9a** and **c**, exhibit peaks in the ranges of 600 - 800 nm and 800 - 950 nm, respectively. In the case of the blend film of PBDT-TDF:Y6, a high PL quenching efficiency of 96.8% was observed for the PBDT-TDF phase, indicating efficient exciton diffusion in the donor phase and exciton dissociation at the donor-acceptor interface.[103] The PL quenching in the acceptor phase was also significant, reaching an efficiency of 97.8%. The high quenching efficiency observed suggests that exciton diffusion within the Y6 phase and subsequent exciton dissociation at the interface between the acceptor and the donor are also highly efficient. Similar to PBDT-TDF, the neat PBDT-TDCl also exhibits photoluminescence in the region of 600 - 800 nm. The blend film of PBDT-TDCl:Y6 exhibits high quenching efficiencies in the donor and acceptor phases, measured at 95.2% and 91.5%, respectively, also indicating favorable exciton diffusion and dissociation processes. It is noteworthy that the quenching efficiencies in the PBDT-TDF:Y6 blend film are higher than those in the PBDT-TDCl:Y6 blend film. Therefore, it appears that the lower J_{sc} observed in the PBDT-TDF:Y6-based devices compared to the PBDT-TDCl:Y6-based devices cannot be attributed to inefficient exciton diffusion and/or dissociation in the blend active layer.

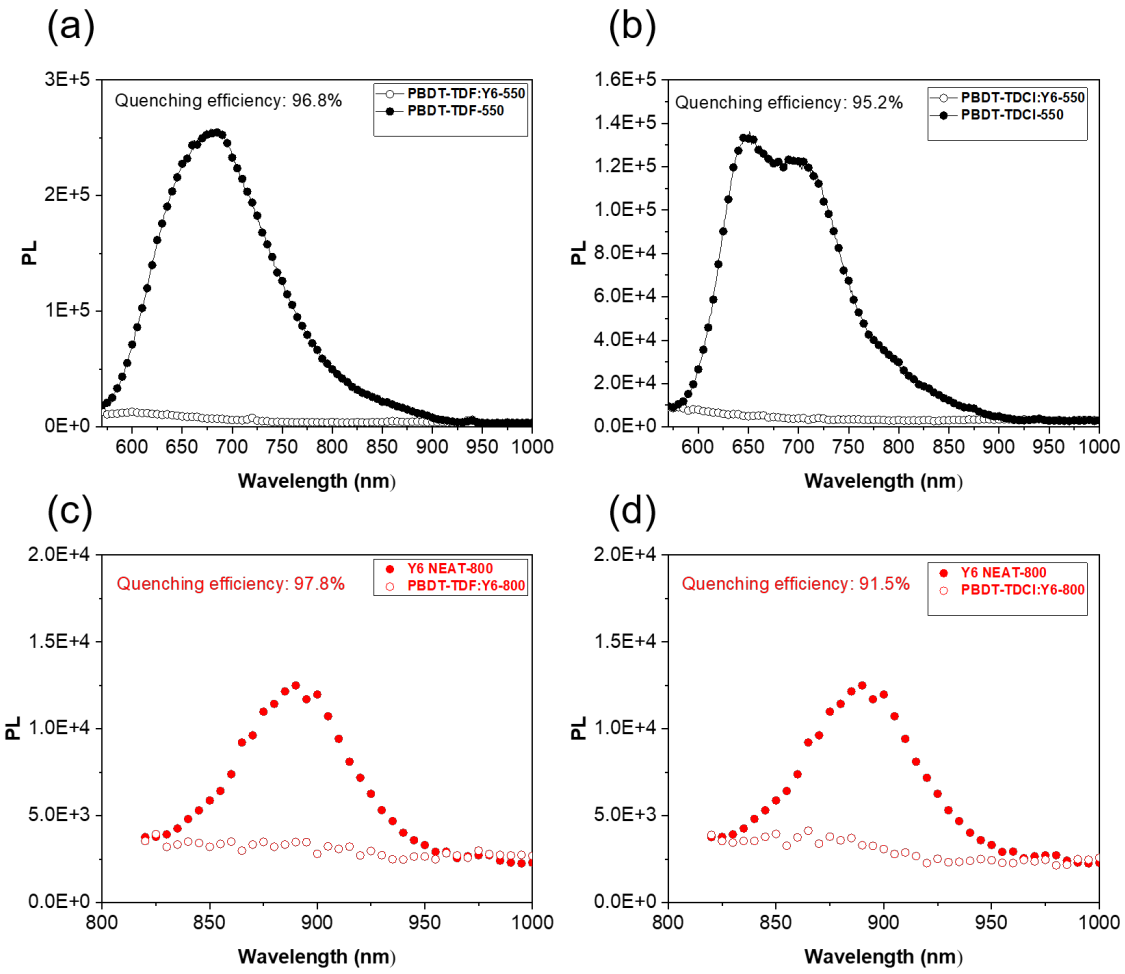


Figure 3-9. Photoluminescence (PL) quenching data for neat and blend films of PBDT-TDF (a, c) and PBDT-TDCl (b, d) on glass substrates. The excitation wavelength was set at 550 nm for the donor and 800 nm for the acceptor.

The hole and electron mobilities of the blend films along the direction normal to the substrate were obtained SCLC method. As depicted in **Table 3-6**, the average hole and electron mobilities of the PBDT-TDF:Y6 device are 2.76×10^{-4} cm^2 V^{-1} s^{-1} and 8.20×10^{-5} cm^2 V^{-1} s^{-1}, respectively, with an average μ_h/μ_e ratio of 3.37. While in the PBDT-TDCl:Y6 device, the average hole and electron mobilities are 4.46×10^{-4} cm^2 V^{-1} s^{-1} and 1.48×10^{-4} cm^2 V^{-1} s^{-1}, respectively, with an average μ_h/μ_e ratio of 3.95. The average SCLC hole mobility of the neat PBDT-TDF film was measured to be 1.84×10^{-4} cm^2 V^{-1} s^{-1}, which is lower than the value observed in the blend film. This suggests that the presence of the small molecule Y6 can promote charge transport of PBDT-TDF, a phenomenon observed in other

systems as well.[131] On the other hand, the quality of the neat PBDT-TDCl film is too poor to measure its SCLC mobility, due to the poor solubility of this polymer. It is worth noting that the solubility of PBDT-TDCl was significantly improved in the presence of Y6, probably due to their strong interaction in the solution, enabling the fabrication of high-quality blend films. Based on the above results, it appears that the higher SCLC hole and electron mobilities in the PBDT-TDCl:Y6 blend film, particularly the higher electron mobility, can be attributed to the higher EQE and J_{sc} observed in the OSC devices. In addition, the higher FF observed for the PBDT-TDCl:Y6-based devices is also, in part, due to the high hole and electron mobilities in the PBDT-TDCl:Y6 blend film.[47,48,105]

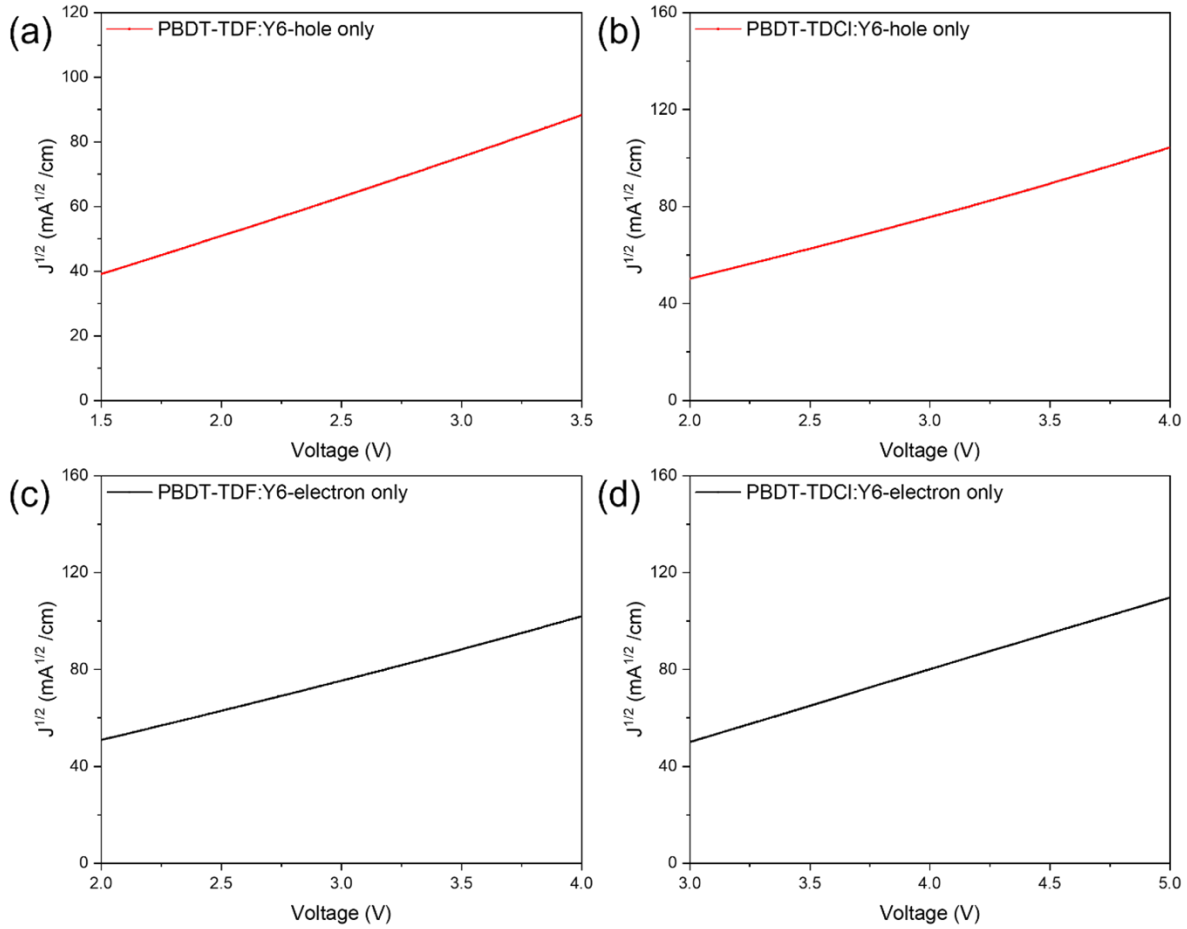


Figure 3-10. $J^{1/2}$-V curves of hole-only (a and b) and electron-only (c and d) devices of PBDT-TDF:Y6 and PBDT-TDCl:Y6 by fitting the modified Mott-Gurney equation: $J = 9\varepsilon_0\varepsilon_r\mu V^2/8L^3$, where ε_0 is the permittivity of the free space (8.8542×10^{-12} $CV^{-1}m^{-1}$), ε_r is the active layer electric constant, μ is the carrier mobility and L is active layer thickness.

Table 3-6. SCLC mobility data of PBDT-TDF and PBDT-TDCl.

	Electron mobility, $cm^2 V^{-1} s^{-1}$		Hole mobility, $cm^2 V^{-1} s^{-1}$	
	Maximum	**Average [SD][a]**	**Maximum**	**Average [SD][a]**
PBDT-TDF:Y6	2.94×10^{-4}	8.20×10^{-5} [7.62×10^{-5}]	4.52×10^{-4}	2.76×10^{-4} [9.00×10^{-5}]
PBDT-TDCl:Y6	1.55×10^{-4}	1.48×10^{-4} [8.02×10^{-6}]	6.13×10^{-4}	4.46×10^{-4} [1.67×10^{-4}]
Neat PBDT-TDF	-	-	3.95×10^{-4}	1.84×10^{-4} [9.62×10^{-5}]
Neat PBDT-TDCl	-	-	-[b]	-[b]

[a] SD: Standard deviation from at least 4 devices.

[b] Data is not available due to the limited solubility of neat PBDT-TDCl, leading to the inability to fabricate operational SCLC devices.

3.4.5 Film morphology and microstructure

The performance of OSCs is critically influenced by the morphology of the active layer. The morphological feature of the blend films of PBDT-TDF:Y6 and PBDT-TDCl:Y6 was examined using atomic force microscopy (AFM). Height images in **Figures 3-11a** and **3-11c** reveal that the PBDT-TDF:Y6 film exhibits a smooth surface morphology with a low root-mean square roughness (RMS) of 0.8 nm, while the PBDT-TDCl:Y6 blend film shows slightly increased roughness with an RMS of 1.2 nm. Notably, the PBDT-TDCl film comprises smaller grains that are well-interconnected. **Figures 3-11b** and **3-11d** displays the AFM phase images of the two blend films, clearly illustrating that the PBDT-TDCl:Y6 film exhibits a significantly finer and more uniform phase separation compared to the PBDT-TDF:Y6 film. The higher film quality of PBDT-TDCl:Y6 may contribute to its enhanced charge carrier mobilities.

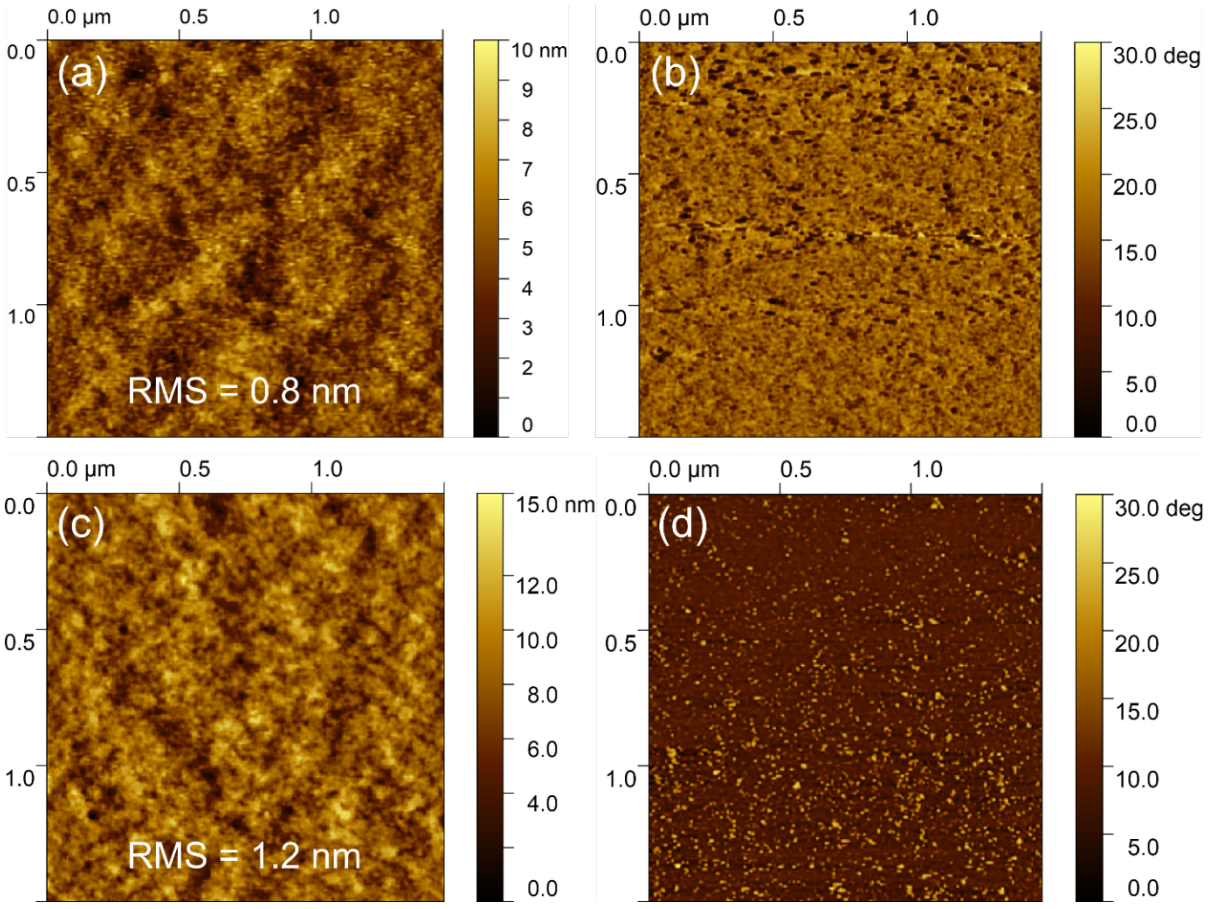


Figure 3-11. AFM height and phase images of blend films based on PBDT-TDF:Y6 (a, b) and PBDT-TDCl:Y6 (c, d).

To investigate the microstructure of the neat and blend polymer films, two-dimensional grazing incidence X-ray diffraction (2D-GIXD) patterns were measured. **Figures 3-12a** and **3-12b** show the out-of-plane (OOP) and in-plane (IP) X-ray diffraction patterns of the neat PBDT-TDF thin film samples. The as-spun PBDT-TDF film showed featureless diffraction patterns in both IP and OOP directions, indicating the highly disordered chain packing in this film. As the film was annealed at 50 °C, a weak diffraction peak at 2θ = ~2.65° appeared in the OOP direction. This peak corresponds to the (100) planes with a d-spacing of 3.33 nm of a layer-by-layer lamellar chain packing pattern. With further increasing the annealing temperature, the (100) peak intensified, and for the 200 °C-annealed film, the 2θ shifted to 3.00°, corresponding to a d-spacing of 2.94 nm. As for the IP direction, only the PBDT-TDF film annealed at 100°C showed a broad peak at 2θ = ~23° in the IP direction and also in

the OOP direction, which may be assigned to the (010) planes along the π-π stacking direction with a d-spacing of 0.387 nm.

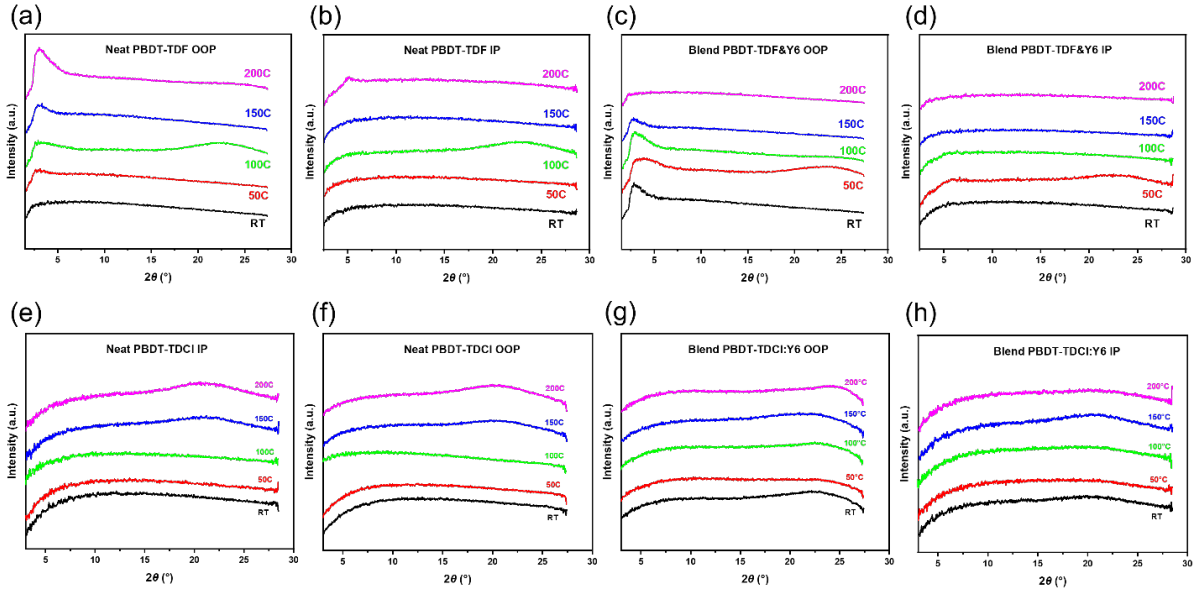


Figure 3-12. Out-of-plane (OOP) and in-plane (IP) 2D-GIXD patterns of neat film PBDT-TDF (a, b), neat film PBDT-TDCl (e, f), blend film PBDT-TDF:Y6 (c, d) and blend film PBDT-TDCl:Y6 (g, h) without annealing (RT) and annealed at different temperatures.

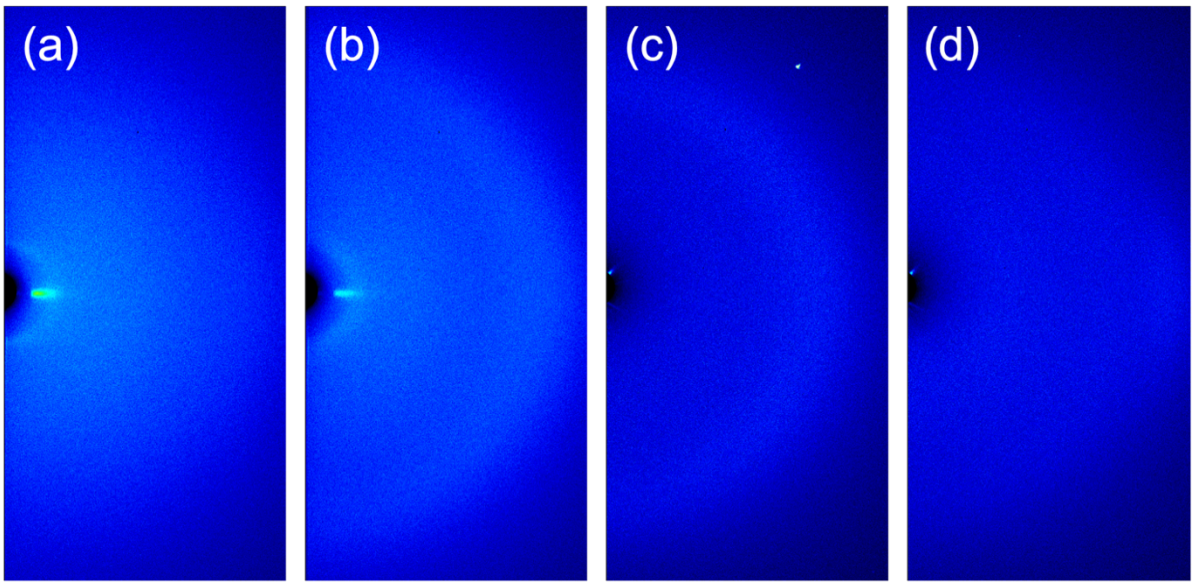


Figure 3-13. 2D XRD images for thin films of (a) PBDT-TDF annealed at 200 °C, (b) PBDT-TDF:Y6 annealed at 50 °C, (c) PBDT-TDCl annealed at 200 °C and (d) PBDT-TDCl:Y6 annealed at 200 °C.

As shown in **Figures 3-12c** and **3-12d**, in the OOP direction, the as-spun blend film showed a peak at 2.75° (d = 3.21 nm), which represents the (100) lamellar planes. Upon annealing, the (100) peak in the film initially intensified, reaching its maximum intensity at an annealing temperature of 100 °C. Subsequently, it weakened at 150 °C and eventually disappeared entirely at 200 °C. Additionally, the position of this peak exhibited a shifting pattern, starting at a higher diffraction angle of 3.12° (d = 2.83 nm) at 50 °C. As the annealing temperature increased, the diffraction angle progressively decreased to 2.88° (d = 3.07 nm) at 100 °C and further to 2.71° (d = 3.26 nm) at 150 °C.

Regarding the IP direction in the PBDT-TDF:Y6 blend film, a broad (010) peak at ~23° (d = ~0.387 nm) was observed only for the sample annealed at 50 °C. In addition, a (010) peak was also present in the OOP direction. Interestingly, similar to the neat PBDT-TDF film annealed at 100 °C, it appears that π-π stacking is enhanced at this particular annealing temperature. As illustrated in **Figures 3-12 e-h**, no discernible (100) peak was observed in either the OOP direction or the IP direction for both the neat PBDT-TDCl film and the PBDT-TDCl:Y6 blend film across all annealing temperatures. This observation suggests the absence of organized lamellar packing within the polymer phase. However, compared to the PBDT-TDF or PBDT-TDF:Y6 films, noticeable (010) diffraction peaks were observed for these samples under several annealing temperatures. Specifically, in the case of the PBDT-TDCl:Y6

sample, the presence of a (010) peak along the OOP direction was observed at most of the annealing temperatures, with the exception of 50°C (**Figure 3-12h**). The formation of π-π stacks in the OOP direction is widely recognized as essential for facilitating efficient charge transport in OSCs. The microstructure of the PBDT-TDCl phase observed in the PBDT-TDCl:Y6-based devices could provide significant advantages in achieving high J_{sc}. Nonetheless, both the PBDT-TDF:Y6 and PBDT-TDCl:Y6 systems exhibited low crystallinity, suggesting that there was no excessive growth of either the polymer phase or the Y6 phase that could hinder exciton diffusion. This observation aligns with the results obtained from PL quenching measurements. However, it is worth noting that the limiting factor for the photovoltaic performance (FF and J_{sc}) in both systems appears to be the relatively low electron mobility. This is underscored by the observation that the SCLC electron mobility of Y6 in these systems is limited to only up to 1.5×10^{-4} cm^2 V^{-1} s^{-1}, whereas literature reports indicate that it can reach ca. 10^{-3} cm^2 V^{-1} s^{-1}.[113] Hence, to enhance the solar cell performance, particularly the FF, of these two polymer systems, it is crucial to improve the electron mobility beyond the threshold 4×10^{-4} cm^2 V^{-1} s^{-1}, as established by prior studies.[48] This can be accomplished through meticulous optimization of the film processing conditions to improve the crystallinity and connectivity of the acceptor phase.[132–134] The FF can also be enhanced by other strategies,[105,135] such as improving the interfacial contacts[136,137] and choosing NFAs with high dielectric constant.[138] Furthermore, to achieve higher V_{oc} in OSC devices, the HOMO energy level of PBDT-TDCl can be further reduced by choosing other donor units or by selecting alternative acceptor materials with higher LUMO energy levels.

3.5 Conclusion

To summarize, we have successfully developed two novel *gem*-dihalovinyl thiophene-based weak electron-accepting building blocks, namely 3-(2,2-difluorovinyl)thiophene (TDF) and 3-(2,2-dichlorovinyl)thiophene (TDCl), using straightforward synthetic methods. These building blocks have been employed to create two structurally simple and potentially cost-effective wide bandgap polymer donors for high-performance organic solar cells (OSCs) based on non-fullerene acceptors (NFAs). The polymer PBDT-TDF, synthesized using benzodithiophene (BDT) as the donor unit and TDF as the acceptor unit, exhibited an E_{HOMO} of -5.62 eV, an E_{LUMO} of -3.60 eV, and a wide E_g of 2.02 eV. These energy levels were well-matched with the NFA Y6, ensuring efficient light harvesting and energy level alignment. OSC devices based on the PBDT-TDF:Y6 blend showed a PCE of 8.83%. Another polymer,

PBDT-TDCl, composed of BDT and TDCl building blocks, displayed a wide bandgap of 1.99 eV, an E_{HOMO} of -5.48 eV, and an E_{LUMO} of -3.49 eV. The PBDT-TDCl:Y6 blend-based OSC devices achieved a significantly higher PCE of 11.02%, primarily attributed to the enhanced J_{sc} of 25.95 mA cm^{-2}. The improved charge transport ability in the PBDT-TDCl:Y6 blend film played a crucial role in enhancing the overall solar cell performance. A noteworthy discovery is that the bulkier dichlorovinyl group appears to induce a conformational locking effect, resulting in a more coplanar polymer backbone. This effect plays a crucial role in the increased hole mobility observed in PBDT-TDCl when compared to PBDT-TDF. This study demonstrates the promising potential of these two *gem*-dihalovinyl thiophenes as weak electron-accepting building blocks for developing cost-effective high-performance polymer semiconductors for solar cells and other printed electronics applications.

3.6 Experimental Section

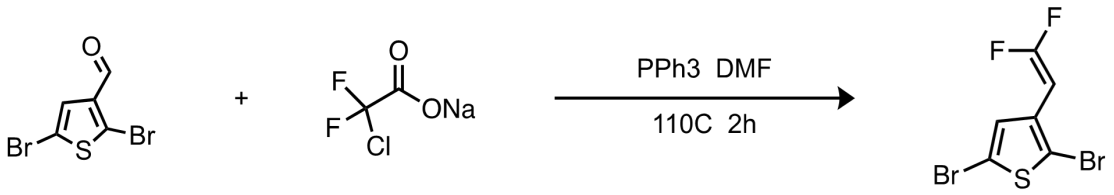
3.6.1 General Methods.

Density functional theory (DFT) calculations were conducted using GaussView 9.0 at the B3LYP/6-31G (d,p) level. ^{1}H NMR and ^{13}C NMR spectra were recorded on Bruker DPX 300-MHz spectrometer in $CDCl_3$. Chemical shifts were reported relative to internal tetramethylsilane (TMS, 0 ppm). High temperature gel permeation chromatography (GPC) measurements were performed on an Agilent PL-GPC220 system using 1, 2, 4-trichlorobenzene as an eluent at 110 °C with a sample concentration of 10 mg mL^{-1}. Specifically, the GPC column is a highly cross-linked, porous polystyrene/divinylbenzene column of the type PLgel MIXED-B, and the detector employed is a differential refractive index (RI) detector. The UV-Vis absorption spectra of polymers were recorded on a Cary 7000 Universal Measurement Spectrophotometer (UMS). Cyclic voltammetry (CV) data were obtained on a CHI600E electrochemical analyzer using an Ag/AgCl reference electrode and two Pt disk electrodes as the working and counter electrodes, respectively, in 0.1 M tetrabutylammonium hexafluorophosphate solution in dry acetonitrile at a scan rate of 100 mV s^{-1}. Ferrocene was used as the reference, which has a HOMO energy level of -4.8 eV. Atomic force microscopy (AFM) images of polymer films were taken using a Dimension 3100 scanning probe microscope. Photoluminescence (PL) measurements were conducted on thin films spin-coated on glass substrates using a Horiba PTI QuantaMaster™ 8000 Series Fluorimeter. X-ray diffraction (XRD) patterns were collected using a Bruker D8 Discover powder diffractometer with standard Bragg-Brentano geometry and Cu Kα radiation (λ = 1.5418 Å).

3.6.2 Synthetic Procedures

2,5-Dibromothiophene-3-carbaldehyde (**1**)[87] was prepared by bromination of thiophene-3-carbaldehyde according to literature procedures. 2,6-Bis(trimethytin)-4,8-bis(5-(2-ethylhexyl)thiophen-2-yl)benzo[1,2-b:4,5-b']dithiophene (**6**) was purchased from 1-Material. Other chemicals were purchased from commercial sources and used as received.

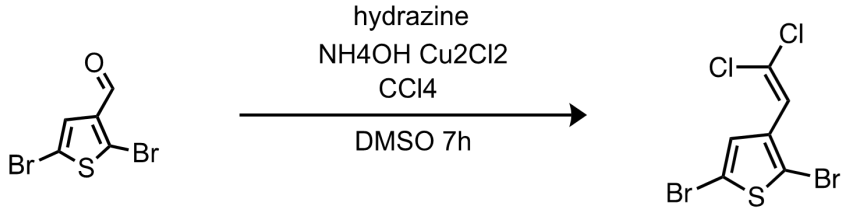
Synthesis of 2,5-dibromo-3-(2,2-difluorovinyl)thiophene (7)



1 **7**

Sodium 2-chloro-2,2-difluoroacetate (0.68 g, 4.45 mmol) was added in a mixture of 2.5-dibromothiophene-3-carbaldehyde (**1**) (1.00 g, 3.70 mmol) and triphenyl phosphine (1.46 g, 5.56 mmol) in N, N-dimethylformamide (DMF) (11 mL), the reaction was heated at 110 °C and kept at this temperature until no further evolution of CO_2 was observed. Then water was added to the reaction mixture slowly and the resultant mixture was extracted with diethyl ether. The combined organic layer was dried over Na_2SO_4, filtered, and concentrated in vacuo. The residue was purified by flash column chromatography on silica gel to afford 2,5-dibromo-3-(2,2-difluorovinyl)thiophene (**7**) as a yellow liquid. Yield: 0.78 g (70%). ^{1}H NMR (300 MHz, $CDCl_3$): δ 7.09 (s, 1H), 5.37 (d, J = 24 Hz, 1H). ^{13}C NMR (75 MHz, $CDCl_3$): δ 109.42, 111.83, 128.87, 131.11, 156.86, 160.76.

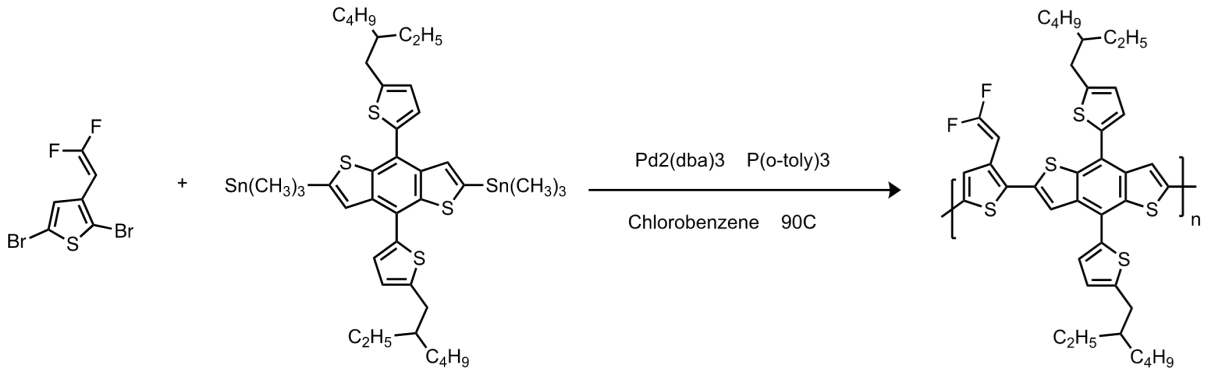
Synthesis of 2,5-dibromo-3-(2,2-dichlorovinyl)thiophene (8)



1 **8**

A solution of 2,5-dibromothiophene-3-carbaldehyde (**1**) (0.60 g, 2.22 mmol) in dimethyl sulfoxide (DMSO) (2mL) was added dropwise to a solution of 100% hydrazine hydrate (0.11 g, 2.22 mmol) in DMSO (2 mL). The reaction mixture was stirred for 3 h. An aqueous ammonia (NH_4OH) solution (25%, 0.74 mL) and Cu_2Cl_2 (22 mg, 0.22 mmol) were added to the resulting solution of hydrazone. Then CCl_4 (1.71 g, 11.11 mmol) was added dropwise at 20 °C for 10 min. The reaction mixture was stirred for 4 h and 0.1 M HCl (300 mL) was added. The reaction product was extracted with CH_2Cl_2 (3 × 50 mL), the extract was dried with Na_2SO_4, then the organic solvent was evaporated. The residue was purified by flash column chromatography on silica gel to afford 2,5-dibromo-3-(2,2-dichlorovinyl)thiophene (**8**) as a colorless liquid. Yield: 0.46 g (61%). ^{1}H NMR (300 MHz, $CDCl_3$): δ 7.52 (s, 1H), 6.77 (s, 1H). ^{13}C NMR (75 MHz, $CDCl_3$): δ 111.60, 113.36, 121.23, 123.21, 129.05, 134.36.

Synthesis of PBDT-TDF

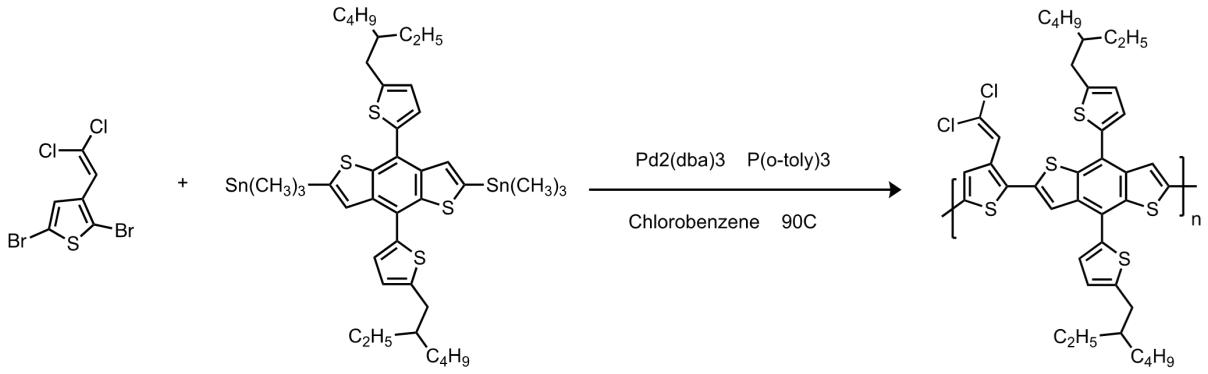


7 **6** **PBDT-TDF**

To a 25 mL two-neck round bottom flask, 2,5-dibromo-3-(2,2-difluorovinyl)thiophene (**7**) (50.4 mg, 0.1658 mmol), 2,6-Bis(trimethytin)-4,8-bis(5-(2-ethylhexyl)thiophen-2-yl)benzo[1,2-b:4,5-

b']dithiophene (**6**) (150 mg, 0.1658 mmol) and tris(o-tolyl)phosphine (P(o-tolyl)$_3$) (4 mg, 0.0133 mmol) were added. After the reaction system was purged with argon and evacuated three times, anhydrous chlorobenzene (5 mL) was added to dissolve the mixture, and then tris(dibenzylideneacetone)dipalladium(0) ($Pd_2(dba)_3$) (3 mg, 0.0033 mmol) was added. The reaction mixture was stirred under argon at 90 °C for 24 h before it was cooled to room temperature. Then the reaction mixture was poured into methanol (100 mL), stirred for 1 h, and filtered to obtain a dark red solid. The solid was extracted with acetone, hexane, and then chloroform in a Soxhlet apparatus for 24 h each to give PBDT-TDF as a red solid from the chloroform portion. Yield: 118 mg (99%). GPC: M_n = 18.4 kg mol^{-1}, M_w = 50.1 kg mol^{-1}, and $Đ$ = 2.72.

Synthesis of PBDT-TDCl



8 **6** **PBDT-TDCl**

To a 25 mL two-neck round bottom flask, 2,5-dibromo-3-(2,2-dichlorovinyl)thiophene (**8**) (55.8 mg, 0.1658 mmol), 2,6-Bis(trimethytin)-4,8-bis(5-(2-ethylhexyl)thiophen-2-yl)benzo[1,2-b:4,5-b']dithiophene (**6**) (150 mg, 0.1658 mmol) and P(o-tolyl)$_3$ (4 mg, 0.0133 mmol) were added. After the reaction system was purged with argon and evacuated three times, anhydrous chlorobenzene (5 mL) was added to dissolve the mixture, followed by $Pd_2(dba)_3$ (3 mg, 0.0033 mmol). The reaction mixture was then stirred under argon at 90 °C for 24 h before it was cooled to room temperature. Then the reaction mixture was poured into methanol (100 mL), stirred for 1 h, and filtered to obtain a dark red solid. The solid was extracted with acetone, hexane, chloroform and then chlorobenzene in a Soxhlet apparatus for 24 h each to give PBDT-TDCl as a red solid from the chloroform and chlorobenzene portions. Yield: 35 mg (28%) in the chloroform fraction and 89 mg (71%) in the chlorobenzene fraction,

resulting in a combined yield of 99%. The polymer portion in chlorobenzene was used for all characterizations and device fabrications. GPC: M_n = 28.1 kg mol^{-1}, M_w = 63.1 kg mol^{-1}, and $Đ$ = 2.25.

3.6.3 OSC device fabrication

Inverted polymer solar cells were fabricated with the configuration of ITO (150 nm)/ ZnO (35 nm)/ Active layer/ MoO_x (10 nm)/ Ag (100 nm). The conductive indium-doped tin oxide (ITO) glass substrate was cleaned with deionized water and acetone in an ultrasonic bath at 40 °C for 20 min each. The substrate was then removed and cleaned with a cotton swab moistened with acetone. The substrate was again sonicated in isopropanol (IPA) at 40 °C for 20 min. The substrate was dried with an N2 stream and treated in an air plasma cleaner for 10 min. A thin layer of ZnO (~35 nm) was deposited by spin-coating a freshly prepared ZnO precursor solution at 3500 rpm and subsequently annealed at 200 °C for 1 h in air. (The ZnO precursor solution was prepared by stirring a mixture of zinc acetate (197 mg), ethanolamine (54 μL), and 2-methoxyethanol (2 mL) at 50 °C overnight.) Then the substrates were transferred to a nitrogen filled glove box, where the donor (PBDT-TDF or PBDT-TDCl) and acceptor (Y6) mixture (at a 1:1 or other mass ratios) solution in chloroform (CF) was spin-coated onto the ZnO layer at various speeds to obtain the blend layers with the desired thickness. The concentration of the donor/acceptor solution is 16 mg mL^{-1} in CF. It is worth noting that while PBDT-TDCl extracted from CB exhibits poor solubility in CF, it can be easily dissolved in CF when blended with Y6, possibly due to the donor-acceptor interaction. Following an optional annealing process (for 10 min), a thin MoO_x hole transport layer (10 nm) and an Ag electrode layer (100 nm) were sequentially deposited onto the substrate using thermal deposition under a pressure below 5.0 × 10^{-6} Pa. The active area of each OSC device is 0.0256 cm^2 defined by a mask. The current density–voltage (*J*-*V*) characteristics of the solar cells were measured on an Agilent B2912A Semiconductor Analyzer and a ScienceTech SLB300-A Solar Simulator. A 450 W xenon lamp and an air mass (AM) 1.5 filter were used as the light source. External quantum efficiency (EQE) measurements were performed in air within 3 h after device fabrication using an IQE-200B Solar Cell Quantum Efficiency Measurement System (Newport, Inc.).

3.6.4 Appendix

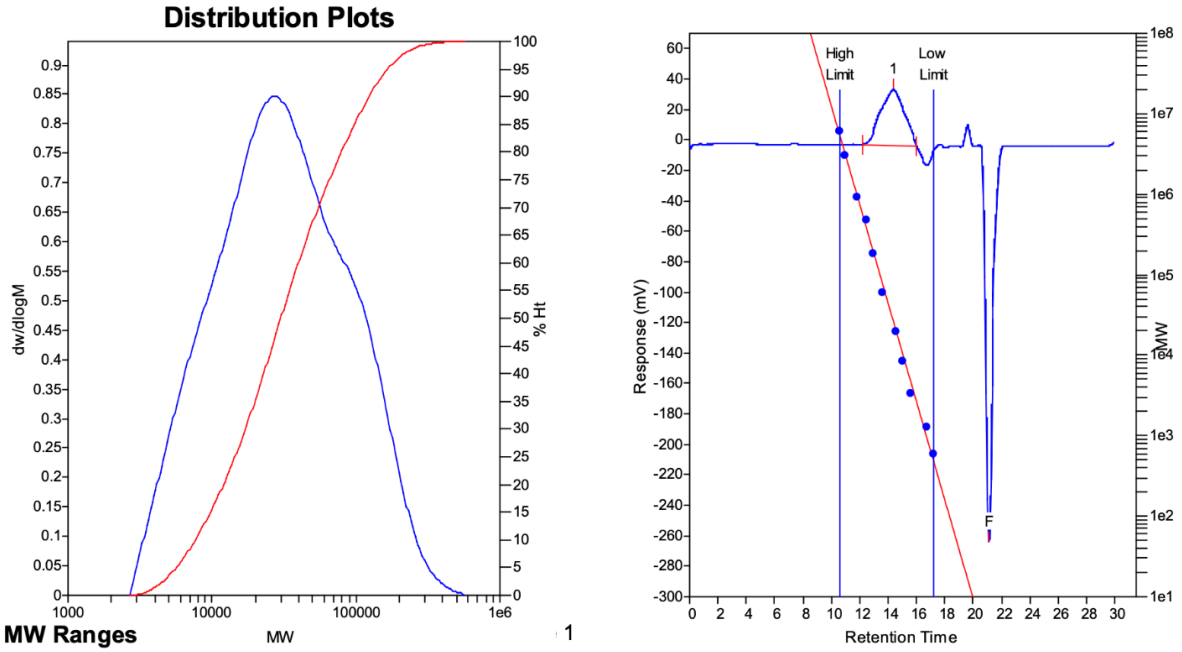


Figure 3-14. HT-GPC data of PBDT-TDF.

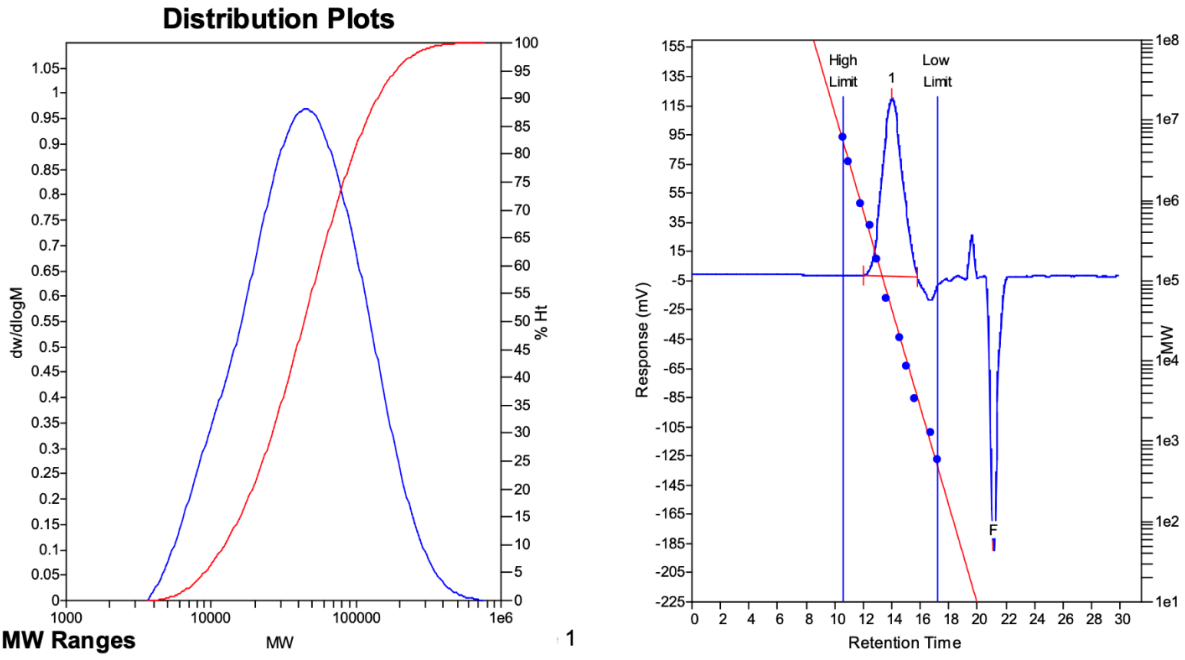


Figure 3-15. HT-GPC data of PBDT-TDCl.

Table 3-7. Summary of photovoltaic properties of PBDT-TDF:Y6-based devices processed at different spin coating rates (in rotations per minute, RPM) and different annealing temperatures. Active layer thickness: ~120 nm for films spin-coated at 1500 RPM, ~100 nm for films spin-coated at 2500 RPM.

RPM	Annealing Temperature, °C	J_{sc}, mA cm^{-2}	V_{oc}, V	FF	PCE, %	R_s, Ω cm^2	R_{sh}, Ω cm^2
1500	RT	-23.16	0.77	0.47	8.38	5.84	264.19
2500	RT	-19.87	0.79	0.52	8.25	4.77	387.39
1500	50	-20.76	0.78	0.52	8.34	3.74	314.95
2500	50	-20.03	0.79	0.55	8.66	4.34	412.51
1500	100	-21.16	0.76	0.53	8.53	3.38	345.96
2500	100	-20.54	0.77	0.56	8.83	3.66	449.24
1500	150	-22.84	0.73	0.50	8.25	4.78	406.06
2500	150	-22.27	0.73	0.55	8.81	2.50	554.77

Table 3-8. Summary of photovoltaic properties of PBDT-TDF:Y6-based devices processed with different donor: acceptor mass ratios, spin-coated at 2500 RPM, and annealed at 100 °C.

Mass Ratio	J_{sc}, mA cm^{-2}	V_{oc}, V	FF	PCE, %	R_s, Ω cm^2	R_{sh}, Ω cm^2
1:1.2	-19.39	0.67	0.50	6.50	2.56	134.18
1:1.4	-19.77	0.62	0.48	5.89	2.19	208.17
1.1:1	-21.07	0.75	0.53	8.73	2.36	546.77
1.2:1	-21.55	0.77	0.51	8.36	4.02	337.52

Table 3-9. Summary of photovoltaic properties of PBDT-TDF:Y6-based devices processed using chloroform with different solvent additives, spin-coated at 2500 RPM, and annealed at 100 °C.

Additives	J_{sc}, mA cm^{-2}	V_{oc}, V	FF	PCE, %	R_s, Ω cm^2	R_{sh}, Ω cm^2
CN [0.25% v/v]	-21.14	0.68	0.51	7.44	2.68	418.32
CN [0.5% v/v]	-22.79	0.69	0.51	8.12	2.48	369.67
DIO [0.25% v/v]	-22.32	0.69	0.55	8.53	2.26	624.26
DIO [0.5% v/v]	-21.40	0.67	0.58	8.41	2.06	511.59

Table 3-10. Summary of photovoltaic properties of PBDT-TDCl:Y6-based devices processed at different spin-coating rates and annealed at 100 °C. Active layer thickness: Active layer thickness: ~140 nm for films spin-coated at 500 RPM, ~130 nm for films spin-coated at 1000 RPM, and ~120 nm for films spin-coated at 1500 RPM.

RPM	J_{sc}, mA cm^{-2}	V_{oc}, V	FF	PCE, %	R_s, Ω cm^2	R_{sh}, Ω cm^2
500	-25.95	0.71	0.60	11.02	3.74	450.53
1000	-25.91	0.70	0.58	10.64	3.61	485.71
1500	-22.99	0.71	0.61	10.08	3.42	753.89

Table 3-11. Summary of photovoltaic properties of devices based on PBDT-TDCl:Y6 films spin-coated at 500 RPM and annealed at different temperatures.

Annealing Temperature, °C	J_{sc}, mA cm^{-2}	V_{oc}, V	FF	PCE, %	R_s, Ω cm^2	R_{sh}, Ω cm^2
RT	-24.52	0.67	0.56	9.27	3.49	393.37
100	-25.95	0.71	0.60	11.02	3.74	450.53
150	-25.23	0.67	0.56	9.45	3.72	413.12
200	-25.20	0.65	0.52	8.50	3.90	282.53

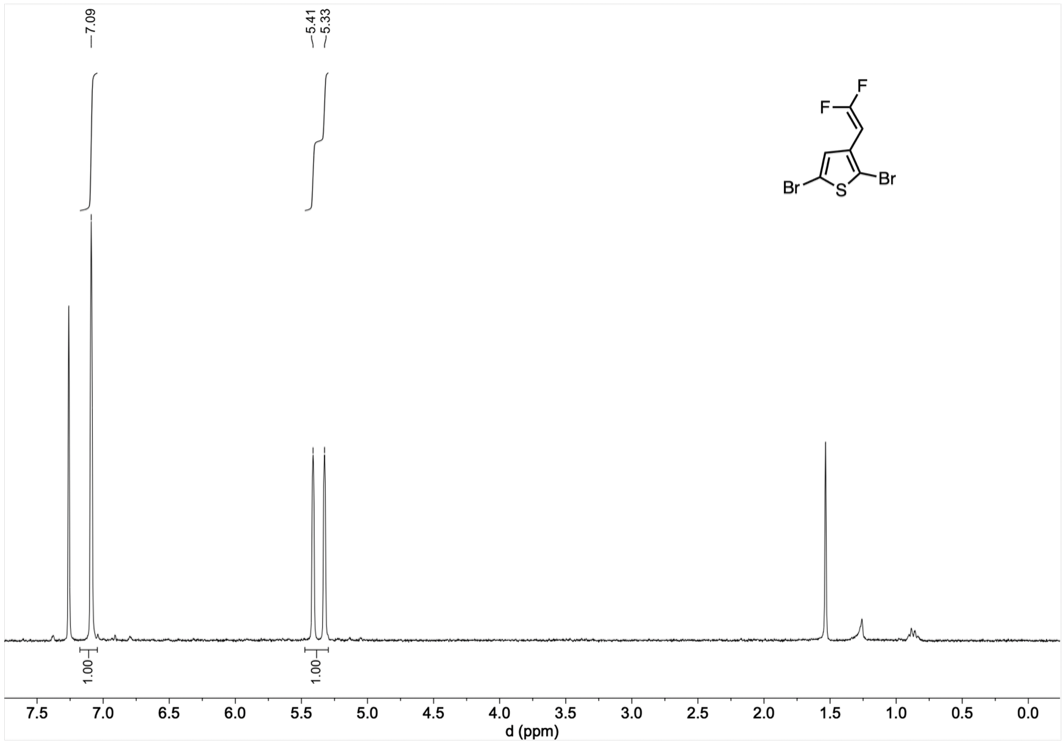


Figure 3-16. ^{1}H NMR (300 MHz, $CDCl_3$) spectrum of 2,5-dibromo-3-(2,2-difluorovinyl)thiophene (7).

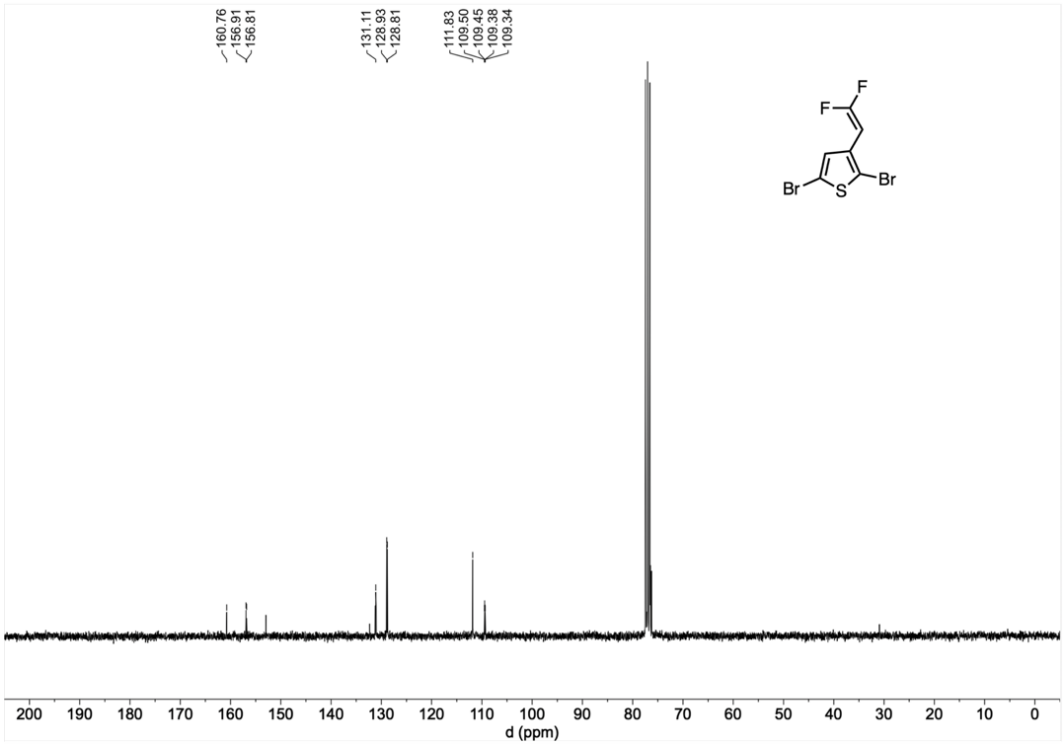


Figure 3-17. ^{13}C NMR (75 MHz, $CDCl_3$) spectrum of 2,5-dibromo-3-(2,2-difluorovinyl)thiophene (7).

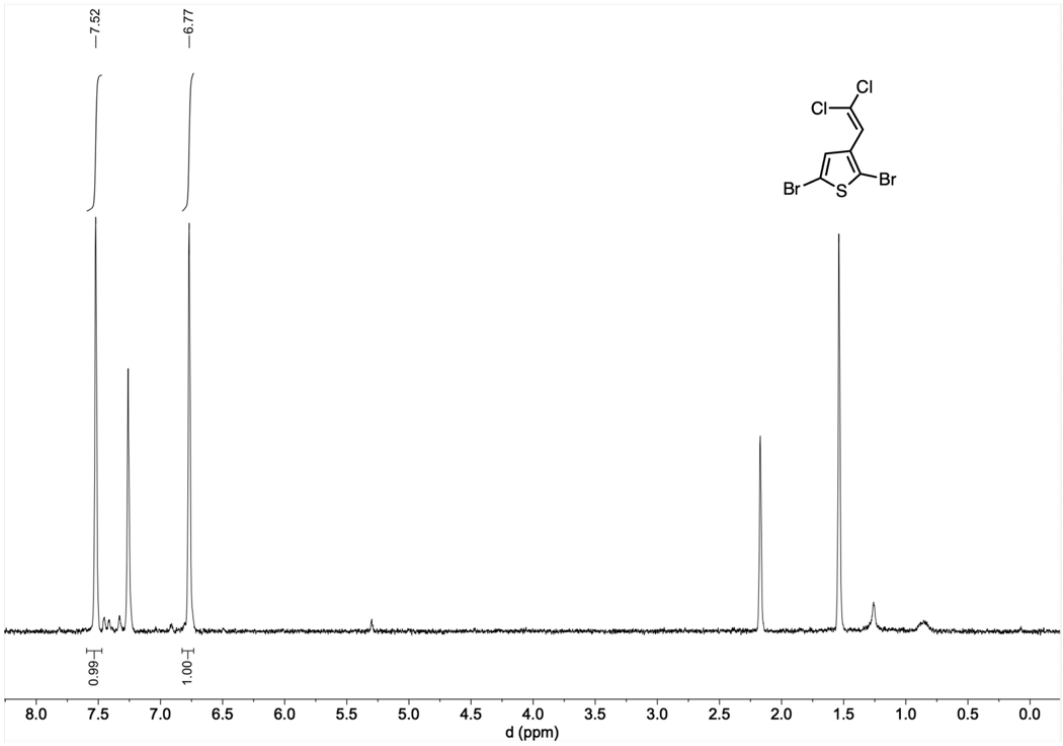


Figure 3-18. ^{1}H NMR (300 MHz, $CDCl_3$) spectrum of 2,5-dibromo-3-(2,2-dichlorovinyl)thiophene (8).

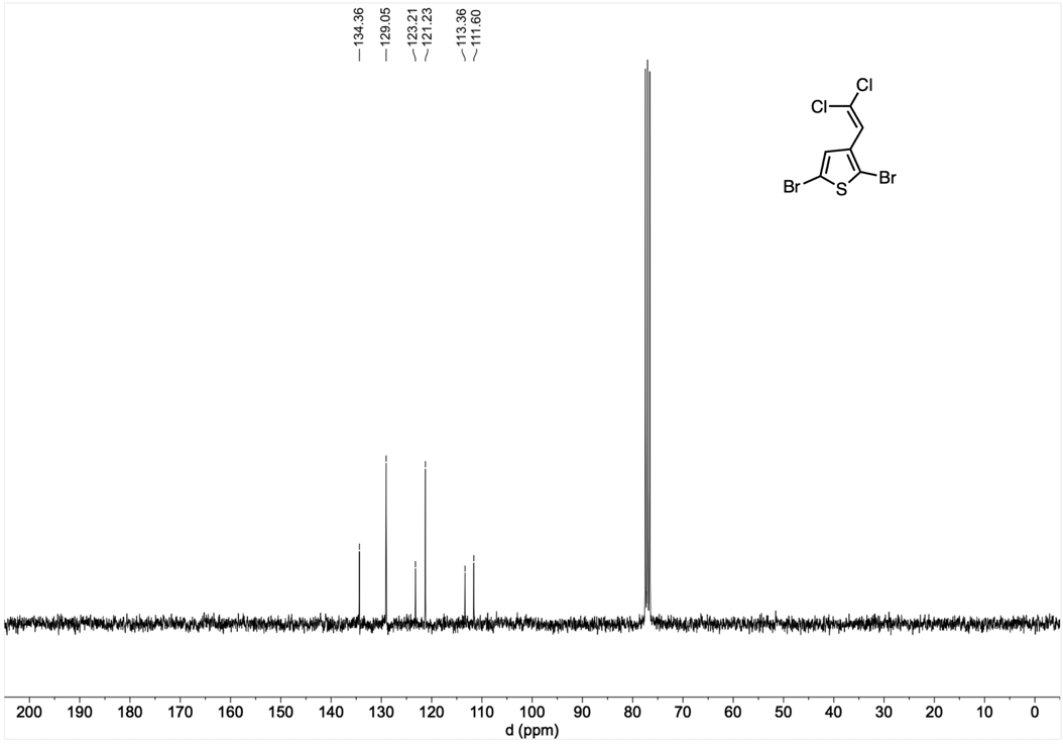


Figure 3-19. ^{13}C NMR (75 MHz, $CDCl_3$) spectrum of 2,5-dibromo-3-(2,2-dichlorovinyl)thiophene (8).

Chapter 4
Synthesis and Characterization of Succinimide-substituted Thiophene-based Polymers

This chapter is based on the following publication:

Y. Yuan, S. Flynn, X. Li, H. Liu, J. Wang, Y. Li, *Macromol. Rapid Commun.* **2024**, 2400275.

4.1 Introduction

Polymer donors incorporating a benzodithiophene (BDT) unit and a substituted thiophene (TX) unit in each repeat unit, namely PBDT-TX and PBDT-TXBT, have emerged as an important class of materials for organic solar cells (OSCs) over the past decade due to their high performance and structural simplicity (**Figure 4-1**).[56,139–141] Initially, these polymers have been tailored as narrow bandgap donors to complement wide bandgap acceptors.[6,142] Recently, numerous polymers within this class have been specifically designed to match with Y6 and other narrow bandgap NFAs, significantly contributing to the achievement of record-high PCEs. The BDT unit serves as the electron-donating moiety, while the TX unit acts as the electron-accepting component. Thiophene π-spacers are frequently introduced between the BDT and TX units to confer multiple advantages such as enhanced backbone coplanarity for improved carrier mobility and increased separation distance between the BDT donor unit and the TX acceptor unit to reduce binding energy, facilitating efficient exciton separation.[59,60]

In this study, we have developed a series of simple TX building blocks for constructing wide bandgap polymers donors, which show promising solar cell performance when paired with NFAs.[57,87,129,143–145] We introduce a novel electron-withdrawing TX building block, namely succinimide-substituted thiophene (TS) (**Figure 4-1**), which was used to develop three new wide bandgap polymer donors, PBDT-TS-C5 without thiophene spacers, and PBDT-TSBT-C12 and PBDTF-TSBT-C16 with thiophene spacers (**Scheme 4-1**). These polymers have wide bandgaps in the range of 1.91 to 2.00 eV, which are in the favorable range for matching that of the narrow bandgap acceptor Y6. PBDT-TS-C5 has E_{HOMO} and E_{LUMO} energy levels of -5.53 eV and -3.53 eV, respectively. With the addition of thiophene as π-spacers, PBDT-TSBT-C12 exhibited higher E_{HOMO} and E_{LUMO} energy levels of -5.35 eV and -3.44 eV, respectively, while PBDTF-TSBT-C16 has lower levels of -5.51 eV and -3.57 eV,

respectively, attributed to the incorporation of electron-withdrawing fluorine substituents at BDT units. The OSC device based on the blend of PBDT-TS-C5:Y6 showed a V_{oc} of 0.89 V, a J_{sc} of 19.36 mA cm^{-2}, an FF of 0.50, resulting in a PCE of 8.51%. PBDT-TSBT-C12:Y6 based device exhibited a V_{oc} of 0.71 V, a J_{sc} of 24.84 mA cm^{-2}, an FF of 0.60, resulting in a higher PCE of 10.47%. The OSC device based on the blend of PBDTF-TSBT-C16:Y6 demonstrated a V_{oc} of 0.80 V, a J_{sc} of 26.83 mA cm^{-2}, an FF of 0.62, resulting in the best PCE of 13.21%. The blend film of PBDTF-TSBT-C16:Y6 exhibited high and balanced space-charge-limited current (SCLC) hole and electron mobilities of 1.04×10^{-3} cm^2 V^{-1} s^{-1} and 1.09×10^{-3} cm^2 V^{-1} s^{-1}, respectively, contributing to the enhanced J_{sc} and FF in the OSC devices. Although the FF of OSCs based on PBDTF-TSBT-C16:Y6 is suboptimal, its $V_{oc} \times J_{sc}$ product reaches 20.66 mW cm^{-2}, highlighting the potential of the succinimide-substituted thiophene as an electron acceptor building block for the development of wide bandgap polymer donors for high-performance OSCs.

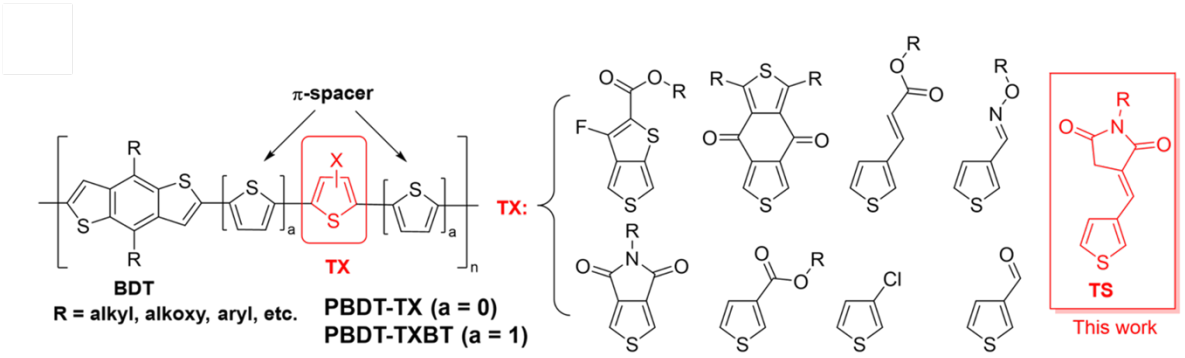


Figure 4-1. General structure of polymer donors comprising BDT and thiophene building blocks, and representative substituted thiophene (TX) acceptor building blocks, including the succinimide-substituted thiophene reported in this work.

4.2 Theoretical Study of Succinimide Based Polymers

DFT calculations were performed on the dimer units of PBDT-TS-C5, PBDT-TSBT-C12 and PBDTF-TSBT-C16, denoted as di-BDT-TS, di-BDT-TSBT and di-BDTF-TSBT, respectively, using the B3LYP/6-31G (d,p) level of the theory (**Figure 4-2**). These simulations aimed to provide insights into the geometry and frontier molecular orbitals (FMOs) of these polymers. Methyl groups were

employed as substitutes for the 2-ethylhexyl side chains on the BDT units and alkyl side chains on the succinimide units to expedite the computational process.

As depicted in **Figure 4-2a**, in di-BDT-TS, the succinimide side chain on TS exerts a significant steric effect on the adjacent BDT unit, leading to a large dihedral angle (38.1° and 34.9° in the first and second repeat units, respectively) between BDT and TS on the side with the side chain. Upon inserting a sterically less demanding thiophene π-spacer between BDT and TS, as illustrated in **Figures 4-2e&i**, the dihedral angle between BDT and TS on the side with the side chain remains substantial (~35 to 41°) in the resulting di-BDT-TSBT and di-BDTF-TSBT. However, it makes the BDT units highly coplanar, resulting in enhanced backbone coplanarity compared to di-BDT-TS, as depicted in **Figures 4-2b, f, &j**.

The calculated E_{HOMO}/E_{LUMO} values for di-BDT-TS are -5.08 eV/-2.30 eV, which are lower than those of the dimer of BDT and non-substituted thiophene, di-BDT-T (E_{HOMO}/E_{LUMO} = -4.88 eV/-2.11 eV),[145] indicating that the TS unit has a strong electron-withdrawing effect. The dimer di-BDT-TSBT exhibits a higher E_{HOMO} at -4.97 eV and a lower E_{LUMO} at -2.47 eV due to its more extended conjugation resulting from the insertion of sterically less demanding thiophene π-spacers. In di-BDTF-TSBT, both E_{HOMO} and E_{LUMO} are lower at -5.10 eV and -2.56 eV, respectively, owing to the introduction of electron-withdrawing fluorine substituents on the BDT units. The reduced E_{HOMO} would potentially increase the V_{oc} of its solar cell devices.

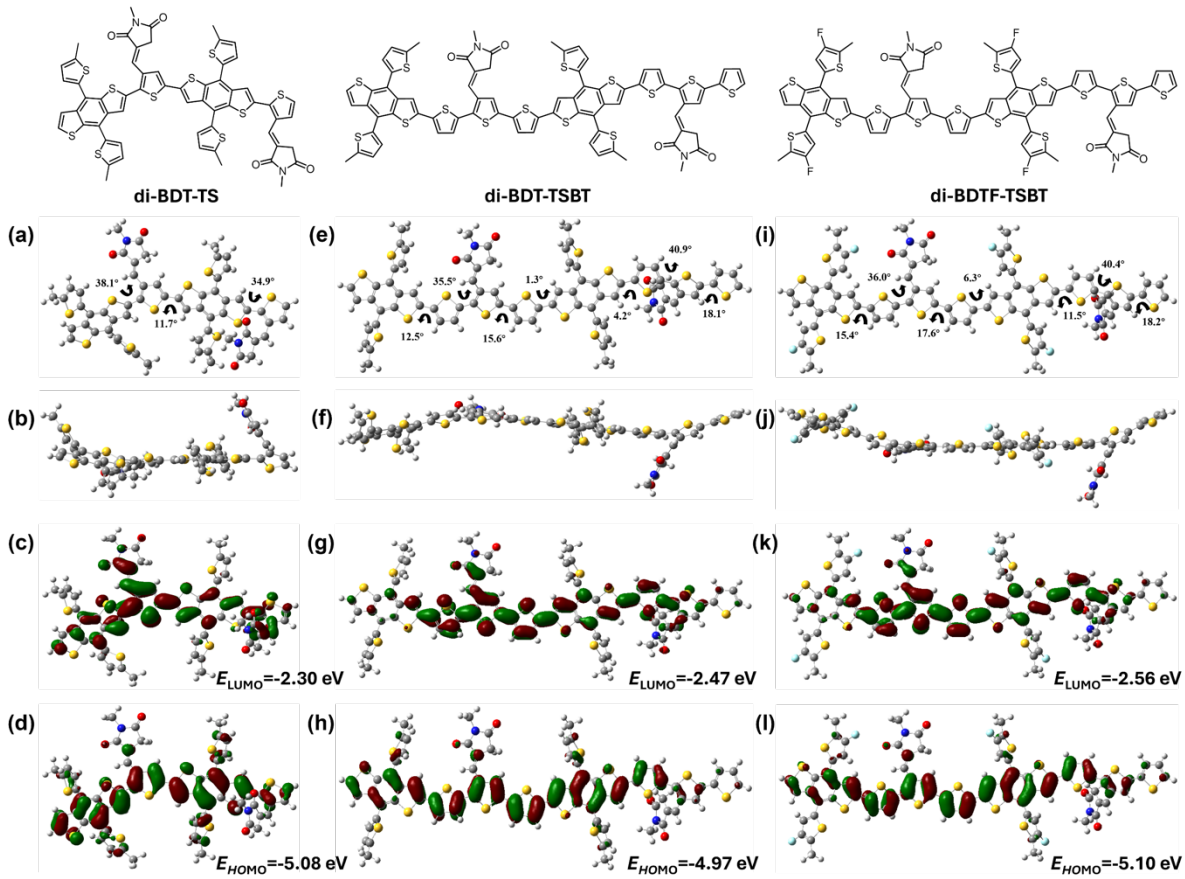
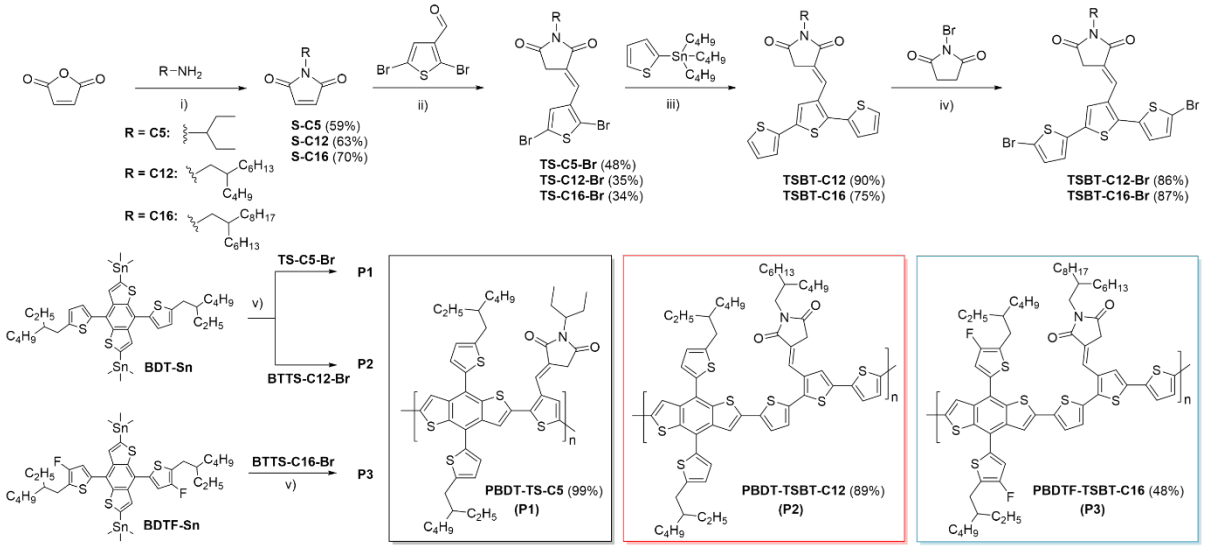


Figure 4-2. DFT simulation results of model compounds di-BDT-TS (a dimer of PBDT-TS-C5), di-BDT-TSBT (a dimer of PBDT-TSBT-C12) and di-BDTF-TSBT (a dimer of PBDTF-TSBT-C16): Molecular geometries (a, b, e, f, i, j), LUMOs (c, g, k), and HOMOs (d, h, l).

4.3 Synthesis of Succinimide Based Polymers

PBDT-TS-C5, PBDT-TSBT-C12, and PBDTF-TSBT-C16 were synthesized following the routes illustrated in **Scheme 4-1**. First, N-alkyl maleimides with different alkyl substituents, S-C5, S-C12, and S-C16, were conveniently synthesized by reacting maleic anhydride with the respective alkylamines. Then, succinimide-substituted 2,5-dibromothiophenes, TS-C5-Br, TS-C12-Br, and TS-C16-Br, were prepared via Knoevenagel condensation reactions between N-alkyl maleimides and 2,5-dibromothiophene-3-carbaldehyde with PPh_3. Next, TS-C12-Br and TS-C16-Br were reacted with 2-(tributylstannyl)thiophene through Still coupling reaction to form TSBT-C12-Br and TSBT-C16-Br,

which were further brominated using N-bromosuccinimide (NBS) to produce TSBT-C12-Br and TSBT-C16-Br, respectively. Finally, Stille coupling polymerization between TS-C5-Br or TSBT-C12-Br and BDT-Sn, and between TSBT-C16-Br and BDTF-Sn yielded PBDT-TS-C5, PBDT-TSBT-C12 and PBDTF-TSBT-C16, respectively. Following the Soxhlet extraction purification process, high yields of 99% and 89% were obtained for PBDT-TS-C5 and PBDT-TSBT-C12, respectively, from their respective chloroform extracts. However, due to its poor solubility in chloroform, PBDTF-TSBT-C16 was obtained in a lower yield of 48% using a higher boiling solvent, chlorobenzene. The number average molecular weight (M_n), weight average molecular weight (M_w), and dispersity ($Đ$) of the polymers were measured by high-temperature gel-permeation chromatography (HT-GPC) using 1,2,4-trichlorobenzene as the eluent at 110 ˚C and the results are shown in **Table 4-1**.



Scheme 4-1. Synthesis of PBDT-TS-C5, PBDT-TSBT-C12 and PBDTF-TSBT-C16: i) alkylamine/acetic acid, reflux/8 h; ii) 2,5-dibromothiophene-3-carboxaldehyde/PPh_3/DCM, r.t./24 h; iii) 2-(tributylstannyl)thiophene/$Pd(PPh_3)_4$/DMF, 100 ˚C/24 h; iv) NBS/DMF, r.t./24 h; v) $Pd_2(dba)_3$/P(o-tolyl)$_3$/chlorobenzene, 90 ˚C/24 h.

Table 4-1. GPC, UV-vis and CV data of PBDT-TS-C5, PBDT-TSBT-C12 and PBDTF-TSBT-C16.

Polymer	M_n, kDa	M_w, kDa	$Đ$	λ_{max}, nm (sol)	λ_{max}, nm (film)	E_g^{opt}, eV	E_{HOMO}, eV	E_{LUMO},[a] eV
PBDT-TS-C5	18.2	48.4	2.67	549	556	2.00	-5.53	-3.53
PBDT-TSBT-C12	18.0	47.6	2.64	541	554	1.91	-5.35	-3.44
PBDTF-TSBT-C16	36.4	89.2	2.45	548	547	1.94	-5.51	-3.57

[a] $E_{LUMO} = E_{HOMO} + E_g^{opt}$

4.4 Characterization of Succinimide Based Polymers

4.4.1 Thermal properties

Differential scanning calorimetry (DSC) measurements and thermogravimetric analysis (TGA) were employed to examine the thermal properties of these polymers. The DSC diagrams of all three polymers, depicted in **Figure 4-3**, revealed no distinct thermal transitions, indicating their amorphous states. Additionally, the TGA graphs presented in **Figure 4-4** showed that the 5% weight loss temperatures for these polymers are about 390 °C, indicating their excellent thermal stability.

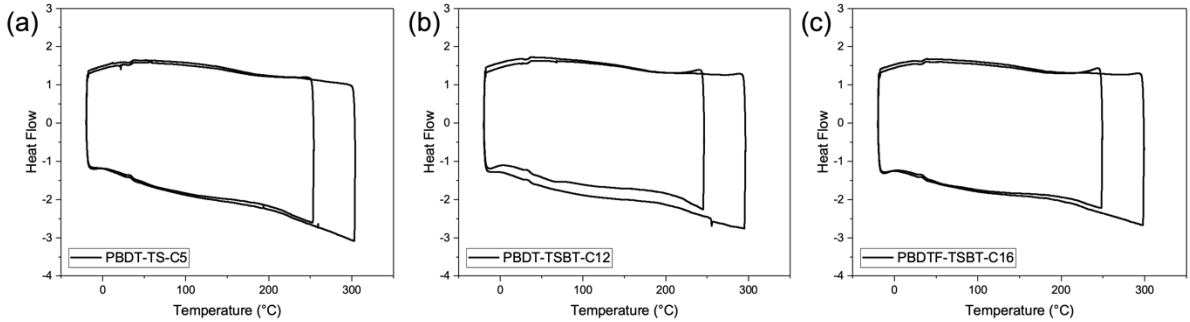


Figure 4-3. DSC measurement of (a) PBDT-TS-C5, (b) PBDT-TSBT-C12 and (c) PBDTF-TSBT-C16.

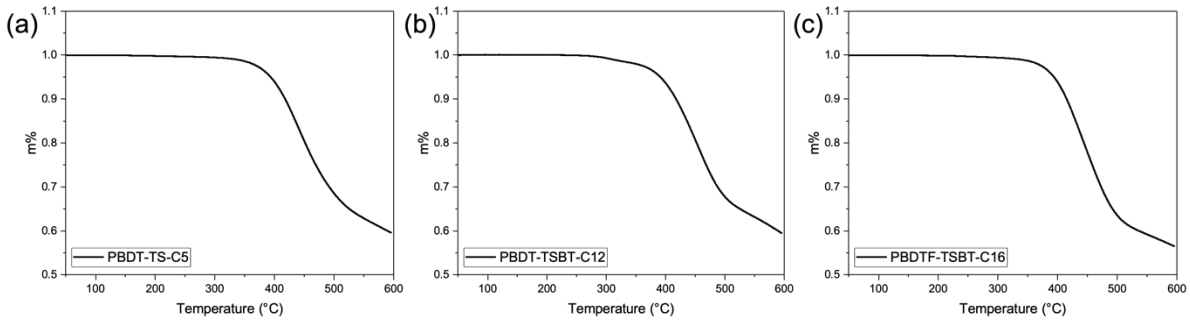


Figure 4-4. TGA measurement of (a) PBDT-TS-C5, (b) PBDT-TSBT-C12 and (c) PBDTF-TSBT-C16.

4.4.2 Optical and electrochemical properties

PBDT-TS-C5, PBDT-TSBT-C12 and PBDTF-TSBT-C16 were characterized by ultraviolet-visible (UV-Vis) spectroscopy. In chloroform solution, they showed similar wavelengths of maximum absorption (λ_{max}) at 549 nm, 541 nm, and 548 nm, with corresponding molar absorption coefficients of 3.67×10^4 M^{-1} cm^{-1}, 3.30×10^4 M^{-1} cm^{-1}, and 3.88×10^4 M^{-1} cm^{-1}, respectively (**Figure 4-5a** and **Table 4-1**). The as-cast thin films of PBDT-TS-C5 and PBDT-TSBT-C12 exhibited red shifts in λ_{max} by 7 nm and 13 nm, respectively, along with pronounced shifts of their absorption profiles towards longer wavelengths compared to their solution spectra. These red shifts suggest an extension of the π-conjugation, attributed to backbone planarization and intermolecular interactions in the solid state. For the PBDTF-TSBT-C16 thin film, a slight blue shift in λ_{max} by 1 nm was observed, but the overall absorption profile also demonstrated a red shift.

The optical bandgaps of PBDT-TS-C5, PBDT-TSBT-C12, and PBDTF-TSBT-C16 were determined as 2.00 eV, 1.91 eV, and 1.94 eV, respectively, from their onset absorption wavelengths. Their relatively wide bandgaps allow them to pair with narrow bandgap non-fullerene acceptors like Y6 to form a complementary absorption spectrum.

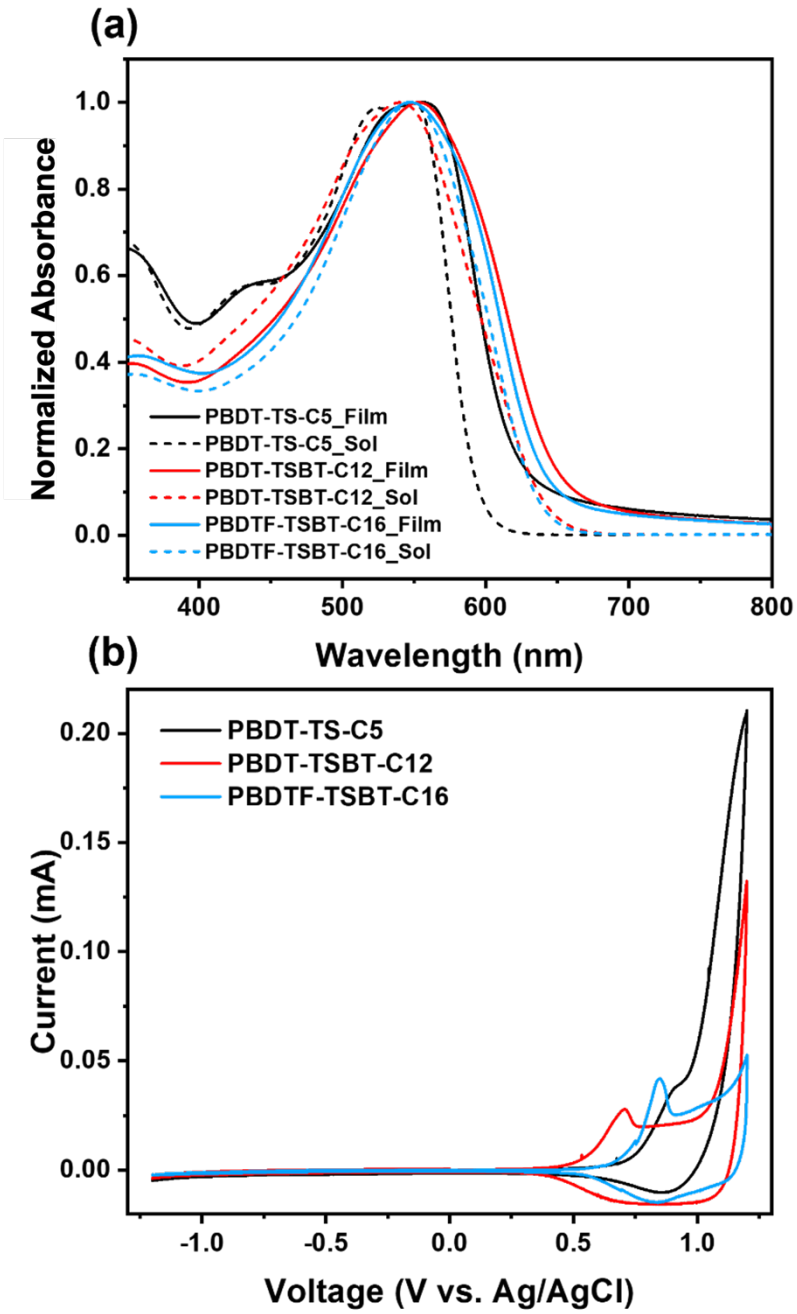


Figure 4-5. (a) UV-Vis spectra of PBDT-TS-C5, PBDT-TSBT-C12 and PBDTF-TSBT-C16 in solution (chloroform) and thin film states and (b) Cyclic voltammograms of PBDT-TS-C5, PBDT-TSBT-C12 and PBDTF-TSBT-C16 films.

Cyclic voltammetry (CV) measurements were conducted on these polymers to determine their FMO energy levels. As shown in **Figure 4-5b**, the CV curves of PBDT-TS-C5 revealed an oxidation onset potential relative to the Ag/AgCl couple at 0.73 V, corresponding to an E_{HOMO} of -5.53 eV. No reduction peak was observed for PBDT-TS-C5 due to its electron rich structure, so the E_{LUMO} of PBDT-TS-C5 was calculated by adding the optical bandgap to the E_{HOMO}, to be -3.53 eV. Similarly, the E_{HOMO} and E_{LUMO} of PBDT-TSBT-C12 were determined to be -5.35 eV and -3.44 eV, respectively, while those of PBDTF-TSBT-C16 were estimated to be -5.51 eV and -3.57 eV, respectively (**Table 4-1**).

4.4.3 I-V Characterization

Carrier mobilities dominate the transport of free holes and electrons generated from exciton dissociation, which impact the J_{sc} significantly. High hole and electron mobilities are desired for efficient charge transport and achieving high J_{sc}. All succinimide based polymers were evaluated as channel semiconductors in BGBC devices. All OTFT devices with PBDT-TS-C5, PBDT-TSBT-C12 or PBDTF-TSBT-C16 film showed typical hole dominating field effect transistor performance (**Figures 4-6**, **4-7** and **4-8**, **Tables 4-2**, **4-3** and **4-4**). The device based on PBDT-TS-C5 film exhibited a hole mobility of 4.18×10^{-3} cm^2 V^{-1} s^{-1} at the annealing temperature of 150 °C, while PBDT-TSBT-C12 and PBDTF-TSBT-C16 based OTFT devices showed 1.79×10^{-2} cm^2 V^{-1} s^{-1} with the annealing temperature of 200 °C and 2.19×10^{-2} cm^2 V^{-1} s^{-1} with the annealing temperature of 100 °C, respectively. The results indicate that the hole transport of PBDT-TSBT-C12 and PBDTF-TSBT-C16 is more efficient compared to that of PBDT-TS-C5 due to their more coplanar polymer backbone.

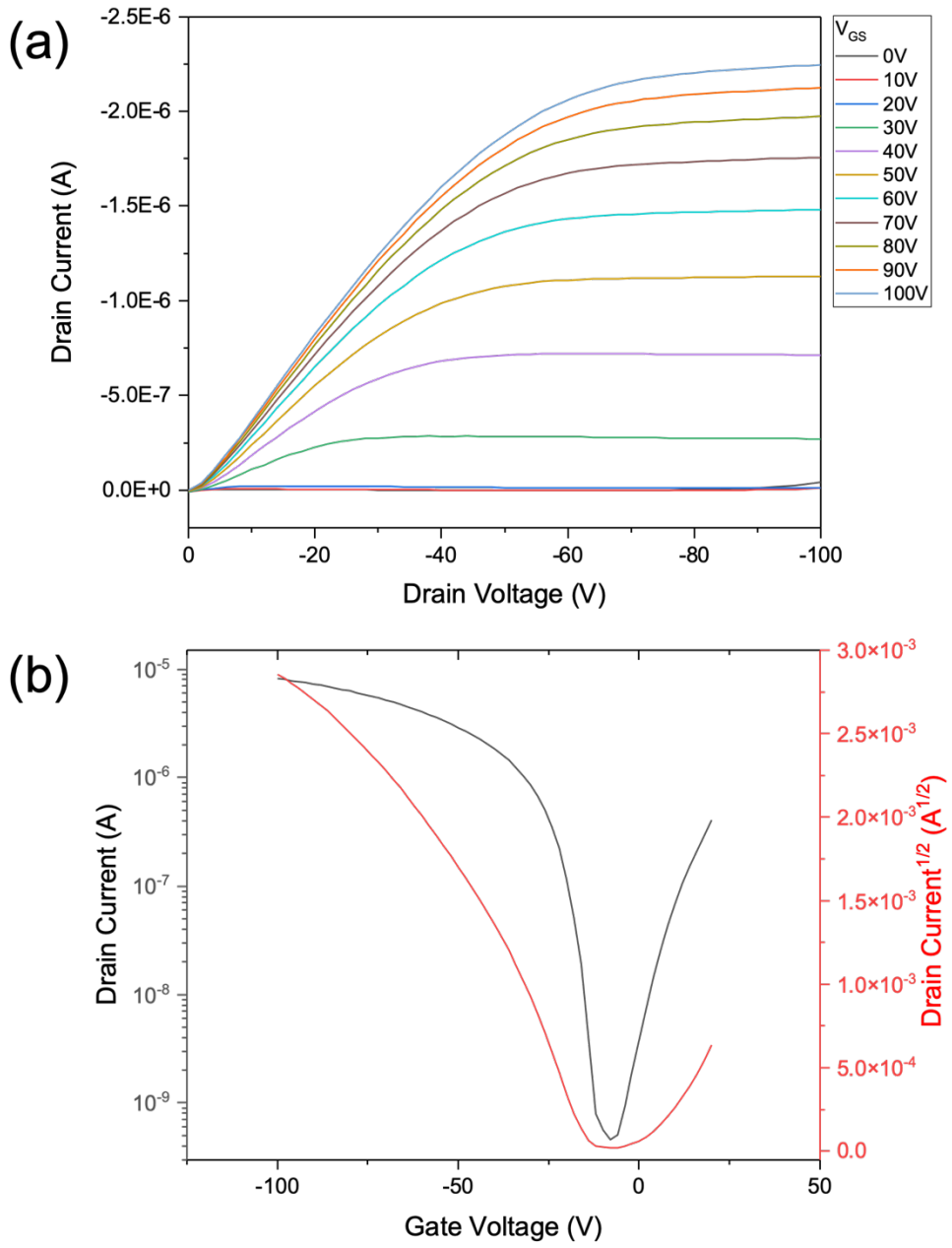


Figure 4-6. (a) Output and (b) transfer (V_{DS} = -100 V) characteristics of a representative OTFT device using PBDT-TS-C5 with an annealing temperature of 150 °C.

Table 4-2. OTFT properties of PBDT-TS-C5.

Temperature (°C)	**Best mobility ($cm^2V^{-1}s^{-1}$)**	**Avg mobility ($cm^2V^{-1}s^{-1}$)**	**Avg I_{on}/I_{off}**	**Avg V_{th} (V)**
RT	2.45×10^{-3}	$2.02\times10^{-3}\pm5.40\times10^{-4}$	70000	40.77±16.17
50	3.16×10^{-3}	$2.68\times10^{-3}\pm4.37\times10^{-4}$	70000	22.43±4.93
100	2.96×10^{-3}	$2.95\times10^{-3}\pm4.79\times10^{-6}$	100000	15.26±6.78
150	4.18×10^{-3}	$3.63\times10^{-3}\pm4.78\times10^{-4}$	70000	4.96±4.80
200	3.80×10^{-3}	$3.26\times10^{-3}\pm4.96\times10^{-4}$	10000	7.24±11.54

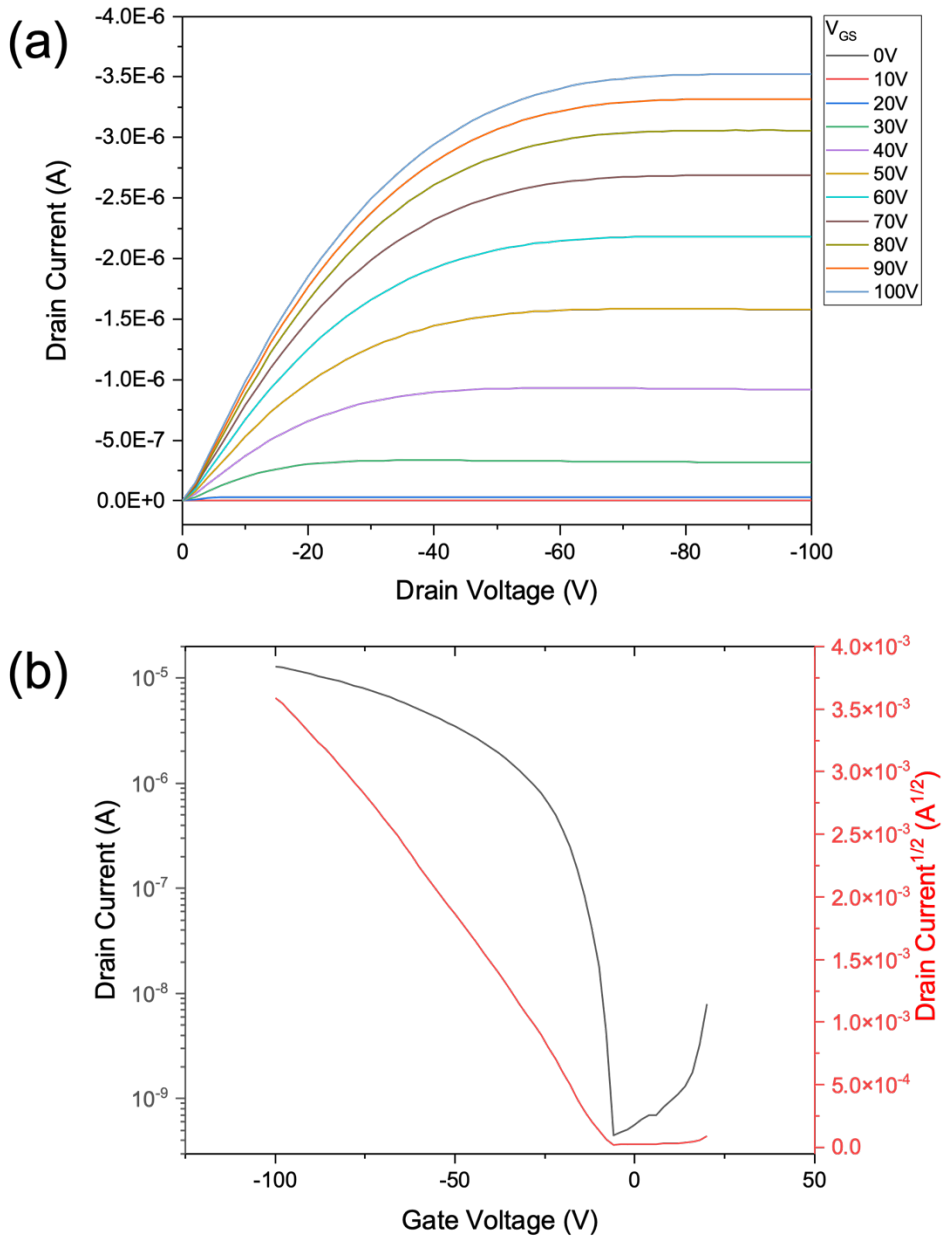


Figure 4-7. (a) Output and (b) transfer (V_{DS} = -100 V) characteristics of a representative OTFT device using PBDT-TSBT-C12 with an annealing temperature of 200 °C.

Table 4-3. OTFT properties of PBDT-TSBT-C12.

Temperature (°C)	**Best mobility ($cm^2V^{-1}s^{-1}$)**	**Avg mobility ($cm^2V^{-1}s^{-1}$)**	**Avg I_{on}/I_{off}**	**Avg V_{th} (V)**
RT	5.53×10^{-3}	$5.03\times10^{-3}\pm4.79\times10^{-4}$	40000	-6.02±5.16
50	5.13×10^{-3}	$5.01\times10^{-3}\pm9.99\times10^{-5}$	40000	-5.22±6.50
100	7.23×10^{-3}	$6.61\times10^{-3}\pm9.76\times10^{-4}$	70000	-1.02±1.66
150	1.52×10^{-2}	$9.36\times10^{-3}\pm5.31\times10^{-3}$	40000	-1.02±3.57
200	1.79×10^{-2}	$1.05\times10^{-2}\pm1.05\times10^{-2}$	55000	6.29±25.18

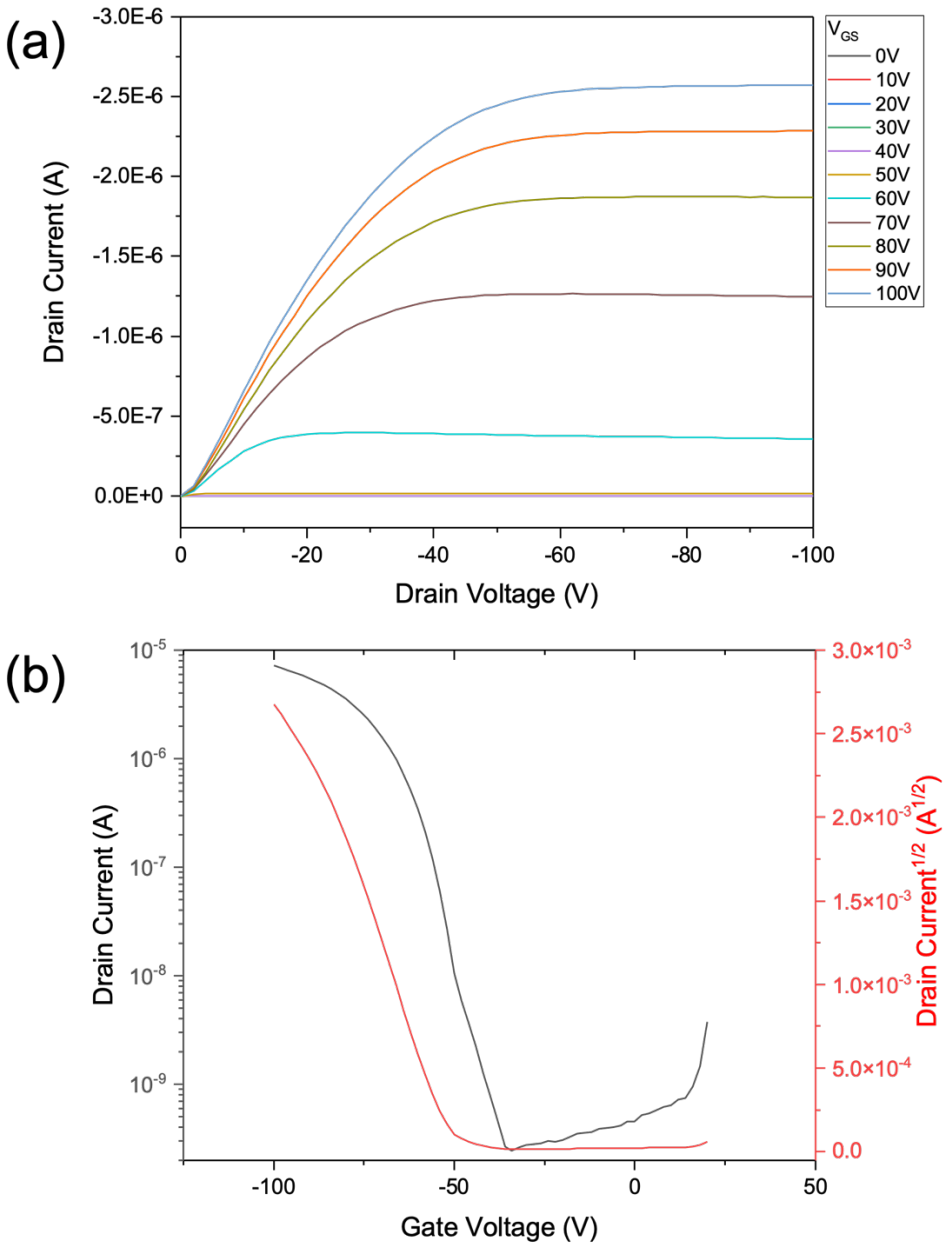


Figure 4-8. (a) Output and (b) transfer (V_{DS} = -100 V) characteristics of a representative OTFT device using PBDTF-TSBT-C16 with an annealing temperature of 100 °C.

Table 4-4. OTFT properties of PBDTF-TSBT-C16.

Temperature (°C)	Best mobility ($cm^2V^{-1}s^{-1}$)	Avg mobility ($cm^2V^{-1}s^{-1}$)	Avg I_{on}/I_{off}	Avg V_{th} (V)
RT	1.37×10^{-2}	$1.28\times10^{-2}\pm1.47\times10^{-3}$	700000	-38.31±1.56
50	1.94×10^{-2}	$1.34\times10^{-2}\pm5.26\times10^{-3}$	3700000	-43.62±4.48
100	2.19×10^{-2}	$1.47\times10^{-2}\pm8.24\times10^{-3}$	70000	-26.93±33.91
150	7.69×10^{-3}	$6.16\times10^{-3}\pm1.41\times10^{-3}$	100000	-10.81±6.14
200	1.09×10^{-2}	$6.31\times10^{-3}\pm4.33\times10^{-3}$	70000	-24.63±1.46

4.4.4 Photovoltaic performance

The photovoltaic performance of these polymers was evaluated in the OSC devices with a configuration of ITO/ZnO (35 nm)/active layer/MoO_3 (10 nm)/Ag (100 nm). A blend film of PBDT-TS-C5, PBDT-TSBT-C12 or PBDTF-TSBT-C16 and Y6 was used as the active layer. Several parameters, including the spin-coating rate, thermal annealing temperature, donor-acceptor mass ratio, solvent additives were studied, and the results are summarized in **Tables 4-7** to **4-18**. The photovoltaic properties of the devices fabricated under optimized conditions are shown in **Table 4-5**, while the current density-voltage (*J-V*) curves of the best performing devices are shown in **Figure 4-9b**. The PBDT-TS-C5:Y6 based device achieved a maximum PCE of 8.51% with a V_{oc} of 0.89 V, a J_{sc} of 19.36 mA cm^{-2}, and an FF of 0.50. The PBDT-TSBT-C12:Y6-based OSC device, where PBDT-TSBT-C12 has π-spacers, showed a higher PCE of 10.47%, with a reduced V_{oc} of 0.71 V, but a much higher J_{sc} of 24.84 mA cm^{-2} and an improved FF of 0.60. The PBDTF-TSBT-C16:Y6 based device, where fluorine substituents are incorporated on the BDT units, demonstrated the highest PCE of 13.21%, with a significantly improved V_{oc} of 0.80 V compared to PBDT-TSBT-C12-based devices, a highest J_{sc} of 26.83 mA cm^{-2}, and the best FF of 0.62.

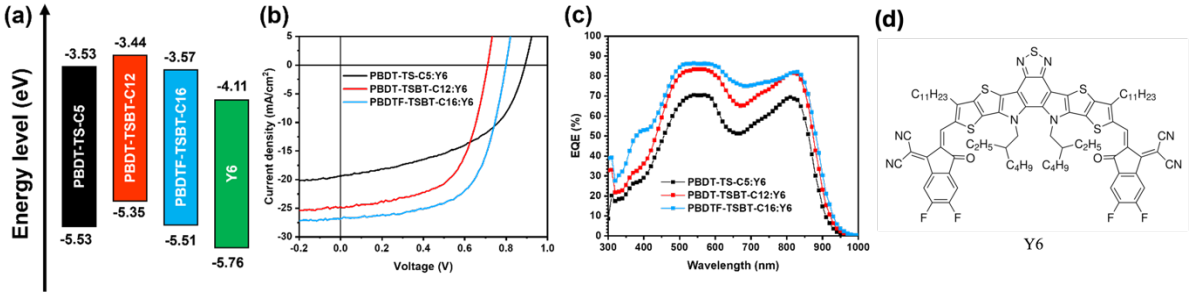


Figure 4-9. (a) The energy diagrams of PBDT-TS-C5, PBDT-TSBT-C12, PBDTF-TBST-C16 and Y6, (b) *J-V* curves, (c) EQE curves of PBDT-TS-C5, PBDT-TSBTC-C12 and PBDTF-TSBT-C16 based devices, and (d) the chemical structure of Y6.

Table 4-5. Photovoltaic parameters of OSCs fabricated using PBDT-TS-C5:Y6, PBDT-TSBT-C12:Y6 and PBDTF-TSBT-C16:Y6 under optimized conditions.[a]

Active layer	J_{sc},[b] mA cm^{-2}	V_{oc},[b] V	FF[b]	PCE,[b] %
PBDT-TS-C5:Y6	19.36[c] (18.81±0.55)	0.89 (0.89±0.01)	0.50 (0.49±0.02)	8.51 (8.11±0.37)
PBDT-TSBT-C12:Y6	24.84[d] (23.56±0.83)	0.71 (0.71±0.01)	0.60 (0.59±0.01)	10.47 (9.99±0.35)
PBDTF-TSBT-C16:Y6	26.83[e] (25.42±0.99)	0.80 (0.79±0.01)	0.62 (0.62±0.02)	13.21 (12.39±0.84)

[a] D/A ratio: 1/1; active layer thickness: ~100 nm for PBDT-TS-C5:Y6, ~120 nm for PBDT-TSBT-C12:Y6, and ~130 nm for PBDTF-TSBT-C16:Y6; annealing temperature: 150 °C for PBDT-TS-C5:Y6, 100 °C for PBDT-TSBT-C12:Y6, and 150 °C for PBDTF-TSBT-C16:Y6.

[b] Maximum value (average value ± standard deviation) from at least 5 devices.

[c] Integrated J_{sc} from the EQE spectrum in **Figure 4-9c**: 19.15 mA cm^{-2}.

[d] Integrated J_{sc} from the EQE spectrum in **Figure 4-9c**: 23.63 mA cm^{-2}.

[e] Integrated J_{sc} from the EQE spectrum in **Figure 4-9c**: 25.64 mA cm^{-2}.

The product of V_{oc} and J_{sc} can serve as an indicator of the power output achievable by an ideal solar cell, effectively reflecting the performance potential of the practical solar cell.[146,147] The maximum $V_{oc}\times J_{sc}$ value of 21.46 mW cm^{-2} achieved by the PBDTF-TSBT-C16:Y6-based devices reached that of the OSCs based on the benchmark D:A system, PM6:Y6 (20.66 mW cm^{-2} at a similar active layer thickness of ~100 nm).[18] However, the FF of our OSCs is inferior, which may be related to the suboptimal film morphology and energy alignment of the active materials with the adjacent hole and electron transport layers.[105] Refining the processing conditions of the active layer can substantially increase the $V_{oc}\times J_{sc}$ product, as demonstrated by the PM6:Y6-based OSCs, where the $V_{oc}\times J_{sc}$ has been increased from the originally reported value of 20.66 mW cm^{-2} to up to 23.50 mW cm^{-2}.[17,148] Additionally, switching from Y6 to more compatible NFAs may further enhance the overall solar cell performance.[17,20,148,149] Nonetheless, our results indicate that TS is a potentially useful building block for the development of polymer donors for high performance NFA-based OSCs.

The energy loss (E_{loss}) of OSC devices is defined as the difference between the achieved V_{oc} and the maximum theoretical V_{oc} (corresponding to the optical bandgap of the active layer), namely, $E_{loss} = E_g/q - V_{oc}$, where E_g is the smallest optical bandgap among the donor and acceptor components, and q is the elementary charge.[99,101,102] The device based on PBDT-TS-C5:Y6 demonstrated a relatively low E_{loss} of 0.44 eV, while PBDT-TSBT-C12:Y6 and PBDTF-TSBT-C16:Y6-based devices showed E_{loss} of 0.62 eV and 0.53 eV, respectively. The E_{loss} values of these devices are comparable to those of high-performing OSCs, which are typically ca. 0.5-0.6 eV.[130,150]

The external quantum efficiency (EQE) curves of the PBDT-TS-C5:Y6, PBDT-TSBT-C12:Y6 and PBDTF-TSBT-C16:Y6 devices all exhibited high values in the wavelength range of ~500-850 nm, reflecting the effective complementary absorption by the polymer and Y6 (**Figure 4-9c**). The EQE curve of the PBDT-TS-C5:Y6-based device showed two prominent peaks (~70%) at 540 nm and 810 nm, corresponding to the absorption peaks of PBDT-TS-C5 and Y6, respectively. A valley with a lower efficiency of 50% is observed between these two peaks at 660 nm. In contrast, the EQE curve of the PBDT-TSBT-C12:Y6-based device showed high efficiencies in the wavelength range of 500 nm and 820 nm, with a maximum value of 83.5% at 540 nm. As for the PBDTF-TSBT-C16:Y6-based device, over 75% EQE values were achieved in the range of 500 nm to 820 nm, with a maximum value of 86.4% at 540 nm. The much higher EQE values of the PBDT-TSBT-C12:Y6 and PBDTF-TSBT-C16:Y6-based devices resulted in their higher J_{sc} values compared to that of PBDT-TS-C5:Y6-based device in the *J-V* curves. The integrated J_{sc} from the EQE curves are calculated as 19.15 mA cm^{-2}, 23.63

mA cm^{-2} and 25.64 mA cm^{-2} for PBDT-TS-C5:Y6, PBDT-TSBT-C12:Y6 and PBDTF-TSBT-C16:Y6-based devices, respectively. They are highly consistent with the J_{sc} values (with differences < 5%) obtained from the corresponding *J-V* curves.

To further investigate the factors contributing to the different J_{sc} values of the PBDT-TS-C5:Y6, PBDT-TSBT-C12:Y6 and PBDTF-TSBT-C16:Y6-based devices, photoluminescence (PL) quenching experiments were conducted to probe the effectiveness of exciton diffusion and dissociation in their active layers. As shown in **Figure 4-10**, the PL curves for the neat films of three polymers and Y6 showed notable peaks in the range of 600-800 nm and 800-950 nm, respectively. In the case of the PBDT-TS-C5:Y6 blend film, notable PL quenching efficiencies of 97.4% for the PBDT-TS-C5 phase and 97.1% for the Y6 phase were attained. This indicates efficient exciton diffusion in both the donor and acceptor phases, as well as successful exciton dissociation at the donor-acceptor interface.[103] The PBDT-TSBT-C12:Y6 blend film exhibited slightly lower PL quenching efficiencies of 96.1% and 92.9% in the donor and acceptor phases, respectively. The PBDTF-TSBT-C16:Y6 blend film showed quenching efficiencies of 92.4% and 90.0% in the donor and acceptor phases, respectively, the lowest among these polymer blend films, although still quite high. As the quenching efficiencies of these three blend films exhibited an opposite order to the J_{sc} values in their OSC devices, it suggests that the observed differences in J_{sc} values may not be attributed to the exciton diffusion and dissociation processes.

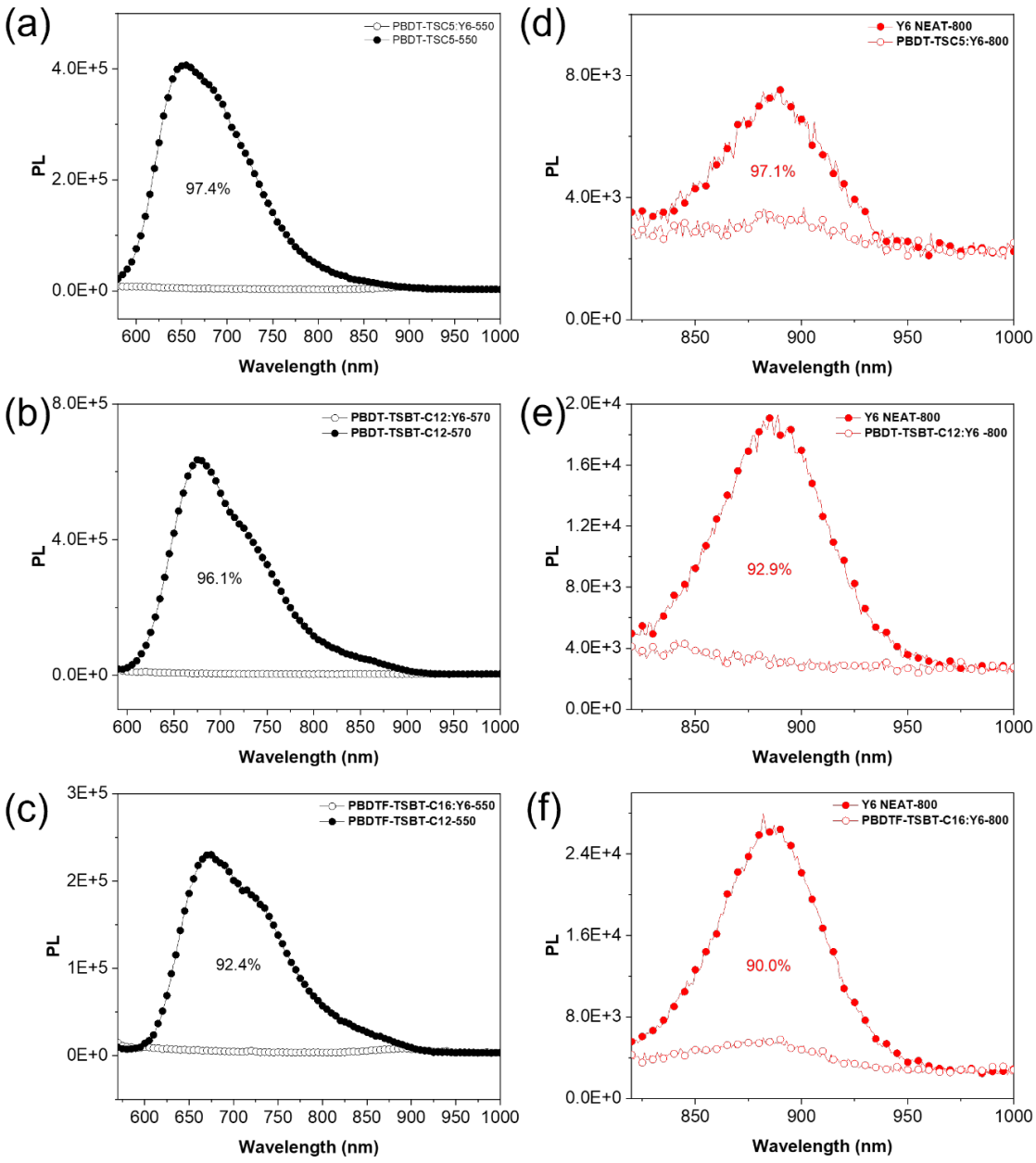


Figure 4-10. PL quenching data for PBDT-TS-C5 (a, d), PBDT-TSBT-C12 (b, e) and PBDTF-TSBT-C16 (c, f) and their blend films with Y6 (with a 1:1 ratio) on glass. The excitation wavelengths were 550 nm (PBDT-TS-C5), 570 nm (PBDT-TSBT-C12). and 550 nm (PBDTF-TSBT-C16) for donors respectively and 800 nm for the acceptor (Y6).

The charge transport properties in the direction vertical to the substrate surface, which is more relevant to the charge transport scenario in OSCs, can be accomplished through the space charge limited current (SCLC) method. The SCLC hole and electron mobilities of the neat and blend films were measured using device architectures of ITO/PEDOT:PSS (30 nm)/active layer/MoO_x (10 nm)/Ag (100 nm) and ITO/ZnO (35 nm)/active layer/LiF (1 nm)/Al (100 nm), respectively. As shown in **Table 4-6**, the highest SCLC hole mobility (μ_h) of the PBDT-TS-C5 neat film is 5.58×10^{-5} cm^2 V^{-1} s^{-1}, while the highest μ_h and SCLC electron mobility (μ_e) of the PBDT-TS-C5:Y6 blend film are 1.52×10^{-4} cm^2 V^{-1} s^{-1} and 4.96×10^{-4} cm^2 V^{-1} s^{-1}, respectively, with a μ_h/μ_e ratio of 0.31. The μ_h of the PBDT-TSBT-C12 neat film was determined to be 2.82×10^{-5} cm^2 V^{-1} s^{-1}, while μ_h and μ_e of the PBDT-TSBT-C12:Y6 blend film are 1.50×10^{-3} cm^2 V^{-1} s^{-1} and 4.57×10^{-4} cm^2 V^{-1} s^{-1}, respectively, with a μ_h/μ_e ratio of 3.28. As for the PBDTF-TSBT-C16 neat film, it exhibited the highest μ_h of 7.15×10^{-5} cm^2 V^{-1} s^{-1}. The PBDTF-TSBT-C16:Y6 blend film showed μ_h and μ_e values of up to 1.04×10^{-3} cm^2 V^{-1} s^{-1} and 1.09×10^{-3} cm^2 V^{-1} s^{-1}, respectively, with a μ_h/μ_e ratio of 0.95.

The results indicate that the incorporation of π-spacers significantly enhances the hole transport properties of PBDT-TSBT-C12 and PBDTF-TSBT-C16 in their blend films compared to PBDT-TS-C5. This enhancement is believed to largely contribute to the improved J_{sc} observed in their OSC devices. Particularly noteworthy is the high and balanced SCLC hole and electron mobilities exhibited by the PBDTF-TSBT-C16:Y6 blend film, which may account for its highest J_{sc} and FF among the three blends. Interestingly, the presence of Y6 seems to enhance the charge transport characteristics of all three polymers, a phenomenon observed in other systems as well.[144] This is likely due to an antiplasticization effect of the small Y6 molecules, promoting the ordering of the donor polymer chains.[131]

Table 4-6. SCLC data of PBDT-TS-C5, PBDT-TSBT-C12 and PBDTF-TSBT-C16.

	Electron mobility [$cm^2 V^{-1} s^{-1}$]		Hole mobility [$cm^2 V^{-1} s^{-1}$]	
	Maximum	**Average [SD]**	**Maximum**	**Average [SD]**
PBDT-TS-C5	-	-	5.58×10^{-5}	3.22×10^{-5} [1.30×10^{-5}]
PBDT-TSBT-C12	-	-	2.82×10^{-5}	2.75×10^{-5} [7.50×10^{-7}]
PBDTF-TSBT-C16	-	-	7.15×10^{-5}	5.96×10^{-5} [1.73×10^{-5}]
PBDT-TS-C5:Y6	4.96×10^{-4}	3.79×10^{-4} [1.65×10^{-4}]	1.52×10^{-4}	1.10×10^{-4} [2.85×10^{-5}]
PBDT-TSBT-C12:Y6	4.57×10^{-4}	3.60×10^{-4} [9.75×10^{-5}]	1.50×10^{-3}	9.45×10^{-4} [4.52×10^{-4}]
PBDTF-TSBT-C16:Y6	1.09×10^{-3}	4.03×10^{-4} [4.10×10^{-4}]	1.04×10^{-3}	2.54×10^{-4} [3.22×10^{-4}]

SD: standard deviation from min 4 devices

4.4.5 Film morphology and microstructure

The morphological properties of the active layer in OSCs, such as surface roughness, grain size, and phase separation, significantly influence solar cell performance.[151–153] Atomic force microscopy (AFM) was utilized to examine the morphologies of the polymer blend films.

As depicted in **Figure 4-11**, the PBDT-TSBT-C12:Y6 blend film exhibited the lowest root-mean square roughness (RMS) of 0.88 nm, followed by the PBDT-TS-C5:Y6 blend film with a slightly higher RMS of 1.13 nm, while the PBDTF-TSBT-C16:Y6 blend film showed the highest RMS of 1.32 nm. The PBDT-TS-C5:Y6 film contained very fine grains, whereas the PBDT-TSBT-C12:Y6 film is composed of larger grains, some tens of nanometers in size. The PBDTF-TSBT-C16:Y6 film exhibited slightly larger and more distinct grains, along with numerous pinholes, which could be due to the lower solubility of PBDTF-TSBT-C16, leading to inferior mixing with Y6.

A smooth surface of the active layer is critical for establishing a favorable interface with the subsequent MoO_3 hole transporting layer to facilitate efficient charge collection. The higher roughness, poor mixing with Y6, and presence of pinholes in the PBDTF-TSBT-C16:Y6 film may result in lower SCLC mobilities and decreased shunt resistance, ultimately leading to suboptimal FF values compared to state-of-the-art OSCs (FF: ~0.8). Strategies, such as increasing the length of side chains on BDT or

TS units, could be employed to improve the solubility of PBDTF-TSBT-C16, thus achieving a better morphology for enhanced OSC performance.

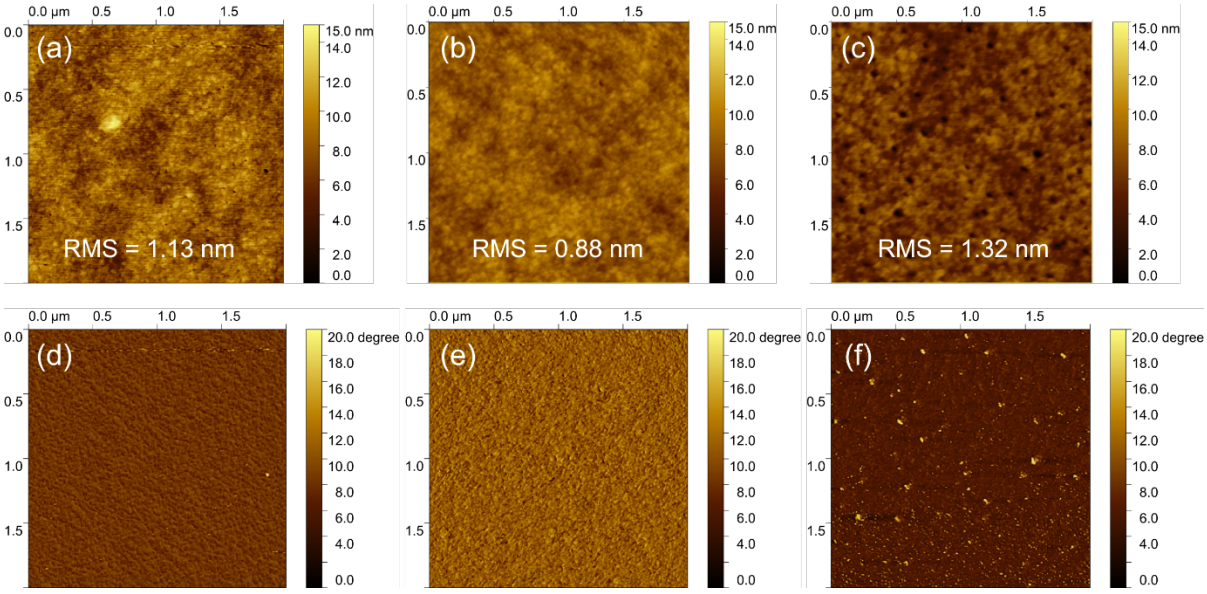


Figure 4-11. AFM height and phase images of blend films based on PBDT-TS-C5:Y6 (a, d), PBDT-TSBT-C12:Y6 (b, e) and PBDTF-TSBT-C16:Y6 (c, f).

Two-dimensional grazing incidence X-ray diffraction (2D-GIXD) measurements were conducted on both neat and blend films to examine their molecular packing. As depicted in **Figures 4-12a&b**, no distinct peaks were observed for the out-of-plane (OOP) and in-plane (IP) X-ray diffraction patterns of the neat PBDT-TS-C5 and PBDT-TS-C5:Y6 blend thin film samples, indicating disordered molecular packing in both the polymer and Y6 phases even after annealing at high temperatures up to 200 °C. When blended with the small molecule Y6, as shown in **Figures 4-12c&d**, the films retained their amorphous nature in both the IP and OOP directions at all annealing temperatures. The neat PBDT-TSBT-C12 film exhibited a weak diffraction peak at 2θ = ~4.34° in the OOP direction starting at an annealing temperature of 50 °C (**Figures 4-12e&f**). This peak corresponds to the (100) planes with a d-spacing of 2.04 nm of a layer-by-layer lamellar polymer chain packing pattern. However, no obvious peak was observed in the IP direction, suggesting a lack of chain ordering in this direction.

For the PBDT-TSBT-C12:Y6 blend film without annealing, a weak (100) peak at 2θ = 4.45° (d = 1.99 nm), was observed in the OOP direction (**Figures 4-12g&h**). As the annealing temperature increased, this (100) peak weakened. Intriguingly, a peak at ~25.7° (d = 0.35 nm), corresponding to the

(010) π-π stacking peak, started to appear at an annealing temperature of 150 °C. The enhanced ordering along the π-π stacking direction is beneficial for efficient interchain charge transport, potentially explaining the significantly increased SCLC hole mobility of this polymer in blend films compared to neat films, due to the antiplasticization effect of Y6 mentioned earlier. However, this film remained disordered in the IP direction at all annealing temperatures.

For neat PBDTF-TSBT-C16 films, as shown in **Figures 4-12i&j**, no distinct diffraction peaks were observed at all annealing temperatures in either the OOP or IP directions, indicating the highly disordered nature of this polymer. The PBDTF-TSBT-C16:Y6 blend films also remained amorphous in the IP direction (**Figures 4-12k&l**). However, a (010) peak was observed at $2\theta = 26.0°$ ($d = 0.34$ nm) in the OOP direction at an annealing temperature of 150 °C or higher, indicating the establishment of a π-π stacking order, similar to the observation for the PBDT-TSBT-C12:Y6 blend films. These findings suggest that the introduction of thiophene π-spacers promotes the improvement of chain packing, particularly π-π stacking, in the presence of the small molecule acceptor Y6, leading to higher SCLC hole mobility and improved device performance.

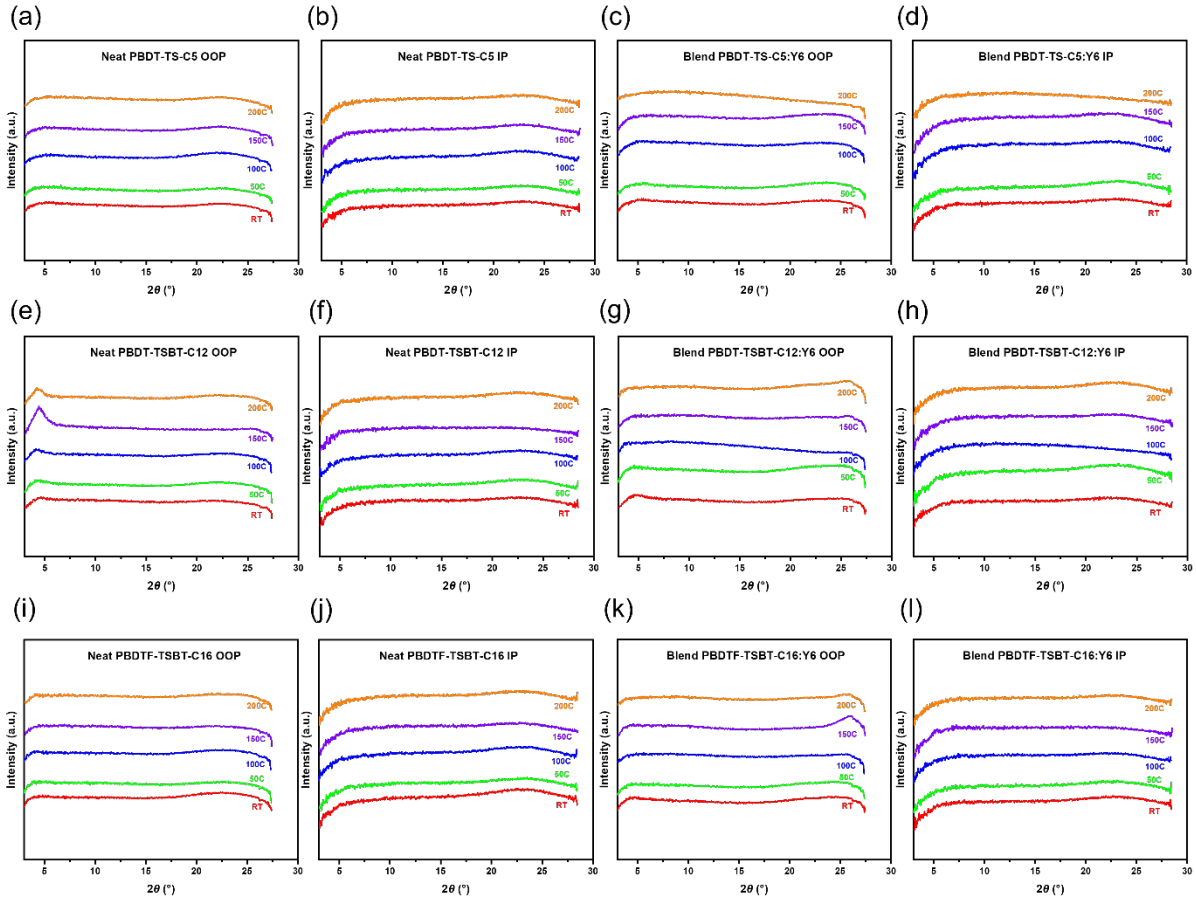


Figure 4-12. Out-of-plane (OOP) and in-plane (IP) 2D-GIXD patterns of neat film PBDT-TS-C5 (a, b), neat film PBDT-TSBT-C12 (e, f), neat film PBDTF-TSBT-C16 (i, j), blend film PBDT-TS-C5:Y6 (c, d), blend film PBDT-TSBT-C12:Y6 (g, h), and blend film PBDTF-TSBT-C16:Y6 (k, l) without annealing (RT) and annealed at different temperatures.

4.5 Conclusion

In summary, we have successfully developed a novel weak electron-withdrawing building block, succinimide-substituted thiophene (TS), and utilized it to synthesize three wide bandgap polymer donors: PBDT-TS-C5, PBDT-TSBT-C12, and PBDTF-TSBT-C16, by incorporating benzodithiophene (BDT or BDTF) units and optional thiophene spacer (T) units. These polymers exhibit E_{HOMO} values of -5.53 eV, -5.35 eV, and -5.51 eV, respectively, and wide bandgaps (E_g) of 2.00 eV, 1.91 eV, and 1.94 eV, respectively, well-suited for matching with the extensively studied NFA, Y6. The SCLC

hole/electron mobilities of the blend films of PBDT-TS-C5:Y6, PBDT-TSBT-C12:Y6, and PBDTF-TSBT-C16:Y6 are 1.52×10^{-4} cm^2 V^{-1} s^{-1}/4.96×10^{-4} cm^2 V^{-1} s^{-1} (with a μ_h/μ_e ratio of 0.31), 1.50×10^{-3} cm^2 V^{-1} s^{-1}/4.57×10^{-4} cm^2 V^{-1} s^{-1} (with a μ_h/μ_e ratio of 3.28), and 1.04×10^{-3} cm^2 V^{-1} s^{-1} and 1.09×10^{-3} cm^2 V^{-1} s^{-1} (with a μ_h/μ_e ratio of 0.95), respectively. The incorporation of thiophene spacers appears to enhance charge transport in PBDT-TSBT-C12 and PBDTF-TSBT-C16 compared to PBDT-TS-C5. The high and balanced SCLC hole and electron mobilities of PBDTF-TSBT-C16:Y6 resulted in a J_{sc} of up to 26.83 mA cm^{-2}, the highest among the three polymer blends. Additionally, the lowered E_{HOMO} for PBDTF-TSBT-C16, achieved through fluorine substitution on the BDT unit, helped attain a relatively high V_{oc} of 0.80 V compared to PBDT-TSBT-C12. Consequently, a highest PCE of 13.21% has been achieved for the PBDTF-TSBT-C16:Y6-based OSC. Notably, the high $V_{oc} \times J_{sc}$ of 20.66 mW cm^{-2} of this device demonstrates the high potential of this wide bandgap polymer donor for high-performance OSCs. However, a suboptimal FF of 0.62 was observed, which is primarily attributed to the poor solubility of PBDTF-TSBT-C16, leading to poor morphology. Nonetheless, this work highlights the promising potential of the simple and conveniently synthesized TS as a new weakly electron-withdrawing building block for wide bandgap polymers in narrow-bandgap NFA-based OSCs and functional conjugated polymers for other applications.

4.6 Experimental Section

4.6.1 General Methods.

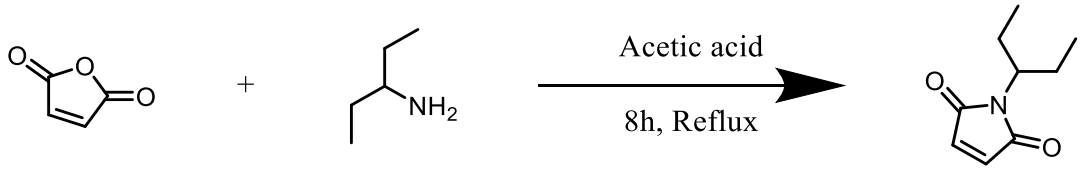
Density functional theory (DFT) calculations were conducted using GaussView 16.0 at the B3LYP/6-31G (d,p) level. ^1H NMR and ^{13}C NMR spectra were recorded on Bruker DPX 300-MHz spectrometer in $CDCl_3$. Chemical shifts were reported relative to internal tetramethylsilane (TMS, 0 ppm). High temperature gel permeation chromatography (GPC) measurements were performed on an Agilent PL-GPC220 system using 1, 2, 4-trichlorobenzene as an eluent at 110 °C with a sample concentration of 10 mg mL^{-1}. Specifically, the GPC column is a highly cross-linked, porous polystyrene/divinylbenzene column of the type PLgel MIXED-B, and the detector employed is a differential refractive index (RI) detector. The UV-Vis absorption spectra of polymers were recorded on a Cary 7000 Universal Measurement Spectrophotometer (UMS). Cyclic voltammetry (CV) data were obtained on a CHI600E electrochemical analyzer using an Ag/AgCl reference electrode and two Pt disk electrodes as the working and counter electrodes, respectively, in 0.1 M tetrabutylammonium

hexafluorophosphate solution in dry acetonitrile at a scan rate of 20 mV s^{-1}. Ferrocene was used as the reference, which has a HOMO energy level of -4.8 eV. Atomic force microscopy (AFM) images of polymer films were taken using a Dimension 3100 scanning probe microscope. Photoluminescence (PL) measurements were conducted on thin films spin-coated on glass substrates using a Horiba PTI QuantaMaster™ 8000 Series Fluorimeter. X-ray diffraction (XRD) patterns were collected using a Bruker D8 Discover powder diffractometer with standard Bragg-Brentano geometry and Cu Kα radiation (λ = 1.5418 Å).

4.6.2 Synthetic Procedures

2,5-Dibromothiophene-3-carboxaldehyde was prepared by bromination of thiophene-3-carboxaldehyde according to literature procedures. 2,6-Bis(trimethytin)-4,8-bis(5-(2-ethylhexyl)thiophen-2-yl)benzo[1,2-b:4,5-b']dithiophene (BDT-Sn) and 2,6-bis(trimethytin)-4,8-bis(5-(2-ethylhexyl)-4-fluorothiophen-2-yl)benzo[1,2-b:4,5b']dithiophene (BDTF-Sn) were purchased from 1-Material. Other chemicals were purchased from commercial sources and used as received.

Synthesis of 1-(pentan-3-yl)-1H-pyrrole-2,5-dione (S-C5)

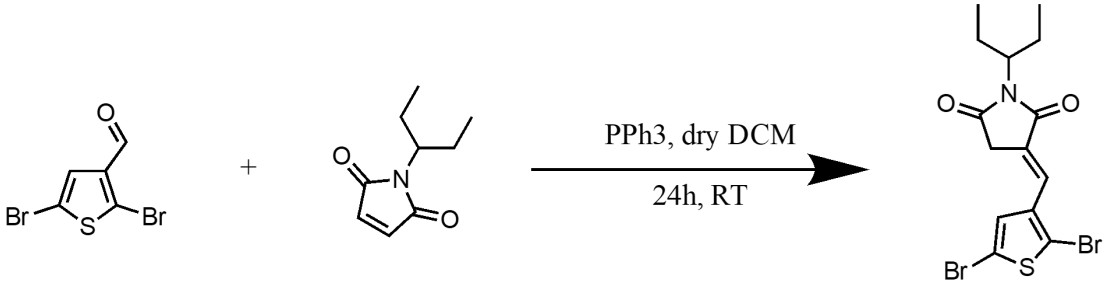


S-C5

A mixture of maleic anhydride (0.98 g, 10 mmol) and 3-aminopentane (0.44 g, 5 mmol) in acetic acid (7.5 mL) was stirred under reflux for 8 h. Then, the reaction mixture was cooled down to room temperature and the reaction mixture was transferred to a beaker. Saturated sodium bicarbonate aqueous solution was added to the beaker under stirring until bubbling stopped. The mixture was extracted with ethyl acetate and the organic layer was washed with 0.1 M dilute HCl (aq.) and then brine solution, respectively. The organic solvent was removed under reduced pressure and the residue was purified by column chromatography on silica gel using ethyl acetate: hexane = 1: 1 to obtain 1-(pentan-3-yl)-1H-

pyrrole-2,5-dione (S-C5). Yield: 0.59 g (59%) ^{1}H NMR (300 MHz, $CDCl_3$): δ 6.60 (s, 2H), 3.73-3.83 (m, 1H), 1.80-1.93 (m, 2H), 1.57-1.72 (m, 2H), 0.75-0.80 (t, J = 7.5 Hz, 6H).

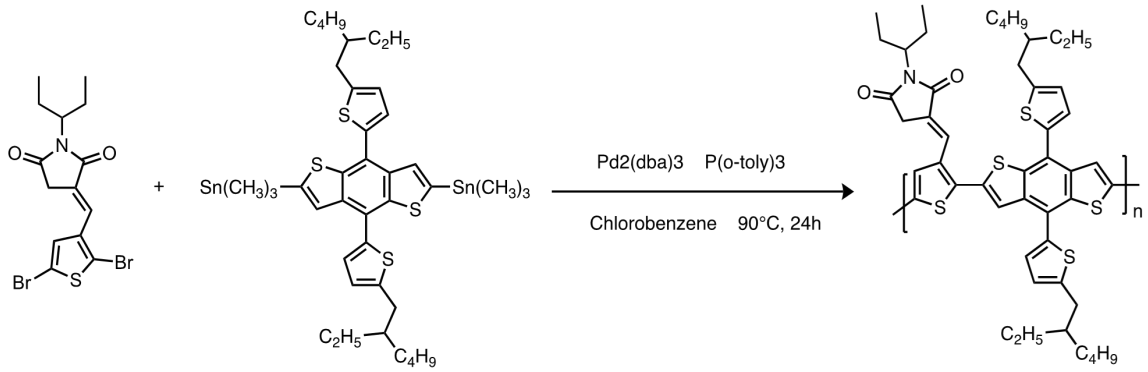
Synthesis of 3-((2,5-dibromothiophen-3-yl)methylene)-1-(pentan-3-yl)pyrrolidine-2,5-dione (TS-C5-Br)



S-C5 **TS-C5-Br**

1-(Pentan-3-yl)-1H-pyrrole-2,5-dione (S-C5) (0.20 g, 1 mmol), 2,5-dibromothiophene-3-carbaldehyde (0.27 g, 1 mmol) and triphenylphosphine (0,26 g, 1 mmol) were dissolved in anhydrous dichloromethane (DCM) (3 mL) and stirred at room temperature for 24 h. After that, the reaction mixture was purified by column chromatography using DCM: hexane = 3:1 and the resulting solid was further washed with methanol and was filtered to obtain 3-((2,5-dibromothiophen-3-yl)methylene)-1-(pentan-3-yl)pyrrolidine-2,5-dione (TS-C5-Br) as a white solid. Yield: 0.20 g (48%) ^{1}H NMR (300 MHz, $CDCl_3$): δ 7.52 (s, 1H), 7.09 (s, 1H), 3.99-4.09 (m, 1H), 3.45 (s, 2H), 1.94-2.10 (m, 2H), 1.69-1.83 (m, 2H), 0.82-0.87 (t, J = 7.5 Hz, 6H). ^{13}C NMR (75 MHz, $CDCl_3$): δ 11.11, 24.52, 33.42, 56.60, 113.13, 118.59, 124.07, 124.64, 128.26, 135.88, 170.95, 173.70. MALDI-MS (m/z): calcd, 421.2; found, 422.0.

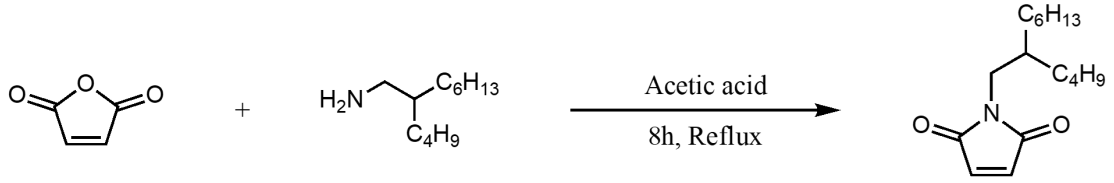
Synthesis of PBDT-TS-C5



TS-C5-Br **BDT-Sn** **PBDT-TS-C5**

To a 25 mL two-neck round bottom flask, 3-((2,5-dibromothiophen-3-yl)methylene)-1-(pentan-3-yl)pyrrolidine-2,5-dione (TS-C5-Br) (69.8 mg, 0.1658 mmol), 2,6-Bis(trimethytin)-4,8-bis(5-(2-ethylhexyl)thiophen-2-yl)benzo[1,2-b:4,5-b']dithiophene (BDT-Sn) (150 mg, 0.1658 mmol) and tris(o-tolyl)phosphine (P(o-tolyl)$_3$) (4 mg, 0.0133 mmol) were added. After the reaction system was purged with argon and evacuated three times, anhydrous chlorobenzene (5 mL) was added to dissolve the mixture, and then tris(dibenzylideneacetone)dipalladium(0) ($Pd_2(dba)_3$) (3 mg, 0.0033 mmol) was added. The reaction mixture was stirred under argon at 90 °C for 24 h before it was cooled to room temperature. Then the reaction mixture was poured into methanol (100 mL), stirred for 1 h, and filtered to obtain a dark red solid. The solid was extracted with acetone, hexane, and then chloroform in a Soxhlet apparatus for 24 h each to give PBDT-TS-C5 as a red solid from the chloroform portion. Yield: 138 mg (99%). GPC: M_n = 18.2 kg mol^{-1}, M_w = 48.4 kg mol^{-1}, and $Đ$ = 2.67.

Synthesis of 1-(2-butyloctyl)-1H-pyrrole-2,5-dione (S-C12)

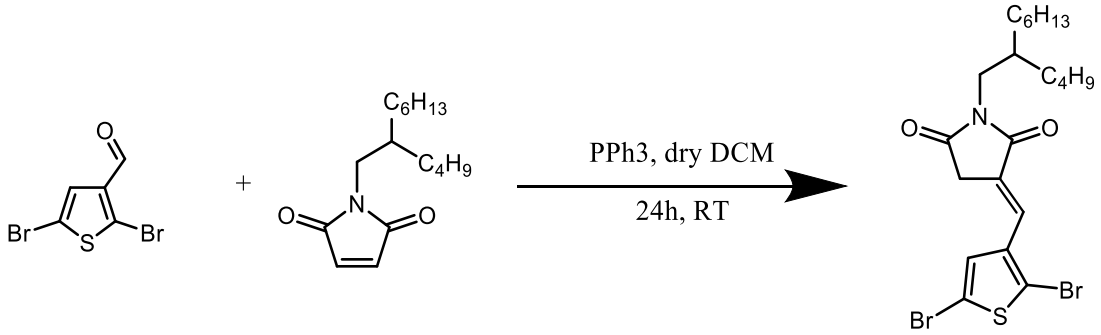


S-C12

A mixture of maleic anhydride (0.84 g, 8.5662 mmol) and 2-butyloctan-1-amine (0.80 g, 4.2831 mmol) in acetic acid (7.5 mL) was stirred under reflux for 8 h at 125 ºC. Then, the reaction mixture

was cooled down to room temperature and the reaction mixture was transferred to a beaker. Saturated sodium bicarbonate aqueous solution was added to the beaker until bubbling stopped. The mixture was extracted with ethyl acetate and the organic layer was washed with 0.1M dilute HCl (aq.) and then brine solution, respectively. The organic solvent was removed under reduced pressure and the residue was purified by column chromatography on silica gel using ethyl acetate: hexane = 1: 1 to obtain 1-(2-butyloctyl)-1H-pyrrole-2,5-dione (S-C12). Yield: 0.72 g (63%) ^{1}H NMR (300MHz, $CDCl_3$): δ 6.68 (s, 2H), 3.38-3.41 (d, J = 9 Hz, 1H), 1.75 (s, 1H), 1.22-1.28 (m, 16H), 0.85-0.90 (m, 6H).

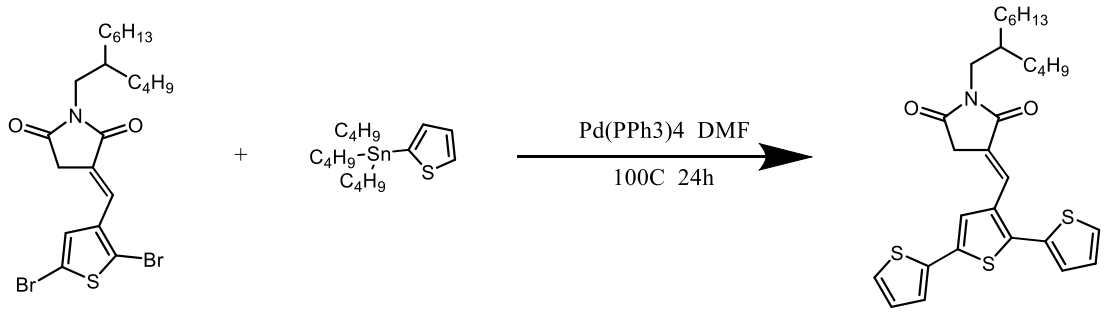
Synthesis of 1-(2-butyloctyl)-3-((2,5-dibromothiophen-3-yl)methylene)pyrrolidine-2,5-dione (TS-C12-Br)



S-C12 **TS-C12-Br**

1-(2-Butyloctyl)-1H-pyrrole-2,5-dione (S-C12) (0.50 g, 1.8840 mmol), 2,5-dibromothiophene-3-carbaldehyde (0.51 g, 1.8840 mmol) and triphenylphosphine (0.49 g, 1.8840 mmol) were dissolved in anhydrous DCM (6 mL) and stirred at room temperature for 24 h. Then, the organic solver was removed and the residue was purified by column chromatography using DCM: hexane = 3:1 and the resulting solid was further washed with methanol and was filtered to obtain 1-(2-butyloctyl)-3-((2,5-dibromothiophen-3-yl)methylene)pyrrolidine-2,5-dione (TS-C12-Br) as a white solid. Yield: 0.34 g (35%) ^{1}H NMR (300 MHz, $CDCl_3$): δ 8.24 (s, 1H), 7.54 (s, 1H), 7.09 (s, 1H), 6.75 (s, 1H), 3.51-3.53 (d, J = 6Hz, 2H), 3.46 (s, 2H), 1.85 (s, 1H), 1.26 (s, 16H), 0.89 (s, 6H).

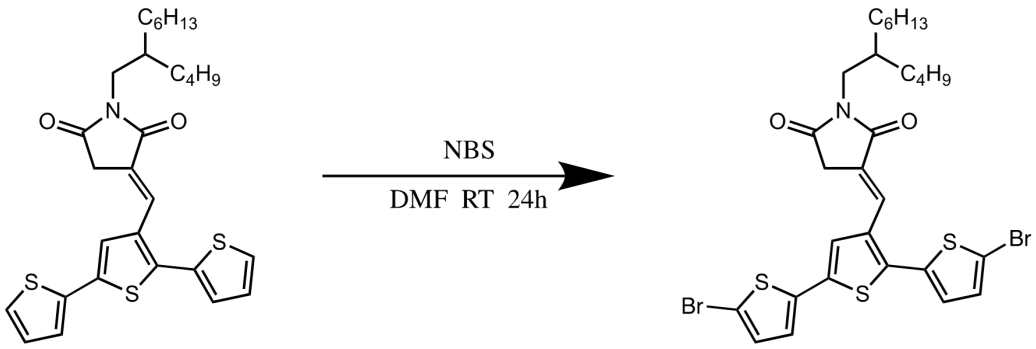
Synthesis of 3-([2,2':5',2''-terthiophen]-3'-ylmethylene)-1-(2-butyloctyl)pyrrolidine-2,5-dione (TSBT-C12)



TS-C12-Br **TSBT-C12**

1-(2-Butyloctyl)-3-((2,5-dibromothiophen-3-yl)methylene)pyrrolidine-2,5-dione (TS-C12-Br) (0.20 g, 0.3859 mmol), 2-(tributylstannyl)thiophene (0.36 g, 0.9648 mmol) were added to a 50 mL two-neck round bottom flask. After the reaction system was purged with argon and evacuated three times, anhydrous N, N-dimethylformamide (DMF) (5 mL) was added to dissolve the mixture, followed by the addition of a solution of tetrakis(triphenylphosphine)palladium ($Pd(PPh_3)_4$) (5 mg, 0.0039 mmol) in DMF using a syringe. The reaction mixture was heated at 100 ºC under argon atmosphere in the dark for 24 h. After cooling to room temperature, a potassium fluoride (KF) aqueous solution was added. The crude product was collected by filtration and purified by column chromatography on silica gel using DCM: hexane = 1: 5 as eluent to afford 3-([2,2':5',2''-terthiophen]-3'-ylmethylene)-1-(2-butyloctyl)pyrrolidine-2,5-dione (TSBT-C12) as a yellow solid. Yield: 0.18 g (90%) ^{1}H NMR (300 MHz, $CDCl_3$): δ 7.82 (s, 1H), 7.43-7.45 (d, J = 6 Hz, 1H), 7.30-7.31 (d, J = 3 Hz, 1H), 7.20-7.23 (m, 2H), 7.12-7.15 (m, 1H), 7.05-7.08 (m, 1H), 3.58 (s, 2H), 3.51-3.54 (d, J = 9 Hz, 2H), 1.86 (s, 1H), 1.27 (s, 16H), 0.89 (s, 6H). ^{13}C NMR (75 MHz, $CDCl_3$): δ 14.09, 22.67, 23.02, 26.27, 28.47, 29.67, 31.18, 31.55, 31.83, 34.04, 36.41, 43.28, 112.64, 122.92, 124.74, 125.56, 126.62, 127.92, 128.13, 128.29, 128.39, 132.59, 133.65, 135.83, 137.15, 139.50, 171.31, 174.21.

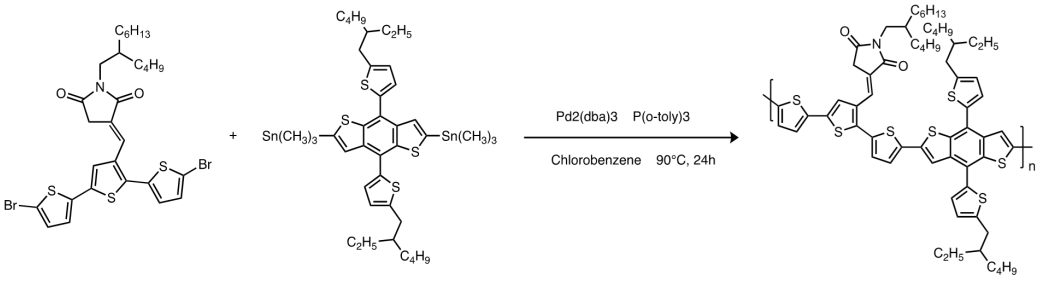
Synthesis of 1-(2-butyloctyl)-3-((5,5’’-dibromo-[2,2’:5’,2’’-terthiophen]-3’-yl)methylene)pyrrolidine-2,5-dione (TSBT-C12-Br)



TSBT-C12 **TSBT-C12-Br**

3-([2,2’:5’,2’’-Terthiophen]-3’-ylmethylene)-1-(2-butyloctyl)pyrrolidine-2,5-dione (TSBT-C12) (0.16 g, 0.3043 mmol) was dissolved in in DMF (5 mL) and N-bromosuccinimide (NBS) (0.11 g, 0.6238 mmol) was added in one portion. The reaction mixture was stirred at room temperature for 24 h in the dark. Then, water was added into the mixture, followed by extraction with DCM. The organic layer was washed with brine and dried over anhydrous sodium sulfate. After evaporating the organic solvent under reduced pressure, the residue was purified by column chromatography on silica gel using DCM: hexane = 2: 1 to afford 1-(2-butyloctyl)-3-((5,5’’-dibromo-[2,2’:5’,2’’-terthiophen]-3’-yl)methylene)pyrrolidine-2,5-dione (TSBT-C12-Br) as a yellow oil. Yield: 0.18 g (86%) ^{1}H NMR (300 MHz, $CDCl_3$): δ 7.73 (s, 1H), 7.16 (s, 1H), 7.09-7.10 (d, J = 3 Hz, 1H), 7.02-7.03 (d, J = 3 Hz, 1H), 6.94-6.97 (m, 2H), 3.53 (s, 2H), 3.51 (s, 2H), 1.86 (s, 1H), 1.26 (s, 16H), 0.85-0.91 (m, 6H). ^{13}C NMR (75 MHz, $CDCl_3$): δ 14.08, 22.66, 23.00, 26.26, 28.46, 29.66, 31.19, 31.56, 31.82, 33.94, 36.41, 43.35, 112.61, 115.01, 122.85, 123.78, 125.03, 125.82, 128.68, 130.97, 131.14, 133.05, 134.82, 136.52, 136.98, 138.22, 171.07, 173.87. MALDI-MS (m/z): calcd, 683.6; found, 683.1.

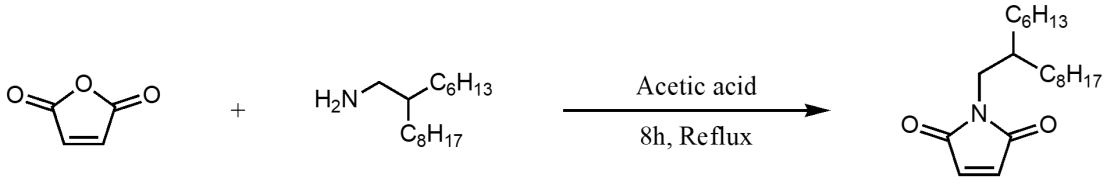
Synthesis of PBDT-TSBT-C12



TSBT-C12-Br **BDT-Sn** **PBDT-TSBT-C12**

To a 25 mL two-neck round bottom flask, 1-(2-butyloctyl)-3-((5,5''-dibromo-[2,2':5',2''-terthiophen]-3'-yl)methylene)pyrrolidine-2,5-dione (TSBT-C12-Br) (83.7 mg, 0.1224 mmol), 2,6-Bis(trimethytin)-4,8-bis(5-(2-ethylhexyl)thiophen-2-yl)benzo[1,2-b:4,5-b']dithiophene (BDT-Sn) (110.7 mg, 0.1224 mmol) and P(o-tolyl)$_3$ (3 mg, 0.0098 mmol) were added. After the reaction system was purged with argon and evacuated three times, anhydrous chlorobenzene (4 mL) was added to dissolve the mixture, and then $Pd_2(dba)_3$ (2.3 mg, 0.0025 mmol) was added. The reaction mixture was stirred under argon at 90 °C for 24 h before it was cooled to room temperature. Then the reaction mixture was poured into methanol (100 mL), stirred for 1 h, and filtered to obtain a dark red solid. The solid was extracted with acetone, hexane, and then chloroform in a Soxhlet apparatus for 24 h each to give PBDT-TSBT-C12 as a red solid from the chloroform portion. Yield: 120 mg (89%). GPC: M_n = 18.0 kg mol^{-1}, M_w = 47.6 kg mol^{-1}, and $Đ$ = 2.64.

Synthesis of 1-(2-hexyldecyl)-1H-pyrrole-2,5-dione (S-C16)

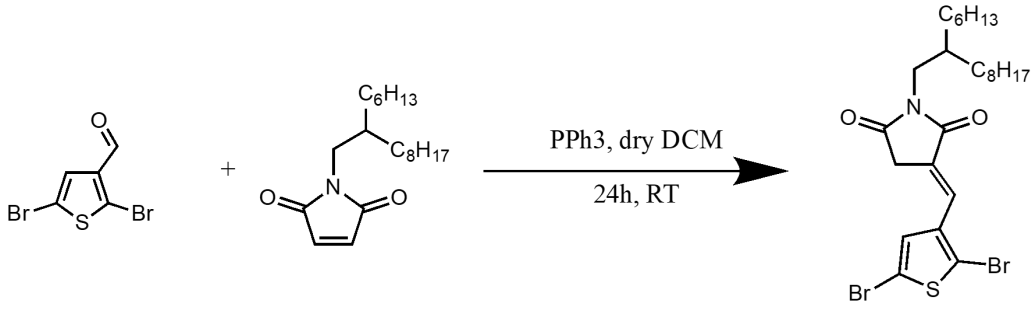


S-C16

A mixture of maleic anhydride (2.12 g, 21.5796 mmol) and 2-hexyldecyl amine (2.61 g, 10.7898 mmol) in acetic acid (16.2 mL) were stirred under reflux for 8 h. Then, the reaction mixture was cooled

down to room temperature and the reaction mixture was transferred to a beaker. A saturated sodium bicarbonate aqueous solution was added to the beaker until bubbling stopped. The mixture was extracted with ethyl acetate and the organic layer was washed with 0.1 M dilute HCl (aq.) and then brine solution, respectively. The solvent was removed under reduced pressure and the residue was purified by column chromatography on silica gel using ethyl acetate: hexane = 1: 1 to obtain 1-(2-hexyldecyl)-1H-pyrrole-2,5-dione (S-C16). Yield: 2.0 g (70%) ^{1}H NMR (300MHz, $CDCl_3$): δ 6.68 (s, 2H), 3.38-3.41 (d, J = 9 Hz, 2H), 1.75 (s, 1H), 1.25 (s, 24H), 0.85-0.90 (t, J = 9 Hz, 6H). ^{13}C NMR (75 MHz, $CDCl_3$): δ 14.09, 22.64, 26.19, 29.30, 29.53, 29.63, 29.97, 31.37, 31.79, 31.89, 36.94, 42.11, 133.96, 171.15.

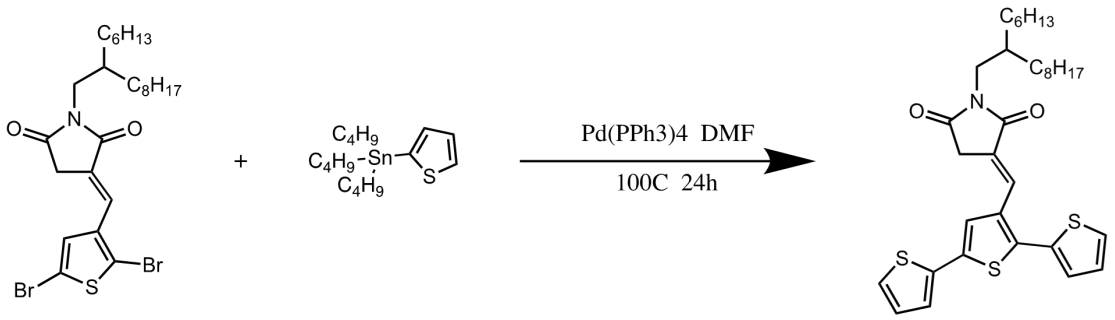
Synthesis of 3-((2,5-dibromothiophen-3-yl)methylene)-1-(2-hexyldecyl)pyrrolidine-2,5-dione (TS-C16-Br)



S-C16 **TS-C16-Br**

1-(2-Hexyldecyl)-1H-pyrrole-2,5-dione (S-C16) (2.0 g, 6.2206 mmol), 2,5-dibromothiophene-3-carbaldehyde (2.02 g, 7.4647 mmol) and triphenylphosphine (1.63 g, 6.2206 mmol) were dissolved in anhydrous DCM (18 mL) and stirred at room temperature for 24 h. After evaporating the solvent under reduced pressure, the residue was purified by column chromatography using DCM: hexane = 3:1 and the resulting solid was further washed with methanol and was filtered to obtain 3-((2,5-dibromothiophen-3-yl)methylene)-1-(2-hexyldecyl)pyrrolidine-2,5-dione (TS-C16-Br) as a white solid. Yield: 1.2 g (34%) ^{1}H NMR (300 MHz, $CDCl_3$): δ 8.24 (s, 1H), 7.54 (s, 1H), 7.09 (s, 1H), 6.75 (s, 1H), 3.51-3.53 (d, J = 6Hz, 2H), 3.46 (s, 2H), 1.85 (s, 1H), 1.26 (s, 24H), 0.89 (s, 6H).

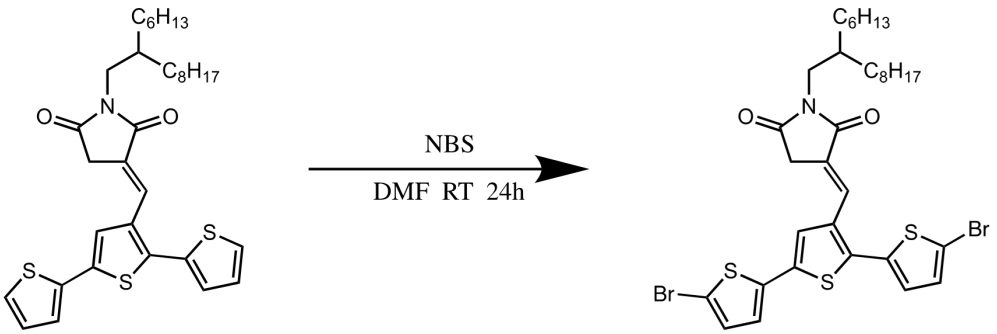
Synthesis of 3-([2,2':5',2''-terthiophen]-3'-ylmethylene)-1-(2-hexyldecyl)pyrrolidine-2,5-dione (TSBT-C16)



TS-C16-Br **TSBT-C16**

3-((2,5-Dibromothiophen-3-yl)methylene)-1-(2-hexyldecyl)pyrrolidine-2,5-dione (TS-C16-Br) (0.50 g, 0.8689 mmol), 2-(tributylstannyl)thiophene (0.81 g, 2.1723 mmol) were added to a 50 mL two-neck round bottom flask. After the reaction system was purged with argon and evacuated three times, anhydrous DMF (10 mL) was added to dissolve the mixture and then a solution of $Pd(PPh_3)_4$ (10 mg, 0.0087 mmol) in DMF was added with a syringe. The reaction mixture was heated at 100 ºC under argon atmosphere in the dark for 24 h. After cooling to room temperature, potassium fluoride (KF) aqueous solution was added, then the crude product was collected by filtration, and purified by column chromatography on silica gel using DCM: hexane = 1: 2 as eluent to afford 3-([2,2':5',2''-terthiophen]-3'-ylmethylene)-1-(2-hexyldecyl)pyrrolidine-2,5-dione (TSBT-C16) as yellow solid. Yield: 0.38 g (75%) ^{1}H NMR (300 MHz, $CDCl_3$): δ 7.82 (s, 1H), 7.43-7.45 (d, J = 6 Hz, 1H), 7.29-7.31 (d, J = 6 Hz, 1H), 7.20-7.23 (m, 2H), 7.12-7.15 (m, 1H), 7.05-7.08 (m, 1H), 3.58 (s, 2H), 3.51-3.53 (d, J = 6 Hz, 2H), 1.86 (s, 1H), 1.25 (s, 24H), 0.84-0.89 (m, 6H).

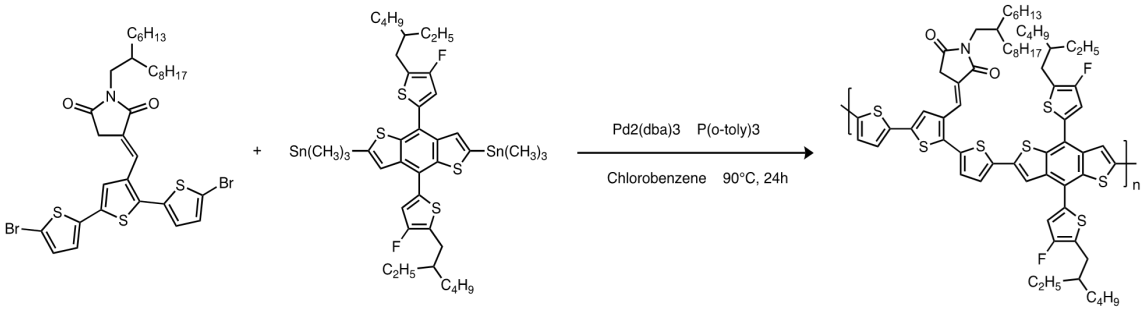
Synthesis of 3-((5,5’’-dibromo-[2,2’:5’,2’’-terthiophen]-3’-yl)methylene)-1-(2-hexyldecyl)pyrrolidine-2,5-dione (TSBT-C16-Br)



TSBT-C16 **TSBT-C16-Br**

3-([2,2’:5’,2’’-terthiophen]-3’-ylmethylene)-1-(2-hexyldecyl)pyrrolidine-2,5-dione (TSBT-C16) (0.30 g, 0.5156 mmol) was added into DMF (10 mL). After the solid dissolved completely, N-bromosuccinimide (NBS) (0.19 g, 1.2331 mmol) was added in one portion, and the reaction mixture was stirred at room temperature for 24 h. Then, water was added into the mixture, and the mixture was extracted with DCM. The organic layer was washed with brine and dried over anhydrous sodium sulfate. The solvent was removed under reduced pressure, and the residue was purified by column chromatography on silica gel using DCM: hexane = 2: 1 to afford 3-((5,5’’-dibromo-[2,2’:5’,2’’-terthiophen]-3’-yl)methylene)-1-(2-hexyldecyl)pyrrolidine-2,5-dione (TSBT-C16-Br) as a yellow oil. Yield: 0.33 g (87%) ^{1}H NMR (300 MHz, $CDCl_3$): δ 7.72 (s, 1H), 7.16 (s, 1H), 7.09-7.10 (d, J = 3 Hz, 1H), 7.02-7.03 (d, J = 3 Hz, 1H), 6.94-6.97 (m, 2H), 3.53 (s, 2H), 3.51 (s, 2H), 1.86 (s, 1H), 1.26 (s, 24H), 0.87 (s, 6H). ^{13}C NMR (75 MHz, $CDCl_3$): δ 14.12, 22.66, 26.25, 29.32, 29.56, 29.65, 29.98, 31.55, 31.82, 33.95, 36.44, 43.37, 112.60, 115.01, 122.84, 123.77, 125.03, 125.81, 128.68, 130.97, 131.14, 133.04, 134.82, 136.52, 136.98, 138.22, 171.07, 173.87. MALDI-MS (m/z): calcd, 739.7; found, 739.1.

Synthesis of PBDTF-TSBT-C16



TSBT-C16-Br **BDTF-Sn** **PBDTF-TSBT-C16**

To a 25 mL two-neck round bottom flask, 3-((5,5''-dibromo-[2,2':5',2''-terthiophen]-3'-yl)methylene)-1-(2-hexyldecyl)pyrrolidine-2,5-dione (TSBT-C16-Br) (122.6 mg, 0.1658 mmol), 2,6-bis(trimethytin)-4,8-bis(5-(2-ethylhexyl)-4-fluorothiophen-2-yl)benzo[1,2-b:4,5b']dithiophene (BDTF-Sn) (155.9 mg, 0.1658 mmol) and P(o-tolyl)$_3$ (4 mg, 0.0133 mmol) were added. After the reaction system was purged with argon and evacuated three times, anhydrous chlorobenzene (5 mL) was added to dissolve the mixture, and then $Pd_2(dba)_3$ (3 mg, 0.0033 mmol) was added. The reaction mixture was stirred under argon at 90 °C for 24 h before it was cooled to room temperature. Then the reaction mixture was poured into methanol (100 mL), stirred for 1 h, and filtered to obtain a dark red solid. The solid was extracted with acetone, hexane, and then chloroform in a Soxhlet apparatus for 24 h each to give PBDTF-TSBT-C16 as a red solid from the chlorobenzene portion. Yield: 95 mg (48%) from the chlorobenzene fraction. GPC: M_n = 36.4 kg mol^{-1}, M_w = 89.2 kg mol^{-1}, and $Đ$ = 2.45. The remaining fraction (~50%) is insoluble in any solvent.

4.6.3 OSC device fabrication

Inverted polymer solar cells were fabricated with the configuration of ITO (150 nm)/ ZnO (35 nm)/ Active layer/ MoO_x (10 nm)/ Ag (100 nm). The conductive indium-doped tin oxide (ITO) glass substrate was cleaned with deionized water and acetone in an ultrasonic bath at 40 °C for 20 min each. The substrate was then removed and cleaned with a cotton swab moistened with acetone. The substrate was again sonicated in isopropanol (IPA) at 40 °C for 20 min. The substrate was dried with an N2 stream and treated in an air plasma cleaner for 10 min. A thin layer of ZnO (~35 nm) was deposited by spin-coating a freshly prepared ZnO precursor solution at 3500 rpm and subsequently annealed at 200

°C for 1 h in air. (The ZnO precursor solution was prepared by stirring a mixture of zinc acetate (197 mg), ethanolamine (54 μL), and 2-methoxyethanol (2 mL) at 50 °C overnight.) Then the substrates were transferred to a nitrogen filled glove box, where the donor (PBDT-TS-C5, PBDT-TSBT-C12 or PBDTF-TSBT-C16) and acceptor (Y6) mixture (at a 1:1 or other mass ratios) solution in chloroform (CF) was spin-coated onto the ZnO layer at various speeds to obtain the blend layers with the desired thickness. The concentration of the donor/acceptor solution is 16 mg mL^{-1} in CF. Following an optional annealing process (for 10 min), a thin MoO_x hole transport layer (10 nm) and an Ag electrode layer (100 nm) were sequentially deposited onto the substrate using thermal deposition under a pressure below 5.0×10^{-6} Pa. The active area of each OSC device is 0.0256 cm^2 defined by a mask. The current density-voltage (*J-V*) characteristics of the solar cells were measured on an Agilent B2912A Semiconductor Analyzer and a ScienceTech SLB300-A Solar Simulator. A 450 W xenon lamp and an air mass (AM) 1.5 filter were used as the light source. External quantum efficiency (EQE) measurements were performed in air within 3 h after device fabrication using a QEX10 Solar Cell Quantum Efficiency Measurement System (PV measurements, Inc.).

4.6.4 Appendix

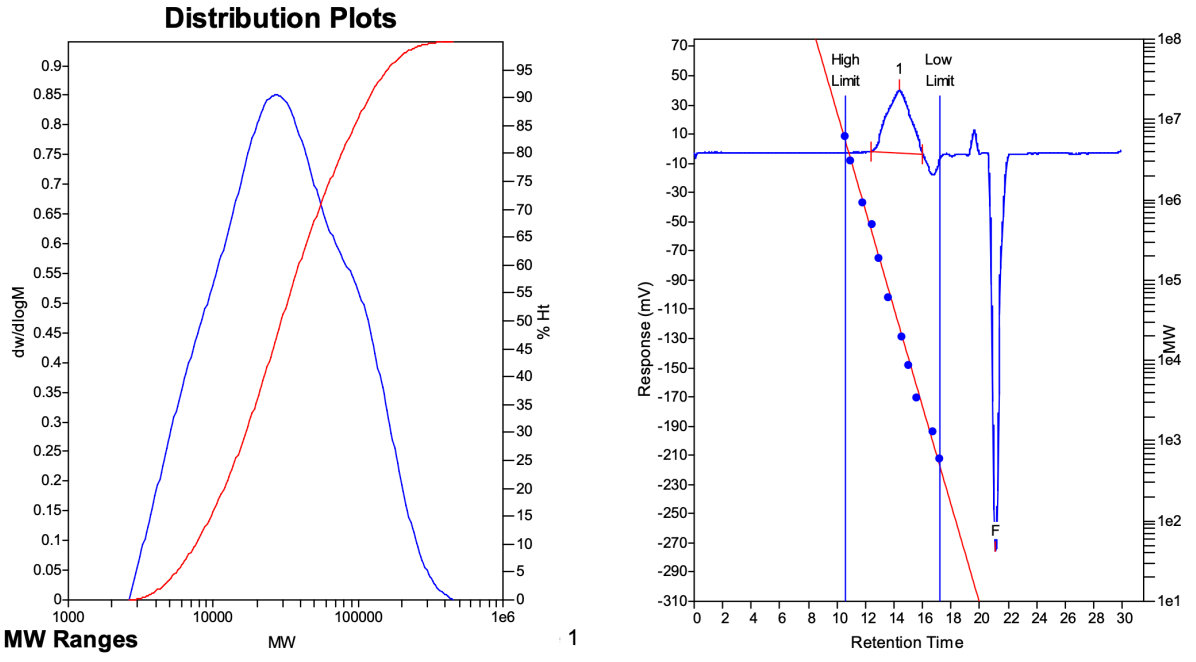


Figure 4-13. HT-GPC data of polymer PBDT-TS-C5.

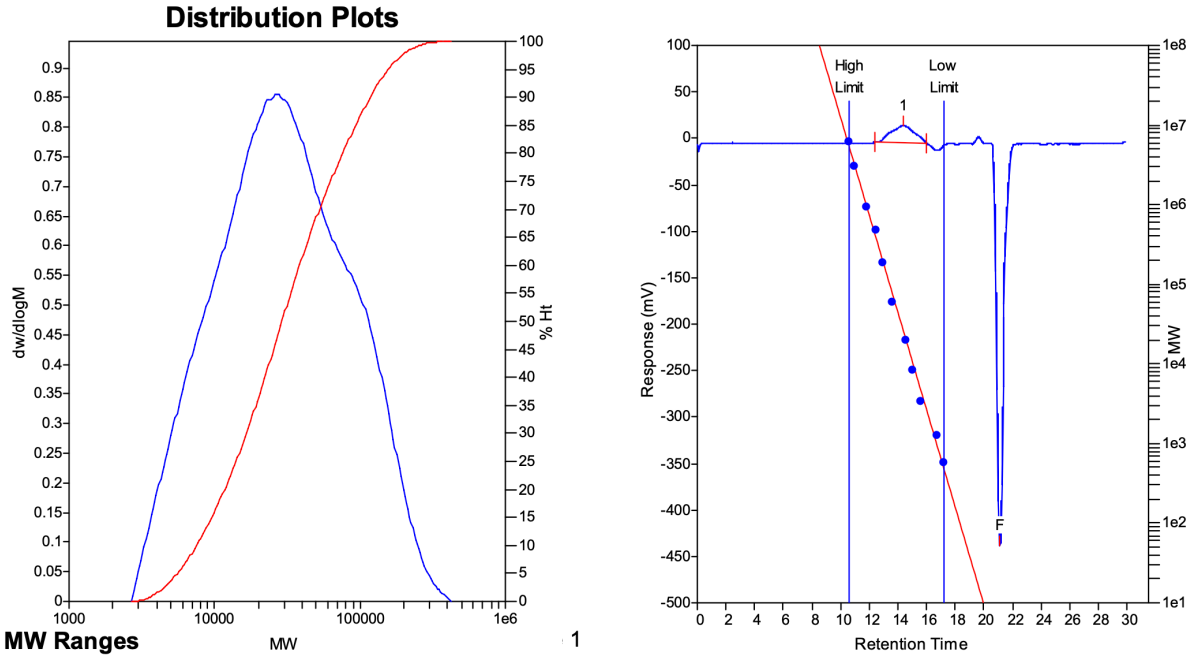


Figure 4-14. HT-GPC data of polymer PBDT-TSBT-C12.

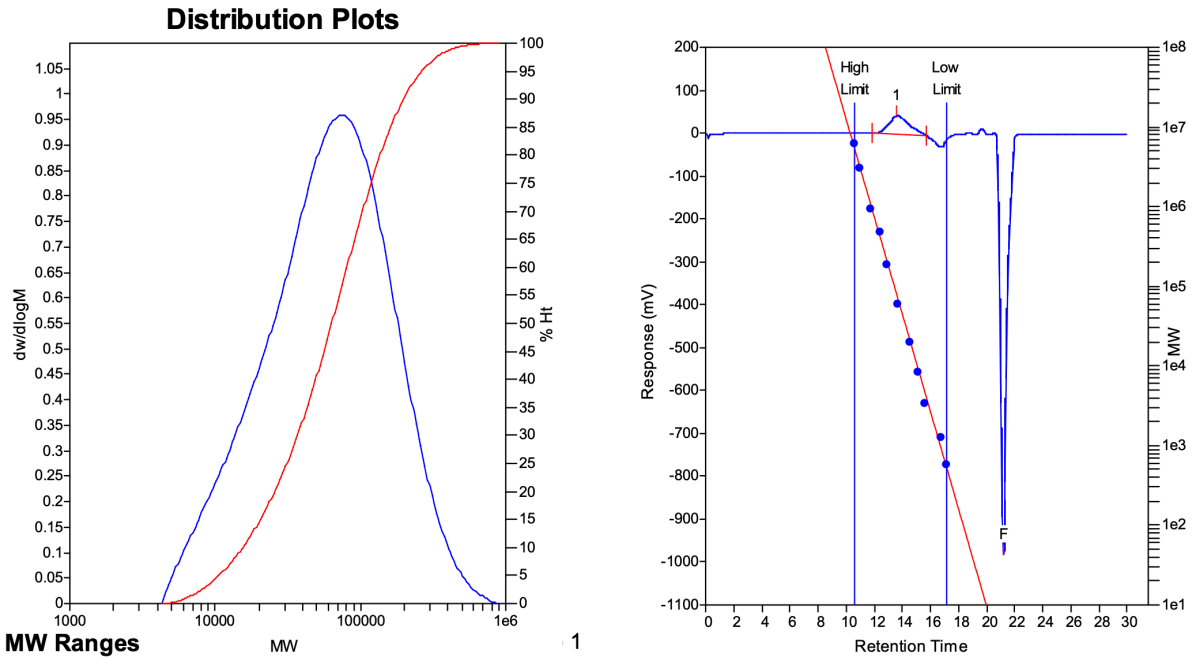


Figure 4-15. HT-GPC data of polymer PBDTF-TSBT-C16.

Table 4-7. Summary of the photovoltaic properties of the PBDT-TS-C5:Y6 devices processed with chloroform at different RPMs at room temperature.

Materials	RPM	J_{sc} (mA/cm^2)	V_{oc} (V)	FF	PCE (%)	Rs, Ω cm^2	Rsh, Ω cm^2
PBDT-TS-C5:Y6	1500	-17.51	0.90	0.41	6.57	24.57	138.72
PBDT-TS-C5:Y6	2000	-16.85	0.89	0.42	6.29	22.73	139.18
PBDT-TS-C5:Y6	2500	-16.70	0.89	0.45	6.63	20.81	197.97

Active layer thickness: ~100 nm for RPM 2500.

Table 4-8. Summary of the photovoltaic properties of the PBDT-TS-C5:Y6 devices processed with chloroform at different annealing temperatures with 2500 RPM.

Materials	Annealing Temperature	J_{sc} (mA/cm^2)	V_{oc} (V)	FF	PCE (%)	Rs, Ω cm^2	Rsh, Ω cm^2
PBDT-TS-C5:Y6	RT	-17.76	0.91	0.48	7.72	6.72	181.92
PBDT-TS-C5:Y6	50°C	-17.40	0.92	0.47	7.42	8.53	187.72
PBDT-TS-C5:Y6	100°C	-17.34	0.89	0.48	7.33	5.76	225.24
PBDT-TS-C5:Y6	150°C	-19.36	0.89	0.50	8.51	5.81	179.53

Table 4-9. Summary of the photovoltaic properties of the PBDT-TS-C5:Y6 devices processed with chloroform with different solvent additives annealed at 150°C with 2500 RPM.

Materials	Additives	J_{sc} (mA/cm^2)	V_{oc} (V)	FF	PCE (%)	Rs, Ω cm^2	Rsh, Ω cm^2
PBDT-TS-C5:Y6	CN [0.5% v/v]	-19.03	0.88	0.44	7.33	8.61	151.69
PBDT-TS-C5:Y6	DIO [0.5% v/v]	-15.87	0.84	0.44	5.88	9.32	193.54

Table 4-10. Summary of the photovoltaic properties of the PBDT-TS-C5:Y6 devices processed with chloroform with different weight ratio of donor and acceptor annealed at 150°C with 2500 RPM.

Materials	Weight Ratio (D:A)	J_{sc} (mA/cm^2)	V_{oc} (V)	FF	PCE (%)	Rs, Ω cm^2	Rsh, Ω cm^2
PBDT-TS-C5:Y6	1.1:1	-18.36	0.89	0.44	7.17	7.43	168.73
PBDT-TS-C5:Y6	1:1.1	-19.57	0.89	0.46	8.01	7.01	192.43

Table 4-11. Summary of the photovoltaic properties of the PBDT-TSBT-C12:Y6 devices processed with chloroform at different RPMs at room temperature.

Materials	RPM	J_{sc} (mA/cm^2)	V_{oc} (V)	FF	PCE (%)	Rs, Ω cm^2	Rsh, Ω cm^2
PBDT-TSBT-C12:Y6	1500	-25.32	0.69	0.54	9.44	4.56	330.14
PBDT-TSBT-C12:Y6	2000	-24.88	0.68	0.54	9.13	4.24	261.62
PBDT-TSBT-C12:Y6	2500	-22.01	0.70	0.58	8.84	4.27	631.04

Active layer thickness: ~120 nm for RPM 1500.

Table 4-12. Summary of the photovoltaic properties of the PBDT-TSBT-C12:Y6 devices processed with chloroform at different annealing temperatures with 1500 RPM.

Materials	Annealing Temperature	J_{sc} (mA/cm^2)	V_{oc} (V)	FF	PCE (%)	Rs, Ω cm^2	Rsh, Ω cm^2
PBDT-TSBT-C12:Y6	RT	-24.37	0.72	0.58	10.24	3.97	349.37
PBDT-TSBT-C12:Y6	50°C	-24.29	0.72	0.60	10.45	3.90	305.92
PBDT-TSBT-C12:Y6	100°C	-24.84	0.71	0.60	10.47	3.88	339.25
PBDT-TSBT-C12:Y6	150°C	-26.15	0.65	0.61	10.44	3.52	442.03

Table 4-13. Summary of the photovoltaic properties of the PBDT-TSBT-C12:Y6 devices processed with chloroform with different solvent additives annealed at 100°C with 1500 RPM.

Materials	Additives	J_{sc} (mA/cm^2)	V_{oc} (V)	FF	PCE (%)	Rs, Ω cm^2	Rsh, Ω cm^2
PBDT-TSBT-C12:Y6	CN [0.5% v/v]	-25.01	0.67	0.59	9.86	4.10	453.19
PBDT-TSBT-C12:Y6	DIO [0.5% v/v]	-23.13	0.64	0.54	8.01	4.99	233.85

Table 4-14. Summary of the photovoltaic properties of the PBDT-TSBT-C12:Y6 devices processed with chloroform with different weight ratio of donor and acceptor annealed at 100°C with 1500 RPM.

Materials	Weight Ratio (D:A)	J_{sc} (mA/cm^2)	V_{oc} (V)	FF	PCE (%)	Rs, Ω cm^2	Rsh, Ω cm^2
PBDT-TSBT-C12:Y6	1.1:1	-24.10	0.68	0.63	10.29	3.42	454.66
PBDT-TSBT-C12:Y6	1:1.1	-24.09	0.67	0.63	10.17	3.48	453.88

Table 4-15. Summary of the photovoltaic properties of the PBDTF-TSBT-C16:Y6 devices processed with chloroform at different RPMs at room temperature.

Materials	RPM	J_{sc} (mA/cm^2)	V_{oc} (V)	FF	PCE (%)	Rs, Ω cm^2	Rsh, Ω cm^2
PBDTF-TSBT-C16:Y6	1500	-22.50	0.82	0.53	9.81	4.83	357.06
PBDTF-TSBT-C16:Y6	2000	-22.83	0.83	0.55	10.34	5.09	317.65
PBDTF-TSBT-C16:Y6	2500	-22.32	0.83	0.59	10.82	4.67	215.46

Active layer thickness: ~100 nm for RPM 2500.

Table 4-16. Summary of the photovoltaic properties of the PBDTF-TSBT-C16:Y6 devices processed with chloroform at different annealing temperatures with 2500 RPM.

Materials	Annealing Temperature	J_{sc} (mA/cm^2)	V_{oc} (V)	FF	PCE (%)	Rs, Ω cm^2	Rsh, Ω cm^2
PBDTF-TSBT-C16:Y6	RT	-21.73	0.84	0.60	10.96	3.82	466.40
PBDTF-TSBT-C16:Y6	50°C	-21.82	0.84	0.60	11.06	3.80	318.14
PBDTF-TSBT-C16:Y6	100°C	-21.76	0.83	0.60	10.97	3.73	383.48
PBDTF-TSBT-C16:Y6	150°C	-21.72	0.81	0.64	11.21	3.60	652.14

Table 4-17. Summary of the photovoltaic properties of the PBDTF-TSBT-C16:Y6 devices processed with chloroform with different solvent additives annealed at 150°C with 2500 RPM.

Materials	Additives	J_{sc} (mA/cm^2)	V_{oc} (V)	FF	PCE (%)	Rs, Ω cm^2	Rsh, Ω cm^2
PBDTF-TSBT-C16:Y6[a]	CN [0.5% v/v]	-26.83	0.80	0.62	13.21	3.90	470.41
PBDTF-TSBT-C16:Y6	DIO [0.5% v/v]	-18.53	0.78	0.66	9.48	3.51	497.80

Active layer thickness: ~130 nm.

Table 4-18. Summary of the photovoltaic properties of the PBDTF-TSBT-C16:Y6 devices processed with chloroform and 0.5%CN with different weight ratio of donor and acceptor annealed at 150°C with 2500 RPM.

Materials	Weight Ratio (D:A)	J_{sc} (mA/cm^2)	V_{oc} (V)	FF	PCE (%)	Rs, Ω cm^2	Rsh, Ω cm^2
PBDTF-TSBT-C16:Y6	1.1:1	-23.76	0.81	0.62	11.82	3.65	467.38
PBDTF-TSBT-C16:Y6	1:1.1	-22.00	0.82	0.64	11.47	3.47	558.05

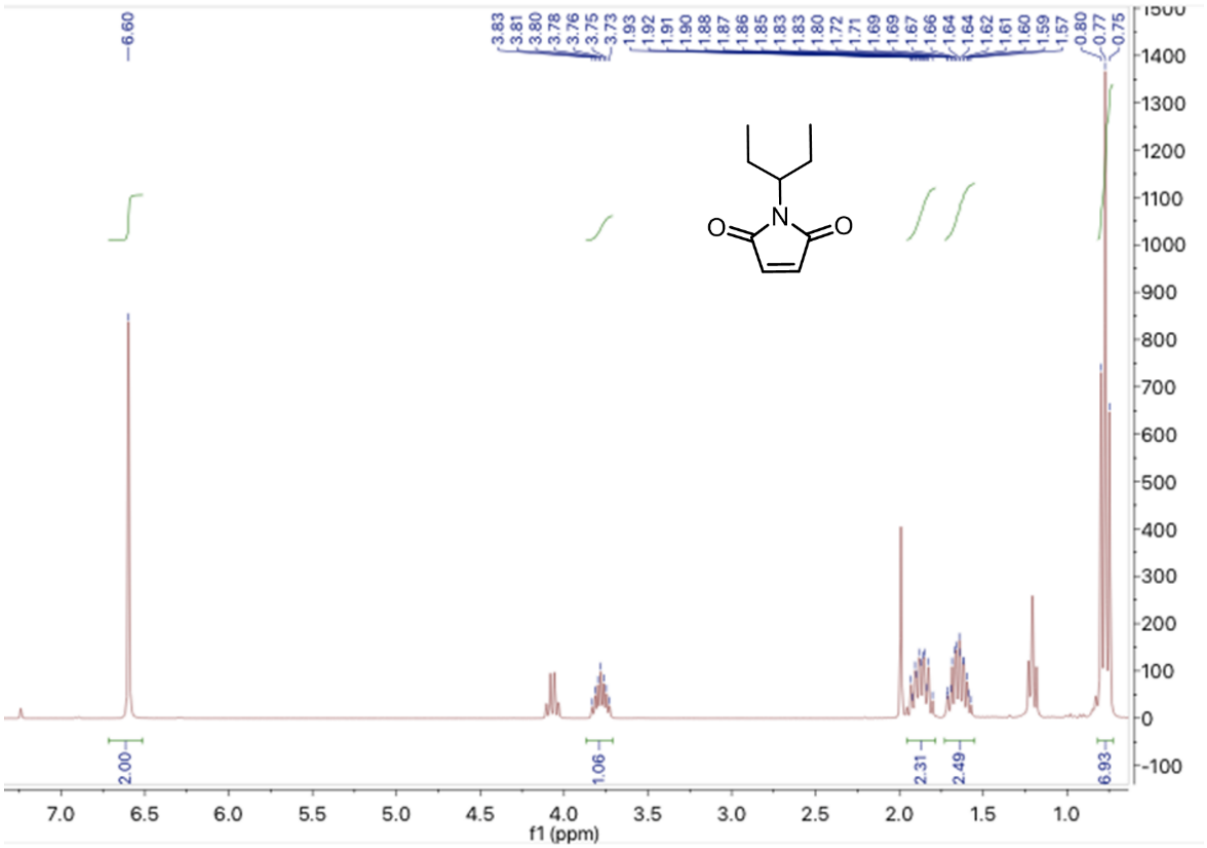


Figure 4-16. ^{1}H NMR (300MHz, $CDCl_3$) spectra of 1-(pentan-3-yl)-1H-pyrrole-2,5-dione (S-C5).

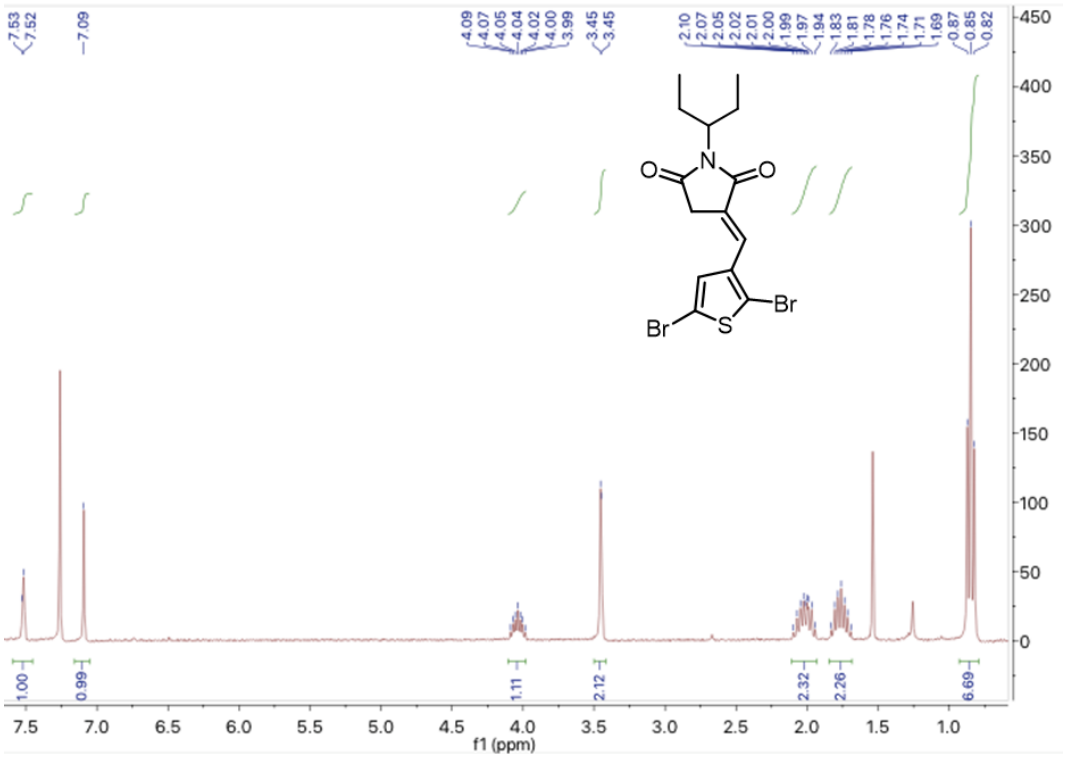


Figure 4-17. ^{1}H NMR (300MHz, $CDCl_3$) spectra of 3-((2,5-dibromothiophen-3-yl)methylene)-1-(pentan-3-yl)pyrrolidine-2,5-dione (TS-C5-Br).

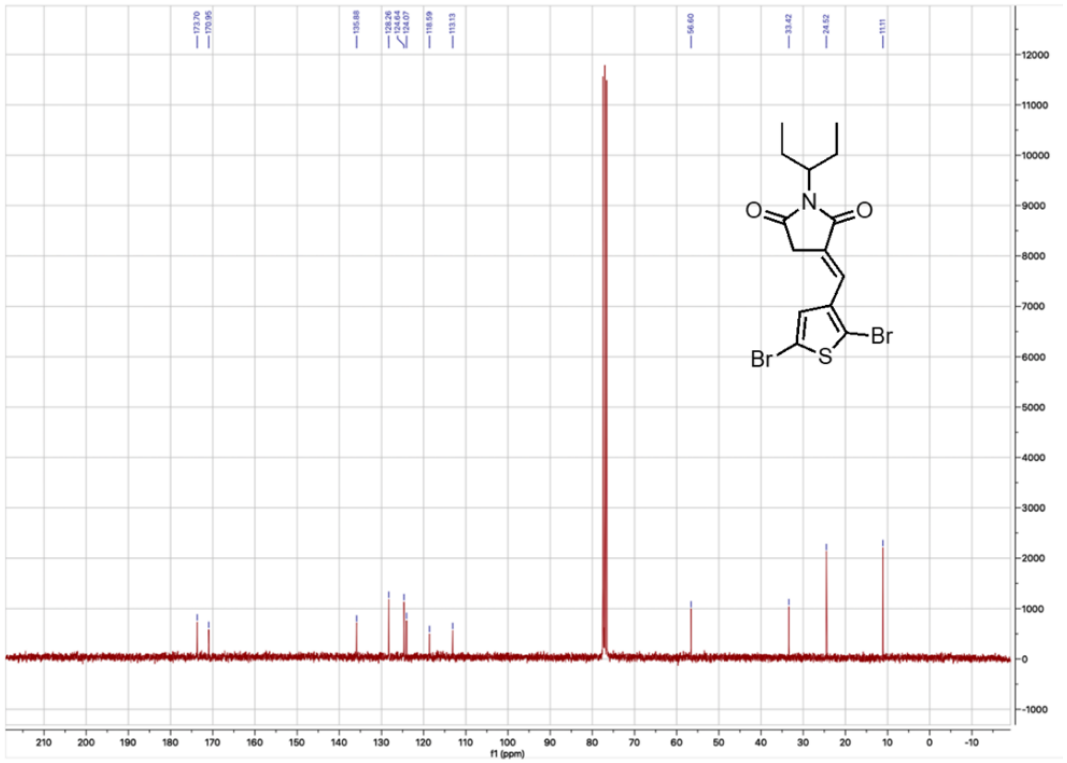


Figure 4-18. ^{13}C NMR (75MHz, $CDCl_3$) spectra of 3-((2,5-dibromothiophen-3-yl)methylene)-1-(pentan-3-yl)pyrrolidine-2,5-dione (TS-C5-Br).

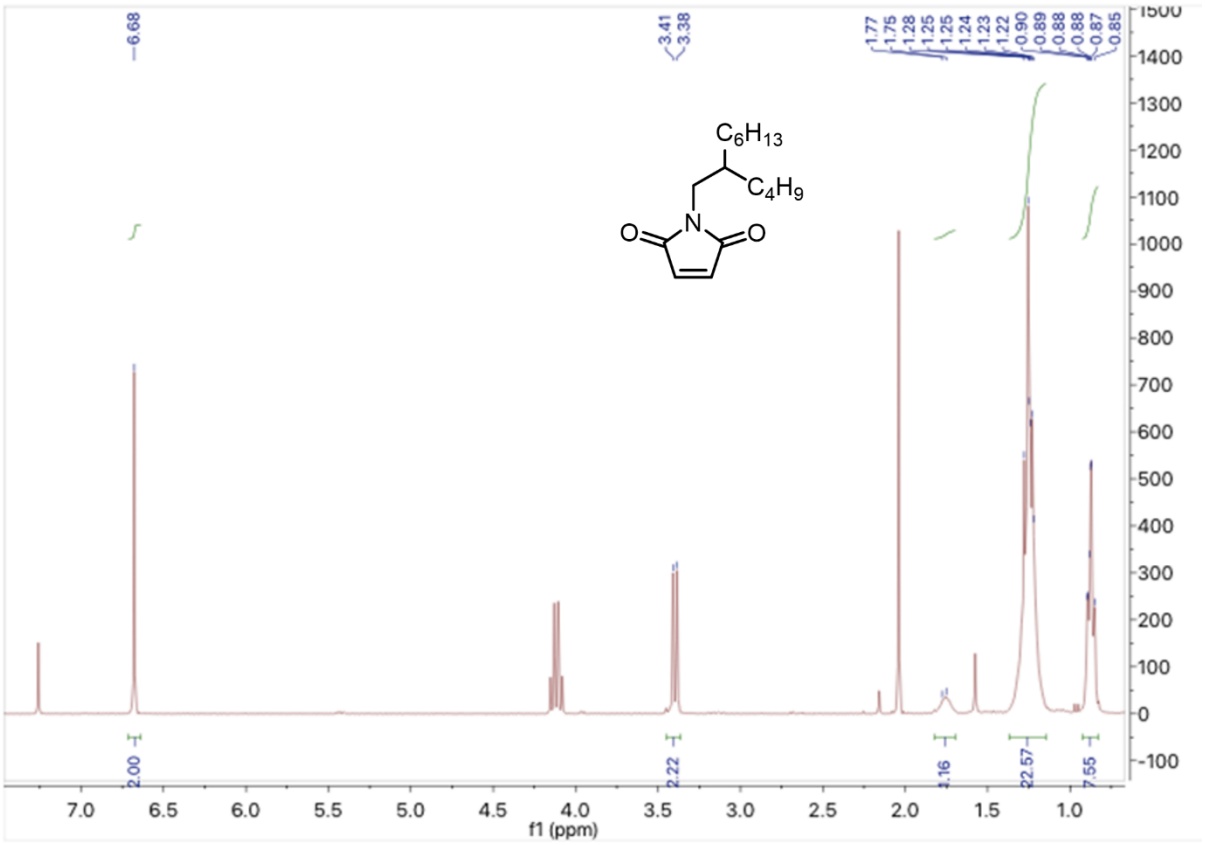


Figure 4-19. ^{1}H NMR (300MHz, $CDCl_3$) spectra of 1-(2-butyloctyl)-1H-pyrrole-2,5-dione (S-C12).

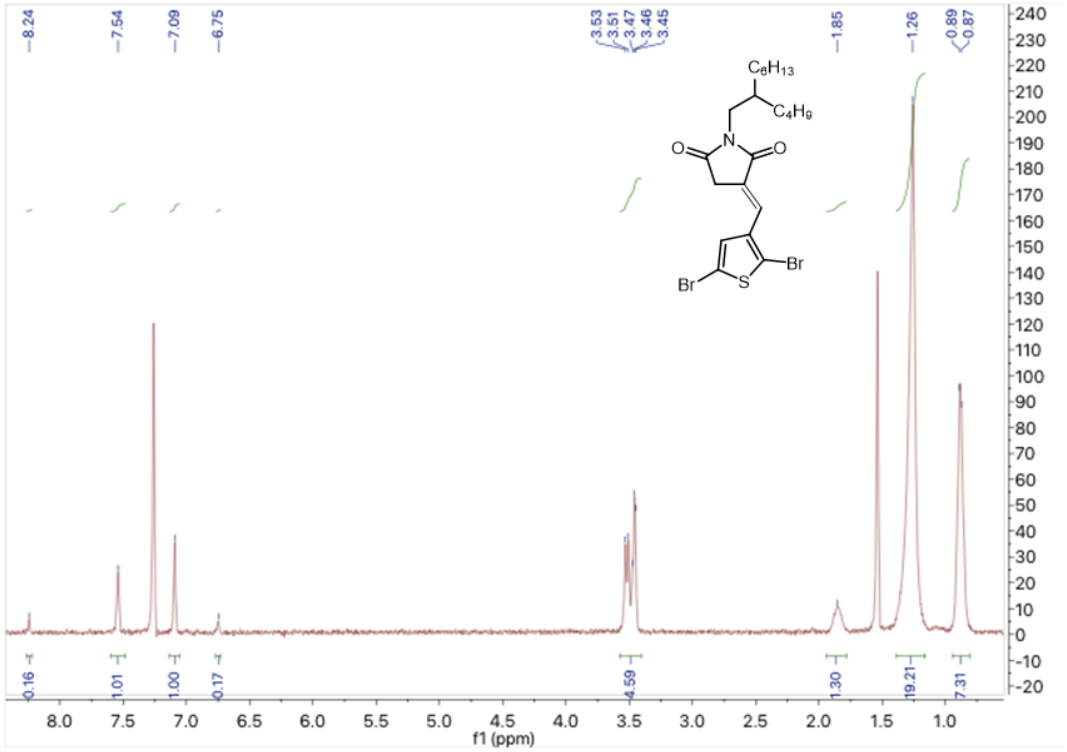


Figure 4-20. ^{1}H NMR (300MHz, $CDCl_3$) spectra of 1-(2-butyloctyl)-3-((2,5-dibromothiophen-3-yl)methylene)pyrrolidine-2,5-dione (TS-C12-Br).

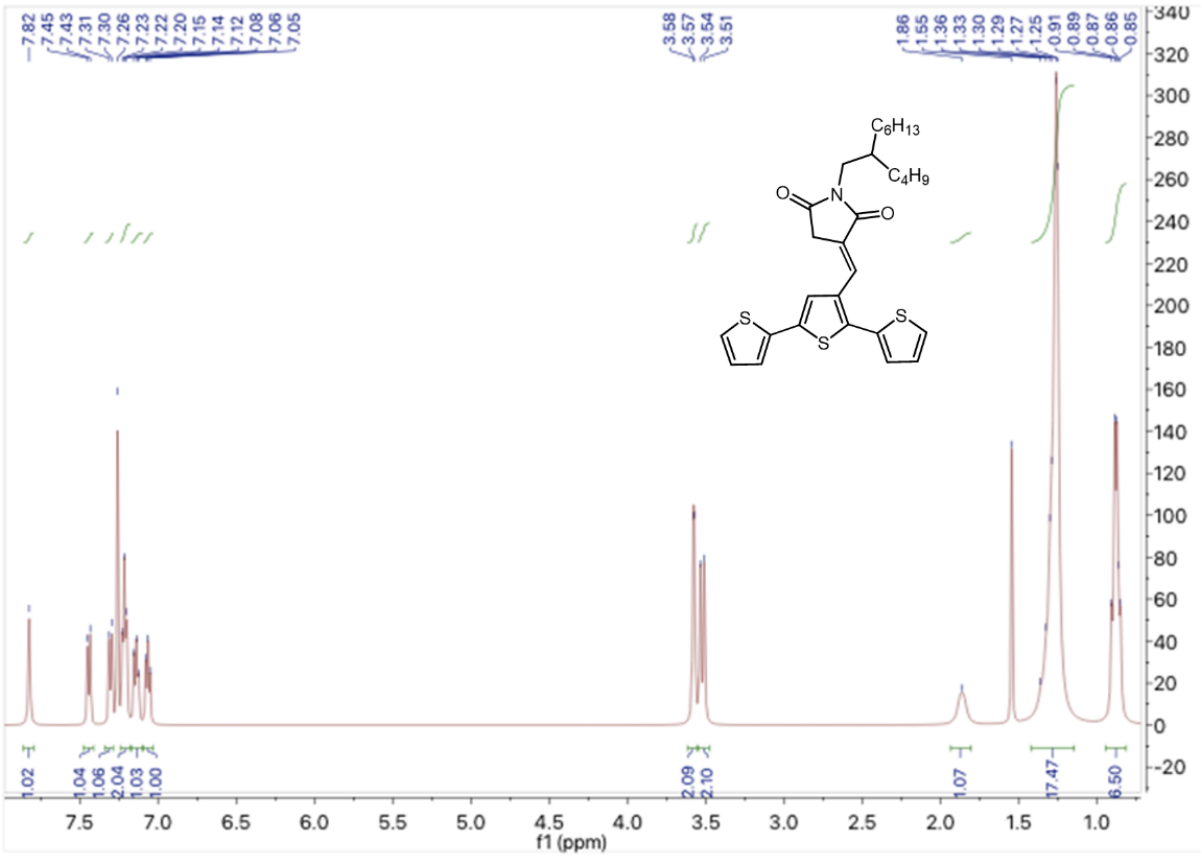


Figure 4-21. [1]H NMR (300MHz, CDCl3) spectra of 3-([2,2':5',2''-terthiophen]-3'-ylmethylene)-1-(2-butyloctyl)pyrrolidine-2,5-dione (TSBT-C12).

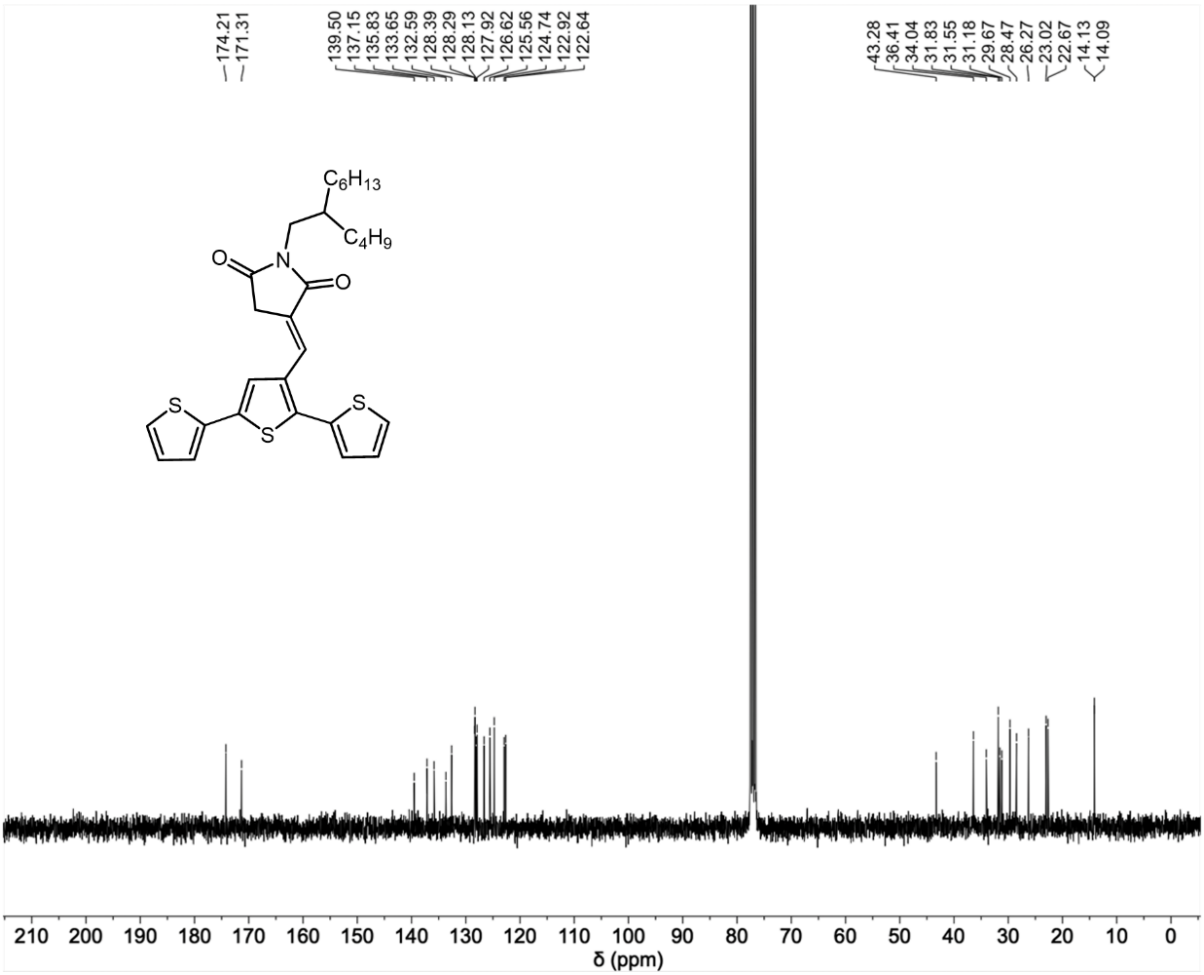


Figure 4-22. ^{13}C NMR (75MHz, $CDCl_3$) spectra of 3-([2,2':5',2''-terthiophen]-3'-ylmethylene)-1-(2-butyloctyl)pyrrolidine-2,5-dione (TSBT-C12).

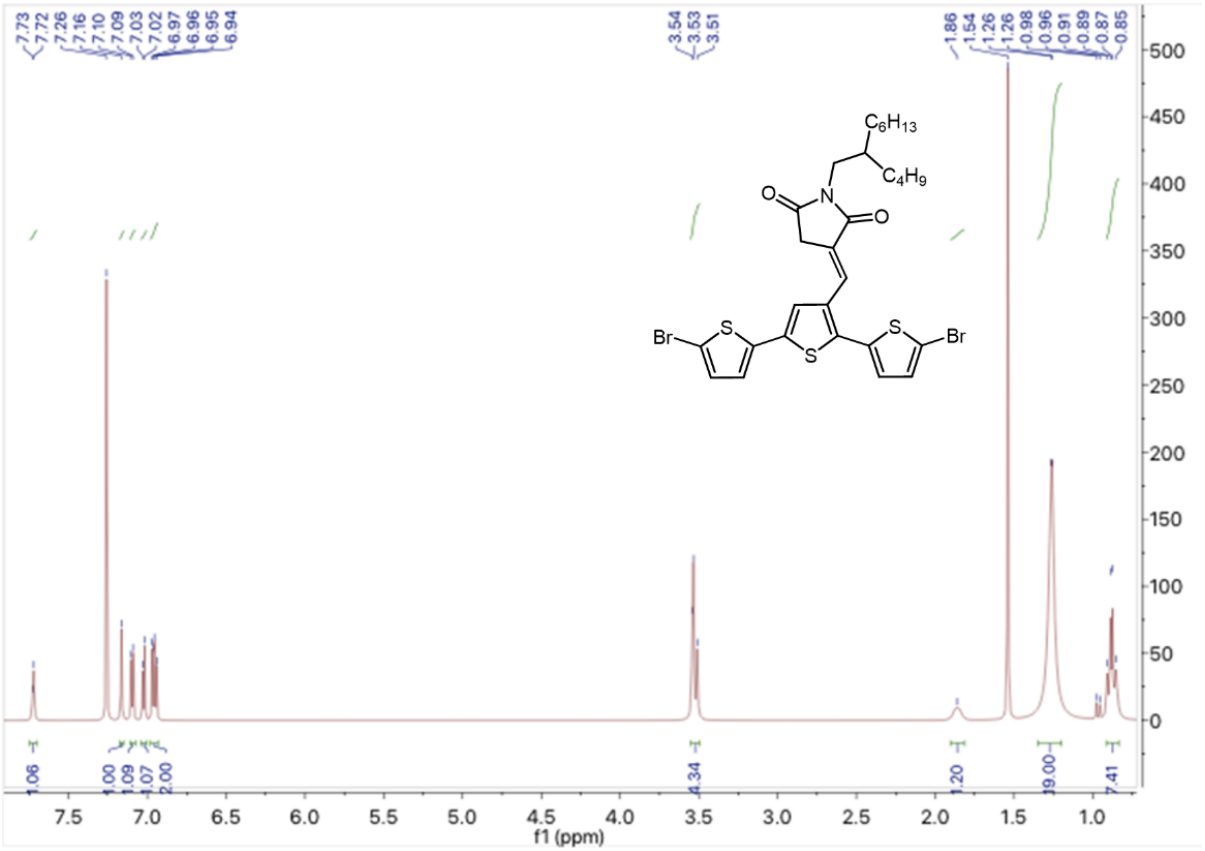


Figure 4-23. ^{1}H NMR (300MHz, $CDCl_3$) spectra of 1-(2-butyloctyl)-3-((5,5’’-dibromo-[2,2’:5’,2’’-terthiophen]-3’-yl)methylene)pyrrolidine-2,5-dione (TSBT-C12-Br).

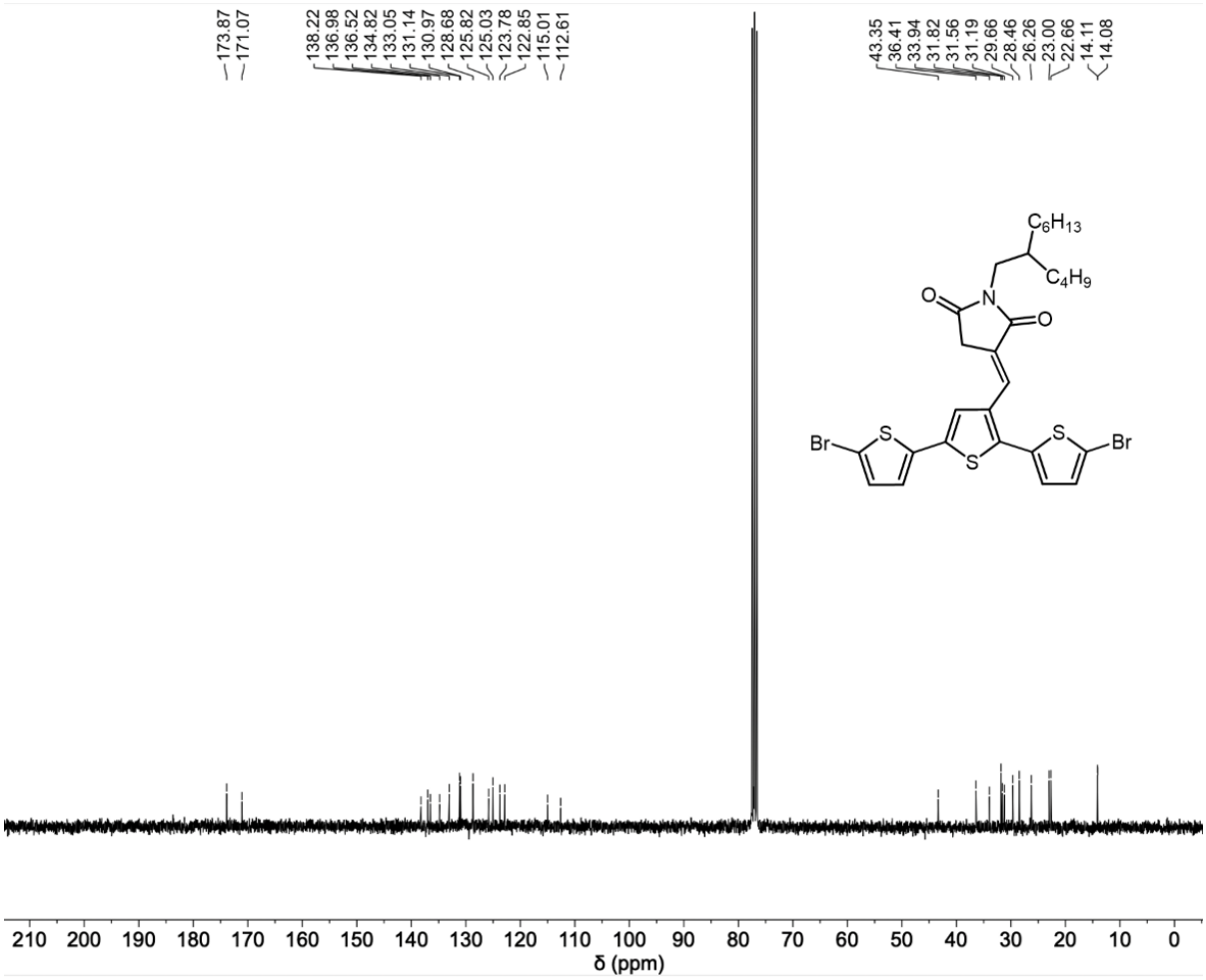


Figure 4-24. ^{13}C NMR (300MHz, $CDCl_3$) spectra of 1-(2-butyloctyl)-3-((5,5''-dibromo-[2,2':5',2''-terthiophen]-3'-yl)methylene)pyrrolidine-2,5-dione (TSBT-C12-Br).

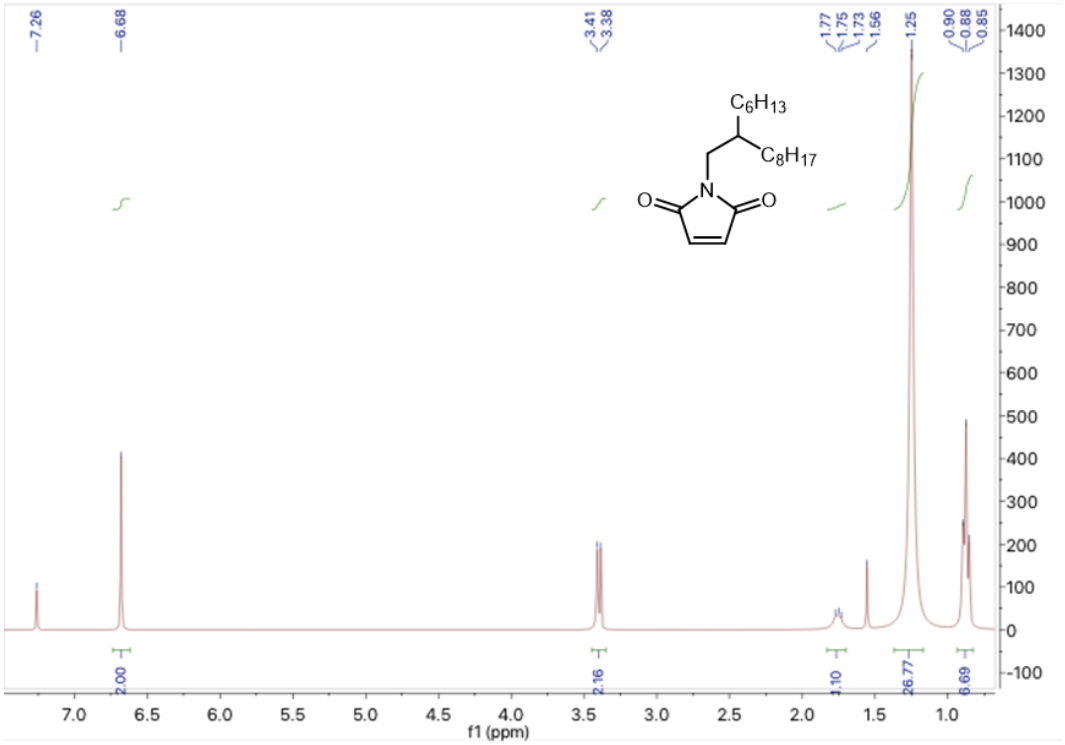


Figure 4-25. ^{1}H NMR (300MHz, $CDCl_3$) spectra of 1-(2-hexyldecyl)-1H-pyrrole-2,5-dione (S-C16).

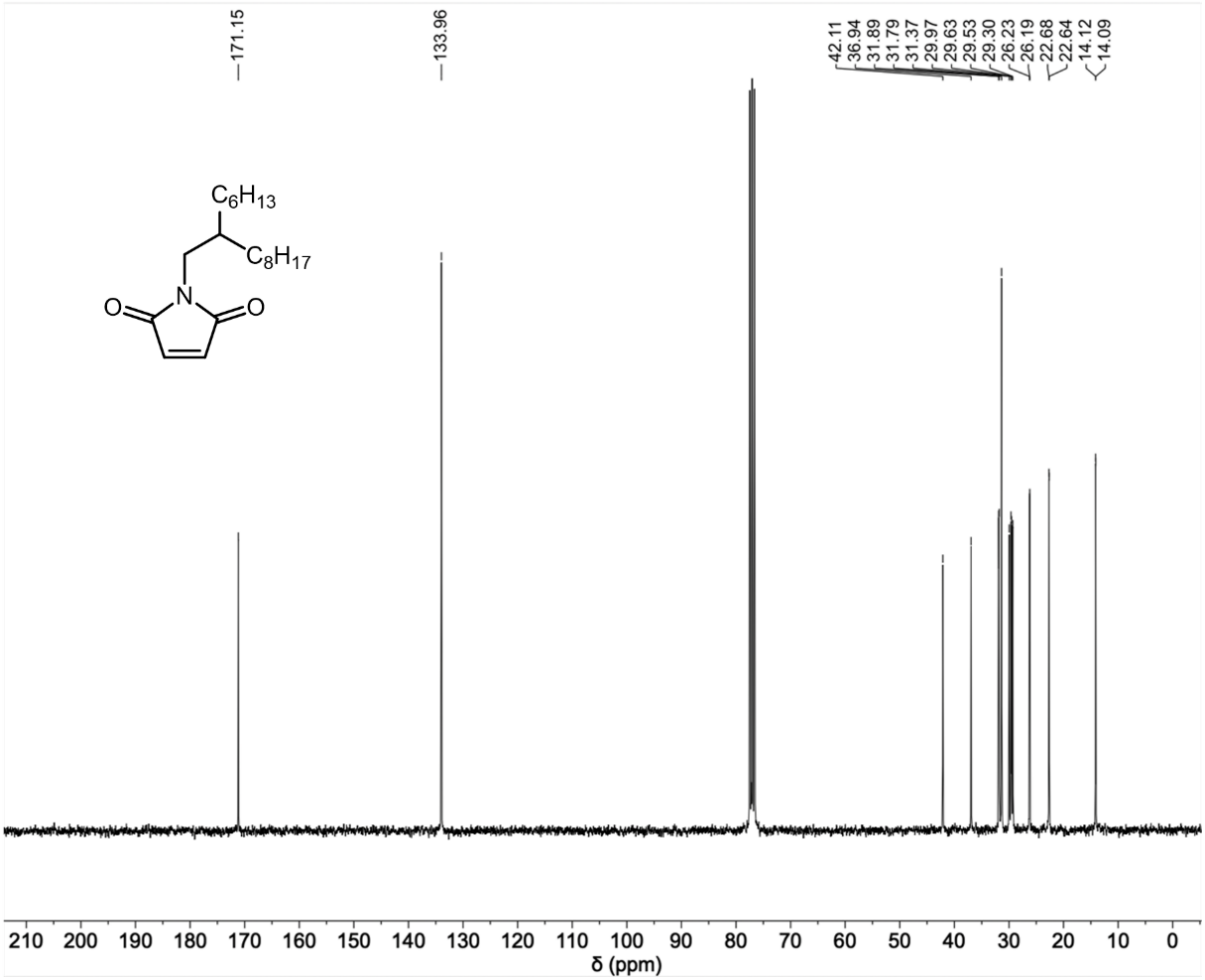


Figure 4-26. ^{13}C NMR (75MHz, $CDCl_3$) spectra of 1-(2-hexyldecyl)-1H-pyrrole-2,5-dione (S-C16).

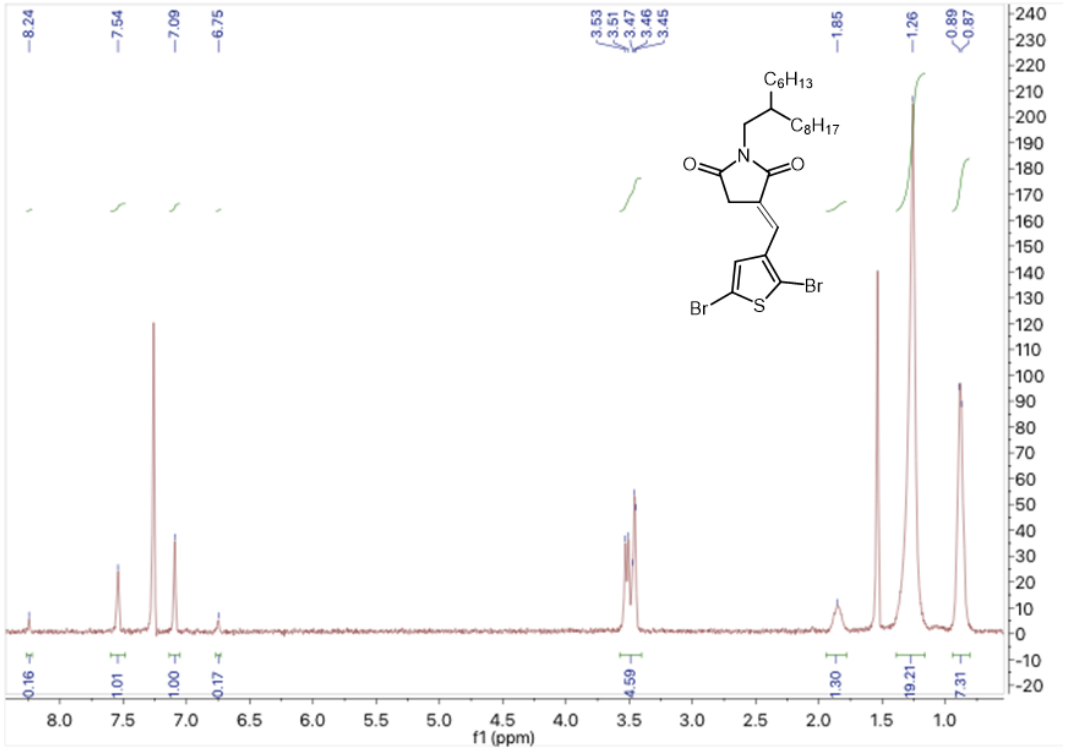


Figure 4-27. ^{1}H NMR (300MHz, $CDCl_3$) spectra of 3-((2,5-dibromothiophen-3-yl)methylene)-1-(2-hexyldecyl)pyrrolidine-2,5-dione (TS-C16-Br).

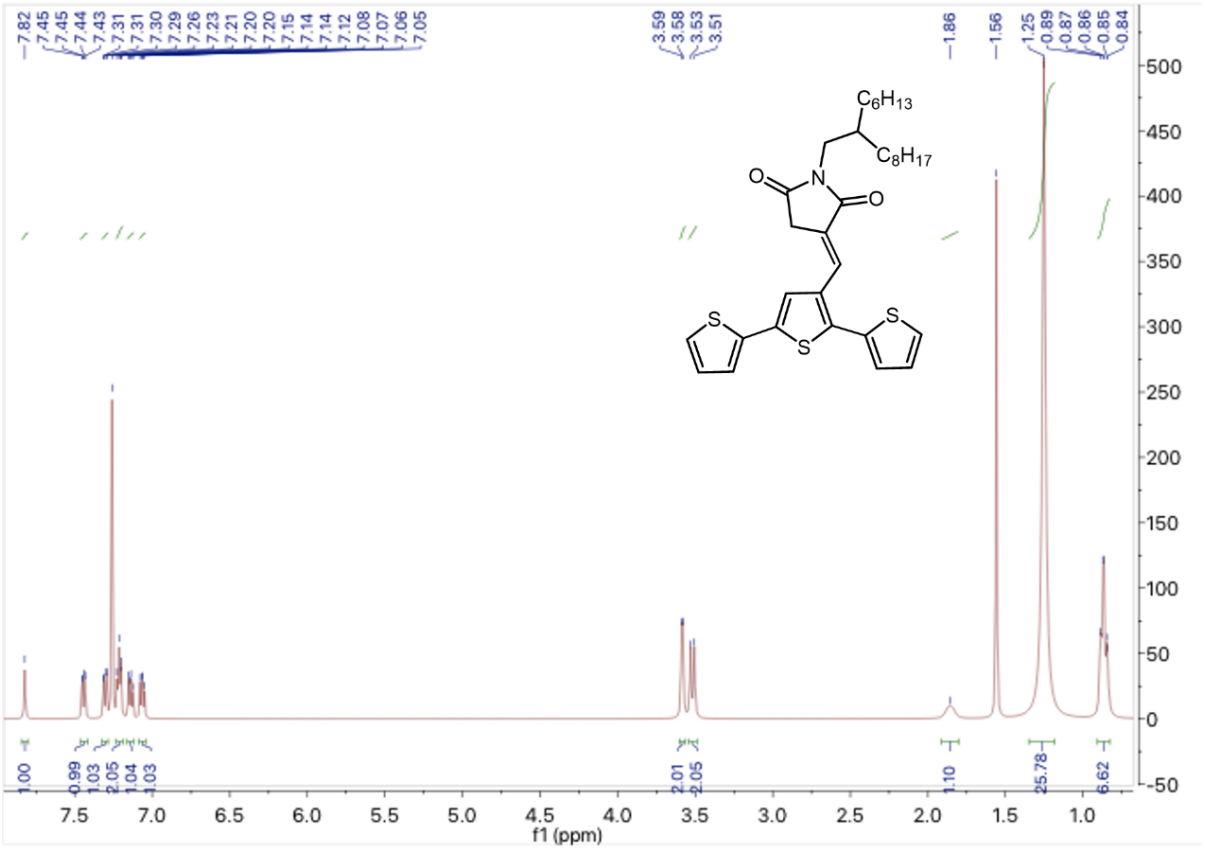


Figure 4-28. ^{1}H NMR (300MHz, $CDCl_3$) spectra of 3-([2,2':5',2''-terthiophen]-3'-ylmethylene)-1-(2-hexyldecyl)pyrrolidine-2,5-dione (TSBT-C16).

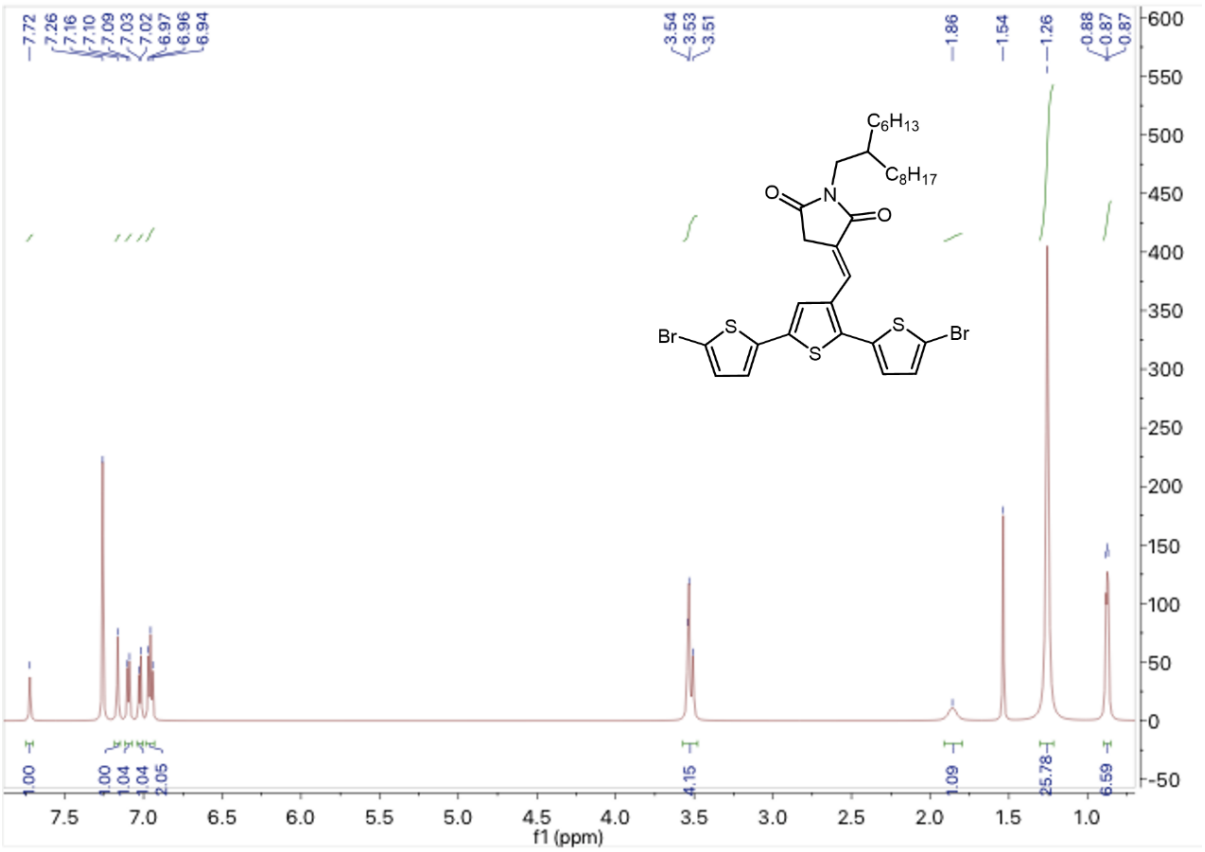


Figure 4-29. ^{1}H NMR (300MHz, $CDCl_3$) spectra of 3-((5,5''-dibromo-[2,2':5',2''-terthiophen]-3'-yl)methylene)-1-(2-hexyldecyl)pyrrolidine-2,5-dione (TSBT-C16-Br).

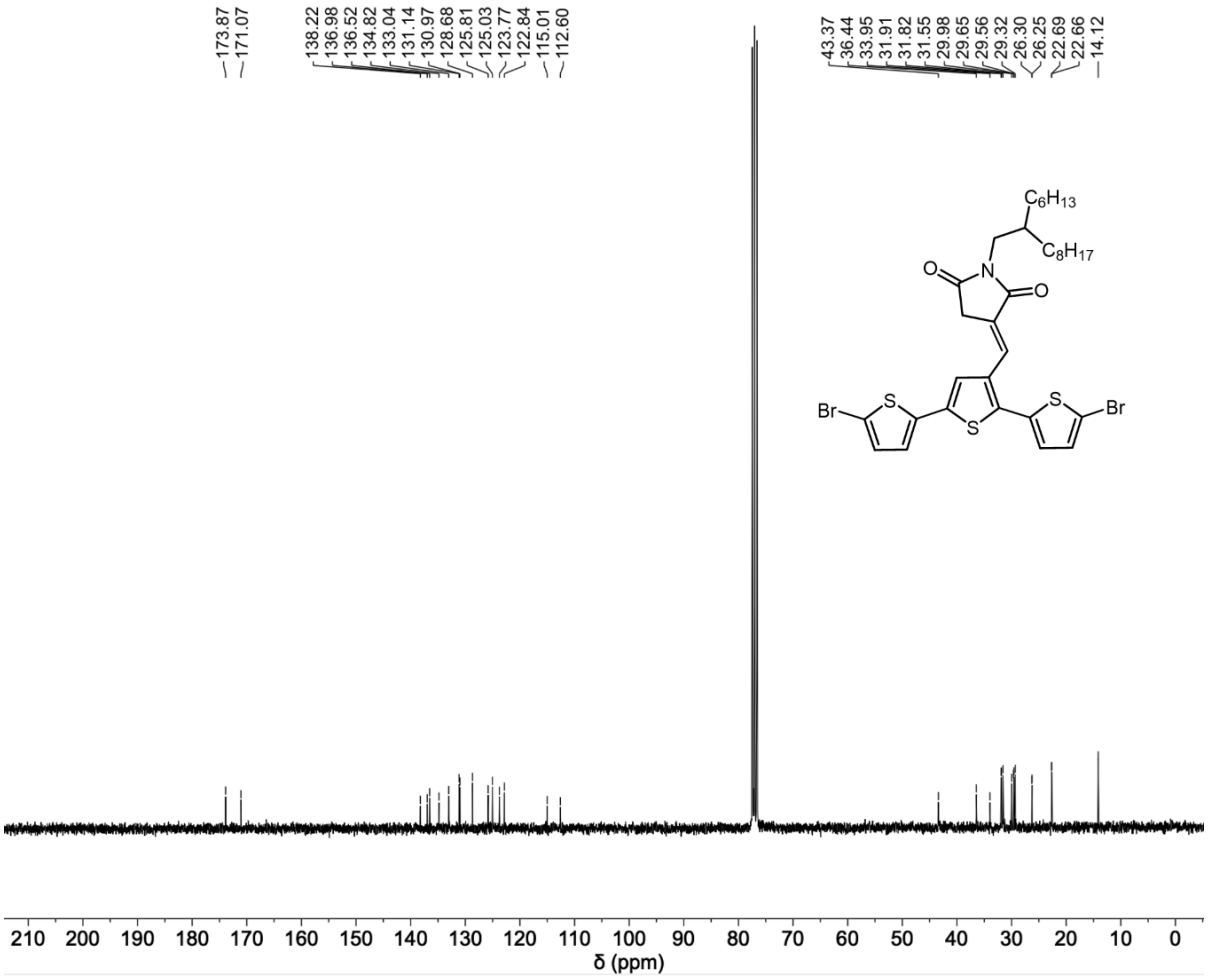


Figure 4-30. ^{13}C NMR (75MHz, $CDCl_3$) spectra of 3-((5,5''-dibromo-[2,2':5',2''-terthiophen]-3'-yl)methylene)-1-(2-hexyldecyl)pyrrolidine-2,5-dione (TSBT-C16-Br).

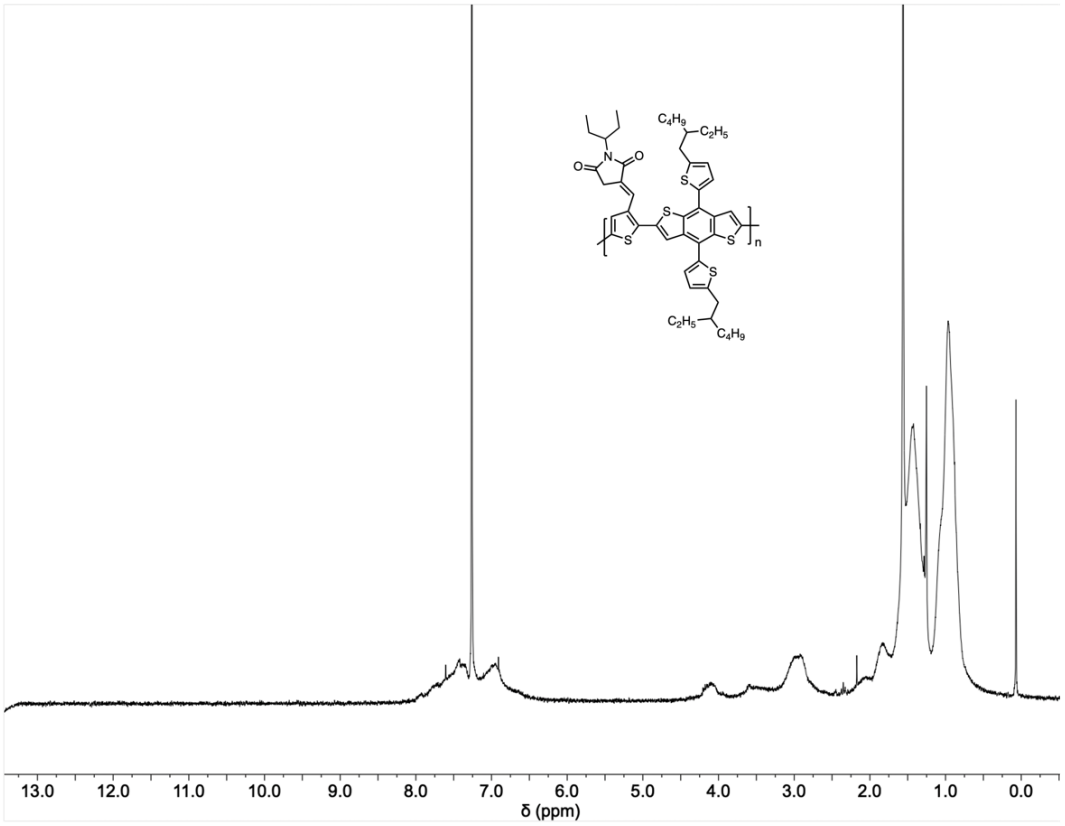


Figure 4-31. ^{1}H NMR (300MHz, $CDCl_3$) spectra of PBDT-TS-C5.

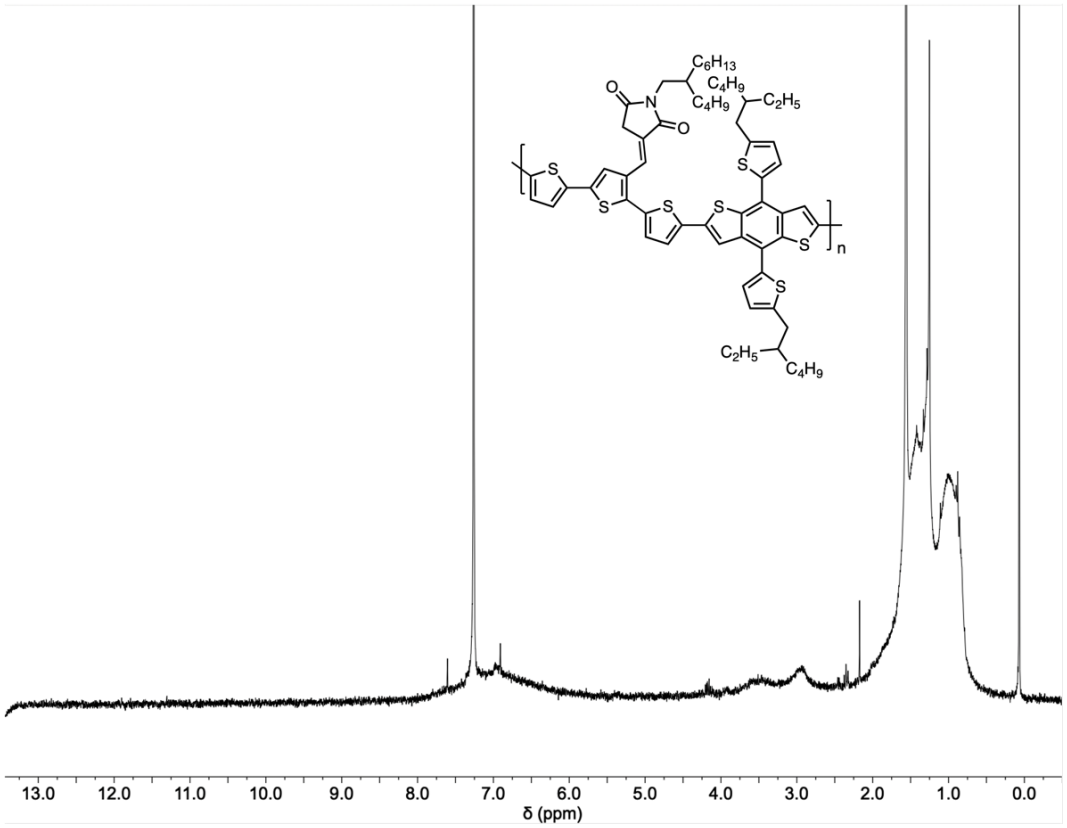


Figure 4-32. ^{1}H NMR (300MHz, $CDCl_3$) spectra of PBDT-TSBT-C12.

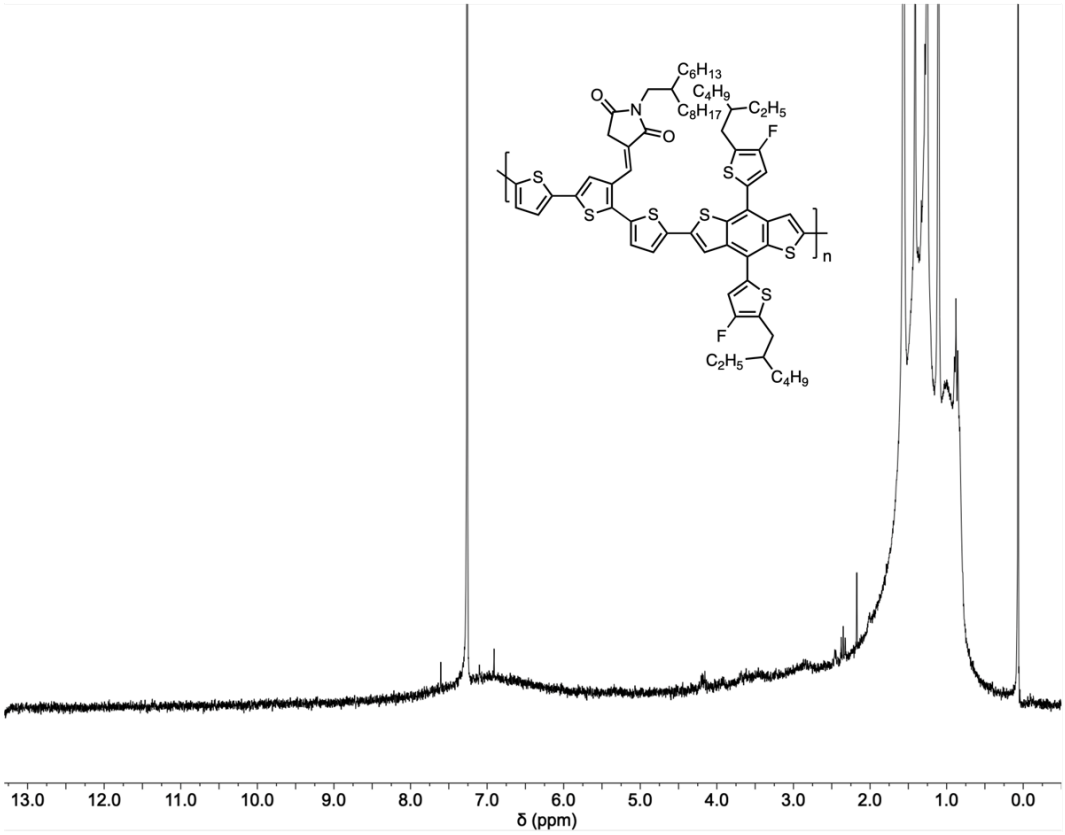


Figure 4-33. ^{1}H NMR (300MHz, $CDCl_3$) spectra of PBDTF-TSBT-C16.

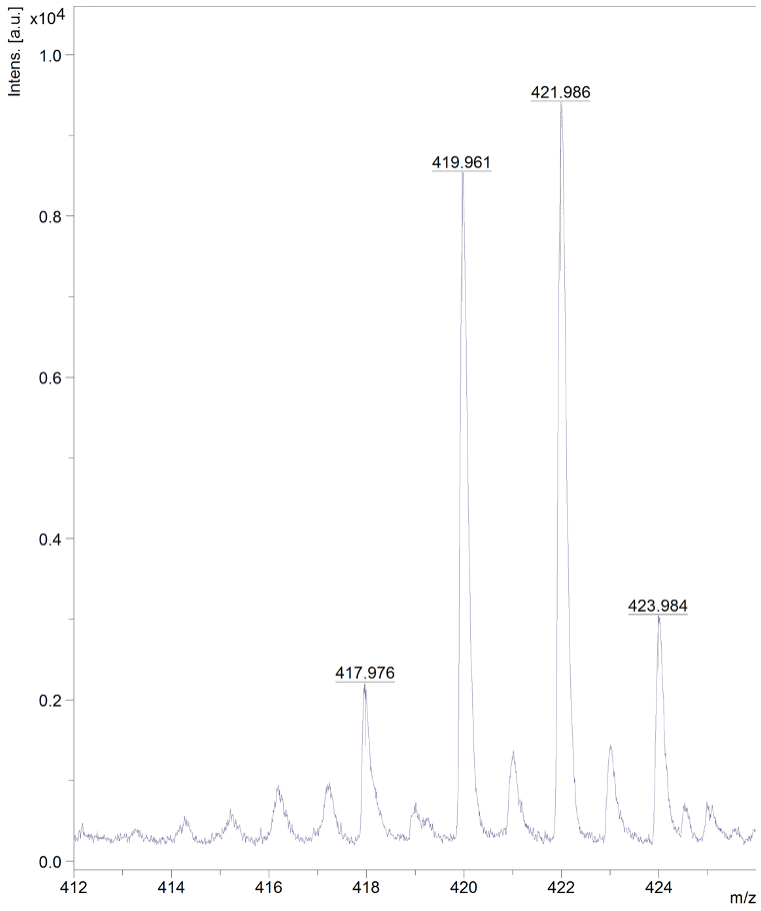


Figure 4-34. MALDI MS spectrum of 3-((2,5-dibromothiophen-3-yl)methylene)-1-(pentan-3-yl)pyrrolidine-2,5-dione (TS-C5-Br).

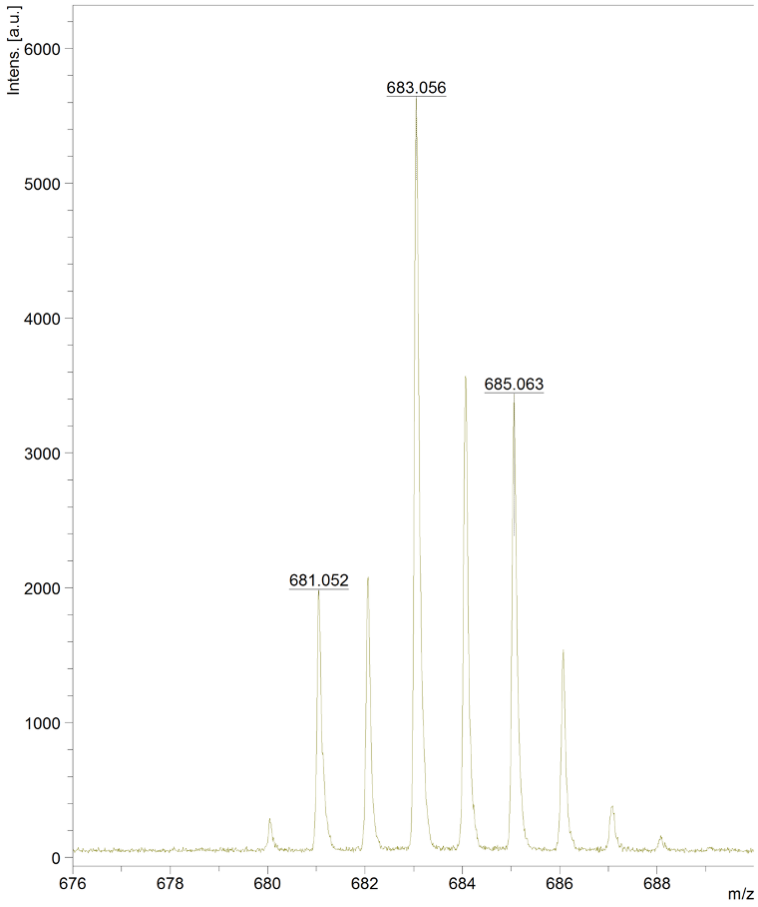


Figure 4-35. MALDI MS spectrum of 1-(2-butyloctyl)-3-((5,5’’-dibromo-[2,2’:5’,2’’-terthiophen]-3’-yl)methylene)pyrrolidine-2,5-dione (TSBT-C12-Br).

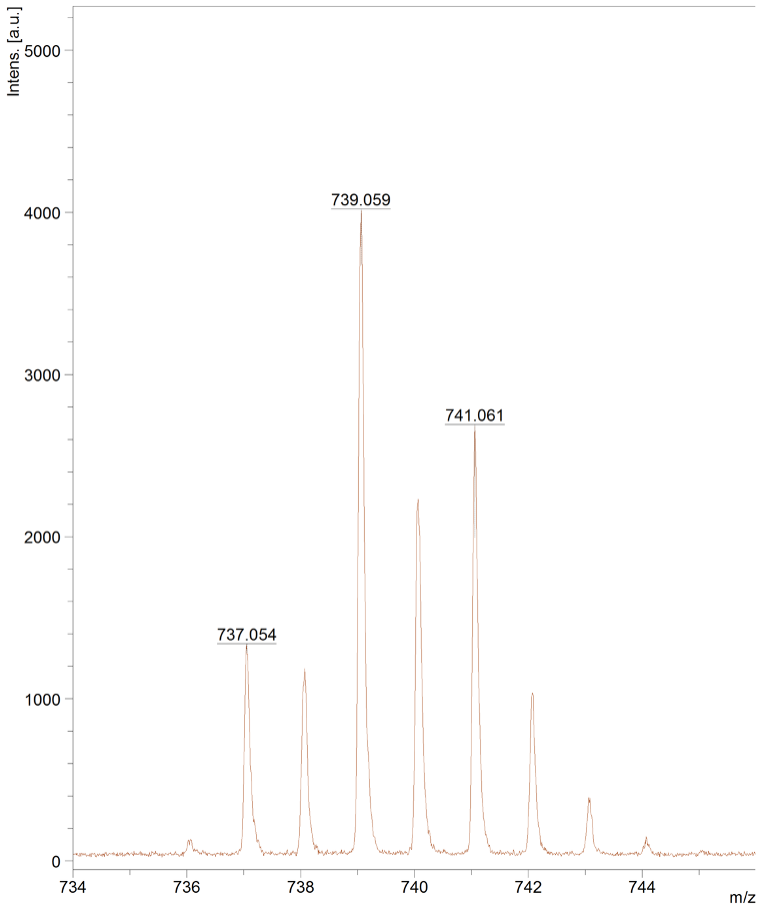


Figure 4-36. MALDI MS spectrum of 3-((5,5’’-dibromo-[2,2’:5’,2’’-terthiophen]-3’-yl)methylene)-1-(2-hexyldecyl)pyrrolidine-2,5-dione (TSBT-C16-Br).

Chapter 5
Conclusion and Future Direction

OSCs have gained considerable attention due to their advantageous features, including lightweight design, affordability, mechanical flexibility, non-toxicity, and roll-to-roll processing capability. These advantages explain why OSC are being considered as a promising technology, complementing commercial silicon solar cells and emerging alternatives like perovskite solar cells. Due to the limited electron accepting building blocks, it is challenging to develop new conjugated WBG polymer donors for high performance OSCs after considering the cost-efficiency balance. Therefore, it is essential to design new donor materials with novel electron accepting building blocks to achieve high photovoltaic performance without cumbersome synthesis and purification procedures. This thesis presents the synthesis and characterization of several new polymer donor materials for non-fullerene OSCs, which demonstrates the promising potential of these thiophene-containing building blocks for the development of polymer semiconductors for solar cells and other printed electronics applications.

In chapter 2, methyl acrylate was used as a weakly electron-withdrawing side chain for the electron rich thiophene to prepare a new building block, methyl thiophene-3-acrylate (TA), with increased polarity. A wide bandgap polymer PBDT-TA synthesized using TA and a benzodithiophene (BDT) monomer shows increased dielectric constant (ε_r = 3.78) and reduced exciton binding energy (E_b = 0.415 eV) compared to those (ε_r = 3.55; E_b = 0.430 eV) of the analogous polymer PBDT-TC, which is made of BDT and methyl thiophene-3-carboxylate (TC). An organic solar cell device based on PBDT-TA:ITIC also achieves a higher power conversion efficiency of 10.47% than that of the PBDT-TC:ITIC based solar cell (9.68%), mainly ascribed to the improved J_{sc} of 19.43 mA/cm^2. Besides the larger dielectric constant and reduced exciton binding energy of PBDT-TA, the SCLC hole and electron mobilities of PBDT-TA:ITIC-based device improved to 1.11×10^{-4} cm^2 V^{-1} s^{-1} (8.68×10^{-5} in average) and 2.17×10^{-4} cm^2 V^{-1} s^{-1} (2.00×10^{-4} in average), leading to a more sufficient charge transport among PBDT-TA:ITIC-based device. The reduced RMS (0.98 nm) of PBDT-TA:ITIC-based film morphology also help enhance J_{sc} of the OSC device. This work demonstrates that the introduction of a vinyl bridge can increase the dielectric constant, reduce exciton binding energy, which is a useful strategy to improve photovoltaic performance of OSC devices.

In chapter 3, two *gem*-dihalovinyl thiophene-based electron accepting building blocks, namely 3-(2,2-difluorovinyl)thiophene (TDF) and 3-(2,2-dichlorovinyl)thiophene (TDCl), were successfully

synthesized via simple synthetic routes. The wide bandgap polymer PBDT-TDF synthesized using TDF and a benzodithiophene (BDT) monomer exhibits an E_{HOMO} of -5.62 eV, an E_{LUMO} of -3.60 eV and an E_g of 2.02 eV. While polymer PBDT-TDCl, which consists of TDCl and a BDT monomer, shows an E_{HOMO} of -5.48 eV, an E_{LUMO} of -3.49 eV and an E_g of 1.99 eV. The energy levels of both polymers are matched with the NFA Y6. The OSC device based on the blend of PBDT-TDF:Y6 achieved a good PCE of 8.83%, while the PBDT-TDCl:Y6-based OSC device demonstrated a higher PCE of 11.02%, which is mainly due to the enhanced J_{sc}. It is notable that the polymer PBDT-TDCl showed a conformational locking effect which resulted in a more coplanar backbone compared to that of PBDT-TDF. Higher coplanarity of PBDT-TDCl led to a better charge transport ability, which primarily contributed to enhanced J_{sc} than that of PBDT-TDF. This work demonstrates that the simple *gem*-dihalovinyl groups have the potential to be the electron-accepting building blocks for the development of cost-effective high performance OSCs.

In chapter 4, three WBG polymers, namely PBDT-TS-C5, PBDT-TSBT-C12 and PBDTF-TSBT-C16, were successfully developed. The wide bandgap polymer PBDT-TS-C5 contained TS and a benzodithiophene (BDT) monomer exhibits an E_{HOMO} of -5.53 eV, an E_{LUMO} of -3.53 eV and an E_g of 2.00 eV. Another polymer PBDT-TSBT-C12 synthesized using TS, BDT and π-spacers shows an E_{HOMO} of -5.35 eV, an E_{LUMO} of -3.44 eV and an E_g of 1.91 eV. The polymer PBDTF-TSBT-C16 which is consist of TS, a fluorinated BDT monomer and π-spacers demonstrates an E_{HOMO} of -5.51 eV, an E_{LUMO} of -3.57 eV and an E_g of 1.94 eV. All polymers are well matched with the acceptor Y6. The OSC device based on the blend of PBDT-TS-C5:Y6 exhibited a PCE of 8.51%, with a V_{oc} of 0.89 V, a J_{sc} of 19.36 mA cm^{-2} and an FF of 0.50. Ascribed to the introduction of π-spacers which reduced the steric effect of the polymer backbone, the PBDT-TSBT-C12:Y6-based OSC devices showed a higher PCE of 10.47%, with an enhanced J_{sc} of 24.84 mA cm^{-2}, a higher FF of 0.60 and a reduced V_{oc} of 0.71 V. To encounter the electron donating effect from π-spacers which led to a reduced V_{oc} of the device, the polymer PBDTF-TSBT-C16 was synthesized using the fluorinated BDT unit to replace the normal BDT. The PBDTF-TSBT-C16:Y6-based devices demonstrate an improved V_{oc} of 0.80 V, an enhanced J_{sc} of 26.83 mA cm^{-2} and an improved FF of 0.62, achieving the highest PCE of 13.21%. This work shows the potential of using succinimide-substituted thiophene as electron-accepting building blocks for achieving high-performance solar cells.

Nevertheless, there is still room for improving the photovoltaic performance of the polymer donors by tuning their chemical structures. Specifically, for polymer PBDT-TA with an E_{HOMO} of -5.46 eV,

the HOMO energy level can be even lower to reduce ΔE_{HOMO} and maximize V_{oc} of the device. This can be tuned by using fluorinated or chlorinated BDT monomer to copolymerize with TA monomer. Since the E_{HOMO} would be lower, if ITIC could not match with the energy level of new proposed polymer, another acceptor may be chosen to match the energy level of the new polymer. Although the polymer PBDT-TSBT-C12 and PBDTF-TSBT-C16 demonstrate the improvement of photovoltaic performance of original polymer PBDT-TS-C5, the offset of HOMO energy level between PBDTF-TSBT-C16 (E_{HOMO} = -5.51 eV) and Y6 (E_{HOMO} = -5.65 eV) is still much larger than the requirement energy for exciton dissociation. To maximize the V_{oc} of the device, chlorinated BDT can be used to replace fluorinated BDT in PBDTF-TSBT-C16 since the chlorine atom has stronger electron-withdrawing effects than the fluorine atom. Moreover, all the fabricated OSC devices showed low FF compared to those in the literature, it is necessary to improve the crystallinity of all the polymers by synthesizing regioregular polymers instead, thus the crystallinity and hole mobility are expected to be improved, which contribute to the FF.

References

(1) Haase, F.; Hollemann, C.; Schäfer, S.; Merkle, A.; Rienäcker, M.; Krügener, J.; Brendel, R.; Peibst, R. Laser Contact Openings for Local Poly-Si-Metal Contacts Enabling 26.1%-Efficient POLO-IBC Solar Cells. *Sol. Energy Mater. Sol. Cells* **2018**, *186*, 184–193. https://doi.org/10.1016/j.solmat.2018.06.020.

(2) Polman, A.; Knight, M.; Garnett, E. C.; Ehrler, B.; Sinke, W. C. Photovoltaic Materials: Present Efficiencies and Future Challenges. *Science* **2016**, *352* (6283), aad4424. https://doi.org/10.1126/science.aad4424.

(3) Andersen, T. R.; Dam, H. F.; Hösel, M.; Helgesen, M.; Carlé, J. E.; Larsen-Olsen, T. T.; Gevorgyan, S. A.; Andreasen, J. W.; Adams, J.; Li, N.; Machui, F.; Spyropoulos, G. D.; Ameri, T.; Lemaître, N.; Legros, M.; Scheel, A.; Gaiser, D.; Kreul, K.; Berny, S.; Lozman, O. R.; Nordman, S.; Välimäki, M.; Vilkman, M.; Søndergaard, Roar. R.; Jørgensen, M.; Brabec, C. J.; Krebs, F. C. Scalable, Ambient Atmosphere Roll-to-Roll Manufacture of Encapsulated Large Area, Flexible Organic Tandem Solar Cell Modules. *Energy Environ. Sci.* **2014**, *7* (9), 2925. https://doi.org/10.1039/C4EE01223B.

(4) Li, G.; Zhu, R.; Yang, Y. Polymer Solar Cells. *Nat. Photonics* **2012**, *6* (3), 153–161. https://doi.org/10.1038/nphoton.2012.11.

(5) Kaltenbrunner, M.; White, M. S.; Głowacki, E. D.; Sekitani, T.; Someya, T.; Sariciftci, N. S.; Bauer, S. Ultrathin and Lightweight Organic Solar Cells with High Flexibility. *Nat. Commun.* **2012**, *3* (1), 770. https://doi.org/10.1038/ncomms1772.

(6) Lu, L.; Zheng, T.; Wu, Q.; Schneider, A. M.; Zhao, D.; Yu, L. Recent Advances in Bulk Heterojunction Polymer Solar Cells. *Chem. Rev.* **2015**, *115* (23), 12666–12731. https://doi.org/10.1021/acs.chemrev.5b00098.

(7) Inganäs, O. Organic Photovoltaics over Three Decades. *Adv. Mater.* **2018**, *30* (35), 1800388. https://doi.org/10.1002/adma.201800388.

(8) Lee, C.; Lee, S.; Kim, G.-U.; Lee, W.; Kim, B. J. Recent Advances, Design Guidelines, and Prospects of All-Polymer Solar Cells. *Chem. Rev.* **2019**, *119* (13), 8028–8086. https://doi.org/10.1021/acs.chemrev.9b00044.

(9) Cui, C.; Li, Y. High-Performance Conjugated Polymer Donor Materials for Polymer Solar Cells with Narrow-Bandgap Nonfullerene Acceptors. *Energy Environ. Sci.* **2019**, *12* (11), 3225–3246. https://doi.org/10.1039/C9EE02531F.

(10) He, K.; Kumar, P.; Yuan, Y.; Li, Y. Wide Bandgap Polymer Donors for High Efficiency Non-Fullerene Acceptor Based Organic Solar Cells. *Mater. Adv.* **2021**, *2* (1), 115–145. https://doi.org/10.1039/D0MA00790K.

(11) Yan, C.; Barlow, S.; Wang, Z.; Yan, H.; Jen, A. K.-Y.; Marder, S. R.; Zhan, X. Non-Fullerene Acceptors for Organic Solar Cells. *Nat. Rev. Mater.* **2018**, *3* (3), 18003. https://doi.org/10.1038/natrevmats.2018.3.

(12) Luo, D.; Jang, W.; Babu, D. D.; Kim, M. S.; Wang, D. H.; Kyaw, A. K. K. Recent Progress in Organic Solar Cells Based on Non-Fullerene Acceptors: Materials to Devices. *J. Mater. Chem. A* **2022**, *10* (7), 3255–3295. https://doi.org/10.1039/D1TA10707K.

(13) Meng, L.; Zhang, Y.; Wan, X.; Li, C.; Zhang, X.; Wang, Y.; Ke, X.; Xiao, Z.; Ding, L.; Xia, R.; Yip, H.-L.; Cao, Y.; Chen, Y. Organic and Solution-Processed Tandem Solar Cells with 17.3% Efficiency. *Science* **2018**, *361* (6407), 1094–1098. https://doi.org/10.1126/science.aat2612.

(14) Yu, G.; Gao, J.; Hummelen, J. C.; Wudl, F.; Heeger, A. J. Polymer Photovoltaic Cells: Enhanced Efficiencies via a Network of Internal Donor-Acceptor Heterojunctions. *Science* **1995**, *270* (5243), 1789–1791. https://doi.org/10.1126/science.270.5243.1789.
(15) Zhu, L.; Zhang, M.; Xu, J.; Li, C.; Yan, J.; Zhou, G.; Zhong, W.; Hao, T.; Song, J.; Xue, X.; Zhou, Z.; Zeng, R.; Zhu, H.; Chen, C.-C.; MacKenzie, R. C. I.; Zou, Y.; Nelson, J.; Zhang, Y.; Sun, Y.; Liu, F. Single-Junction Organic Solar Cells with over 19% Efficiency Enabled by a Refined Double-Fibril Network Morphology. *Nat. Mater.* **2022**, *21* (6), 656–663. https://doi.org/10.1038/s41563-022-01244-y.
(16) Cui, Y.; Xu, Y.; Yao, H.; Bi, P.; Hong, L.; Zhang, J.; Zu, Y.; Zhang, T.; Qin, J.; Ren, J.; Chen, Z.; He, C.; Hao, X.; Wei, Z.; Hou, J. Single-Junction Organic Photovoltaic Cell with 19% Efficiency. *Adv. Mater.* **2021**, *33* (41), 2102420. https://doi.org/10.1002/adma.202102420.
(17) Fu, J.; Fong, P. W. K.; Liu, H.; Huang, C.-S.; Lu, X.; Lu, S.; Abdelsamie, M.; Kodalle, T.; Sutter-Fella, C. M.; Yang, Y.; Li, G. 19.31% Binary Organic Solar Cell and Low Non-Radiative Recombination Enabled by Non-Monotonic Intermediate State Transition. *Nat. Commun.* **2023**, *14* (1), 1760. https://doi.org/10.1038/s41467-023-37526-5.
(18) Liu, K.; Jiang, Y.; Ran, G.; Liu, F.; Zhang, W.; Zhu, X. 19.7% Efficiency Binary Organic Solar Cells Achieved by Selective Core Fluorination of Nonfullerene Electron Acceptors. *Joule* **2024**, *8* (3), 835–851. https://doi.org/10.1016/j.joule.2024.01.005.
(19) Wang, J.; Wang, Y.; Bi, P.; Chen, Z.; Qiao, J.; Li, J.; Wang, W.; Zheng, Z.; Zhang, S.; Hao, X.; Hou, J. Binary Organic Solar Cells with 19.2% Efficiency Enabled by Solid Additive. *Adv. Mater.* **2023**, *35* (25), 2301583. https://doi.org/10.1002/adma.202301583.
(20) He, C.; Pan, Y.; Ouyang, Y.; Shen, Q.; Gao, Y.; Yan, K.; Fang, J.; Chen, Y.; Ma, C.-Q.; Min, J.; Zhang, C.; Zuo, L.; Chen, H. Manipulating the D:A Interfacial Energetics and Intermolecular Packing for 19.2% Efficiency Organic Photovoltaics. *Energy Environ. Sci.* **2022**, *15* (6), 2537–2544. https://doi.org/10.1039/D2EE00595F.
(21) Best Research-Cell Efficiency Chart _ Photovoltaic Research _ NREL.Html.
(22) Hummelen, J. C.; Knight, B. W.; LePeq, F.; Wudl, F.; Yao, J.; Wilkins, C. L. Preparation and Characterization of Fulleroid and Methanofullerene Derivatives. *J. Org. Chem.* **1995**, *60* (3), 532–538. https://doi.org/10.1021/jo00108a012.
(23) Zhao, J.; Li, Y.; Yang, G.; Jiang, K.; Lin, H.; Ade, H.; Ma, W.; Yan, H. Efficient Organic Solar Cells Processed from Hydrocarbon Solvents. *Nat. Energy* **2016**, *1* (2), 15027. https://doi.org/10.1038/nenergy.2015.27.
(24) Armin, A.; Li, W.; Sandberg, O. J.; Xiao, Z.; Ding, L.; Nelson, J.; Neher, D.; Vandewal, K.; Shoaee, S.; Wang, T.; Ade, H.; Heumüller, T.; Brabec, C.; Meredith, P. A History and Perspective of Non-Fullerene Electron Acceptors for Organic Solar Cells. *Adv. Energy Mater.* **2021**, *11* (15), 2003570. https://doi.org/10.1002/aenm.202003570.
(25) He, K.; Kumar, P.; Yuan, Y.; Li, Y. Wide Bandgap Polymer Donors for High Efficiency Non-Fullerene Acceptor Based Organic Solar Cells. *Mater. Adv.* **2021**, 10.1039.D0MA00790K. https://doi.org/10.1039/D0MA00790K.
(26) Zhang, G.; Zhao, J.; Chow, P. C. Y.; Jiang, K.; Zhang, J.; Zhu, Z.; Zhang, J.; Huang, F.; Yan, H. Nonfullerene Acceptor Molecules for Bulk Heterojunction Organic Solar Cells. *Chem. Rev.* **2018**, *118* (7), 3447–3507. https://doi.org/10.1021/acs.chemrev.7b00535.
(27) Lin, Y.; Wang, J.; Zhang, Z.-G.; Bai, H.; Li, Y.; Zhu, D.; Zhan, X. An Electron Acceptor Challenging Fullerenes for Efficient Polymer Solar Cells. *Adv. Mater.* **2015**, *27* (7), 1170–1174. https://doi.org/10.1002/adma.201404317.
(28) Li, X.; Huang, G.; Zheng, N.; Li, Y.; Kang, X.; Qiao, S.; Jiang, H.; Chen, W.; Yang, R. High-Efficiency Polymer Solar Cells Over 13.9% With a High V_{OC} Beyond 1.0 V by Synergistic

Effect of Fluorine and Sulfur. *Sol. RRL* **2019**, *3* (4), 1900005. https://doi.org/10.1002/solr.201900005.
(29) Li, S.; Ye, L.; Zhao, W.; Zhang, S.; Mukherjee, S.; Ade, H.; Hou, J. Energy-Level Modulation of Small-Molecule Electron Acceptors to Achieve over 12% Efficiency in Polymer Solar Cells. *Adv. Mater.* **2016**, *28* (42), 9423–9429. https://doi.org/10.1002/adma.201602776.
(30) Zhao, W.; Li, S.; Yao, H.; Zhang, S.; Zhang, Y.; Yang, B.; Hou, J. Molecular Optimization Enables over 13% Efficiency in Organic Solar Cells. *J. Am. Chem. Soc.* **2017**, *139* (21), 7148–7151. https://doi.org/10.1021/jacs.7b02677.
(31) Yang, Y.; Zhang, Z.-G.; Bin, H.; Chen, S.; Gao, L.; Xue, L.; Yang, C.; Li, Y. Side-Chain Isomerization on an n-Type Organic Semiconductor ITIC Acceptor Makes 11.77% High Efficiency Polymer Solar Cells. *J. Am. Chem. Soc.* **2016**, *138* (45), 15011–15018. https://doi.org/10.1021/jacs.6b09110.
(32) Wang, J.; Wang, W.; Wang, X.; Wu, Y.; Zhang, Q.; Yan, C.; Ma, W.; You, W.; Zhan, X. Enhancing Performance of Nonfullerene Acceptors via Side-Chain Conjugation Strategy. *Adv. Mater.* **2017**, *29* (35), 1702125. https://doi.org/10.1002/adma.201702125.
(33) Lin, Y.; Zhao, F.; He, Q.; Huo, L.; Wu, Y.; Parker, T. C.; Ma, W.; Sun, Y.; Wang, C.; Zhu, D.; Heeger, A. J.; Marder, S. R.; Zhan, X. High-Performance Electron Acceptor with Thienyl Side Chains for Organic Photovoltaics. *J. Am. Chem. Soc.* **2016**, *138* (14), 4955–4961. https://doi.org/10.1021/jacs.6b02004.
(34) Zhao, F.; Dai, S.; Wu, Y.; Zhang, Q.; Wang, J.; Jiang, L.; Ling, Q.; Wei, Z.; Ma, W.; You, W.; Wang, C.; Zhan, X. Single-Junction Binary-Blend Nonfullerene Polymer Solar Cells with 12.1% Efficiency. *Adv. Mater.* **2017**, *29* (18), 1700144. https://doi.org/10.1002/adma.201700144.
(35) Lin, Y.; He, Q.; Zhao, F.; Huo, L.; Mai, J.; Lu, X.; Su, C.-J.; Li, T.; Wang, J.; Zhu, J.; Sun, Y.; Wang, C.; Zhan, X. A Facile Planar Fused-Ring Electron Acceptor for As-Cast Polymer Solar Cells with 8.71% Efficiency. *J. Am. Chem. Soc.* **2016**, *138* (9), 2973–2976. https://doi.org/10.1021/jacs.6b00853.
(36) Jia, B.; Wang, J.; Wu, Y.; Zhang, M.; Jiang, Y.; Tang, Z.; Russell, T. P.; Zhan, X. Enhancing the Performance of a Fused-Ring Electron Acceptor by Unidirectional Extension. *J. Am. Chem. Soc.* **2019**, *141* (48), 19023–19031. https://doi.org/10.1021/jacs.9b08988.
(37) Dai, S.; Zhao, F.; Zhang, Q.; Lau, T.-K.; Li, T.; Liu, K.; Ling, Q.; Wang, C.; Lu, X.; You, W.; Zhan, X. Fused Nonacyclic Electron Acceptors for Efficient Polymer Solar Cells. *J. Am. Chem. Soc.* **2017**, *139* (3), 1336–1343. https://doi.org/10.1021/jacs.6b12755.
(38) Wang, J.; Zhang, J.; Xiao, Y.; Xiao, T.; Zhu, R.; Yan, C.; Fu, Y.; Lu, G.; Lu, X.; Marder, S. R.; Zhan, X. Effect of Isomerization on High-Performance Nonfullerene Electron Acceptors. *J. Am. Chem. Soc.* **2018**, *140* (29), 9140–9147. https://doi.org/10.1021/jacs.8b04027.
(39) Li, T.; Dai, S.; Ke, Z.; Yang, L.; Wang, J.; Yan, C.; Ma, W.; Zhan, X. Fused Tris(Thienothiophene)-Based Electron Acceptor with Strong Near-Infrared Absorption for High-Performance As-Cast Solar Cells. *Adv. Mater.* **2018**, *30* (10), 1705969. https://doi.org/10.1002/adma.201705969.
(40) Yuan, J.; Zhang, Y.; Zhou, L.; Zhang, G.; Yip, H.-L.; Lau, T.-K.; Lu, X.; Zhu, C.; Peng, H.; Johnson, P. A.; Leclerc, M.; Cao, Y.; Ulanski, J.; Li, Y.; Zou, Y. Single-Junction Organic Solar Cell with over 15% Efficiency Using Fused-Ring Acceptor with Electron-Deficient Core. *Joule* **2019**, *3* (4), 1140–1151. https://doi.org/10.1016/j.joule.2019.01.004.
(41) Liu, Q.; Jiang, Y.; Jin, K.; Qin, J.; Xu, J.; Li, W.; Xiong, J.; Liu, J.; Xiao, Z.; Sun, K.; Yang, S.; Zhang, X.; Ding, L. 18% Efficiency Organic Solar Cells. *Sci. Bull.* **2020**, *65* (4), 272–275. https://doi.org/10.1016/j.scib.2020.01.001.

(42) Wei, Y.; Chen, Z.; Lu, G.; Yu, N.; Li, C.; Gao, J.; Gu, X.; Hao, X.; Lu, G.; Tang, Z.; Zhang, J.; Wei, Z.; Zhang, X.; Huang, H. Binary Organic Solar Cells Breaking 19% via Manipulating the Vertical Component Distribution. *Adv. Mater.* **2022**, *34* (33), 2204718. https://doi.org/10.1002/adma.202204718.
(43) Han, C.; Wang, J.; Zhang, S.; Chen, L.; Bi, F.; Wang, J.; Yang, C.; Wang, P.; Li, Y.; Bao, X. Over 19% Efficiency Organic Solar Cells by Regulating Multidimensional Intermolecular Interactions. *Adv. Mater.* **2023**, *35* (10), 2208986. https://doi.org/10.1002/adma.202208986.
(44) Xu, X.; Yu, L.; Meng, H.; Dai, L.; Yan, H.; Li, R.; Peng, Q. Polymer Solar Cells with 18.74% Efficiency: From Bulk Heterojunction to Interdigitated Bulk Heterojunction. *Adv. Funct. Mater.* **2022**, *32* (4), 2108797. https://doi.org/10.1002/adfm.202108797.
(45) Yuan, J.; Zhang, H.; Zhang, R.; Wang, Y.; Hou, J.; Leclerc, M.; Zhan, X.; Huang, F.; Gao, F.; Zou, Y.; Li, Y. Reducing Voltage Losses in the A-DA′D-A Acceptor-Based Organic Solar Cells. *Chem* **2020**, *6* (9), 2147–2161. https://doi.org/10.1016/j.chempr.2020.08.003.
(46) Jao, M.-H.; Liao, H.-C.; Su, W.-F. Achieving a High Fill Factor for Organic Solar Cells. *J. Mater. Chem. A* **2016**, *4* (16), 5784–5801. https://doi.org/10.1039/C6TA00126B.
(47) Liu, S.; Yuan, J.; Deng, W.; Luo, M.; Xie, Y.; Liang, Q.; Zou, Y.; He, Z.; Wu, H.; Cao, Y. High-Efficiency Organic Solar Cells with Low Non-Radiative Recombination Loss and Low Energetic Disorder. *Nat. Photonics* **2020**, *14* (5), 300–305. https://doi.org/10.1038/s41566-019-0573-5.
(48) Tokmoldin, N.; Vollbrecht, J.; Hosseini, S. M.; Sun, B.; Perdigón-Toro, L.; Woo, H. Y.; Zou, Y.; Neher, D.; Shoaee, S. Explaining the Fill-Factor and Photocurrent Losses of Nonfullerene Acceptor-Based Solar Cells by Probing the Long-Range Charge Carrier Diffusion and Drift Lengths. *Adv. Energy Mater.* **2021**, *11* (22), 2100804. https://doi.org/10.1002/aenm.202100804.
(49) Po, R.; Bianchi, G.; Carbonera, C.; Pellegrino, A. "All That Glisters Is Not Gold": An Analysis of the Synthetic Complexity of Efficient Polymer Donors for Polymer Solar Cells. *Macromolecules* **2015**, *48* (3), 453–461. https://doi.org/10.1021/ma501894w.
(50) Li, N.; McCulloch, I.; Brabec, C. J. Analyzing the Efficiency, Stability and Cost Potential for Fullerene-Free Organic Photovoltaics in One Figure of Merit. *Energy Environ. Sci.* **2018**, *11* (6), 1355–1361. https://doi.org/10.1039/C8EE00151K.
(51) Jeon, S. J.; Han, Y. W.; Moon, D. K. Chlorine Effects of Heterocyclic Ring-Based Donor Polymer for Low-Cost and High-Performance Nonfullerene Polymer Solar Cells. *Sol. RRL* **2019**, *3* (7), 1900094. https://doi.org/10.1002/solr.201900094.
(52) Yuan, D.; Pan, F.; Zhang, L.; Jiang, H.; Chen, M.; Tang, W.; Qin, G.; Cao, Y.; Chen, J. Improved Average Figure-of-Merit of High-Efficiency Nonfullerene Solar Cells via Minor Combinatory Side Chain Approach. *Sol. RRL* **2020**, 2000062. https://doi.org/10.1002/solr.202000062.
(53) Rech, J. J.; Neu, J.; Qin, Y.; Samson, S.; Shanahan, J.; Josey, R. F.; Ade, H.; You, W. Designing Simple Conjugated Polymers for Scalable and Efficient Organic Solar Cells. *ChemSusChem* **2021**, *14* (17), 3561–3568. https://doi.org/10.1002/cssc.202100910.
(54) Pan, H.; Li, Y.; Wu, Y.; Liu, P.; Ong, B. S.; Zhu, S.; Xu, G. Low-Temperature, Solution-Processed, High-Mobility Polymer Semiconductors for Thin-Film Transistors. *J. Am. Chem. Soc.* **2007**, *129* (14), 4112–4113. https://doi.org/10.1021/ja067879o.
(55) Pan, H.; Wu, Y.; Li, Y.; Liu, P.; Ong, B. S.; Zhu, S.; Xu, G. Benzodithiophene Copolymer—A Low-Temperature, Solution-Processed High-Performance Semiconductor for Thin-Film Transistors. *Adv. Funct. Mater.* **2007**, *17* (17), 3574–3579. https://doi.org/10.1002/adfm.200601242.

(56) Yao, H.; Ye, L.; Zhang, H.; Li, S.; Zhang, S.; Hou, J. Molecular Design of Benzodithiophene-Based Organic Photovoltaic Materials. *Chem. Rev.* **2016**, *116* (12), 7397–7457. https://doi.org/10.1021/acs.chemrev.6b00176.
(57) He, K.; Kumar, P.; Yuan, Y.; Zhang, Z.; Li, X.; Liu, H.; Wang, J.; Li, Y. A Wide Bandgap Polymer Donor Composed of Benzodithiophene and Oxime-Substituted Thiophene for High-Performance Organic Solar Cells. *ACS Appl. Mater. Interfaces* **2021**, *13* (22), 26441–26450. https://doi.org/10.1021/acsami.1c02442.
(58) Liu, Q.; Jiang, Y.; Jin, K.; Qin, J.; Xu, J.; Li, W.; Xiong, J.; Liu, J.; Xiao, Z.; Sun, K.; Yang, S.; Zhang, X.; Ding, L. 18% Efficiency Organic Solar Cells. *Sci. Bull.* **2020**, *65* (4), 272–275. https://doi.org/10.1016/j.scib.2020.01.001.
(59) Rani, A.; Zafar, F.; Hussain, R.; Adnan, M.; Iqbal, J.; Zafar, W.-U.-I.; Noureen Shahi, M.; Kousar, S. Impact of π-Linker Modifications on the Photovoltaic Performance of Organic Solar Cells: A Theoratical Perspective. *Comput. Theor. Chem.* **2023**, *1225*, 114137. https://doi.org/10.1016/j.comptc.2023.114137.
(60) Kranthiraja, K.; Gunasekar, K.; Cho, W.; Park, Y. G.; Lee, J. Y.; Shin, Y.; Kang, I.-N.; Song, M.; Chae, K. H.; Kim, B.; Jin, S.-H. Influential Effects of π-Spacers, Alkyl Side Chains, and Various Processing Conditions on the Photovoltaic Properties of Alkylselenyl Substituted Benzodithiophene Based Polymers. *J. Mater. Chem. C* **2015**, *3* (4), 796–808. https://doi.org/10.1039/C4TC02092H.
(61) Tong, Y.; Xiao, Z.; Du, X.; Zuo, C.; Li, Y.; Lv, M.; Yuan, Y.; Yi, C.; Hao, F.; Hua, Y.; Lei, T.; Lin, Q.; Sun, K.; Zhao, D.; Duan, C.; Shao, X.; Li, W.; Yip, H.-L.; Xiao, Z.; Zhang, B.; Bian, Q.; Cheng, Y.; Liu, S.; Cheng, M.; Jin, Z.; Yang, S.; Ding, L. Progress of the Key Materials for Organic Solar Cells. *Sci. China Chem.* **2020**, *63* (6), 758–765. https://doi.org/10.1007/s11426-020-9726-0.
(62) Knupfer, M. Exciton Binding Energies in Organic Semiconductors. *Appl. Phys. A* **2003**, *77* (5), 623–626. https://doi.org/10.1007/s00339-003-2182-9.
(63) Li, H.-W.; Guan, Z.; Cheng, Y.; Lui, T.; Yang, Q.; Lee, C.-S.; Chen, S.; Tsang, S.-W. On the Study of Exciton Binding Energy with Direct Charge Generation in Photovoltaic Polymers. *Adv. Electron. Mater.* **2016**, *2* (11), 1600200. https://doi.org/10.1002/aelm.201600200.
(64) Ramki, K.; Venkatesh, N.; Sathiyan, G.; Thangamuthu, R.; Sakthivel, P. A Comprehensive Review on the Reasons behind Low Power Conversion Efficiency of Dibenzo Derivatives Based Donors in Bulk Heterojunction Organic Solar Cells. *Org. Electron.* **2019**, *73*, 182–204. https://doi.org/10.1016/j.orgel.2019.05.047.
(65) Mehmood, U.; Al-Ahmed, A.; Hussein, I. A. Review on Recent Advances in Polythiophene Based Photovoltaic Devices. *Renew. Sustain. Energy Rev.* **2016**, *57*, 550–561. https://doi.org/10.1016/j.rser.2015.12.177.
(66) Wang, G.; Melkonyan, F. S.; Facchetti, A.; Marks, T. J. All-Polymer Solar Cells: Recent Progress, Challenges, and Prospects. *Angew. Chem. Int. Ed.* **2019**, *58* (13), 4129–4142. https://doi.org/10.1002/anie.201808976.
(67) Seif, J. P. Window Layers for Silicon Heterojunction Solar Cells: Properties and Impact on Device Performance.
(68) Li, Y.; Sonar, P.; Murphy, L.; Hong, W. High Mobility Diketopyrrolopyrrole (DPP)-Based Organic Semiconductor Materials for Organic Thin Film Transistors and Photovoltaics. *Energy Environ. Sci.* **2013**, *6* (6), 1684. https://doi.org/10.1039/c3ee00015j.
(69) Zhou, K.; Dong, H.; Zhang, H.; Hu, W. High Performance N-Type and Ambipolar Small Organic Semiconductors for Organic Thin Film Transistors. *Phys Chem Chem Phys* **2014**, *16* (41), 22448–22457. https://doi.org/10.1039/C4CP01700E.

(70) Quinn, J. T. E.; Zhu, J.; Li, X.; Wang, J.; Li, Y. Recent Progress in the Development of N-Type Organic Semiconductors for Organic Field Effect Transistors. *J. Mater. Chem. C* **2017**, *5* (34), 8654–8681. https://doi.org/10.1039/C7TC01680H.
(71) Koster, L. J. A.; Shaheen, S. E.; Hummelen, J. C. Pathways to a New Efficiency Regime for Organic Solar Cells. *Adv. Energy Mater.* **2012**, *2* (10), 1246–1253. https://doi.org/10.1002/aenm.201200103.
(72) Sun, L.; Xu, X.; Song, S.; Zhang, Y.; Miao, C.; Liu, X.; Xing, G.; Zhang, S. Medium-Bandgap Conjugated Polymer Donors for Organic Photovoltaics. *Macromol. Rapid Commun.* **2019**, *40* (14), 1900074. https://doi.org/10.1002/marc.201900074.
(73) Liao, S.-H.; Jhuo, H.-J.; Cheng, Y.-S.; Chen, S.-A. Fullerene Derivative-Doped Zinc Oxide Nanofilm as the Cathode of Inverted Polymer Solar Cells with Low-Bandgap Polymer (PTB7-Th) for High Performance. *Adv. Mater.* **2013**, *25* (34), 4766–4771. https://doi.org/10.1002/adma.201301476.
(74) Zhao, J.; Li, Q.; Liu, S.; Cao, Z.; Jiao, X.; Cai, Y.-P.; Huang, F. Bithieno[3,4- *c*]Pyrrole-4,6-Dione-Mediated Crystallinity in Large-Bandgap Polymer Donors Directs Charge Transportation and Recombination in Efficient Nonfullerene Polymer Solar Cells. *ACS Energy Lett.* **2020**, *5* (2), 367–375. https://doi.org/10.1021/acsenergylett.9b02842.
(75) Qian, D.; Ye, L.; Zhang, M.; Liang, Y.; Li, L.; Huang, Y.; Guo, X.; Zhang, S.; Tan, Z.; Hou, J. Design, Application, and Morphology Study of a New Photovoltaic Polymer with Strong Aggregation in Solution State. *Macromolecules* **2012**, *45* (24), 9611–9617. https://doi.org/10.1021/ma301900h.
(76) Sworakowski, J.; Lipiński, J.; Janus, K. On the Reliability of Determination of Energies of HOMO and LUMO Levels in Organic Semiconductors from Electrochemical Measurements. A Simple Picture Based on the Electrostatic Model. *Org. Electron.* **2016**, *33*, 300–310. https://doi.org/10.1016/j.orgel.2016.03.031.
(77) Dandrade, B.; Datta, S.; Forrest, S.; Djurovich, P.; Polikarpov, E.; Thompson, M. Relationship between the Ionization and Oxidation Potentials of Molecular Organic Semiconductors. *Org. Electron.* **2005**, *6* (1), 11–20. https://doi.org/10.1016/j.orgel.2005.01.002.
(78) Chandross, M.; Mazumdar, S.; Jeglinski, S.; Wei, X.; Vardeny, Z. V.; Kwock, E. W.; Miller, T. M. Excitons in Poly(*Para* -Phenylenevinylene). *Phys. Rev. B* **1994**, *50* (19), 14702–14705. https://doi.org/10.1103/PhysRevB.50.14702.
(79) Wang, Z. B.; Helander, M. G.; Greiner, M. T.; Qiu, J.; Lu, Z. H. Analysis of Charge-Injection Characteristics at Electrode-Organic Interfaces: Case Study of Transition-Metal Oxides. *Phys Rev B* **2009**, *80* (23), 235325. https://doi.org/10.1103/PhysRevB.80.235325.
(80) Kokil, A.; Yang, K.; Kumar, J. Techniques for Characterization of Charge Carrier Mobility in Organic Semiconductors. *J. Polym. Sci. Part B Polym. Phys.* **2012**, *50* (15), 1130–1144. https://doi.org/10.1002/polb.23103.
(81) Dunlap, W. C.; Watters, R. L. Direct Measurement of the Dielectric Constants of Silicon and Germanium. *Phys. Rev.* **1953**, *92* (6), 1396–1397. https://doi.org/10.1103/PhysRev.92.1396.
(82) Yang, Z.; Surrente, A.; Galkowski, K.; Bruyant, N.; Maude, D. K.; Haghighirad, A. A.; Snaith, H. J.; Plochocka, P.; Nicholas, R. J. Unraveling the Exciton Binding Energy and the Dielectric Constant in Single-Crystal Methylammonium Lead Triiodide Perovskite. *J. Phys. Chem. Lett.* **2017**, *8* (8), 1851–1855. https://doi.org/10.1021/acs.jpclett.7b00524.
(83) Cho, N.; Schlenker, C. W.; Knesting, K. M.; Koelsch, P.; Yip, H.; Ginger, D. S.; Jen, A. K. -Y. High-Dielectric Constant Side-Chain Polymers Show Reduced Non-Geminate Recombination in Heterojunction Solar Cells. *Adv. Energy Mater.* **2014**, *4* (10), 1301857. https://doi.org/10.1002/aenm.201301857.

(84) Macfarlane, G. G.; McLean, T. P.; Quarrington, J. E.; Roberts, V. Exciton and Phonon Effects in the Absorption Spectra of Germanium and Silicon. *J. Phys. Chem. Solids* **1959**, *8*, 388–392. https://doi.org/10.1016/0022-3697(59)90372-5.
(85) Lin, Q.; Armin, A.; Nagiri, R. C. R.; Burn, P. L.; Meredith, P. Electro-Optics of Perovskite Solar Cells. *Nat. Photonics* **2015**, *9* (2), 106–112. https://doi.org/10.1038/nphoton.2014.284.
(86) Chen, X.; Lu, H.; Yang, Y.; Beard, M. C. Excitonic Effects in Methylammonium Lead Halide Perovskites. *J. Phys. Chem. Lett.* **2018**, *9* (10), 2595–2603. https://doi.org/10.1021/acs.jpclett.8b00526.
(87) He, K.; Li, X.; Liu, H.; Zhang, Z.; Kumar, P.; Ngai, J. H. L.; Wang, J.; Li, Y. D-A Polymer with a Donor Backbone - Acceptor-side-chain Structure for Organic Solar Cells. *Asian J. Org. Chem.* **2020**, *9* (9), 1301–1308. https://doi.org/10.1002/ajoc.202000172.
(88) Mohapatra, A. A.; Dong, Y.; Boregowda, P.; Mohanty, A.; Sadhanala, A.; Jiao, X.; Narayan, A.; McNeill, C. R.; Durrant, J. R.; Patil, S. Rational Design of Donor–Acceptor Based Semiconducting Copolymers with High Dielectric Constants. *J. Phys. Chem. C* **2021**, *125* (12), 6886–6896. https://doi.org/10.1021/acs.jpcc.1c00340.
(89) Brebels, J.; Manca, J. V.; Lutsen, L.; Vanderzande, D.; Maes, W. High Dielectric Constant Conjugated Materials for Organic Photovoltaics. *J. Mater. Chem. A* **2017**, *5* (46), 24037–24050. https://doi.org/10.1039/C7TA06808E.
(90) Wang, C.; Zhang, Z.; Pejić, S.; Li, R.; Fukuto, M.; Zhu, L.; Sauvé, G. High Dielectric Constant Semiconducting Poly(3-Alkylthiophene)s from Side Chain Modification with Polar Sulfinyl and Sulfonyl Groups. *Macromolecules* **2018**, *51* (22), 9368–9381. https://doi.org/10.1021/acs.macromol.8b01895.
(91) Gao, Y.; Cui, M.; Qu, S.; Zhao, H.; Shen, Z.; Tan, F.; Dong, Y.; Qin, C.; Wang, Z.; Zhang, W.; Wang, Z.; Lei, Y. Efficient Organic Solar Cells Enabled by Simple Non-Fused Electron Donors with Low Synthetic Complexity. *Small* **2022**, *18* (3), 2104623. https://doi.org/10.1002/smll.202104623.
(92) Qin, Y.; Uddin, M. A.; Chen, Y.; Jang, B.; Zhao, K.; Zheng, Z.; Yu, R.; Shin, T. J.; Woo, H. Y.; Hou, J. Highly Efficient Fullerene-Free Polymer Solar Cells Fabricated with Polythiophene Derivative. *Adv. Mater.* **2016**, *28* (42), 9416–9422. https://doi.org/10.1002/adma.201601803.
(93) Yao, H.; Cui, Y.; Qian, D.; Ponseca, C. S.; Honarfar, A.; Xu, Y.; Xin, J.; Chen, Z.; Hong, L.; Gao, B.; Yu, R.; Zu, Y.; Ma, W.; Chabera, P.; Pullerits, T.; Yartsev, A.; Gao, F.; Hou, J. 14.7% Efficiency Organic Photovoltaic Cells Enabled by Active Materials with a Large Electrostatic Potential Difference. *J. Am. Chem. Soc.* **2019**, *141* (19), 7743–7750. https://doi.org/10.1021/jacs.8b12937.
(94) Park, G. E.; Choi, S.; Park, S. Y.; Lee, D. H.; Cho, M. J.; Choi, D. H. Eco-Friendly Solvent-Processed Fullerene-Free Polymer Solar Cells with over 9.7% Efficiency and Long-Term Performance Stability. *Adv. Energy Mater.* **2017**, *7* (19), 1700566. https://doi.org/10.1002/aenm.201700566.
(95) Liu, Y.; Lu, H.; Li, M.; Zhang, Z.; Feng, S.; Xu, X.; Wu, Y.; Bo, Z. Enhancing the Performance of Non-Fullerene Organic Solar Cells Using Regioregular Wide-Bandgap Polymers. *Macromolecules* **2018**, *51* (21), 8646–8651. https://doi.org/10.1021/acs.macromol.8b01677.
(96) Meng, B.; Miao, J.; Liu, J.; Wang, L. A New Polymer Electron Acceptor Based on Thiophene-*S,S* -Dioxide Unit for Organic Photovoltaics. *Macromol. Rapid Commun.* **2018**, *39* (2), 1700505. https://doi.org/10.1002/marc.201700505.
(97) Magurudeniya, H. D.; Kularatne, R. S.; Rainbolt, E. A.; Bhatt, M. P.; Murphy, J. W.; Sheina, E. E.; Gnade, B. E.; Biewer, M. C.; Stefan, M. C. Benzodithiophene Homopolymers Synthesized

by Grignard Metathesis (GRIM) and Stille Coupling Polymerizations. *J Mater Chem A* **2014**, *2* (23), 8773–8781. https://doi.org/10.1039/C4TA01739K.
(98) Pathiranage, T. M. S. K.; Magurudeniya, H. D.; Biewer, M. C.; Stefan, M. C. Effect of Thiophene Spacers in Benzodithiophene-based Polymers for Organic Electronics. *J. Polym. Sci. Part Polym. Chem.* **2017**, *55* (23), 3942–3948. https://doi.org/10.1002/pola.28781.
(99) Chen, S.; Liu, Y.; Zhang, L.; Chow, P. C. Y.; Wang, Z.; Zhang, G.; Ma, W.; Yan, H. A Wide-Bandgap Donor Polymer for Highly Efficient Non-Fullerene Organic Solar Cells with a Small Voltage Loss. *J. Am. Chem. Soc.* **2017**, *139* (18), 6298–6301. https://doi.org/10.1021/jacs.7b01606.
(100) Li, S.; Ye, L.; Zhao, W.; Yan, H.; Yang, B.; Liu, D.; Li, W.; Ade, H.; Hou, J. A Wide Band Gap Polymer with a Deep Highest Occupied Molecular Orbital Level Enables 14.2% Efficiency in Polymer Solar Cells. *J. Am. Chem. Soc.* **2018**, *140* (23), 7159–7167. https://doi.org/10.1021/jacs.8b02695.
(101) Zhang, J.; Liu, W.; Zhang, M.; Liu, Y.; Zhou, G.; Xu, S.; Zhang, F.; Zhu, H.; Liu, F.; Zhu, X. Revealing the Critical Role of the HOMO Alignment on Maximizing Current Extraction and Suppressing Energy Loss in Organic Solar Cells. *iScience* **2019**, *19*, 883–893. https://doi.org/10.1016/j.isci.2019.08.038.
(102) Kawashima, K.; Tamai, Y.; Ohkita, H.; Osaka, I.; Takimiya, K. High-Efficiency Polymer Solar Cells with Small Photon Energy Loss. *Nat. Commun.* **2015**, *6* (1), 10085. https://doi.org/10.1038/ncomms10085.
(103) Armin, A.; Kassal, I.; Shaw, P. E.; Hambsch, M.; Stolterfoht, M.; Lyons, D. M.; Li, J.; Shi, Z.; Burn, P. L.; Meredith, P. Spectral Dependence of the Internal Quantum Efficiency of Organic Solar Cells: Effect of Charge Generation Pathways. *J. Am. Chem. Soc.* **2014**, *136* (32), 11465–11472. https://doi.org/10.1021/ja505330x.
(104) Murphy, L.; Hong, W.; Aziz, H.; Li, Y. Influences of Using a High Mobility Donor Polymer on Solar Cell Performance. *Org. Electron.* **2013**, *14* (12), 3484–3492. https://doi.org/10.1016/j.orgel.2013.09.024.
(105) Jao, M.-H.; Liao, H.-C.; Su, W.-F. Achieving a High Fill Factor for Organic Solar Cells. *J. Mater. Chem. A* **2016**, *4* (16), 5784–5801. https://doi.org/10.1039/C6TA00126B.
(106) Liu, F.; Gu, Y.; Shen, X.; Ferdous, S.; Wang, H.-W.; Russell, T. P. Characterization of the Morphology of Solution-Processed Bulk Heterojunction Organic Photovoltaics. *Prog. Polym. Sci.* **2013**, *38* (12), 1990–2052. https://doi.org/10.1016/j.progpolymsci.2013.07.010.
(107) Yuan, J.; Zhang, Y.; Zhou, L.; Zhang, G.; Yip, H.-L.; Lau, T.-K.; Lu, X.; Zhu, C.; Peng, H.; Johnson, P. A.; Leclerc, M.; Cao, Y.; Ulanski, J.; Li, Y.; Zou, Y. Single-Junction Organic Solar Cell with over 15% Efficiency Using Fused-Ring Acceptor with Electron-Deficient Core. *Joule* **2019**, *3* (4), 1140–1151. https://doi.org/10.1016/j.joule.2019.01.004.
(108) Zhang, H.; Yao, H.; Hou, J.; Zhu, J.; Zhang, J.; Li, W.; Yu, R.; Gao, B.; Zhang, S.; Hou, J. Over 14% Efficiency in Organic Solar Cells Enabled by Chlorinated Nonfullerene Small-Molecule Acceptors. *Adv. Mater.* **2018**, *30* (28), 1800613. https://doi.org/10.1002/adma.201800613.
(109) Fan, Q.; Zhu, Q.; Xu, Z.; Su, W.; Chen, J.; Wu, J.; Guo, X.; Ma, W.; Zhang, M.; Li, Y. Chlorine Substituted 2D-Conjugated Polymer for High-Performance Polymer Solar Cells with 13.1% Efficiency via Toluene Processing. *Nano Energy* **2018**, *48*, 413–420. https://doi.org/10.1016/j.nanoen.2018.04.002.
(110) Zhang, M.; Zhu, L.; Zhou, G.; Hao, T.; Qiu, C.; Zhao, Z.; Hu, Q.; Larson, B. W.; Zhu, H.; Ma, Z.; Tang, Z.; Feng, W.; Zhang, Y.; Russell, T. P.; Liu, F. Single-Layered Organic Photovoltaics with Double Cascading Charge Transport Pathways: 18% Efficiencies. *Nat. Commun.* **2021**, *12* (1), 309. https://doi.org/10.1038/s41467-020-20580-8.

(111) Liu, Q.; Jiang, Y.; Jin, K.; Qin, J.; Xu, J.; Li, W.; Xiong, J.; Liu, J.; Xiao, Z.; Sun, K.; Yang, S.; Zhang, X.; Ding, L. 18% Efficiency Organic Solar Cells. *Sci. Bull.* **2020**, *65* (4), 272–275. https://doi.org/10.1016/j.scib.2020.01.001.
(112) Qin, J.; Zhang, L.; Zuo, C.; Xiao, Z.; Yuan, Y.; Yang, S.; Hao, F.; Cheng, M.; Sun, K.; Bao, Q.; Bin, Z.; Jin, Z.; Ding, L. A Chlorinated Copolymer Donor Demonstrates a 18.13% Power Conversion Efficiency. *J. Semicond.* **2021**, *42* (1), 010501. https://doi.org/10.1088/1674-4926/42/1/010501.
(113) He, K.; Kumar, P.; Yuan, Y.; Li, Y. Wide Bandgap Polymer Donors for High Efficiency Non-Fullerene Acceptor Based Organic Solar Cells. *Mater. Adv.* **2021**, 10.1039.D0MA00790K. https://doi.org/10.1039/D0MA00790K.
(114) Zhang, S.; Qin, Y.; Zhu, J.; Hou, J. Over 14% Efficiency in Polymer Solar Cells Enabled by a Chlorinated Polymer Donor. *Adv. Mater.* **2018**, *30* (20), 1800868. https://doi.org/10.1002/adma.201800868.
(115) Li, Y.; Vamvounis, G.; Holdcroft, S. Tuning Optical Properties and Enhancing Solid-State Emission of Poly(Thiophene)s by Molecular Control: A Postfunctionalization Approach. *Macromolecules* **2002**, *35* (18), 6900–6906. https://doi.org/10.1021/ma020140o.
(116) Chen, Y.; Li, M.; Wang, Y.; Wang, J.; Zhang, M.; Zhou, Y.; Yang, J.; Liu, Y.; Liu, F.; Tang, Z.; Bao, Q.; Bo, Z. A Fully Non-fused Ring Acceptor with Planar Backbone and Near-IR Absorption for High Performance Polymer Solar Cells. *Angew. Chem.* **2020**, *132* (50), 22903–22909. https://doi.org/10.1002/ange.202010856.
(117) Chelucci, G. Synthesis and Metal-Catalyzed Reactions of *Gem* -Dihalovinyl Systems. *Chem. Rev.* **2012**, *112* (3), 1344–1462. https://doi.org/10.1021/cr200165q.
(118) Bhadury, P. S.; Palit, M.; Sharma, M.; Raza, S. K.; Jaiswal, D. K. Fluorinated Phosphonium Ylides: Versatile in Situ Wittig Intermediates in the Synthesis of Hydrofluorocarbons. *J. Fluor. Chem.* **2002**.
(119) Loska, R.; Szachowicz, K.; Szydlik, D. Synthesis of Alkyl Aryl(Heteroaryl)Acetates from *N* -Oxides, 1,1-Difluorostyrenes, and Alcohols. *Org. Lett.* **2013**, *15* (22), 5706–5709. https://doi.org/10.1021/ol402735m.
(120) Liu, J.; Yang, J.; Ferretti, F.; Jackstell, R.; Beller, M. Pd-Catalyzed Selective Carbonylation of *Gem* -Difluoroalkenes: A Practical Synthesis of Difluoromethylated Esters. *Angew. Chem. Int. Ed.* **2019**, *58* (14), 4690–4694. https://doi.org/10.1002/anie.201813801.
(121) Nenajdenko, V. G.; Shastin, A. V.; Korotchenko, V. N.; Balenkova, E. S. Conversion of Aromatic Aldehydes into 1-Aryl-2,2-Dichloroethenes.
(122) Shin, J.; Um, H. A.; Lee, D. H.; Lee, T. W.; Cho, M. J.; Choi, D. H. High Mobility Isoindigo-Based π-Extended Conjugated Polymers Bearing Di(Thienyl)Ethylene in Thin-Film Transistors. *Polym. Chem.* **2013**, *4* (23), 5688. https://doi.org/10.1039/c3py00735a.
(123) Spano, F. C.; Silva, C. H- and J-Aggregate Behavior in Polymeric Semiconductors. *Annu. Rev. Phys. Chem.* **2014**, *65* (1), 477–500. https://doi.org/10.1146/annurev-physchem-040513-103639.
(124) He, Y.; Guo, C.; Sun, B.; Quinn, J.; Li, Y. (3E,7E)-3,7-Bis(2-Oxoindolin-3-Ylidene)-5,7-Dihydropyrrolo[2,3-f]Indole-2,6(1H,3H)-Dione Based Polymers for Ambipolar Organic Thin Film Transistors. *Chem. Commun.* **2015**, *51* (38), 8093–8096. https://doi.org/10.1039/C5CC01021G.
(125) Bayliss, N. S. The Free-Electron Approximation for Conjugated Compounds. *Q. Rev. Chem. Soc.* **1952**, *6* (4), 319. https://doi.org/10.1039/qr9520600319.

(126) Meier, H.; Gerold, J.; Kolshorn, H.; Mühling, B. Extension of Conjugation Leading to Bathochromic or Hypsochromic Effects in OPV Series. *Chem. – Eur. J.* **2004**, *10* (2), 360–370. https://doi.org/10.1002/chem.200305447.
(127) Elizarov, S. G.; Ozimova, A. E.; Khodarev, A. N.; Paraschuk, D. Yu.; Arnautov, S. A.; Nechvolodova, E. M. Laser Light Scattering as a Probe of Phase Separation in Conjugated Polymer Films of Donor-Acceptor Blends; Bagayev, S. N., Chikishev, A., Dmitriev, A., Ducloy, M., Heinz, T., Letokhov, V., Shkurinov, A., Takahashi, H., Eds.; 2006; pp 62570Z-62570Z – 10. https://doi.org/10.1117/12.678393.
(128) Liu, J.; Chen, S.; Qian, D.; Gautam, B.; Yang, G.; Zhao, J.; Bergqvist, J.; Zhang, F.; Ma, W.; Ade, H.; Inganäs, O.; Gundogdu, K.; Gao, F.; Yan, H. Fast Charge Separation in a Non-Fullerene Organic Solar Cell with a Small Driving Force. *Nat. Energy* **2016**, *1* (7), 16089. https://doi.org/10.1038/nenergy.2016.89.
(129) Jiang, Y.; Liu, H.; Li, X.; Yuan, Y.; Wang, J.; Cui, B.; Li, Y. Alkyloxime-Substituted Thiophene-Based Wide-Band-Gap Polymer Donor Achieving a High Short Circuit Current Density of 30 mA Cm $^{-2}$ in Organic Solar Cells. *Chem. Mater.* **2022**, *34* (9), 4232–4241. https://doi.org/10.1021/acs.chemmater.2c00929.
(130) Menke, S. M.; Ran, N. A.; Bazan, G. C.; Friend, R. H. Understanding Energy Loss in Organic Solar Cells: Toward a New Efficiency Regime. *Joule* **2018**, *2* (1), 25–35. https://doi.org/10.1016/j.joule.2017.09.020.
(131) Sun, B.; Hong, W.; Aziz, H.; Abukhdeir, N. M.; Li, Y. Dramatically Enhanced Molecular Ordering and Charge Transport of a DPP-Based Polymer Assisted by Oligomers through Antiplasticization. *J. Mater. Chem. C* **2013**, *1* (29), 4423. https://doi.org/10.1039/c3tc30667d.
(132) Yao, S.; Huang, C.; Wang, Q.; Yang, T.; Shi, S.; Liu, Y.; Zhao, C.; Zhang, Z.; Shen, X.; Li, T.; He, B.; Lin, W.; Zhang, T.; Zou, B.; Liu, T. Tuning the Crystallinity and Phase Separation by Two-Step Annealing Enables Block Copolymer-Based Organic Solar Cells with 15% Efficiency. *Sol. RRL* **2022**, *6* (10), 2200617. https://doi.org/10.1002/solr.202200617.
(133) Wang, Y.; Xue, J.; Zhong, H.; Everett, C. R.; Jiang, X.; Reus, M. A.; Chumakov, A.; Roth, S. V.; Adedeji, M. A.; Jili, N.; Zhou, K.; Lu, G.; Tang, Z.; Mola, G. T.; Müller-Buschbaum, P.; Ma, W. Control of the Crystallization and Phase Separation Kinetics in Sequential Blade-Coated Organic Solar Cells by Optimizing the Upper Layer Processing Solvent. *Adv. Energy Mater.* **2023**, *13* (7), 2203496. https://doi.org/10.1002/aenm.202203496.
(134) Wang, Z.; Gao, K.; Kan, Y.; Zhang, M.; Qiu, C.; Zhu, L.; Zhao, Z.; Peng, X.; Feng, W.; Qian, Z.; Gu, X.; Jen, A. K.-Y.; Tang, B. Z.; Cao, Y.; Zhang, Y.; Liu, F. The Coupling and Competition of Crystallization and Phase Separation, Correlating Thermodynamics and Kinetics in OPV Morphology and Performances. *Nat. Commun.* **2021**, *12* (1), 332. https://doi.org/10.1038/s41467-020-20515-3.
(135) Qi, B.; Wang, J. Fill Factor in Organic Solar Cells. *Phys. Chem. Chem. Phys.* **2013**, *15* (23), 8972. https://doi.org/10.1039/c3cp51383a.
(136) Di Mario, L.; Garcia Romero, D.; Wang, H.; Tekelenburg, E. K.; Meems, S.; Zaharia, T.; Portale, G.; Loi, M. A. Outstanding Fill Factor in Inverted Organic Solar Cells with SnO_2 by Atomic Layer Deposition. *Adv. Mater.* **2023**, 2301404. https://doi.org/10.1002/adma.202301404.
(137) Tan, J.-K.; Png, R.-Q.; Zhao, C.; Ho, P. K. H. Ohmic Transition at Contacts Key to Maximizing Fill Factor and Performance of Organic Solar Cells. *Nat. Commun.* **2018**, *9* (1), 3269. https://doi.org/10.1038/s41467-018-05200-w.
(138) Zhang, X.; Li, C.; Xu, J.; Wang, R.; Song, J.; Zhang, H.; Li, Y.; Jing, Y.-N.; Li, S.; Wu, G.; Zhou, J.; Li, X.; Zhang, Y.; Li, X.; Zhang, J.; Zhang, C.; Zhou, H.; Sun, Y.; Zhang, Y. High Fill

Factor Organic Solar Cells with Increased Dielectric Constant and Molecular Packing Density. *Joule* **2022**, *6* (2), 444–457. https://doi.org/10.1016/j.joule.2022.01.006.
(139) Cevher, D.; Cevher, S. C.; Cirpan, A. Recently Developed Benzodithiophene Based Organic Solar Cells: A Review on Materials and Strategies. *Mater. Today Commun.* **2023**, *37*, 107524. https://doi.org/10.1016/j.mtcomm.2023.107524.
(140) Zheng, B.; Huo, L.; Li, Y. Benzodithiophenedione-Based Polymers: Recent Advances in Organic Photovoltaics. *NPG Asia Mater.* **2020**, *12* (1), 3. https://doi.org/10.1038/s41427-019-0163-5.
(141) Ye, L.; Zhang, S.; Huo, L.; Zhang, M.; Hou, J. Molecular Design toward Highly Efficient Photovoltaic Polymers Based on Two-Dimensional Conjugated Benzodithiophene. *Acc. Chem. Res.* **2014**, *47* (5), 1595–1603. https://doi.org/10.1021/ar5000743.
(142) Liang, Y.; Wu, Y.; Feng, D.; Tsai, S.-T.; Son, H.-J.; Li, G.; Yu, L. Development of New Semiconducting Polymers for High Performance Solar Cells. *J. Am. Chem. Soc.* **2009**, *131* (1), 56–57. https://doi.org/10.1021/ja808373p.
(143) Li, W.; Abd-Ellah, M.; Liu, H.; Li, X.; Yin, Z.; Kumar, P.; Wang, J.; Li, Y. Novel Wide Bandgap Benzodithiophene-Based Polymer Donors with Electron-Withdrawing Indolin-2-One Side Chains for Efficient Organic Solar Cells with High Open Circuit Voltage. *Dyes Pigments* **2022**, *197*, 109876. https://doi.org/10.1016/j.dyepig.2021.109876.
(144) He, K.; Kumar, P.; Abd-Ellah, M.; Liu, H.; Li, X.; Zhang, Z.; Wang, J.; Li, Y. Alkyloxime Side Chain Enabled Polythiophene Donors for Efficient Organic Solar Cells. *Macromolecules* **2020**, *53* (20), 8796–8808. https://doi.org/10.1021/acs.macromol.0c01548.
(145) Flynn, S.; Yuan, Y.; Cui, S.; Liu, H.; Li, X.; Wang, J.; Li, Y. Acetal- and Aldehyde-Substituted Thiophene-Benzodithiophene Copolymers for Organic Solar Cells. *ACS Appl. Energy Mater.* **2024**, *7* (3), 1277–1286. https://doi.org/10.1021/acsaem.3c02921.
(146) Wang, Z.; Liu, X.; Jiang, H.; Zhou, X.; Zhang, L.; Pan, F.; Qiao, X.; Ma, D.; Ma, W.; Ding, L.; Cao, Y.; Chen, J. Organic Solar Cells Based on High Hole Mobility Conjugated Polymer and Nonfullerene Acceptor with Comparable Bandgaps and Suitable Energy Level Offsets Showing Significant Suppression of $J_{sc} - V_{oc}$ Trade-Off. *Sol. RRL* **2019**, *3* (7), 1900079. https://doi.org/10.1002/solr.201900079.
(147) Zeinalvand Farzin, B.; Parhizkar, M.; Bidadi, H.; Abbasi, F. ZnO Nanoparticles and Polyaniline Blend as an Active Layer for Bulk Heterojunction Solar Cell Applications. *J. Mater. Sci. Mater. Electron.* **2018**, *29* (21), 18128–18135. https://doi.org/10.1007/s10854-018-9924-0.
(148) Li, C.; Gu, X.; Chen, Z.; Han, X.; Yu, N.; Wei, Y.; Gao, J.; Chen, H.; Zhang, M.; Wang, A.; Zhang, J.; Wei, Z.; Peng, Q.; Tang, Z.; Hao, X.; Zhang, X.; Huang, H. Achieving Record-Efficiency Organic Solar Cells upon Tuning the Conformation of Solid Additives. *J. Am. Chem. Soc.* **2022**, *144* (32), 14731–14739. https://doi.org/10.1021/jacs.2c05303.
(149) Li, C.; Zhou, J.; Song, J.; Xu, J.; Zhang, H.; Zhang, X.; Guo, J.; Zhu, L.; Wei, D.; Han, G.; Min, J.; Zhang, Y.; Xie, Z.; Yi, Y.; Yan, H.; Gao, F.; Liu, F.; Sun, Y. Non-Fullerene Acceptors with Branched Side Chains and Improved Molecular Packing to Exceed 18% Efficiency in Organic Solar Cells. *Nat. Energy* **2021**, *6* (6), 605–613. https://doi.org/10.1038/s41560-021-00820-x.
(150) Qian, D.; Zheng, Z.; Yao, H.; Tress, W.; Hopper, T. R.; Chen, S.; Li, S.; Liu, J.; Chen, S.; Zhang, J.; Liu, X.-K.; Gao, B.; Ouyang, L.; Jin, Y.; Pozina, G.; Buyanova, I. A.; Chen, W. M.; Inganäs, O.; Coropceanu, V.; Bredas, J.-L.; Yan, H.; Hou, J.; Zhang, F.; Bakulin, A. A.; Gao, F. Design Rules for Minimizing Voltage Losses in High-Efficiency Organic Solar Cells. *Nat. Mater.* **2018**, *17* (8), 703–709. https://doi.org/10.1038/s41563-018-0128-z.

(151) Yang, X.; Loos, J. Toward High-Performance Polymer Solar Cells: The Importance of Morphology Control. *Macromolecules* **2007**, *40* (5), 1353–1362. https://doi.org/10.1021/ma0618732.
(152) Zhao, F.; Wang, C.; Zhan, X. Morphology Control in Organic Solar Cells. *Adv. Energy Mater.* **2018**, *8* (28), 1703147. https://doi.org/10.1002/aenm.201703147.
(153) Ye, L.; Zhao, W.; Li, S.; Mukherjee, S.; Carpenter, J. H.; Awartani, O.; Jiao, X.; Hou, J.; Ade, H. High-Efficiency Nonfullerene Organic Solar Cells: Critical Factors That Affect Complex Multi-Length Scale Morphology and Device Performance. *Adv. Energy Mater.* **2017**, *7* (7), 1602000. https://doi.org/10.1002/aenm.201602000.